UNIVERSITY OF GENOVA

PHD PROGRAM IN BIOENGINEERING AND ROBOTICS

Force-Torque Sensing in Robotics

by

Francisco Javier Andrade Chavez

Thesis submitted for the degree of *Doctor of Philosophy* (31° cycle)

December 2018

Francesco Nori	Supervisor
Daniele Pucci	Supervisor
Silvio Traversaro	Co-Supervisor
Giorgio Cannata	Head of the PhD program

Thesis Jury and External Reviewers:

Olivier Stasse, *Directeur de Recherche CNRS at LAAS, Toulousse*	Jury, External reviewer
Andrea Del Prete, *Tenure-track assistant professor at University of Trento*	Jury
Matteo Fumagalli, *Associate Professor at Aalborg University Copenhagen*	Jury
Abderrahmane Kheddar, *Director of Research at CNRS-AIST JRL*	External reviewer

Dibris

Department of Informatics, Bioengineering,
Robotics and Systems Engineering

iit DIC
ISTITUTO ITALIANO
DI TECNOLOGIA

Dynamic Interaction Control Lab

I would like to dedicate this thesis to my family that has always believed in me and supported me in any way they can even from afar. To my parents, my sister, grandmas, uncles, aunts, and cousins I love you all. Of course, I dedicate this work also to my wife who brings me joy and is always there with me and for me when I need her. She boarded in the boat of my craziness and has not turned back. For this and many many other things you are my place to be, my home sweet home and my love sweet love. But most especially to my son Francisco Gabriel who changed my life more than I could have changed it myself. Whom would not let me work in his presence while motivating me to work harder, better, and faster with his bare existence. I will strive to give you the opportunity of doing what you love as I do. To you more than anyone I dedicate this thesis including this:

" You are the chaos that brought order to my life.
Of course, I knew I wanted you this bad.
That is why I feared you so hard.
I knew you would change my body, soul and mind.
And now you are here, crushing every escape.
Now I'm trapped because I hope you will hold me forever in your hands.
You hacked my brain, turn upside down my nights,
having me not knowing if I'm awake, hungry or what.
But it all makes sense and its worth every drop of sweat,
when you hold my hand, fall asleep in my lap
or give me the precious gift of your smile.
I'm here to stay, hoping to hear you tell me whatever you want.
Cause from now on I exist to ensure you get a beautiful life.
I am from now to eternity your dad
and there is no way I would have ever changed that. "

Your Dad.

Acknowledgements

I would like to acknowledge Universita degli studi di Genova for the opportunities they have given in these three years. To the National Council of Science and Technology (CONACYT) in Mexico for their support ever since the Master. To the Dynamic Interaction Control lab who took me in and help me grow as a researcher.
I would like to acknowledge as well the people from iCub facility that where there every time I needed something with a welcoming attitude. I would like to acknowledge especially the help of Silvio Traversaro, Gabriele Nava, Nuno Guedelha, and Luca Fiorio. Their help made my research life much easier and I would dare say possible. A special acknowledgment for Francesco Nori who decided I was a good candidate for the lab and to Daniele Pucci for letting me pursue my ideas while motivating me to keep up the good work.
For different reasons but just as important I would like to acknowledge all the people I have met during these three years. They made my life here rich in experiences and fun. Especially to the Team Tequila and the Mexican Mafia group, you guys are my family here.

Abstract

Being able to perform dynamic motions repeatably and reliably is an active research topic. The present thesis aims to contribute to this by improving the accuracy of force-torque sensing in robots. It focuses primarily on six axis force-torque sensors, although other sources of force-torque sensing are explored. Force sensing technologies, calibration procedures of these sensors and the use of force-torque sensing in robotics are described with the aim to familiarize the reader with the problem to solve. The problem is tackled in two ways: improving the accuracy of six axis force-torque sensors and exploring the use of tactile sensor arrays as force-torque sensors. The contributions of this thesis are : the development of the Model Based In situ calibration method for improving measurements of sensors already mounted on robots and the improvement in performance of the robot as a consequence; the design of a calibration device to improve the reliability and speed of calibration; and the improvement of force sensing information of a capacitive tactile array and its use on a robot as force-torque information source. The developed algorithms were tested on the humanoid robotic platform iCub.

Prologue

Robots are expected to perform highly dynamical motions. Being able to perform these motions repeatably and reliably is an active research topic. Achieving this type of motions requires information of the interaction forces that exist whenever a contact is established. This thesis aims to help to research this type of motions by enriching the quality of the information obtained during this kind of behaviors, more specifically force related quantities.
Science fiction has given us a lot of expectations in what a robot should look like and be able to do. It is not uncommon to see a robot walk, run, jump and even parkour in movies and cartoons. There are in fact some videos of actual robots starting to reach some of these dynamic behaviors. But in reality, we are far from reaching a point where a robot can move around in a reliable way. As mentioned by Boston Dynamic's CEO Marc Raibert, "In our videos we typically show the very best behavior. It's not the average behavior or typical behavior. And we think of it as an aspirational target for what the robots do."
A crucial part of these motions is the interaction of the robot with other objects or the environment. Whenever an interaction happens there exist an exchange of forces. As humans, we are only able to walk thanks to the gravity force keeping us anchored to the ground and the friction forces allowing us to propel forward.
A robot, as the machine that it is, bases its behavior on programmed responses to perceived stimulus. Independently of how the behavior is programmed a considerable part of the reliability comes from the perceived stimulus. When the stimulus is limited to a start command the behavior is executed in feedforward. In this way, the robot has no way of understanding if it has full filled its goal or not. By giving relevant information to the robot it is possible to create a self-correcting action to achieve the desired behavior. This relevant information is called feedback.
The nature of what is considered relevant information depends on the nature of the behavior involved. As mentioned, whenever there is an interaction with other objects or the environment there exist forces. It is then straight forward to see that knowledge about the exchanged forces is relevant information for dynamic behaviors.
Force-torque sensing is the ability to sense or measure the forces and torques exchanged

between two objects. There are mainly two interesting force sensing quantities for robots, the joint torques, and the contact forces.
The joint torques have a direct relationship with the output of the motors at the joints. Therefore, joint torques are relevant information for programming the behavior of the motors. This is usually done through joint torque controllers that benefit greatly from using joint torque values as feedback.
On the other hand, contact forces are the actual forces and torques exchanged at the contact location when an interaction between objects is happening. This information has a direct relationship with the effect an object can have on another object or in itself by exploiting the contact.
To measure this quantities many different kinds of sensors have been developed. A sensor is a device that receives a stimulus and responds with an electrical signal [43]. Based on the type and amount of forces that they measure, force sensors can be classified in single-axis force sensor, single-axis torque sensor, and multi-axis force-torque sensor. These sensors are typically placed near the place in the robot where the information might be more useful. For single-axis torque sensors, a common location is near the joints to provide direct feedback on the joint torque. For single-axis force sensors and multi-axis force-torque sensors, the location is usually near the end effectors to measure the contact forces. A special type of multi-axis force-torque sensors are the six axis force-torque (FT) sensors which convey a complete information of a contact force by providing measurements of the three axes of forces and three axes of torques.
A force sensor does not measure the force directly. Measuring a force is the result of converting other physical phenomena that varies in response to force into an electrical signal. The relationship between the change of the phenomena to an actual force value is obtained through a process called calibration. The accuracy of the sensor is then a result of the calibration process. It requires the mathematical model of the phenomena (or a good approximation) and known stimuli paired with the corresponding sensor's response.
The most common phenomena used in force-torque sensors is the change in resistance of silicon due to strain. In more technical words, the piezoresistive response to strain of semiconductor material. This material also changes resistance with temperature. Because of this, depending on the calibration procedure, the sensor might suffer from temperature drift. Temperature drift is defined as the undesired change of measurement due to changes in temperature.
Tactile sensors are based on similar phenomena used for force-torque sensors. But, since the main objective of tactile sensors is the detection of contact and not the measuring of force, they are not accurate enough to be directly used as force-torque sensors. The accuracy required for using them as force-torque sensors might be achieved with the proper calibration procedure.
A pair of known stimuli with the sensor response is called a calibration point. A set of cal-

ibration points is a calibration data set. In this thesis, calibration procedures are classified depending on the place the calibration data set is acquired. If the calibration data set is acquired in the system (or structure) in which is meant to be used, it is referred to as *in situ* calibration. Instead, if the sensor is calibrated in a structure then removed and mounted somewhere else for its use, it is referred to as *ex situ* calibration.

In standard operating conditions, a decrease in the effectiveness of the calibration may occur in months. Leading companies for force-torque (FT) sensors [11, 142] recommend calibrating the sensors at least once a year. The calibration done by the manufacturer is typically an *ex situ* calibration. As such, it usually implies that the sensor must be unmounted, sent back to them, calibrate the sensor in a special setup, receive the sensor again and then mount it.

FT sensors are prone to change performance once mounted in a mechanical structure such as a robot [130, 8]. Different methods have been developed to re-calibrate the sensors once mounted. These *in situ* calibration methods allow to perform the calibration in the sensor's final destination, avoiding the decrease in performance that arises from mounting and removing the sensors from its working structure. The relevance of calibrating *in situ* has become evident, making *in situ* calibration part of the service provided by some FT sensor companies [71].

At present, robots still struggle with handling unexpected interactions with their environment, as it could be observed at the DARPA Robotics Challenge Finals in June 2015 [32]. During the challenge, most of the teams could not take advantage of having FT sensors. The Boston Dynamics ATLAS' six axis FT sensors were not used or fully exploited due to the bad quality of sensors measurements, to the point that the IHMC and MIT teams used the FT sensors only as binary contact sensors.

Therefore the objective of this thesis is to provide the knowledge and algorithms needed to have a reliable and accurate estimation of contact forces and joint torques exchanged between the robot, the environment, and other objects. It focuses on improving the measurement reliability of the six axis FT sensors. This allowed robots to perform better dynamical motions. This was achieved by developing novel *in-situ* calibration methods and proposing a new *ex situ* calibration device. Other sources of force-torque information, such as tactile arrays, were explored. This should enable the research community to better exploit force-torque sensing in complex structures such as robots.

There are three intermediate goals to achieve the general objective previously described:

1. Deep understanding of force-torque (FT) sensors.
2. Improvement of force-torque sensors' performance.
3. Increase performance of dynamical motions in robots through the use of force-torque sensing.

To gain a deep understanding of the FT sensors the following actions were taken:

- Study the functioning principles of the different six axis FT sensing technologies.
- Understand how force-torque sensing is used in robots.
- Investigate how six axis FT sensors are usually calibrated.
- Analyze the performance of six axis FT sensors mounted on robots.

Seeking to improve force-torque sensors' performance the strategies implemented were:

- Development of *in-situ* calibration methods.
- Design of an improved *ex-situ* calibration method.
- Investigate the feasibility of using tactile sensors as force-torque sensors.

Aiming to increase the performance of dynamical motions in robots through the use of force-torque sensing, it was considered necessary to:

- Allow the articulated body to exploit the improved measurements.
- Evaluate the result of improving measurement quality.
- Allow the possibility to exploit other sources of force-torque information, such as tactile sensor arrays.
- Allow the robot to estimate individually forces when more than one force is acting on the same robot.

What follows is a brief summary of the thesis structure. It can broadly be considered to be divided into two parts. One is the accumulation of knowledge deemed necessary to achieve the objectives. The other is the result of the research carried out during the last three years in a collaborative Ph.D. between Istituto Italiano di Tecnologia and Universita degli studi di Genova.

Chapters belonging to part one are:

- Chapter 1 seeks to provide information on the force sensing technologies starting from the principles of measuring force to the most common technologies used in six axis force-torque sensors. The available commercial options for robots are presented in a small survey of commercial solutions. Finally, the general use of force-torque sensing in robotics is depicted.

- Chapter 2 describes the use of force-torque sensing in robotics. A method to exploit the force-torque sensing for estimating joint torques and contact forces is detailed. The current performance of robots doing dynamic motions is also depicted.
- Chapter 3 describes what is calibration. It also shows the models used to calibrate six axis FT sensors and capacitive tactile sensor arrays. Some examples of different calibration procedures both *ex situ* and *in situ* are mentioned. It also describes the reasons behind the presented research and the conditions in which it can be applied.

The chapters belonging to the second part are:

- Chapter 4 aims to provide a detailed description of the tools developed to evaluate the performance of a six axis FT sensors once it is mounted on a robot. This is followed by the results of some tests using the aforementioned tools and a description of typical issues that arise when using these type of sensors.
- Chapter 5 displays improvements in the measurements of six axis FT sensors through *in situ* calibration. An algorithm taking advantage of the knowledge of the robot model was developed to perform *in situ* calibration. A detailed description of the calibration algorithm and the results are shown. This is the main work of the thesis, since improving the measurements of the sensor while mounted on the robot, leads to a direct impact on its performance.
- Chapter 6 presents an alternative solution to the current *ex situ* calibration of the lab, based on insights gained from the *in situ* algorithms. The current calibration method is also described and compared to some extent with the proposed solution.
- Chapter 7 explores the possibility of using the skin as a FT sensor. Algorithms to estimate contact locations, external forces, and joint torques using distributed tactile sensor arrays (artificial skin), kinematic sensors and a single IMU without the need for force-torque sensors are presented.
- Chapter 8 confronts the results with the objectives and mentions the future work.

Some of the results contained in this thesis have been or are about to be published in research papers [8, 7, 6].

Table of contents

List of figures

List of tables

Chapter 1

Force-torque Sensing

The main reference for the relation between motion and forces are the three Newton laws of motion. These laws are:

1. Every object in a state of uniform motion tends to remain in that state of motion unless an external force is applied to it.

2. Force is equal to the change in momentum per change in time. For a constant mass, this is:

$$F = ma, \tag{1.1}$$

   where m (kg) is an object's mass, a ($\frac{\mathrm{m}}{\mathrm{s}^2}$) its acceleration and F (N) the applied force.

3. For every action, there is an equal and opposite reaction.

The second law is the most powerful of Newton's three Laws because it allows quantitative calculations of dynamics. Motion involves actions and interactions of a variety of forces. Given the intrinsic relationship between motion and forces, no measurement is more fundamental to understand and perform dynamical motions than the measurement of force and force related quantities (mass, acceleration, pressure, etc). Force sensing is the ability to sense or measure the forces exchanged between two objects. The system that performs the force sensing is a force sensor. A sensor is a device that receives a stimulus and responds with an electrical signal [43]. Force-torque sensing is a special kind of force sensing, it is described as the ability to sense or measure the forces and torques exchanged between two objects. It allows to have a complete description of the sum all of forces and torques between the two bodies at the location where the contact is happening.

In this Chapter, the different technologies used in force sensing are described as well as the principles in which they are based on.

1.1 Force Sensing Technologies

An unknown force can be measured using one of the following means [31]:

1. Balancing it against the known gravitational force on a standard mass, either directly or through a system of levers.

2. Measuring the acceleration of a body of known mass to which the unknown force is applied.

3. Balancing it against a magnetic force developed by the interaction of a current carrying coil and a magnet.

4. Transducing the force to a fluid pressure and then measuring the pressure.

5. Applying the force to some elastic member and measuring the resulting deflection.

6. Measuring the change in precession of a gyroscope caused by an applied torque related to the measured force

7. Measuring the change in natural frequency of a wire tensioned by the force.

All the previously described force sensing methods are mainly applied to static or slowly varying loads. The method number 5 is widely used for both static and dynamic loads of frequency up to many thousand hertz. Sensors based on method 5 are essentially spring-mass systems with damping. They differ in the geometric form of "spring" employed and in the transducer used to obtain an electrical signal. In modern sensors, the most commonly used method is 5, while 3 and 4 are used occasionally [42].

In many sensors, force is developed in response to some stimulus s. The force is not directly converted into an electric signal, thus some additional steps are usually required. A typical force sensor is a combination of a force-to-displacement transducer and a displacement sensor that converts displacement to an electrical output. In other words, a typical force sensor combines an elastic element (spring, polymer lattice, silicon cantilever, etc.) and a gauge for measuring the degree of the element compression or strain for the purpose of converting it to an electrical output signal E. The trend in modern sensor design focuses on the integration of sensing components with signal conditioning, converting, and communication circuits [43]. Such a combination is called a sensing module, Fig. 1.1. Typical sensing element produces low-level analog signals, its output signals need amplification, filtering, impedance matching, and perhaps a level shifting, before it can be digitized. All these functions are performed by signal conditioners. After conditioning, the signal is converted to digital data using the analog-to-digital converter (ADC). Although all components of the sensing module are important, the thesis focuses more in detail on the elastic element and the displacement sensor.

Their ability to measure dynamic loads coupled with the possibility of a large measurement bandwidth makes strain gauges, plus some elastic element, the main source of force-torque sensing in robotics.

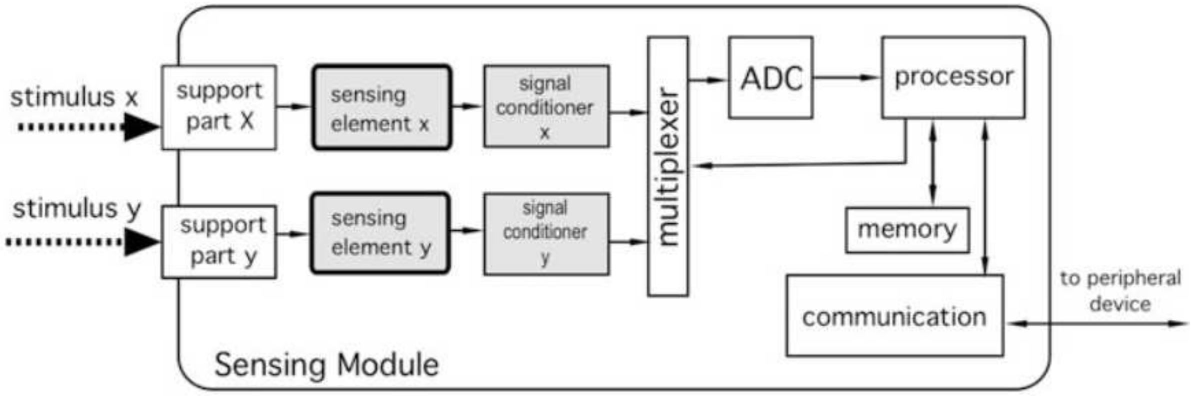

Fig. 1.1 Block diagram of sensing module [43].

1.2 Elastic Element

Elasticity is the ability of an object or material to resume its normal shape after being stretched or compressed. Most materials which possess elasticity in practice remain purely elastic only up to very small deformations. The elastic element is the part of the force sensor that directly responds to the force stimuli.

The relationship between the elastic deformation and forces is given by Hooke's Law. Hooke's law is a law of physics that states:

$$F = k\Delta x, \tag{1.2}$$

where k ($\frac{\mathrm{N}}{\mathrm{m}}$) is a constant of the elastic element, Δx (m) is the change in distance of the elastic element.

Stress σ (Pa) is expressed in terms of force applied to a certain cross-sectional area A (m^2) of an object,

$$\sigma = F/A. \tag{1.3}$$

There are two types of stress depending on the orientation of the force with respect to the cross-sectional area. If the force is perpendicular to the area then it is called normal stress σ_n, Fig. 1.2a. The force can be tensile or compressive depending on the direction of the force. By convention, a compressive force is taken to be negative, which yields a negative stress [20]. Instead, if the force is applied parallel to the cross-sectional area is called shear stress σ_τ. Applying the same stress formula for shear stress results in the average shear stress.

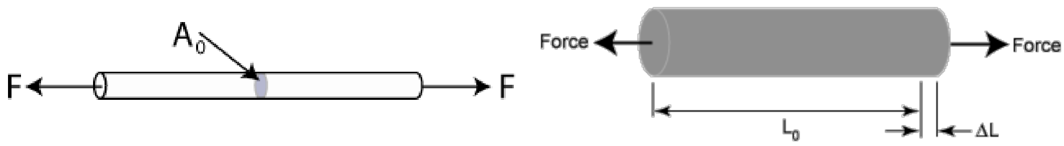

(a) Stress.

(b) Strain.

Fig. 1.2 Effect of a force on a fixed body.

Strain (ε) is the deformation of a physical body under the action of applied forces, Fig. 1.2b. It has no units. Strain is calculated as

$$\varepsilon = \frac{l_i - l_0}{l_0} = \frac{\Delta l}{l_0}, \tag{1.4}$$

where l_0 (m) is the initial length and l_i (m) is length after applying a load. Strains are classified as either normal or shear. A normal strain ε_n is perpendicular to the face of an element, and a shear strain ε_τ is parallel to it. These definitions are consistent with those of normal stress and shear stress.

An object subjected to stress will experience some strain as a result. The relationship between the stress and strain of a particular material is known as the stress-strain curve, Fig. 1.3. It is unique for each material and is found by recording the amount strain at distinct intervals of tensile or compressive stress. The elasticity of materials is described by a stress-strain curve.

An elastic modulus (also known as modulus of elasticity) is a quantity that measures an object's resistance to being deformed elastically (i.e., non-permanently) when a stress is applied to it. The elastic modulus of an object is defined as the slope of its stress-strain curve in the elastic deformation region. A stiffer material will have a higher elastic modulus.

There are various elastic moduli. All of which are measures of the inherent elastic properties of a material as the resistance to deformation under an applied load. The various moduli apply to different kinds of deformation.

Young's modulus E (Pa) is

$$\mathrm{E} = \frac{\sigma_n}{\varepsilon_n} \tag{1.5}$$

, whereas the shear modulus E (Pa) is

$$G = \frac{\sigma_\tau}{\varepsilon_\tau}. \tag{1.6}$$

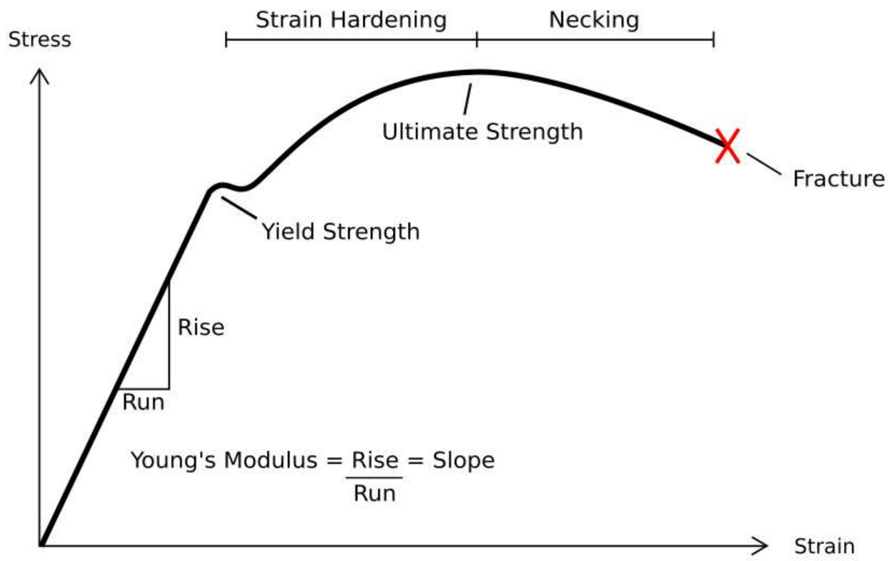

Fig. 1.3 Stress-strain curve.

Hooke's law usually applies to any elastic object, of arbitrary complexity, as long as both the deformation and the stress can be expressed by a single number. Using the elastic moduli, Hooke's law becomes:

$$\sigma_n = E\varepsilon_n \tag{1.7}$$

$$\sigma_\tau = G\varepsilon_\tau \tag{1.8}$$

Depending of the orientation of the force with respect to the cross-section area, an object can be subjected to normal and shear stress simultaneously due to the same force.

Isotropy is uniformity in all orientations. Glass and metals are examples of isotropic materials [20]. For isotropic materials, the complete characterization of the elastic properties, requires at least two constants, the Young and shear moduli.

In the design of the elastic element, considerations have to take into account the geometry and material of choice. This is done with the aim of keeping the elastic element in the linear section of the stress-strain curve where Hooke's law is still valid.

1.2.1 Examples of elastic elements in force-torque sensors

A comprehensive classification of elastic elements consisting of twelve types of elastic elements, based on their shape, strain gauge positioning and force range has been proposed in [153]. Another way of classification is based on their sensitivity to some specific kind of strain:

- Tension-compression or direct (Fig. 1.4a): A columnar element may be in the form of a solid or hollow cross-section having a circular or square shape. To achieve a four-arm bridge circuit two gauges are aligned parallel to the load axis and two gauges aligned at 90°. The cross-sectional area of the column increases in compression and decreases in tension. This is a typical dual sensing elastic element.
- Bending (Fig. 1.4b): A simple cantilever is an example of a bending load cell. When a force F or a torque M is applied to the free end, it deflects the beam so producing opposite strains at the top and bottom faces. Strain gauges may be installed near the root of the beam to sense tensile and compressive strains.
- Shearing (Fig. 1.4c): Shear elements are based on the fact that shear stresses are proportional to the applied force and are independent of loading position. The shear stresses themselves cannot be measured so pairs of gauges with their grid lines aligned at ± 45° to the neutral axis are installed on both sides of the central portion of the beam to measure principal strains.

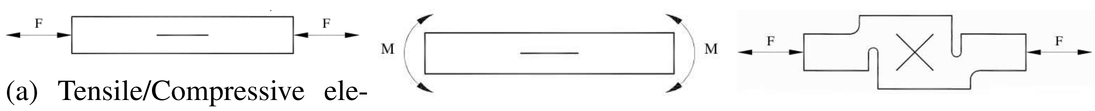

(a) Tensile/Compressive element. (b) Bending element. (c) Shearing element.

Fig. 1.4 Elastic element by sensitivity.

These simple elements can be combined to have sensitivity for forces with arbitrary orientation. The preferred elastic element seems to be variations of the cantilever beams in a cross-beam configuration [97, 139, 109, 143, 135, 145, 4, 64]. Cantilever beam is fixed only on one side. Using them in a cross-beam configuration permits a combination of tensile/compressive and bending elements. Combining multiple elastic elements with this shape has also been explored [98]. They profit from the difference in rigidity between the two elements. With this, they achieved a sensing range from 0.01 N to 1000 N. Some variations of the cross-shaped are shown in Fig.1.8.

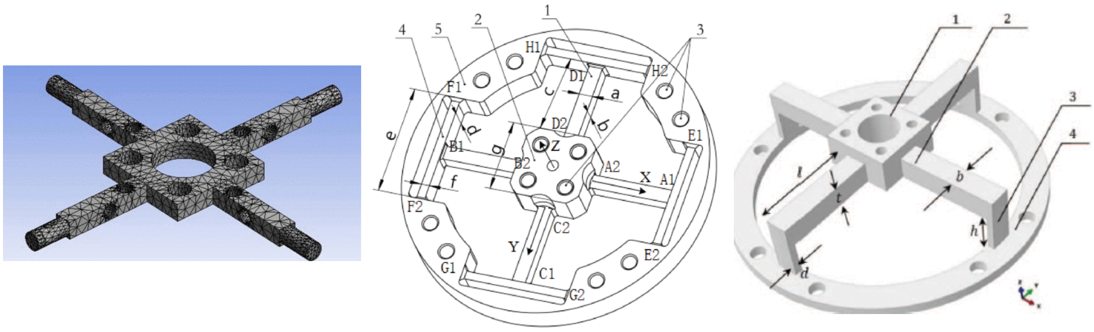

Fig. 1.5 Cross-shaped elastic elements.

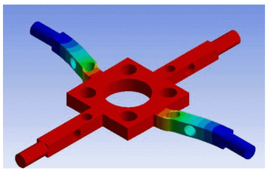

(a) Strain due to x-axis stress.

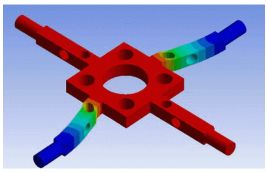

(b) Strain due to y-axis stress.

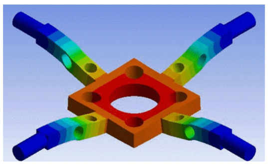

(c) Strain due to z-axis stress.

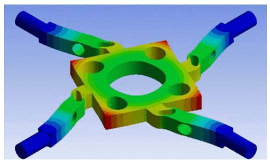

(d) Strain due to shearing stress.

Fig. 1.6 Finite element analysis of choss-shaped elastic element [109].

Another favored shape are cantilever beams in a "Y" configuration [35, 70, 104, 132]. Examples are shown in Fig. 1.7.

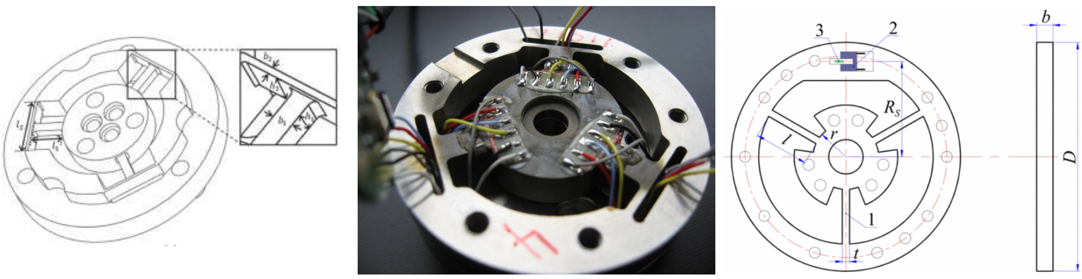

Fig. 1.7 Y-shaped elastic elements.

Besides these two main shapes, other different shapes have been explored in combination with other materials and different sensing technologies. An "E" shape elastic element was used aiming to obtain high measurement sensitivity, overload protection, good linearity, and weak couplings between components [79]. Some 3D-printed S-shaped beams have been used on a capacitive force-torque sensor [76], Fig. 1.8a. Another elastic element used are silicon rubber cubes on a lightweight compliant optical force-torque sensor [2], Fig. 1.8c. Also using silicon rubber, a semi-sphere of rubber has been used coupled with optical technology [128].

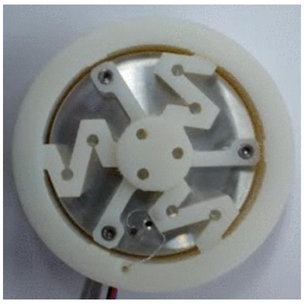

(a) 3D-printed structure.

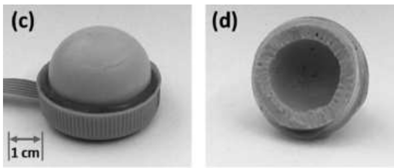

(b) Convex silicon rubber surface [128].

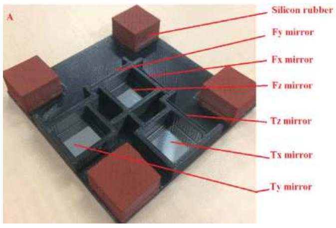

(c) Silicon rubber cubes.

Fig. 1.8 Other elastic element shapes.

Solving a problem of elastic deformations means one should be able to write down all the components of the stress and strain tensors using information on external forces and the elastic moduli. For complex structures, this is usually approximated using finite element analysis, Fig. 1.6.

1.3 Strain Gauges

Several physical effects can be used for measuring strain. Among these effects, there are optical, piezoelectric , and capacitive effects, but by far the most popular is piezoresistive effect [42]. Fundamentally, all strain gauges are designed to convert mechanical motion into an electronic signal. Thus, a strain gauge serves as a transducer that measures a displacement of one section of a deformable component with respect to its other part.

1.3.1 Piezoresistive Strain Gauges

A typical piezoresistive strain gauge is an elastic sensor whose resistance changes with the applied strain (unit deformation), see Fig. 1.9. When a load is applied to the surface, the resulting change in surface length is communicated to the piezoresistive element and the corresponding strain is measured in terms of the electrical resistance, which varies linearly with strain [141]. Since all materials resist deformation, a force must be applied to deform the material. Hence, electrical resistance can be related to the applied force. That relationship is generally called the piezoresistive effect and is expressed through the gauge factor S_ε of the conductor

$$\frac{dR}{R} = S_\varepsilon \varepsilon, \tag{1.9}$$

where R (Ω) is the resistance, dR (Ω) is the change in resistance. For many materials $S_\varepsilon \approx 2$ with the exception of platinum for which $S_\varepsilon \approx 6$. For small variations in resistance not

Material	Gauge factor S_ε	Resistance (Ω)	TCR[1] ($^\circ C^{-1} 10^{-6}$)
57 % Cu–43 % Ni	2	100	10.8
Platinum alloys	4.0–6.0	50	2160
Silicon	-100 to +150	200	90000

Table 1.1 Piezoresistive Strain gauges characteristics [42].

exceeding 2% (which is usually the case), the resistance of a metallic wire can be approximated by a linear equation:

$$R = R_o(1 + S_\varepsilon \varepsilon), \tag{1.10}$$

where R_o (Ω) is the resistance with no stress applied. From the materials shown in Table 1.1, S_ε is constant in Ni for a wide range of strain, it can be used under 260 °C. Platinum alloys are used in high-temperature applications. For semiconductive materials, the relationship depends on the doping concentration, it allows for much higher gauge factors.

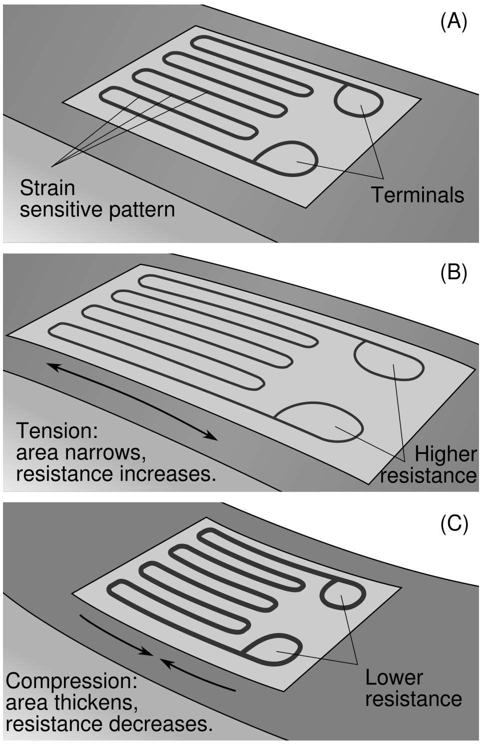

Fig. 1.9 A piezoresistive strain behavior.

The ideal piezoresistive strain gauge would change resistance only due to the deformations of the surface to which the sensor is attached. However, in real applications, temperature,

[1]TCR stands for temperature coefficient of resistance.

material properties, the adhesive that bonds the gauge to the surface, and the stability of the metal all affect the detected resistance. In this context, the term stable refers to the stability of their electron configurations as atoms and as ions. Stable metals do not react with the components of air like oxygen. nitrogen, carbon dioxide, moisture, etc. Because most materials do not have the same properties in all directions, a knowledge of the axial strain alone is insufficient for a complete analysis. Different types of strain require different strain gauge arrangement. When selecting a strain gauge, one must consider not only the strain characteristics of the sensor but also its stability and temperature sensitivity. Unfortunately, the most sensitive strain gauge materials, which are the semiconductors, are also sensitive to temperature variations and tend to change resistance as they age. For tests of short duration, this may not be a serious concern, but for continuous measurement, one must include temperature and drift compensation [99].

Metallic foil Strain Gauge

The metallic foil-type strain gauge consists of a grid of wire filament (a resistor), bonded directly to the strained surface by a thin layer of epoxy resin. Metallic Foil gauges have a low gauge factor. Therefore they require a higher amplification step.

These type strain gauges where the first type of strain gauge technology. It was first developed in 1938 [99], and has been replaced by silicon strain gauge as main force sensing technology in robotics. An image of a typical metallic strain gauge can be seen in Fig. 1.10a.

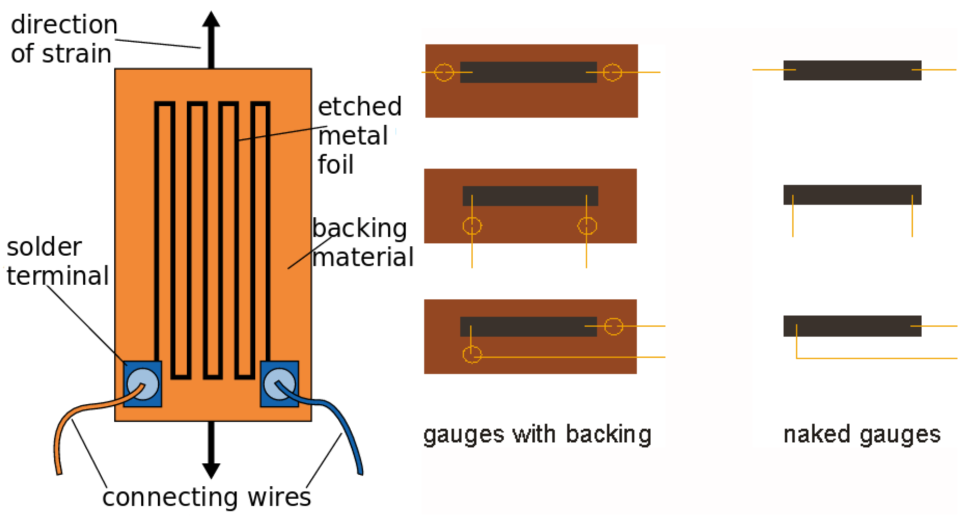

(a) A metallic strain gauge.

(b) A semiconductor strain gauge.

Fig. 1.10 Tactile Sensors.

Semiconductor Strain Gauge

Semiconductor strain gauges are based upon the piezoresistive effects of silicon or germanium. Bonding it to the strained surface needs extra care since only a thin layer of epoxy is used to attach it. The size of a semiconductor strain gauge is much smaller and the cost much lower than for a metallic foil sensor. An example can be appreciated in Fig. 1.10b. While the higher unit resistance and sensitivity of semiconductor sensors are definite advantages, their greater sensitivity to temperature variations and tendency to drift are disadvantages in comparison to metallic foil sensors. This sensing technology is currently the most used.

Wheatstone Bridge

The Wheatstone Bridge is the name given to a combination of four resistances connected to give a null center value. The circuit can be seen in Fig. 1.11. It can be expressed in mathematical terms as:

$$\frac{E_O}{E_I} = \frac{R_1}{R_1 + R_2} - \frac{R_4}{R_3 + R_4} = \frac{R_1 \cdot R_3 - R_2 \cdot R_4}{(R_1 + R_2)(R_3 + R_4)} \tag{1.11}$$

where E_O (V) is the output voltage, E_I (V) is the input voltage and R_i (Ω) is the value of resistance at the i-th position. If $R1 = R_2 = R_3 = R_4$ or $\frac{R_1}{R_2} = \frac{R_3}{R_4}$ then E_O is zero. The resistive elements in the array can have a fixed or variable resistance value.

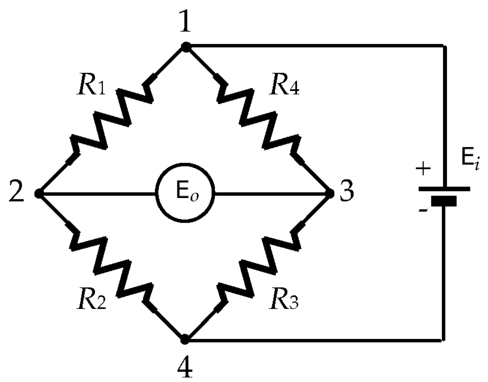

Fig. 1.11 The Wheatstone Bridge circuit.

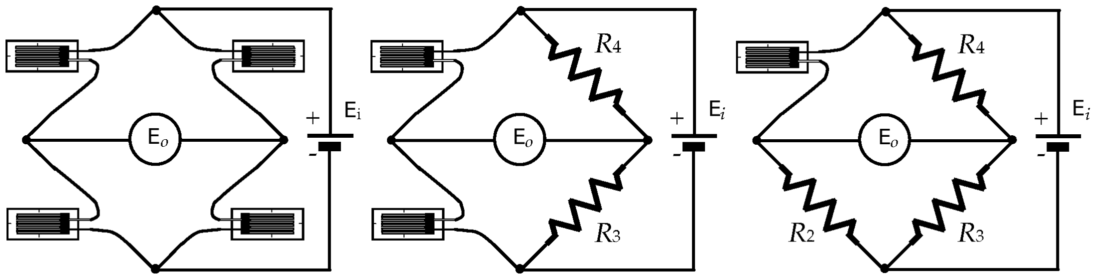

(a) Full Bridge. (b) Half bridge. (c) Quarter bridge.

Fig. 1.12 Types of Wheatstone Bridges.

Depending on the number of variable resistances or strain gauges, it can be classified in a full bridge, half bridge or quarter bridge, see Fig. 1.12. If the variation of resistance ΔR_i is much smaller than the value of R_i, second order factors can be disregarded. This is typically the case for strain gauges.
This arrangement of resistances is well suited for the measurement of small changes in resistance and is, therefore, also suitable for measuring the resistance change in a strain gauge. Another benefit of the Wheatstone Bridge is the fact that it can be arranged to compensate for interference effects, such as temperature, pressure, humidity, magnetic fields, radiation, etc. [57].
The compensation of the temperature expansion is correct only if some conditions are strictly fulfilled. These include:

- symmetry of the bridge,
- identical temperature coefficients of all materials used,
- identical resistances of all parts in the bridge arms which are combined for compensation,
- identical temperatures on all compensating elements in the bridge circuit,
- identical active grid areas.

1.3.2 Capacitive-Pressure Sensors

In simple words, capacitance is the ability of a system to store an electric charge. The capacitive effect can be calculated as:

$$Ca = \frac{q}{E}, \tag{1.12}$$

where q (A) is the current, E (V) is the voltage and Ca (F) is the capacitance . Capacitors are built with two conductive materials with some space in between them. The space can be in vacuum or with some dielectric material. A dielectric material is an electrical insulator that can

be polarized by an applied electric field.
The capacitance is a function only of the geometry of the design (e.g. area of the plates and

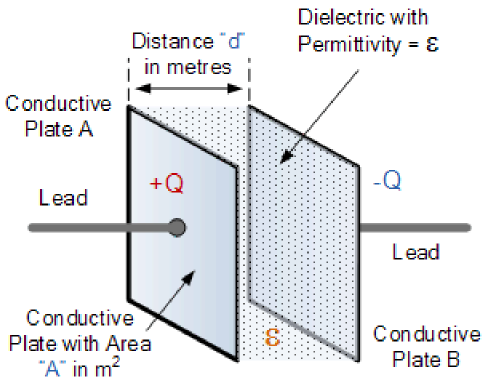

Fig. 1.13 Flat Capacitor.

the distance between them) and the permittivity of the dielectric material between the plates of the capacitor.
A variable capacitance pressure transducer has a capacitive plate (diaphragm) and another capacitive plate (Electrode) fixed to an unpressurized surface gapped a certain distance from the diaphragm, Fig. 1.13. A change in pressure will widen or narrow the gap between the two plates which varies the capacitance. This change in capacitance is then converted into a usable signal for the user [123]. If the shape of the capacitor is flat, the capacitance can be estimated as:

$$Ca = \kappa \varepsilon_0 \frac{A}{d}, \tag{1.13}$$

where κ $(\frac{\mathrm{F}}{\mathrm{m}})$ is the dielectric constant of the material, ε_0 is a constant if the sensor were found in vacuum, A (m^2) is the area of the plates and d (m) is the distance between the plates.
Some dielectrics have a very uniform dielectric constant over a broad frequency range (for instance, polyethylene), while others display strong negative frequency dependence, that is, the dielectric constant decreases with frequency. Temperature dependence is also negative [43]. Examples of force-torque sensors using this technology can be found in [76, 69]. The measuring range is limited to values below 30 N.

1.3.3 Piezoelectric Strain Gauge

The piezoelectric effect is the generation of electric charge by a crystalline material upon subjecting it to stress, or more accurately a redistribution of the electric charge. The charge generated is proportional to an applied force,

$$Q = \kappa_e F, \tag{1.14}$$

where Q (C) is the charge, κ_e ($\frac{\mathrm{C}}{\mathrm{N}}$)is the piezoelectric coefficient along the orthogonal axes of the crystal cut and F (N) is the applied force.

A piezoelectric strain gauge can convert a changing force into a variable electrical signal, while a steady state force produces no electrical response. Therefore it responds only to changing forces. If the stress is maintained, the charges will be neutralized by the internal leakage. So after some time the piezoelectric material will not send any signal.

Since an applied force can change some properties of the piezoelectric material when the sensor is supplied with an excitation signal, a different property can be exploited for more accurate force sensing.

Certain cuts of a quartz crystal, when used as resonators in electronic oscillators, shift the resonant frequency upon being mechanically loaded. The frequency shift induced by the force is due to nonlinear effects in the crystal. The change of frequency Δfr (Hz) can be described as:

$$\Delta fr = F\frac{Kfr_o^2 n}{l} \tag{1.15}$$

where F (N) is the applied force, K is a constant, fr_o (Hz) fundamental frequency when unloaded, n is the number of the overtone mode (it allows to use the quartz in a frequency higher than fr_o and l (m) is the size of the crystal [42]. An image of this kind of sensor can be seen in Fig. 1.14.

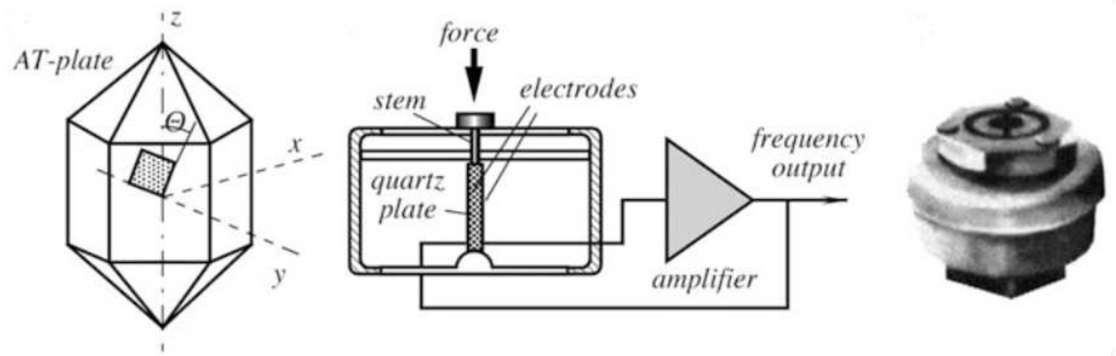

Fig. 1.14 A piezoelectric strain gauge [42].

A fundamental problem in all force sensors that use crystal resonators is based on two contradictory demands. On one hand, the resonator shall have the highest possible quality factor which means the sensor has to be decoupled from the environment and possibly should operate in vacuum. On the other hand, application of force or pressure requires a relatively rigid structure and substantial loading effect on the oscillation crystal, thus reducing its quality factor.

1.3.4 Optical Force Sensor

Although not considered strictly strain sensors, they work by a similar principle of measuring the deformation or displacement of a body. An optical force sensor is typically composed of a light source, a photosensor, a solid object modifying amount of light incident on the optical detector are necessary to measure displacement between an unmovable and a flexible part of the optical sensor.

The photosensors have drawbacks such as nonlinearity and temperature sensitivity, however, they are considerably reliable, cheap and allow simplifying the construction of the design. A displacement can be detected by interrupting light between source and detector, changing the intensity of reflected light or relative movement of source and detector [56]. In this cases the relationship with the strain is completely dependent on the geometry of the sensor. Lately some

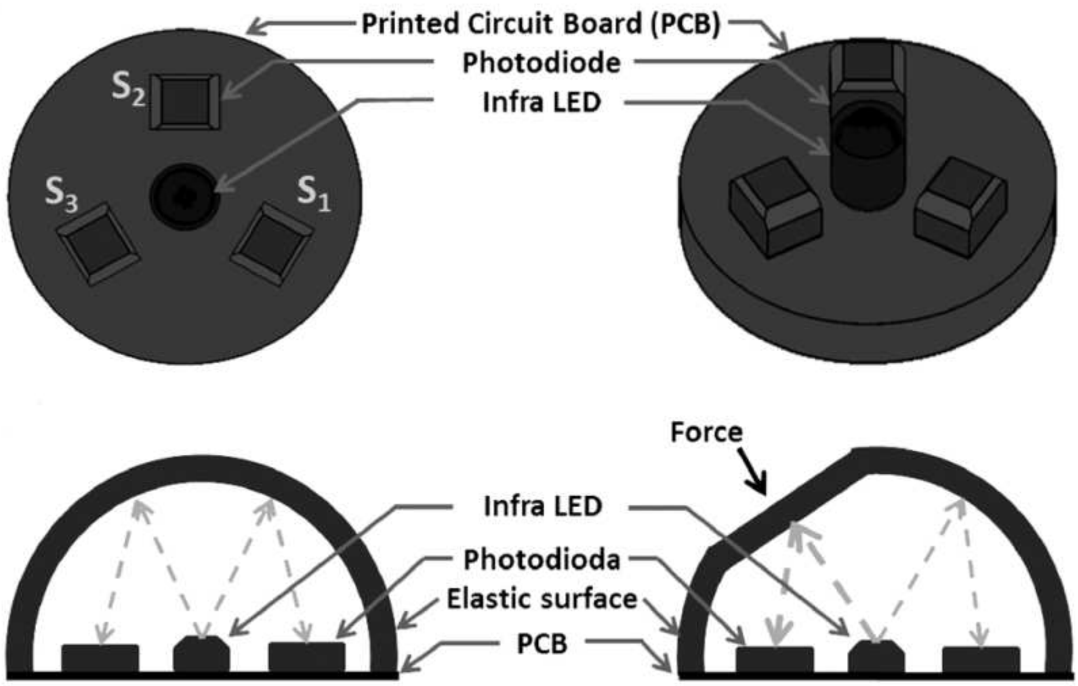

Fig. 1.15 An optic force-torque sensor [128].

force-torque sensors based in optical technology have been developed. Their aim is to have an easy manufacturing process, durability, scalability, low cost and having good sensitivity [128].

A drawback is that the behavior is nonlinear which complicates the calibration procedure. They have yet to become widely used in applications of 100 N or more.

Fiber Optic Sensor

Fiber optic sensors offer a promising alternative to electric measurement systems. For the fiber optic sensor the optical detector is embedded into a holder that acts as a resilient component (spring). Fiber optic FT sensors have recently been presented with varying degrees of freedom (DoF). Fiber optic sensing principles can be categorized by the physical value being measured. Among others the most frequently used measured variables are intensity and wavelength.

Light is reflected back into the fiber by a mirror connected to a deformable structure. The intensity of reflected light depends on the axial and angular deformation of the structure. The reflected intensity is measured and interpreted as axial force. Bend losses in the fiber cannot be distinguished from intensity variation by the measuring device. Measuring the wavelength instead of intensity offers the possibility to become almost independent of losses in the optical fiber. Aside from certain material constants and design parameters the reflected wavelength is determined by mechanical and thermal conditions as given by

$$\frac{\Delta\lambda}{\lambda_0} = (1 - p_{eff})e + \left[(1 - p_{eff})\alpha + \frac{1}{n_0}\frac{dn}{dT}\right]\Delta T, \tag{1.16}$$

with nominal wavelength λ_0 (m), photoelastic coefficient of the fiber $peff$ (Pa^{-1}), thermo-optic coefficient $\frac{dn}{dT}$ (K^{-1}), effective refractive index n_0, linear strain in direction of the fiber axis e, and temperature change ΔT (K).This type of force sensing technology ranges up to 20 N [53].

1.4 Tactile Sensor Technologies

In general, the tactile sensors belong to the special class of force or pressure transducers that are characterized by small thicknesses.
Tactile sensors sensing technologies, similarly to force sensors, can be: capacitive, piezoresistive, piezoelectric, magnetic and optical.

- Piezoresistive sensors (e.g. [61, 124, 68]) are made of materials whose resistance changes with the applied force and can therefore vary the voltage of the signal.
- Capacitive sensors (e.g. [138, 85]) rely on their change in capacitance value as the dielectric between the two conductive plates is compressed. The capacitance value variation can be interpreted by the control circuit.

- There are piezoelectric sensors (e.g. [118]) that create a voltage signal as they are deformed due to their piezoelectric properties.

There are more types of tactile sensors (optical, magnetic etc.), but the mentioned ones are the most commonly used in the industry [47, 46, 150].

(a) Resistive 3D shaped tactile sensor [73].

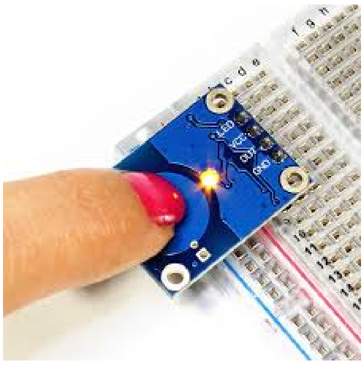

(b) A capacitive touch sensor.

(c) A capacitive slip tactile sensor.

Fig. 1.16 Tactile Sensors.

The tactile sensors loosely can be subdivided into several subgroups [41].

- Touch sensors detect and/or measure contact forces at defined points. They are binary, namely—touch or no touch. It can be analog and use a force measure for having a trigger threshold behavior.
- Contact Sensors detect physical coupling between two objects, regardless of forces. An example is a capacitive touchscreen on a touch-sensitive monitor (e.g., smartphone).
- Spatial Sensors detect and measure the spatial distribution of forces perpendicular to a predetermined sensorized area. A spatial-sensing array can be considered to be a coordinated group of touch sensors.
- Slip Sensors detect and measure the movement of an object relative to the sensor. This can be achieved either by a specially designed slip sensor or by the interpretation of the data from a touch sensor, contact sensor, or a spatial array.

Since their aim is not to measure forces, typically they are not very accurate when using it for force-torque sensing.

1.4.1 Tactile sensor arrays

Tactile sensor arrays, also known as artificial skins, are used in many fields of engineering including neuroprosthetics, humanoid robotics, and wearable robotics [82]. They can be classified as spatial tactile sensors. As implied by the name, they are arrays of tactile sensors arranged, typically, in a distributed manner over a surface. This forms a discrete area where tactile sense is possible. The area is not fully cover and contains gaps between the individual tactile sensors. In humanoid robotics, the artificial skins are usually mounted on the surface of robots in order to detect physical interactions with the external world. They are mainly used to detect contacts. Some attempts have been done to use them as force sensors [66].

Fig. 1.17 A tactile sensor array.

1.5 Force Sensors

Even if there are many possible sensing technologies, the actual sensors used in the robots, regarding force-torque sensing, can be mainly divided into three categories:

- single-axis force sensor
- single-axis torque sensor
- multi-axis force-torque sensor

In robotics, single-axis torque sensors are typically installed at the joints. Joint torque information is crucial because it is directly related to the motor actuating the joint, making them essential feedback for force-torque controllers. Since joint torque sensors provide this information directly, they are commonly used.

Single-axis force sensors are only able to give information about one axis. Multi-axis force-torque sensors can easily give the same information and more.

Six axis FT sensors have an arrangement of strain gauges designed to measure the forces and torques sensed at the sensor frame. Six axis FT sensors give complete information about the sum of the forces and torques exchanged between two bodies. As a result, six axis force-torque sensors are able to directly convey information about interactions with the environment.

Although many robots have six axis FT sensors, they are not exploited to their full potential [32]. Since the six axis FT sensors have the most wasted potential, they are the main focus of the thesis.

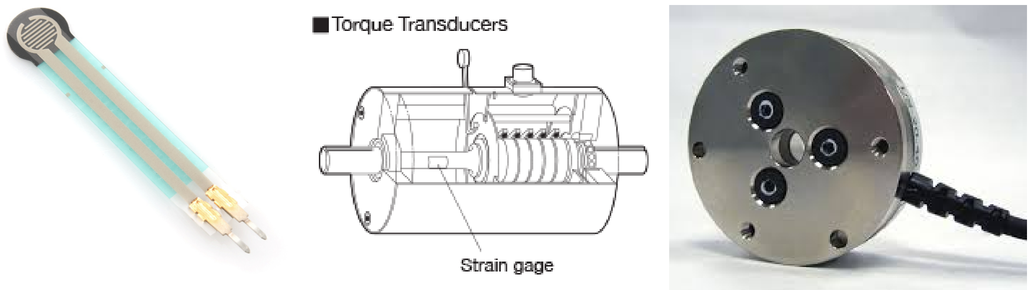

(a) A single-axis force sensor. (b) A single-axis torque sensor. (c) A six axis FT sensor.

Fig. 1.18 Force-torque Sensors.

1.5.1 Commercially Available Six Axis Force-torque Sensors

Looking at the main options in the market may allow to know the most used technology. This way the impact of this research will be more widespread by focusing on that technology. Six axis FT sensors are sold in a big variety of sizes and ranges. Its application span from medical instruments to big industrial manipulators, this includes wearable robotics and other types of robots.

What follows is a non-exhaustive comparison of commercial six axis FT sensors for robotics. The comparison is summarized in Table 1.2. Even if the oldest technology is the metallic foil strain gauge, only one company clearly states they use this technology. Among the sensors in the comparison, most of them use the silicon strain gauge technology. Some companies offer custom calibration upon request. Some specify the possibility to offer a Complex Loading Calibration. By sacrificing some resolution the range of the sensor is guaranteed even under loads that combine different axis.
Most of them recognize the issue of temperature drift as stated in the data sheets of the reviewed sensors. Nonetheless, just a minority offer temperature compensation and in some cases only upon explicit request.
It is important to point out that the information offered in the data sheets of the sensors is not

standardized. Information such as bandwidth, non-linearity, type of sensing technology and expected accuracy is not available for all sensors' data sheets. Some sellers, offer different calibrations for the same sensor. In those cases, only the calibration with the higher range is displayed. The lack of standardized information prevents having a more in depth analysis of the commercial solutions. The shape of the elastic element is not available in any of the data sheets.

It is worth noticing that the Axia80, from ATI, offers dynamically changing calibration. It goes from a high calibration range to a lower calibration range. Is interesting since usually the accuracy is given as a percentage of the full scale. Therefore reducing the full scale reduces the error in the measurements. From all sensors reviewed, it is the only one with this feature.

The range of six axis FT sensors in the comparison is limited to sensors that have a range from 120 N to 1000 N for the forces and 3 Nm to 60 Nm for the torques. This range was considering the requirements of a the 33 kg robot as middle point. The range for a 33 kg robot is 500 N for the forces and 30 Nm for the torques.

Silicon strain gauges are the most common. This type of sensor is based on the piezoresistive technology using semiconductors as material. For this kind of material, the model of the resistance can be approximated to a linear model. As a result, a linear model is also the main approach for the calibration model. Even if they are sensitive to temperature as well.

Sensor	Company	Technology	Fx, Fy (N)	Fz (N)	Tx,Ty (Nm)	Tz(Nm)	Dimension (mm)	Accuracy	Nonlinearity
AD2.5D	AMTI	Strain Gauges Transducers	2224	4448	112	56	63,5*63,5	N/A	± 0.2% Full Scale
FS6	AMTI	Strain Gauges Transducers	±1100	±2200	±56	±28	63,4*37,8	N/A	± 0.2% Full Scale
mini45	ATI	Silicium strain gauges	±580	±1160	±20	±20	15,7*45	0.1% to 5% due to temperature	N/A
mini58	ATI	Silicium strain gauges	±1400	±3400	±60	±60	30*58	0.1% to 5% due to temperature	N/A
75E20A4	JR3	Foil strain gauges	±1000	±2000	±200	±200	50,8*191	±0,25%	N/A
FTS-Theta	Shunk	Silicium strain gauges	±2500	±6250	±400	±400	61,1*155	±1%	N/A
3713A	SunriseInstruments	Strain Gauges Transducers	±400	±800	±14	±14	25*135	N/A	N/A
HEX-H	OPTOFORCE	Optically Measured deformation	±200	±200	±15	±10	43.5*70	Can measure shear forces. More durability	<2%
Barrett	Barret Technology	Silicium strain gauges	±80	±135	±2.75	±2.75	12*90	N/A	N/A
30E12A4	JR3	Foil strain gauges	±200	±400	±16	±16	19*45	N/A	0.50%
FT300	Robotiq	Capacitive	±300	±300	±30	±30	37,5*75	1N,0.02Nm	N/A
FTC050	Shunk	opto-electric measurement	±450	±400	±7	±15	48,5*161	N/A	N/A
FT nano 25	Shunk	Silicon Strain gauges	±250	±1000	±6	±6	21,6*25	N/A	N/A
kms40	Weiss Robotics	Not mentioned	±120	±120	±3	±3	27*76	N/A	N/A
Axia80	ATI	Silicon Strain Gauges dual calibration	±500 ±200	±900 ±360	±20 ±8	±20 ±8	25.4*104	<2%	N/A

Table 1.2 Commercially available six axis FT sensors.

1.6 Conclusion

The principles in which the force-torque sensing is based have been discussed as well as the components of a force-torque sensor. In robotics, most force-torque sensors are based on the relationship between elastic deformation and forces. The knowledge of principles in which they are based, help anticipate some of the behaviors that can be expected from the sensors. The fact that the silicon strain gauge is the main technology used in force-torque sensors coupled with the knowledge that this technology is sensitive to temperature helps to anticipate the possibility of temperature drift. The complexity of the arrangement of strain gauges in the elastic element increases with the number of axes that are meant to be measured. This makes it hard to fulfill all the requirements to perform temperature compensation at hardware level. Understanding the principles behind tactile sensors allows having bases to believe they can be used as force-torque sensors.

While knowledge of the principles gives a clear picture of what happens inside the sensor, the way the sensors are actually used may help understand what should be expected from these sensors. The way force-torque sensing is used in Robotics is discussed in Chapter 2.

Chapter 2

Use of force-torque sensing in Robotics

The principles in which force-torque sensing is based are important to understand the inner workings of force-torque sensors. Having a clear picture of how they are used allows to understand what is expected of these sensors. Among other things, the information of force-torque sensing could be possibly used for controlling dynamic motions or ensure safety when interacting with other bodies, especially humans. In other words, this information allows knowledge of the contacts arising from interactions with the environment or other bodies and could permit their capitalization. Providing force information to the robots is known to increase their operational ability [116]. In this chapter, the main locations of force-torque sensors in robotics are described. Some of the uses of these sensors are briefly mentioned. The dynamic equations of motion are detailed to showcase the connection between force-torque sensing and dynamic motions. The state of the art for estimation of force-torque sensing quantities such as the contact forces and joint torques are provided. Lastly, the current state of dynamic motions performed by robots is mentioned.

2.1 Location of Force-Torque sensors on Robots

Robots with their base fixed to the ground are called fixed based robots. Manipulators fall in this category. When the base of the robot is not fixed to the ground it is called floating base. Single axis torque sensors are position at the joints due to their direct connection with the actuation torque. This makes them a typical force-torque sensor present in robots [122, 147, 83]. On the other hand, six axis force-torque (FT) sensors have been considered important in the design of floating base robots, such as humanoids [104, 55, 9, 62, 63, 34]. Six axis FT sensors have mainly two types of locations in robotics. Either at the end-effector position (wrists and feet), see Fig. 2.1, or near the base of the robot, Fig. 2.2.

FT sensors in the end-effector position are the most widely used. Being less affected by dynamic effects and gravity they have less dynamic errors in the measurements [48]. Although the position can be classified as end-effector, wrists and feet positioned FT sensors have different expected uses. The wrist positioned sensors are mostly used for manipulation tasks while the feet are meant to measure ground reaction forces. Manipulation tasks are mainly described as slow and short motions. Contrary to wrist positioned sensors, the sensors at the feet could experience fast or slow motions depending on the task. This has an impact in the expected excitation of the sensors and the relevance of dynamic effects on the sensor.
FT sensors at the base position are useful to detect contacts along the kinematic chain [121, 48]. As such, they are able to detect unexpected collisions which might happen in both slow or fast motions. In floating base robots the base is typically the torso or the pelvis. Therefore, FT sensors in the shoulders or the hip are classified as near the base.
Regardless of their position this sensors are likewise affected by any extra weight and inertia of a load at the end-effector [48]. By the nature of what they measure and considering their typical locations in robots, six axis FT sensors and single axis torque sensors can provide direct information about forces at contacts and torques at the joints respectively.
Installing force sensors on the robots can result in high maintenance prices, high noise values, soft structure, and complication of the system's dynamic equations. It is well known that information of a force sensor has much noise. Furthermore, an unstable state can be caused by the narrow bandwidth of force information by a force sensor. [67].

(a) Sensor at the wrist of a fixed base robot.

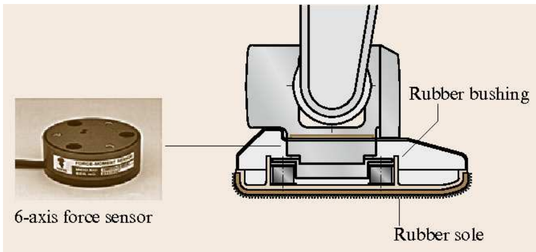

(b) Sensor at the foot of a legged robot.

Fig. 2.1 Examples of force-torque sensors placed near end-effector positions.

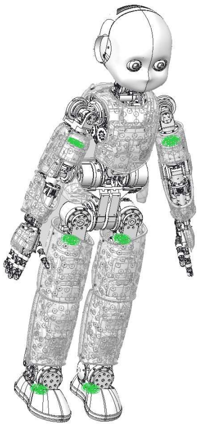

(a) Sensor at the shoulder and hips of floating humanoid.

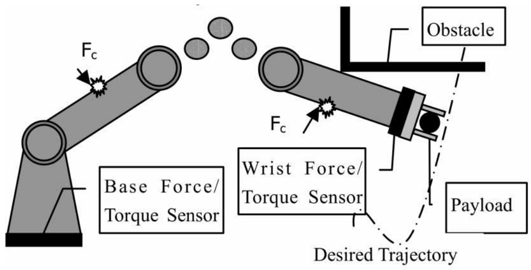

(b) Sensor at the base and wrist on fixed based robot.

Fig. 2.2 Examples of force-torque sensors placed near the base positions.

2.2 Force-Torque sensor uses in robotics

Six axis force-torque (FT) sensors have been used in robotics systems since the 1970's [140]. They have been widely used in fixed based robots, mainly for fine motions [48]. The use of the FT sensor information can be broadly classified into two depending if the information is used directly or not.

Direct use of the information implies that the force or torque knowledge is used to generate some response or take a decision. The simplest use of a force-torque sensor is as a threshold for contact detection. By using a threshold on the forces on the z-axis, the foot in contact with the ground is identified [107, 32]. This can be generalized to logic branching behaviors based on thresholds on the value of the forces [48]. This includes the detection of collisions [51] or slippage conditions [90].

Another way to use directly the information is by using it as feedback for control applications. Joint torque sensors have been successfully used in control applications in the past [74]. It has been shown that joint torque feedback is a fundamental part of force, compliance and impedance control [1, 80, 136]. Conceptually, introducing joint torque sensor feedback in the control loop is similar to introducing a six axis FT sensor feedback [48]. After a contact is established it can be desirable to control the actual interaction between objects. A survey on different interaction control schemes has been presented [22]. These schemes where proposed and tested in fixed based robots. The need for the full dynamic model and force-torque sensing is clearly stated. A six axis FT sensor near the end effector was used. This sensor can also be used in control applications with multiple contact scenarios [59]. In some robots, the

local stability is enforced by a proprietary stabilizer, which exploits the IMU and force-torque sensor feedback [72]. Some whole-body controllers able to exploit contact information have been developed in the past [119]. They require to sense the reaction forces at the contacts to overcome effects of unmodeled friction at the joints due to the the gearing mechanisms.
The indirect use of the information implies that the information provided is processed to generate other knowledge that is then used. Given the relationship between force, mass and acceleration, force information can be used to estimate quantities related to mass and acceleration. For this reason, FT sensors have been used to estimate inertial parameters in fixed based robots [144, 108, 49, 101]. Measurements from six axis FT sensors have also been exploited to track the center of mass(CoM), center of pressure (CoP) and zero moment point(ZMP) [111]. These quantities are commonly used in whole body controllers. They can be used as part of the information required to estimate the momentum of robots [113]. Given the elastic nature of the principles involved in FT sensors the information they provide have been also been used to estimate micro-displacements [48]. Another indirect use of the information is the exploration and shape reconstruction of objects [15].
Given the possible uses of FT sensing information, especially its use as feedback information, FT sensors have permeated through many robotic research areas such as physical human-robot interaction, exoskeletons, teleoperation, haptics, surgical robots, industrial robots, force control and locomotion to name a few [122].

2.3 Robot Dynamics and force-torque sensing quantities

A robot can be seen as a combination of multiple bodies acting as a whole (a multi-body system). An element q can be defined as the following triplet: $q = \left({}^A p_B, {}^A R_B, s\right)$ where ${}^A p_B \in \mathbb{R}^3$ denotes the position of the base frame with respect to the inertial frame, ${}^A R_B \in \mathbb{R}^{3\times 3}$ is a rotation matrix representing the orientation of the base frame, and $s \in \mathbb{R}^n$ is the joint configuration characterising the shape of the robot. The velocity of the multi-body system can be characterized as the triplet $v = \left({}^A \dot{p}_B, {}^A \omega_B, \dot{s}\right) = (\mathrm{v}_B, \dot{s})$, where ${}^A \omega_B$ is the angular velocity of the base frame expressed w.r.t. the inertial frame, i.e. ${}^A \dot{R}_B = S\left({}^A \omega_B\right)^A R_B$. A more detailed description of the floating base model is provided in [131]. Applying the Euler-Poincaré formalism [88] to the multi-body system, yields the following equations of motion for a robot with n_c distinct contacts with the environment:

$$M(q)\dot{v} + C(q,v)v + G(q) = \mathbb{B}\tau + \sum_{k=1}^{n_c} J_{C_k}^T \mathrm{f}_k \tag{2.1}$$

where $M \in \mathbb{R}^{(n+6)\times(n+6)}$ is the mass matrix, $C \in \mathbb{R}^{(n+6)\times(n+6)}$ accounts for Coriolis and centrifugal effects, $G \in \mathbb{R}^{n+6}$ is the gravity term, $\mathbb{B} = (0_{n\times 6}, 1_n)^T$ is a selector matrix, $\tau \in \mathbb{R}^n$ is a vector representing the actuation joint torques, and $\mathrm{f}_k \in \mathbb{R}^6$ denotes the force applied by the environment on the robot at the k-th contact, also called contact forces or external force-torques. The Jacobian $J_{C_k} = J_{C_k}(q)$ is the map between the robot's velocity v and the linear and angular velocity at the k-th contact link. From eq. (2.1), it can be seen that force torque related quantities involved directly with the motion of a robot are the joint torques and the contact forces, Fig. 2.3. Contact forces have great relevance in stabilizing the robot because it is through these forces that the robot can actuate the underactuated degrees of freedom (DoF), like the center of mass (CoM) position and the floating base orientation [23]. Using contact force information is also possible to improve grasping task such as opening doors or turning valves [77]. Likewise, the relevance of joint torques is derived from its relation with the output of the motors. Therefore information of these quantities is crucial for controlling the dynamic motions of a robot. Since there is a direct relationship between force and acceleration, the more dynamic the motions more important it is to have accurate force sensing.

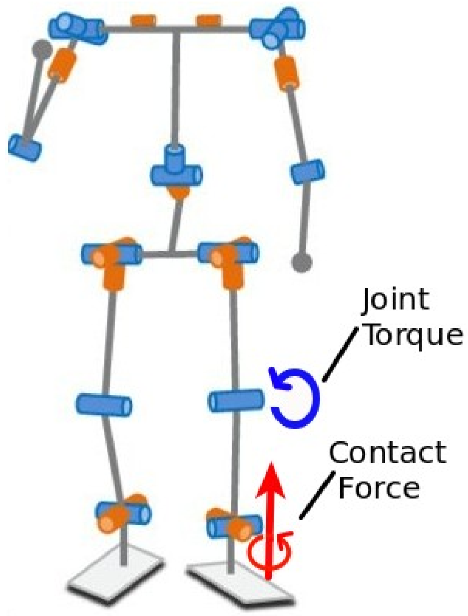

Fig. 2.3 Joint torque and contact force in a robot.

Depending on the available information, it is possible to use eq. (2.1) to estimate the joint torques, the contact forces or both. What follows is a small review of the state of the art on contact force and joint torque estimation. Using end-effector FT sensors for contact force and joint torque sensors for joint torque values are not included in the review since they measure these quantities. This means there is no estimation. Some of the approaches are able to estimate both type of quantities. The different solutions presented use different combinations of the following sensors: tactile sensors, near base six axis FT sensors, inertial measuring units (IMU), encoders, current sensors, cameras, and joint torque sensors.

2.3.1 Contact Force Estimation

Many approaches have been developed to estimate contact forces. They typically separate this problem in three phases: contact detection, contact location estimation, and contact force estimation. This corresponds to the first three stages of the collision event pipeline [51].
A natural solution for the first two phases of the contact force estimation is the use of distributed tactile sensing. Some attempts have been done to calibrate these sensors to obtain also the force at the contact [23, 28, 68]. In these cases, FT sensor information was used to calibrate the tactile arrays. Therefore the accuracy of the calibrated skin will at best be as good as the accuracy of the sensor used to calibrate it. These solutions are able to estimate multiple contacts.

There have been many solutions to contact force estimation based on the momentum-based residual signal concept [81]. The residual is calculated as the difference between the generalized momentum of the robot and the expected generalized momentum due to the commanded torque. This concept sets threshold values for the residual signal. When the value is exceeded it is considered that a contact is detected. The direction of the contact is also reconstructed using the robot generalized momentum. The residual signal grows exponentially with a contact and the actual magnitude of the contact force is not provided. The original residual solution solves the first two phases of contact detection and localization of the link in which the contact happens. Different extensions of the residual have been extended to obtain the value of the contact force. Using external sensors like a Kinect [84] or relaying heavily on the robot model coupled with a particle filter [87]. The original residual approach assumes the robot is able to reach a commanded torque value. Some other solutions have been proposed to circumvent this limitation and still use the residual concept. Others have exploited current sensors and known quasi-static robot configuration to estimate the joint torques in the unloaded case and through comparison with the loaded case reconstruct the forces [89]. An extension of the residual method estimates the joint torques with current measurements taking into consideration backlash and friction [40]. Although the joint torques are estimated, their value are only used as threshold to detect contacts. A non-linear model based on binary-tree prediction has been used when the model of the motor is not trusted using discrepancies in the commanded position [17, 18]. In the last mentioned solution the magnitude of force was not reconstructed. The residual method has some limitations such as the need for enough DoF for a full contact reconstruction (three forces and three torques) and the inability of detecting contacts in the nullspace of the Jacobian. This information is not lost when using six axis FT sensors. Even so, they are theoretically able to distinguish multiple contacts in the same kinematic chain which six axis FT can not do alone.

A strategy to estimate contact wrenches given whole-body distributed FT and tactile sensors was proposed in [30] and extended in [129, 29]. The estimation strategy relies on the joint torque estimations described by [44]. As a by-product of the rearranged Newton-Euler recursion, authors present an algorithm to compute the total (external) contact force acting on a subpart. Subparts are defined by the kinematic subchains obtained by dividing the robot at the level of the available FT sensors. An exact estimation can be given only if there is one contact wrench per subchain. Otherwise, a linear least-squares is proposed to obtain an approximated solution. The contact force is estimated at any subchain even if the contact is far from the FT sensor. Therefore is not strictly measured. This relies heavily in the accuracy of the FT sensors and is susceptible to errors in the model, encoders and IMU measurements used to propagate gravity values. Similarly, the orientation and the velocity of the floating base have been used in a state estimator able to rebuild, in a single state vector, floating base kinematics, contact forces, and external contacts. The state estimator is based on extended Kalman filtering [13]. No force-torque data is used, but the possibility to improve the performance of the estimator with this data is clearly mentioned.

A method for estimating the contact forces using a body-suit of motion capture system was proposed in [105]. A recursive neural network is used to learn the forces based on physics-based optimization. Even if the estimation depends on centroidal dynamics, the collected data set is collected through human motions and are not likely to be equally performed by floating base robots. Contact detection is still required.

A way to make the estimation of localization of contact more robust has been to perform sensor fusion through the combination of hypothesis using a likelihood probabilistic estimation [38]. Each sensor involved and the model provide a different hypothesis with its respective likelihood in a discretized 3D cartesian space. Multiple contacts can be detected, but no value of the force is provided. Another way to fuse data is through the use of the extended kalman filter [33]. In this case, a restriction to the use of flat tactile array prevents from estimating other contact forces beside the one at the foot.

In general, these solutions can be grouped in using tactile sensing as a substitute, using joint torque information, propagating FT sensor measurements using the model or fusing multiple type of sensors. Even among these there is no solution that can detect multiple contacts in every situation in a fast for the possible range of forces.

2.3.2 Joint Torque Estimation

There are many robots that do not include joint torque sensors [91, 17, 89]. Adding series Elastic Actuators (SEA) [103] is a common solution to estimate joint torques. Often, this solution adds a degree of compliance into the robot, which makes the control and planning tasks more complex. Based on the same elastic principle, joint torque estimation can also be achieved by measuring the deformation in the Harmonic Drive to estimate Joint torques [152]. Using any of these techniques for joint torque estimation requires mechanical changes, which may sometimes be not feasible. Another possible solution is to use current measurements and the motor model to estimate the motor torque. The whole model with the gearbox should be taken into account to provide the joint torque [149].

There are techniques that combine the distributed FT to estimate joint torques [44, 29, 30, 129]. The resulting accuracy of the joint torque value depends on the performance of the FT sensor. Some extensions of the momentum-based residual signal method have required to provide some estimate of the joint torques [40, 89, 17, 18]. Even if control actions have been successfully executed with these estimations, accuracy comparisons are not provided.

2.4 A multi-body estimation scheme for contact forces and joint torques

What follows is a description of the theoretical framework proposed in [44, 30] for the estimation of contact force and joint torques on chains, later extended for the whole-body case in [129]. The algorithm consists in cutting the floating-base tree at the level of the (embedded) FT sensors obtaining multiple sub-trees that we call sub-models. The base of a sub-model is the link in the sub-model connected to the FT sensor closer to the floating-base. Each sub-model is considered an independent articulated floating-base structure governed by the Newton-Euler dynamic equations [129]. In the example in Fig. 2.4, measured force-torques are indicated in green and are pointing towards the floating-base, while unknown contact force-torques are drawn in red. There are $n = 5$ FT sensor in the system, that is then decomposed in $n+1 = 6$ sub-models. Other contact force-torques (red arrows in Fig. 2.4 and Fig. 2.5) are estimated with the procedure described below.
This algorithm is used as an evaluation tool in Chapter 4, to calculate the reference wrenches in Chapter 5 and extended in Chapter 7 to consider information from the artificial skin.

2.4.1 Notation

Notation used through the thesis	
A,B	Coordinate frames.
$\|\cdot\|$	Euclidean norm.
A	Inertial frame.
${}^A R_B \in \mathbb{R}^{3\times3}$	3D rotation matrix from B to A
${}^A o_B \in \mathbb{R}^3$	Coordinates of the origin of frame B expressed in frame A.
$u, v \in \mathbb{R}^3, u^\wedge \in \mathbb{R}^{3\times3}$	Skew-symmetric matrix-valued operator associated with the cross product in $\mathbb{R}^3$, such that $u^\wedge v = u \times v$.
${}^A\omega_{A,B}$	with ${}^A\omega^\wedge_{A,B} = {}^A\dot{R}_B {}^A R_B^\top$ Angular velocity of frame B with respect to the frame A expressed in frame A.
${}_B\mathrm{f} = \begin{bmatrix} {}^B f \\ {}^B \tau \end{bmatrix}$	Coordinates of the 6D force f expressed in the B frame.
${}_A X^B = \begin{bmatrix} {}^A R_B & 0_{3\times3} \\ {}^A o_B^\wedge {}^A R_B & {}^A R_B \end{bmatrix}$	6D force transformation from B to A.
$\langle s, p \rangle$	Dot product between vectors s and p.

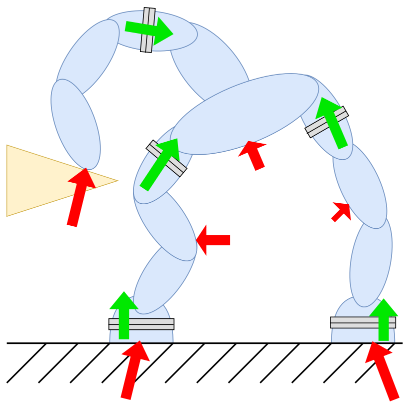

Fig. 2.4 A multi-body system with internal six-axis FT sensors.

2.4.2 Contact Force Estimation

In the simple case of one body, we define the *sensor proper* acceleration of body B of the frame B w.r.t. to the frame A as ${}^B\alpha^g_{A,B} = \begin{bmatrix} {}^B R_A ({}^A \ddot{o}_B - g) \\ {}^B \dot{\omega}_{A,B} \end{bmatrix}$, where ${}^A g$ is the gravitational acceleration in the inertial frame [129].

We also define the inertia tensor of body B expressed with respect to frame B as ${}_B\mathbb{M}_B = \begin{bmatrix} m 1_{3\times3} & m {}^B c^\wedge \\ -m {}^B c^\wedge & {}_B\mathbb{I}_B \end{bmatrix}$, where m is the body mass, ${}^B c$ are the coordinates of the center of mass in frame B and ${}_B\mathbb{I}_B$ is the 3D inertia matrix of the rigid body, expressed with the orientation of frame B and with respect to the frame B origin.

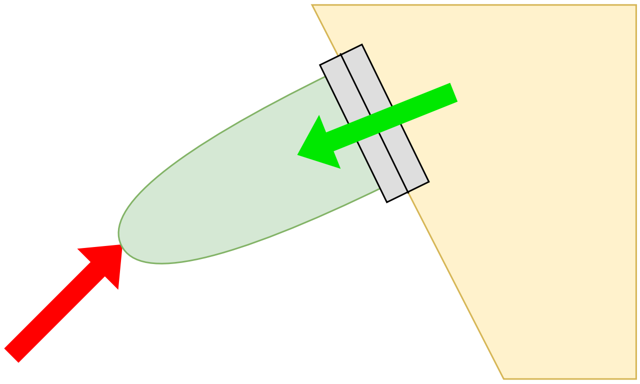

Fig. 2.5 Graphical representation of equation (2.2).

Using the *sensor proper* acceleration of body B (${}^{B}\alpha^{g}_{A,B}$) , the angular velocity of the link B in the B frame (${}^{B}\omega_{A,B}$), FT sensor measurements (${}_{B}\mathrm{f}^{s}$) at a given instant and the inertia tensor of body B (${}_{B}\mathbb{M}_{B}$), we can estimate the contact force-torque ${}_{B}\mathrm{f}^{x}$ by writing the Newton-Euler equations for body B:

$$
{}_{B}\mathrm{f}^{x} = {}_{B}\mathbb{M}_{B}{}^{B}\alpha^{g}_{A,B} + \begin{bmatrix} {}^{B}\omega^{\wedge}_{A,B} & 0_{3\times 3} \\ 0_{3\times 3} & {}^{B}\omega^{\wedge}_{A,B} \end{bmatrix} {}_{B}\mathbb{M}_{B} \begin{bmatrix} 0_{3\times 1} \\ {}^{B}\omega_{A,B} \end{bmatrix} - {}_{B}\mathrm{f}^{s}. \tag{2.2}
$$

In (2.2) the term ${}_{B}\mathrm{f}^{s}$ is the only one that does not depends on acceleration, velocity and the inertial parameters of the body. For convenience, we will indicate all other terms as:

$$
\begin{aligned}
{}_{B}\phi_{B}({}^{B}\alpha^{g}_{A,B}, {}^{B}\omega_{A,B}) = & {}_{B}\mathbb{M}_{B}{}^{B}\alpha^{g}_{A,B} \\
& + \begin{bmatrix} {}^{B}\omega^{\wedge}_{A,B} & 0_{3\times 3} \\ 0_{3\times 3} & {}^{B}\omega^{\wedge}_{A,B} \end{bmatrix} {}_{B}\mathbb{M}_{B} \begin{bmatrix} 0_{3\times 1} \\ {}^{B}\omega_{A,B} \end{bmatrix}.
\end{aligned} \tag{2.3}
$$

From here on, we will omit the dependency on the *proper sensor acceleration* and on the *body angular velocity* indicating this term as ${}_{B}\phi_{B}$ and call it *net force-torque* acting on the body B even if this term does not include the force-torque due to gravity.

A *multi-body* system is composed of two sets. A set $\mathfrak{L}$ of n_L rigid bodies (*links*) interconnected by n_J mechanisms (*joints*) constraining the relative motion of a pair of links. $\mathfrak{J}$ is the set of joints, represented as the two links interconnected by the joint. Each body B is associated with a frame B rigidly attached to it.

When considering the case of a multi-body system, for each link in a sub-model $L \in \mathfrak{L}_{sm}$ we indicate with $\beth_{sm}(L)$ the set of links that are connected with L in the floating-base tree, but belong to a different sub-model., i.e.:

$$\beth_{sm}(L) := \{D \in \mathfrak{L} \mid \{L,D\} \in \mathfrak{J} \wedge D \notin \mathfrak{L}_{sm}\}. \tag{2.4}$$

For the multi-body case, we express the net force-torque of a submodel as:

$$\begin{aligned}\sum_{L \in \mathfrak{L}_{sm}} {}_B X^L {}_L\phi_L = & \sum_{L \in (\mathfrak{C} \cap \mathfrak{L}_{sm})} {}_B X^L {}_L \mathrm{f}^x_L \\ & + \sum_{L \in \mathfrak{L}_{sm}} \sum_{D \in \beth_{sm}(L)} {}_B X^D {}_D \mathrm{f}_{D,L},\end{aligned} \tag{2.5}$$

where ${}_L\mathrm{f}^x_L$ is the contact force-torque of link L expressed in link L frame, ${}_D\mathrm{f}_{D,L}$ is the force-torque that link D exerts on link L as seen by the FT sensor in between both links and $\mathfrak{C} \subseteq \mathfrak{L}$ is the subset of the links where contact force-torques are acting . Noting that in (2.2) and in (2.5) the only unknowns are the contact force-torques, the estimation problem may be solved rewriting these equations in the matrix form $Cx = b$, where $x = \sum_{L \in (\mathfrak{C} \cap \mathfrak{L}_{sm})} {}_L\mathrm{f}^x_L \in \mathbb{R}^u$ contains all the u contact unknowns, whereas $C \in \mathbb{R}^{6 \times u}$ and $b \in \mathbb{R}^6$ are completely determined.

The estimation scheme takes into consideration the following three types of possible contacts:

- pure force-torque : ${}_L\mathrm{f}^x \in \mathbb{R}^6$, unknown vector corresponding to force and torque expressed in the link frame of contact L.
- pure force : $f^x \in \mathbb{R}^3$, unknown vector corresponding to a pure force and no torque.
- force norm : $\|f^x\| \in \mathbb{R}^1$, unknown assuming the pure force to be orthogonal to the contact surface.

The matrix C is built by adding columns for each contact according to its type. The columns associated to pure force-torques (C_w), pure forces (C_f) and pure force norm (C_n) are the following:

$$\begin{aligned} C_w = & \begin{bmatrix} {}_B X^L \end{bmatrix}, \\ C_f = & \begin{bmatrix} {}^B R_L \\ 0_{3\times 3} \end{bmatrix}, \\ C_n = & \begin{bmatrix} {}_B X^L \end{bmatrix} \begin{bmatrix} \hat{u}^x \\ 0_{3\times 1} \end{bmatrix}. \end{aligned}$$

where B is a common frame, in this case the base of the sub-model was selected, and $\hat{u}^x$ is the unit normal vector of the contact force-torque. The matrix C mainly depends on the contact location sensed by the skin. The 6 dimensional vector b is defined from (2.5) in the following way:

$$b = \sum_{L \in \mathfrak{L}_{sm}} {}_B X^L {}_L\phi_L - \sum_{L \in \mathfrak{L}_{sm}} \sum_{D \in \beth_{sm}(L)} {}_B X^D {}_D\mathrm{f}_{D,L}. \tag{2.6}$$

The vector b depends on kinematic quantities derived from whole-body distributed gyros, accelerometers, encoders and the FT sensors [44]. Once C and b have been computed, we can solve the equation $Cx = b$ for estimating contact force-torques.

When only a single contact acts on the sub-model, there are six unknowns for a system of six equations, therefore, the associated force-torque has a unique solution. Whenever two or more contacts are detected, the system admits infinite solutions and it is impossible to get a reliable estimate of the contact wrenches without imposing some constraints to the system. The adopted solution consists in computing the minimum norm x^* that minimizes the square error residual:

$$x^* = C^\dagger b$$

where $C^\dagger$ is the Moore-Penrose pseudo-inverse of C [30]. The above solution distributes equally the total contact force-torque among all contacts.

2.4.3 Joint Torque Estimation

Once an estimate of contact forces are obtained with the method described in subsection 2.4.2, internal force-torques can also be estimated with a standard Recursive Newton-Euler Algorithm (RNEA). The torque $\tau_{\{E,F\}}$ of the joint connecting link E and F comes from the projection of the joint force-torque on the joint motion subspace [129] :

$$\tau_{\{E,F\}} = \left\langle {}^F\mathrm{s}_{E,F}, {}_F\mathrm{f}_{E,F} \right\rangle = \left\langle {}^E\mathrm{s}_{F,E}, {}_E\mathrm{f}_{F,E} \right\rangle, \tag{2.7}$$

$$\begin{aligned}
{}_F\mathrm{f}_{E,F} &= -{}_E\mathrm{f}_{F,E}, &(2.8a)\\
{}_F\mathrm{f}_{E,F} &= \sum_{L \in \gamma_E(F)} {}_F X^L \left({}_L\phi_L + {}_L\mathrm{f}^x_L\right), &(2.8b)\\
{}_E\mathrm{f}_{F,E} &= \sum_{L \in \gamma_F(E)} {}_E X^L \left({}_L\phi_L + {}_L\mathrm{f}^x_L\right), &(2.8c)
\end{aligned}$$

where $\gamma_E(F)$ is the set of the links belonging to the sub-model starting at link F, given E as a base link, ${}^E\mathrm{s}_{F,E}$ is the mapping between the relative 6D velocity of the two bodies connected by the joint and the joint velocity known as *joint motion subspace vector* [37, 129].

2.5 Robots dynamic performance

While is true that some robots are now able to walk, jump, run and even parkour. These behaviors are still not achieved in a consistent reliable way. The most known example is the robot Atlas' videos released by Boston Dynamics, Fig. 2.7. As stated by Boston Dynamics' CEO Marc Raibert, "In our videos, we typically show the very best behavior. It's not the average behavior or the typical behavior. And we think of it as an aspirational target for what the robots do." These type of dynamic behaviors establish different rapidly changing contacts with the environment generating impacts making relevant the dynamics response of the sensor. A situation where is useful to have force-torque sensing is when a contact is established, also called collisions. Fix based robots are able to achieve dynamic behaviors such as handle unexpected collisions to some extent [81] and even cooperate with humans [117]. They achieve this by exploiting force-torque sensing to estimate contact forces and measure or estimate joint torques. Multiple schemes for handling collisions are presented in a survey on robot collisions [51]. The initial problems to be solved in this schemes is the detection of contacts, followed by the location of contacts and the identification of contacts. This can be rephrased as realize a contact happened, understand where it happened and measure the force of the contact. Nonetheless, these schemes are only suitable for robots with their base fixed to the ground.
For floating base systems is possible to obtain and use collision related information using FT sensors, joint torque sensors in addition to encoders, and gyroscopes [137]. In this scheme, an improvement in the force-torque sensing will directly create an increase in the performance of the scheme. There are some robots with only one kind of force sensor like the iCub, described in Section A.1, or with none like Pepper [17]. As a result, this scheme can not be applied directly to these robots.

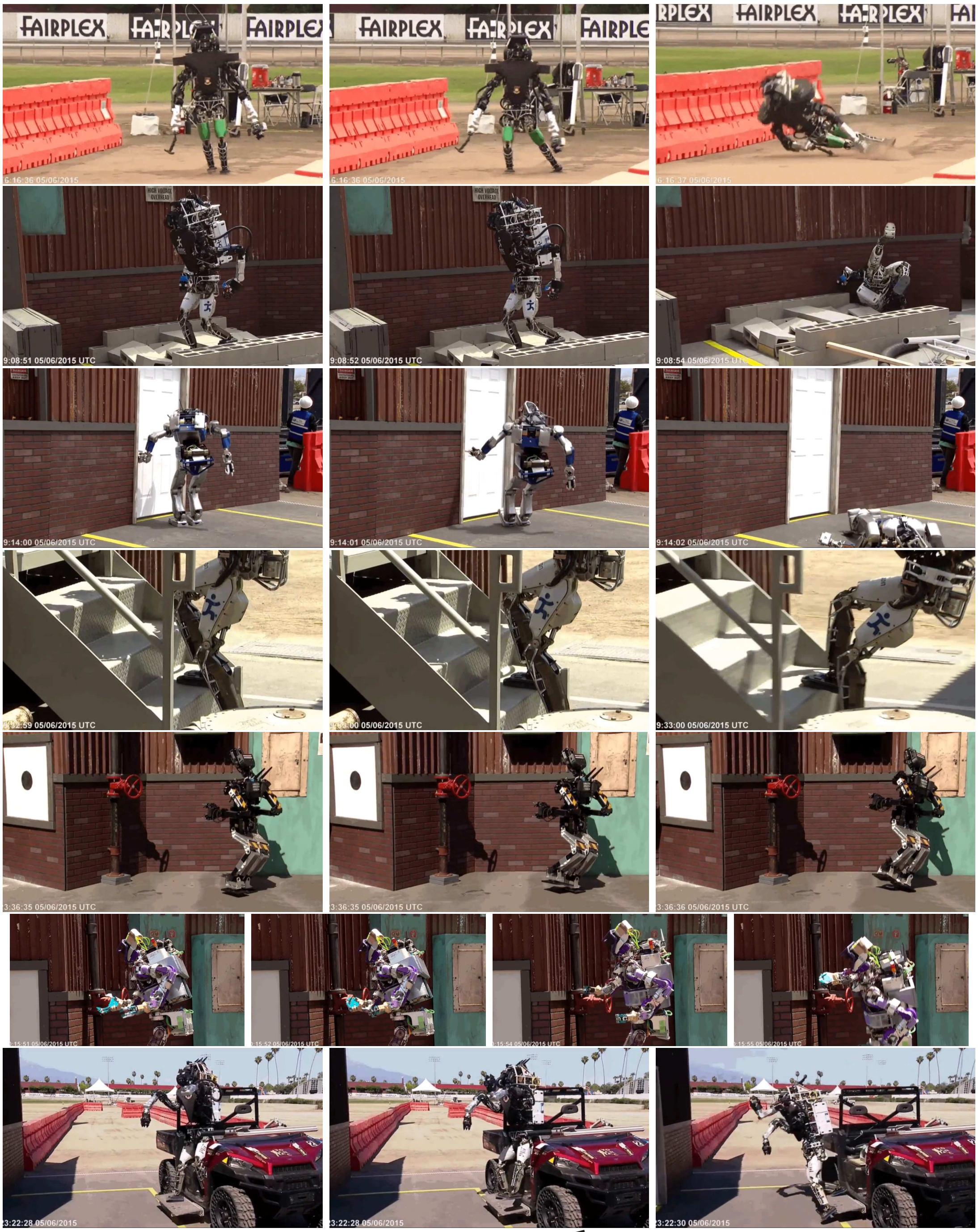

Watch video

Fig. 2.6 DARPA Challenge 2015 failures.

Despite the amount of theoretical background to exploit force-torque sensing, floating base robots in real scenarios still struggle with handling interactions with the environment or other bodies. A good example is the results from the DARPA Robotics Challenge Finals in June 2015 [10, 27, 60, 26].
During the challenge, most of the teams could not take full advantage of having FT sensors. The reason why no other extra objects where used for support or stabilization is mentioned to be the the bad quality of the wrist FT measurements [10]. The Boston Dynamics ATLAS' FT sensor measurements were only used as binary contact sensors by the IHMC and MIT teams [27]. It was mentioned that having more FT sensing information in the form of full six axis FT sensors at the ankle would have allowed to improve results [26]. Examples of failed attempts are shown in Fig. 2.6. Different type of failures can be seen. Being unable to understand if the robot has made contact with the environment (being the ground or a handle). Discerning if the contact is stable enough to shift the weight of the robot to the contact. Problems arising from unexpected contacts can easily happen in reduced spaces. Although there are many reasons for the different failures, the situations previously described are examples of situations in which accurate FT sensing information can provide crucial knowledge to increase the probability of successfully perform the tasks.

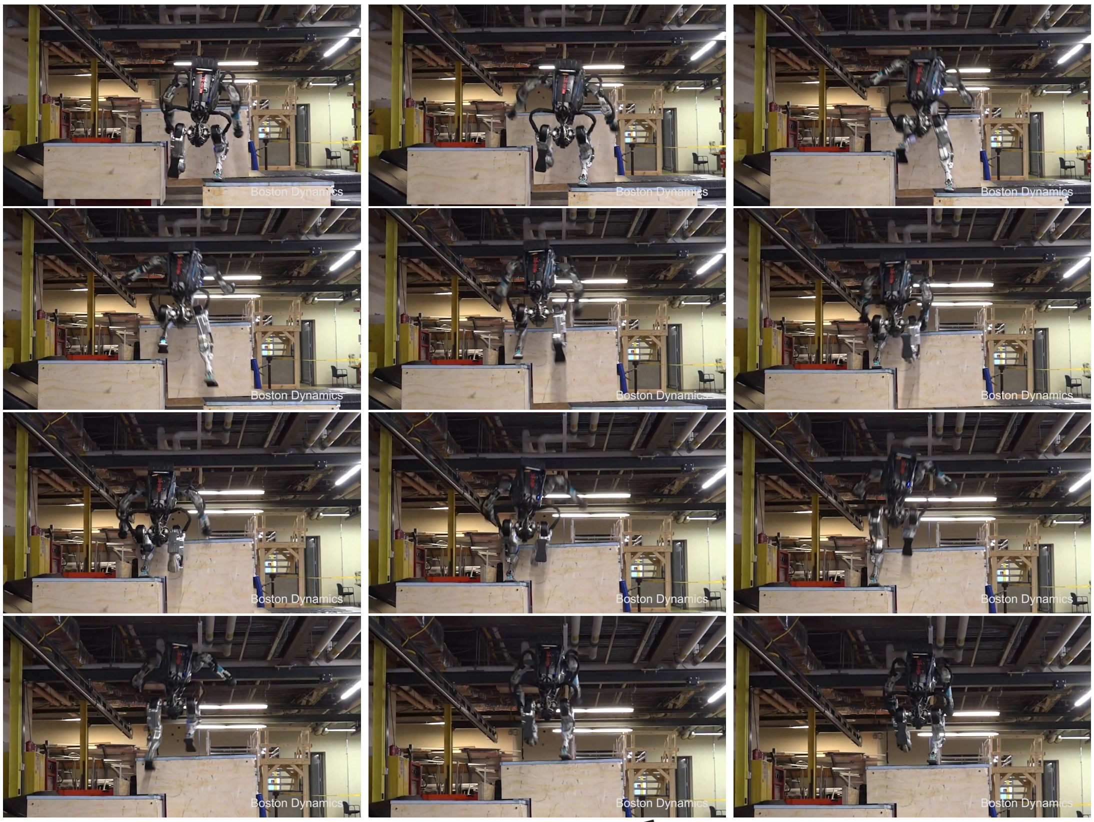

Watch video

Fig. 2.7 Boston Dynamics' Atlas doing parkour.

The fact that force-torque sensors are affected by mounting issues [130, 8] or temperature drift [54, 127, 113], reduces the reliability of these sensors and as a consequence the performance and repeatability of dynamic behaviors in robots. Poor performance of six axis FT sensors have been reported in the literature. Unkown errors in the measured magnitude [13, 52]. Lower performance than other FT solutions like force plates has been mentioned [105].
An example of errors due to bad FT measurements can be seen in Fig. 2.8. The full video can be seen using the QR code or clicking in this link . In this experiment, the contact forces are estimate using the information from six axis FT sensors and the algorithm described in Section 2.4. It can be seen that even if the algorithm is able to detect contact forces while the

robot is not moving. When the robot starts moving contact forces that do not exist appear. Upon inspection it was revealed that the measurements of the FT sensors were not very accurate. Given the performance of six axis FT sensors attempts to improve the measurements. Some rely on redundant sensors [133]. Others rely on reconstructing the ground reaction force through kinematics and IMU measurements. Then use this information to create a Virtual Force Sensor that is constantly compared with FT measurements to detect and recover faulty measurements [52].

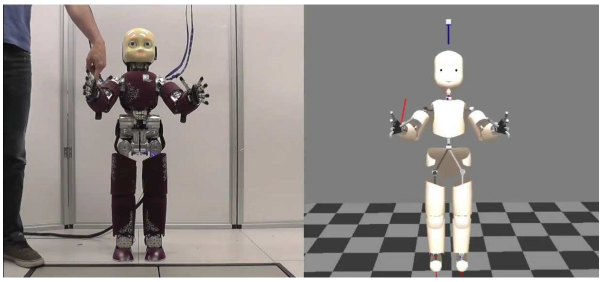

(a) Algorithm correctly detecting contact forces.

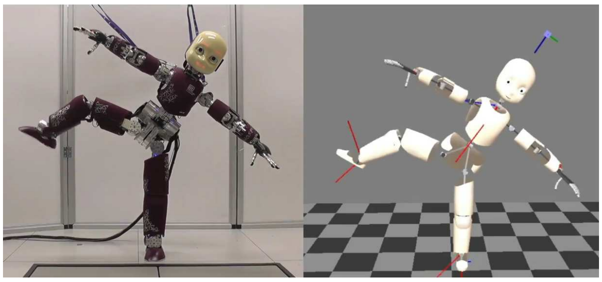

(b) Algorithm incorrectly detecting contact forces.

Watch video

(c) QR code for full video.

Fig. 2.8 Contact Force Estimation using algorithm in Section 2.4.

A common strategy in FT sensors to reduce the effect of drift is to remove the bias just before a change in the load is expected. Robots that have their base fixed to the ground can benefit from this method to some extent. Instead in floating base robots, this is not practical. Most of the time the sensors themselves are used to detect unexpected contacts so the time of collision is not known *a priori*. Besides, the main function of the sensors is to measure the actual force applied or received by the robot. In a scenario in which the robot is already in contact with a surface, removing the bias will make the value of the measured FT incorrect.

From the literature, it can be seen that six axis FT sensors are in more need of improvement than joint torque sensors. It is worth to notice that contact joint torques can be completely reconstructed from the knowledge of the contact forces and the robot model. On the other hand, there are some contact forces that might not be observable when estimating them through the joint torques. As a result, a very promising solution is to increase the performance of force-torque sensors already mounted in the robots while allowing them to cope with sources of drift such as temperature. Typically, in fixed based robots they were used in slow and short motions in industrial applications. Fixed based robots have less chances of encountering changing environments. When used in floating base robots, these sensors might be subjected to a very wide range of motions be it slow and short or fast and wide. They might also experience impacts and inertia constantly changing with the robot configuration. Potentially floating base robots can be used outdoors and be deployed to disaster areas. This means that the environmental conditions might be really different from the fixed base robots. All this should be taken into account when seeking to improve a sensor performance.

Even if the principles of force-torque sensors are well known, there are many things that can become uncertain during the manufacturing process. This complicates the direct use of the theory to derive the relationship between the input of the sensor and the desired output from a sensor. It is possible to obtain force-torque information in more indirect ways by profiting from the relationship forces and torques have with other physical quantities. An example would be the estimation of a motor torque through the current and the model of the motor. Another example is the estimation of forces due to the movement of a body by knowing its mass and acceleration. In fact, these relationships can be exploited to adjust the performance of a sensor by estimating the relationship between the stimuli and the digital output of the sensor. This is what the calibration is for. Chapter 3 explains what calibration is and how is done. It also covers some state of the art in the calibration of FT sensors and tactile arrays.

Chapter 3

Calibration Procedures

Understanding how FT sensors are placed in robots and a general idea of the uses they have in these robots allows to shape the requirements of the performance of the sensor. A sensor converts a stimuli to an electrical signal. The knowledge of the working principles of the sensor may allow to calculate the how the stimuli is converted to the output signal. It is possible that the stimuli have no direct relationship to the electrical signal and intermediate steps are needed. Nonetheless, from the perspective of the user, the sensor should receive the selected stimuli and give a corresponding measurement. Even in cases where the working principle of the sensor is known, reality might differ due to manufacturing or environmental factors. Furthermore the calibration should consider the expected use of the sensor to provide more accurate measurements. In this Chapter, the way to allow a sensor to provide accurate measurements despite these factors is addressed.

3.1 Mathematical Modeling of a Sensor

There is a theoretical input-output (stimulus-response) relationship for every sensor. If a sensor is ideally designed and fabricated with ideal materials by ideal workers working in an ideal environment using ideal tools, the output of such a sensor would always represent the true value of the stimulus. This input-output relationship is called transfer function. In control theory, the transfer function $H(s)$ is often expressed as the ratio between the input function $X(s)$ and the output function $Y(s)$, $H(s) = \frac{Y(s)}{X(s)}$. Nonetheless, for the discussion that follows regarding sensor calibration it is enough to use a general formulation in the form of:

$$E = h(s), \tag{3.1}$$

where s is the stimulus, $h(s)$ is the transfer function and E is the electrical response.

Ideally, the transfer function can be based on a physical or chemical law that forms a basis for the sensor's operation. It is possible that more than one law is required to map all the working principles of the sensor. If such a law can be expressed in the form of a mathematical formula, often it can be used for calculating the sensor's inverse transfer function by inverting the formula ($s = h^{-1}(E)$).

In reality, a sensor does not perfectly comply with the mathematical formula of the phenomena it is based on. Too many ideal conditions are required for this to happen. Besides, readily solvable formulas for many transfer functions, especially for complex sensors, does not exist and one has to resort to various approximations of the direct and inverse transfer functions. Common approximation functions are [43]:

- Simple Models
- Linear Regression
- Polynomial Approximations
- Linear Piece-wise Approximation
- Spline Interpolation
- Neural Networks

The relationship between the change of the phenomena to an electrical value for a specific sensor is obtained through a process called calibration. The objective of the calibration process is to obtain the parameters of the chosen approximation function for the specific sensor. These parameters are referred to as calibration values or calibration parameters.

The accuracy of the sensor is then a result of the calibration process. It requires the mathematical model of the phenomena (or a good approximation) and known stimuli paired with the corresponding sensor's response.

A pair of known stimuli with the sensor response is called a calibration point. A set of calibration points is a calibration data set. The stimuli and sensor response are also called reference data and raw measurement respectively.

3.1.1 Functions Based in Simple Models

It is desirable that a transfer function has a small number of parameters that require estimation. This is the reason why using simple models is convenient. Of course, the choice of the model depends on how good they fit the response of a particular sensor.

Linear Function

The simplest possible transfer function is linear. The math model can be expressed as :

$$E = Cs + O, \tag{3.2}$$

where O is the value of E at $s = 0$, typically called offset or bias; C is the slope of the line, sometimes referred to as sensitivity. The graphical representation can be seen in Fig. 3.1. Eq. (3.2) assumes the possibility of evaluating the sensor at $s = 0$ value. This might not be possible in all cases (think of a temperature sensor in Kelvin scale). For such cases it can be shifted to a known stimulus s_0 using the following equation:

$$E = E_0 + C(s - s_0), \tag{3.3}$$

where E_0 is the known response at s_0. For this linear model, the inverse transfer function $h^{-1}(E)$ has the following form:

$$s = \frac{E - E_0}{C} + s_0 \tag{3.4}$$

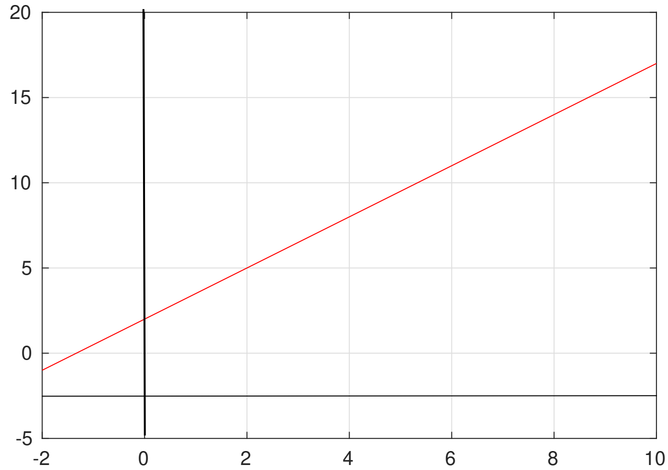

Fig. 3.1 Graphical representation of linear model.

Non linear Functions

A nonlinear transfer function can be approximated by a nonlinear mathematical function. The three main functions based in nonlinear models are the logarithmic, exponential and power

Function	$h(s)$	$h^{-1}(E)$
logarithmic	$C\ln + Os$	$e^{\frac{E-O}{C}}$
exponential	Oe^{ks}	$\frac{1}{k}\ln\frac{E}{O}$
power	$Cs^k + O$	$\sqrt[k]{\frac{E-O}{C}}$

Table 3.1 Simple nonlinear transfer functions.

functions. Their mathematical equations and inverse transfer functions can be seen in Table 3.1. Its corresponding graphical interpretations can be found in Fig. 3.2

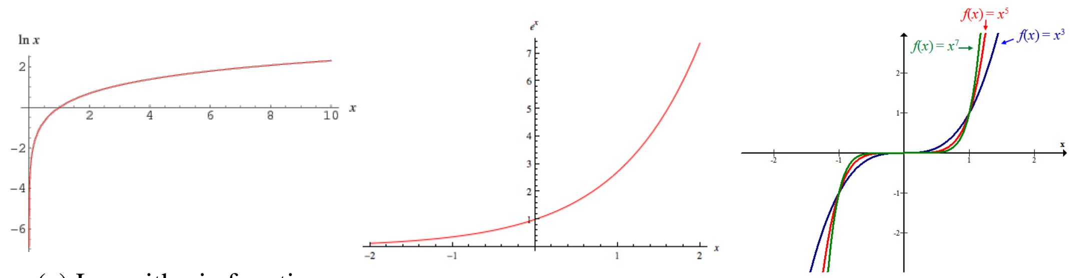

(a) Logarithmic function. (b) Exponential function. (c) Power function.

Fig. 3.2 Graphical represenation of nonlinear transfer functions.

3.1.2 Linear Regression

As the name implies it attempts to find the transfer function using assuming a linear model. It is to be distinguished from the linear model in the fact that this is not a deterministic approach but a statistical approach. This means that it will attempt to find the best linear function that fits the data, even if not all calibration points are on the found line. An example can be seen in Fig. 3.3. The use of linear regression helps to cope with random errors that may appear in the calibration process.

The typical method for performing linear regression comes from the least squares algorithm. The formulation of the least squares problem is:

$$\underset{C}{\arg\min.} \ \frac{1}{N}\sum_{i=1}^{N} \|s_i - CE_i\|^2 \tag{3.5}$$

The solution to this problem is straightforward and well known in statistical literature. It minimizes the sum of squared residuals. The calibration parameters are the solution to the least square problem and have the following form [75]:

$$C = (E^T E)^{-1} E^T s. \tag{3.6}$$

Least square can be extended for solving for multiple variables. Multiple regression is an extension of simple linear regression. It is used when we want to predict the value of a variable based on the value of two or more other variables. Each variable can be considered as a different sensor. There are other extensions to the least squares formulation for nonlinear cases, but those are beyond the scope of the current thesis.

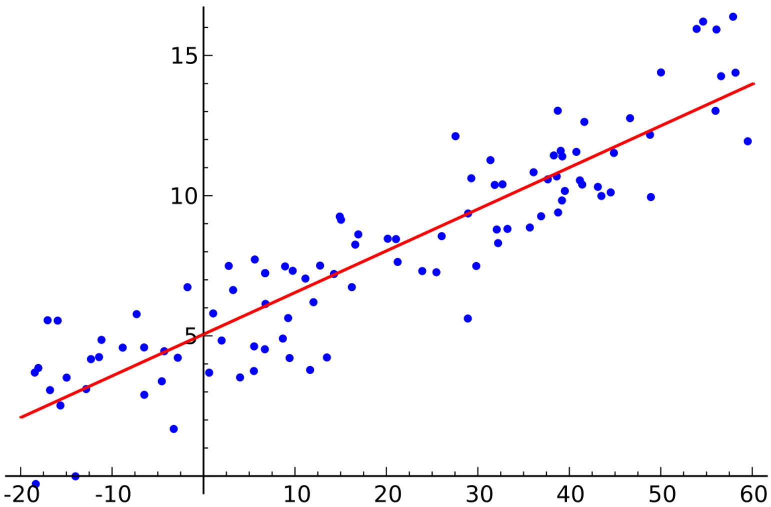

Fig. 3.3 Graphical representation of linear regression.

3.1.3 Polynomial Approximations

Any continuous function, regardless of its shape, can be approximated by a power series, this is also called polynomial approximation. A polynomial approximation function takes the following shape:

$$E = D_0 + D_1 s + D_2 s^2 + \ldots D_n s^n, \tag{3.7}$$

where D_i are the coefficients corresponding to the n-th power or polynomial degree. These parameters allow to shape the curves to obtain $h(s)$. For polynomial approximations is more complex to find $h^{-1}(E)$ starting from $h(s)$. For this reason is common to directly estimate the coefficients of $h^{-1}(E)$:

$$s = C_0 + C_1 E + C_2 E^2 + \ldots C_n E^n, \tag{3.8}$$

where C_i are the calibration parameters corresponding to the n-th power.
An example can be seen in Fig. 3.4. It can be observed that in this case increasing the degree of the polynomial increases the fitting of the data. This depends on the underlying behavior of the system. It is quite common that a real system suffers from noise. In the presence of noise, increasing the polynomial degree risks over-fitting the data, preventing from getting a good generalized approximation function.
A way to solve the polynomial fitting problem is to use multiple regression. Where the other variables are generated by elevating the sensor response up to a n-th degree. Least squares can be used since $h^{-1}(E)$ is linear in terms of the calibration parameters.

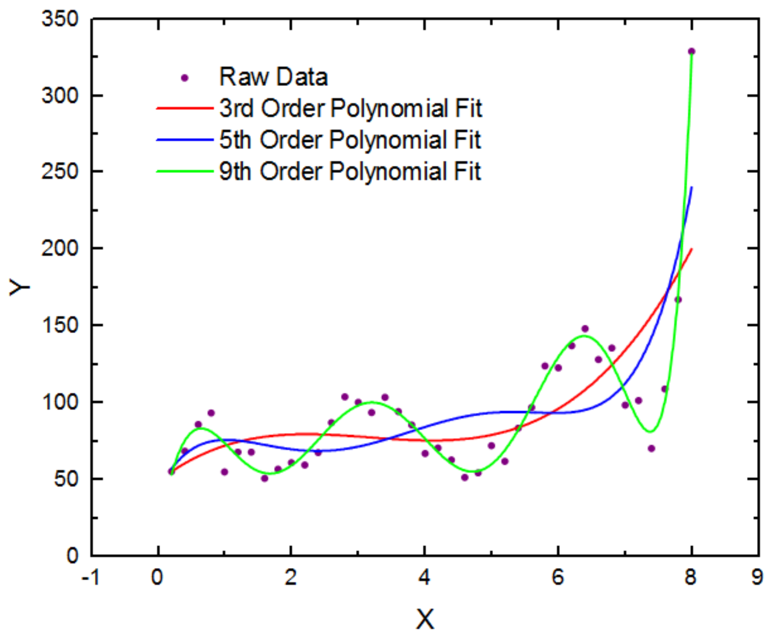

Fig. 3.4 Graphical representation of polynomial approximation using different powers.

3.1.4 Linear Piece-wise Approximation

The idea behind it is to break up a nonlinear transfer function of any shape into sections and consider each such section being linear. Curved segments between the sample points demarcating the sections are replaced with straight line segments, thus greatly simplifying the behavior of the function between the points. This can also be seen as a polygonal approximation of the original nonlinear function. An example is shown in Fig. 3.5.

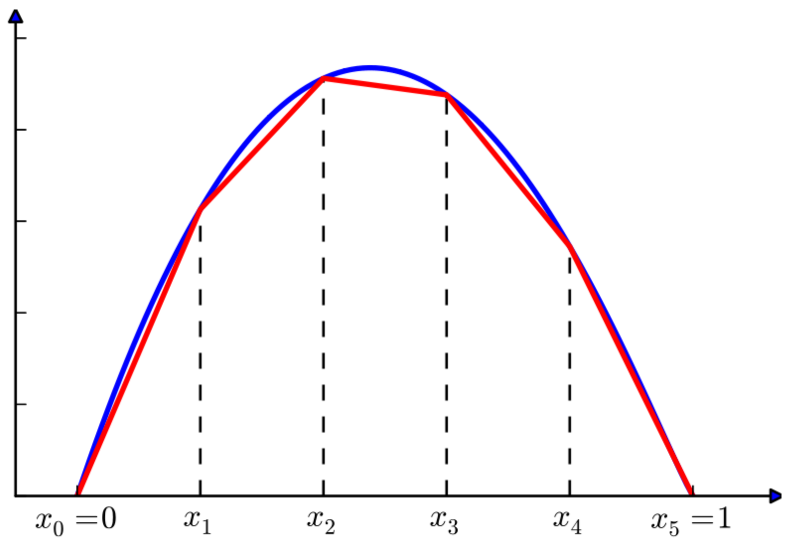

Fig. 3.5 Graphical representation of piece-wise linear approximation.

3.1.5 Spline Interpolation

Approximations by higher order polynomials (third order and higher) have some disadvantages; the selected points at one side of the curve make a strong influence on the remote parts of the curve. This deficiency is resolved by the spline method of approximation. In a similar way to the linear piece-wise interpolation, the spline method uses different third-order polynomial interpolations between the selected experimental points. The graphical representation can be found in Fig. 3.6.

3.1.6 Neural Networks

An artificial neural network, or just neural network, is a mathematical model which models itself after the human brain. Similar to the brain's neurons, it has unit blocks also called neurons or perceptrons. This is normally the most complex approximation function because one or more parameters for each neuron has to be estimated (or learned). Nonetheless, it has the potential to approximate any continuous function. The network learns an input-output mapping (transfer function) with a method called supervised learning. A single neuron is mathematically represented as:

$$y = \phi\left(\sum_{i=1}^{N} w_i x_i + b)\right), \tag{3.9}$$

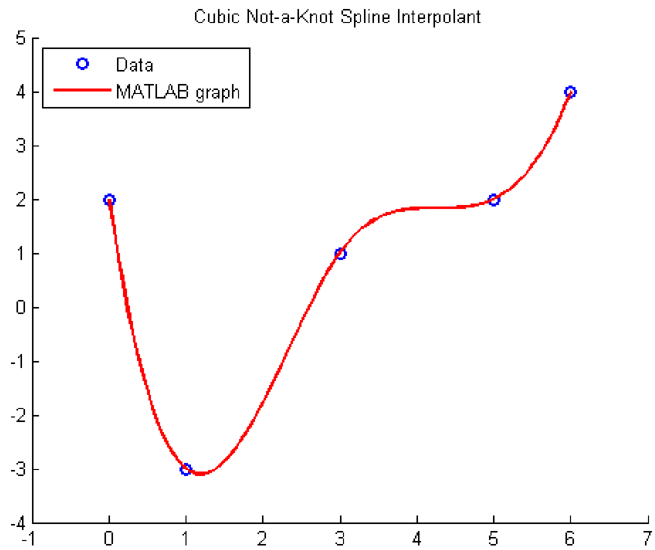

Fig. 3.6 Graphical representation of spline interpolation.

where x_i are the inputs to the neuron, w_i are the weights of each input, b is the bias, ϕ is the activation function and y is the output of the neuron. Each input weight and the bias needs to be learned. A graphical representation of neuron can be seen in Fig. 3.7a

In the mathematical theory of artificial neural networks, the universal approximation theorem states [24] that a feed-forward network with a single hidden layer (Fig.3.7b) containing a finite number of neurons with arbitrary activation function are universal approximators.

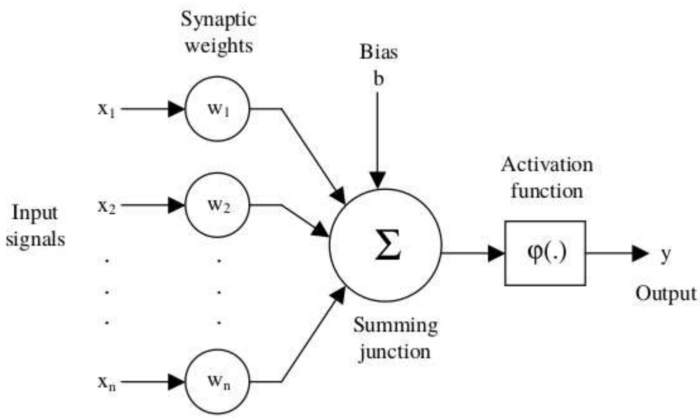

(a) Graphical representation of a neuron.

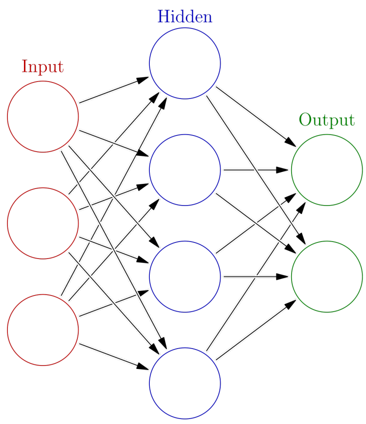

(b) Feed-forward network with a single hidden layer.

Fig. 3.7 Graphical represenation of a neural network.

Neural networks have the potential to approximate any continuous function, but the physical meaning of the solution is usually lost. Neural networks have become a standard tool to tackle problems where we want to make preditions without following a particular algorithm or imposing structure on the available data. Most work to date has focused on the efficiency or quality of predictions of neural networks, without an understanding how they solve the problem [58]. They are often applied as a black box, which from a results point of view, has no contradiction with the aim of calibrating a sensor. Neural Networks is an active research field in its own. Providing deeper knowledge of the topic goes beyond the scope of the thesis.

Independently from the mathematical model, calibration procedures can be classified depending on the place the calibration data set is acquired. If the calibration data set is acquired in the system (or structure) in which is meant to be used, it is referred to as *in situ* calibration. Instead, if the sensor is calibrated in a structure then removed and mounted somewhere else for its use, it is refferred to as *ex situ* calibration.

3.2 Factors that affect sensor accuracy

Accuracy is defined as the maximum difference between the actual value and the sensor's output. Given a sensor design, substantial reductions in the measurement error, can be achieved only by using more sophisticated technologies, materials and components in the construction of the sensor, and finer models of the structure, or more accurate instrumentation for strain measurement and calibration. An improvement of these factors with respect to present sensors is therefore achievable by increasing their cost. However, there are absolute upper bounds to possible reduction of source errors set by present technological state-of-art, and by inherent measurement accuracy limitations.

The right approximation function can be chosen from knowledge of the working principles, but this alone does not ensure the accuracy of the sensor. During calibration, data from the sensor response is mapped to match the reference stimuli. The accurate knowledge of the reference data value coupled with the right approximation function warrants the future performance of the sensor. A factor that needs to be taken into account when calibrating is the expected use of the sensor this may define the range values of the reference stimuli. Other factors include errors during the acquisition of the calibration data. Lastly, conditions during calibration may be different than the conditions in which the sensor is actually used, this may have unforeseen or undesirable effects on the sensor. An ideal calibration procedure should take all these factors into account.

3.2.1 Full Scale and Resolution

All elements in the sensing module provide their own limitations. The sensing element has many design choices. Some of which include the possible range of the sensor based on the elastic limits of the material, the displacement response to a force which can help determine the stiffness of the resulting sensor and its sensitivity.
On the other hand, the combination of the amplification stage in the signal conditioning and the ADC number of possible conversion values place another set of limitations on the sensing module in terms of full-scale and resolution. Full-scale for an analog output is the algebraic difference between the electrical output signals measured with maximum input stimulus and the lowest input stimulus applied. For a digital output, it is the maximum digital count the ADC can resolve for the absolute maximum input [43]. The resolution defines the smallest voltage change that can be measured by the ADC. The number of possible conversion values depends on the number of bits in the output of the ADC called bit_{size}. These elements can be considered as the most limiting factors of the sensor since they are typically selected to be equal or under the limits of the sensing element.
The amplification stage can be characterized by a gain value g_a which is the amplifying factor of the signal. The full-scale is then the difference between the stimuli that generate the maximum voltage value s_{max} and the stimuli that generate the minimum voltage value s_{min} using a selected gain g_a for a given sensing element $Sens_{element}$. Reaching the maximum or minimum value is called saturation. The full-scale FS can be expressed as:

$$s_{max} = h^{-1}(E_{max}^{ref}|g_a, Sens_{element}) \tag{3.10}$$

$$s_{min} = h^{-1}(E_{min}^{ref}|g_a, Sens_{element}) \tag{3.11}$$

$$FS = s_{max} - s_{min} \tag{3.12}$$

where E_{max}^{ref} is the maximum voltage value in V, E_{min}^{ref} is the minimum voltage value in V. The full-scale is given in the units of the phenomena that is measured. The resolution of the ADC is the same as the smallest step size and can be calculated by dividing the reference voltage by the bit_{size}. Since the reference voltage determines the full-scale of a sensor, the sensor resolution is then:

$$res = FS/bit_{size} \tag{3.13}$$

The difference between the smallest and largest physical inputs that can reliably be measured by an instrument determines the dynamic range of the device [141]. For a digital output is determined by the value at saturation and the resolution of the sensor. A change in the stimuli under the resolution value of the sensor will not be measured correctly. Therefore, the resolution affects also the accuracy of a sensor. The resolution can be improved by either reducing the full-scale or augmenting the bit_{size}. So the accuracy of the sensor can be improved by modifying $Sens_{element}$, g_a or bit_{size}. The value of g_a can be made variable without requiring major changes in the sensor even if it implies reducing the full-scale. Any change in the dynamic range of a sensor modifies the transfer function and requires a new calibration of the sensor.

3.2.2 Notes on acquiring calibration data

Ensuring the data used for calibration can be trusted is fundamental for a good performance of the sensor. Therefore, it is crucial to reduce the sources of uncertainty in the reference stimuli during the calibration procedure. Some guidelines for data acquisition are proposed based on the acquired experience. Although errors might still exist during a careful calibration procedure, the following guidelines can help reduce uncertainty:

- The data of the reference stimuli should be of equal or better accuracy than the intended accuracy of the sensor.
- The procedure should take place in a controlled environment.
- The least amount of human intervention helps reducing variability.
- Avoid any interference of external factors during data acquisition.

When something goes wrong during the calibration procedure is usually the case that the whole procedure has to be repeated adding time to a typically time-consuming task. Therefore making the procedure easily repeatable tends to be a desirable feature. Having a way to understand if the acquired calibration data set is useful or not might prevent from performing erroneous calibration. This increases calibration efficiency.

3.3 Calibration of Six Axis Force-Torque Sensors

A force sensor does not measure the force directly. Measuring a force is the result of converting other physical phenomena that varies in response to force into an electrical signal. The relationship between the change of the phenomena to an actual force value is obtained through the calibration procedure.
The most common phenomena used in force-torque sensors is the change in resistance of silicon due to strain. In more technical words, the piezoresistive response to strain of semiconductor material. This material also changes resistance with temperature. Because of this, depending

on the calibration procedure, the sensor might suffer from temperature drift. Which is the undesired change of measurement due to changes in temperature.
For sensors based in metallic foil or silicon strain gauge, the sensor is designed such that the resulting deformation in the structure of the sensors are inside the linear section of the sensing material for the specified range. Because of this, a linear relationship between deformation and forces can be assumed. For single-axis force sensor, it is simple to use an array of strain gauges in a Wheatstone Bridge configuration to perform temperature compensation by itself. Fulfilling the requirements to achieve the same in a multi-axis FT sensor at hardware level complexifies the design, increases the number of components needed and the cost.

3.3.1 Mathematical model

There are two physical laws at play in strain gauge force sensors. One is common to all kinds. It is the relationship between the deformation of a spring and forces, it is the Hooke law of elasticity, described in more detail in Section1.2.

$$f = k\Delta x, \tag{3.14}$$

where f is the force value in N, k is a constant of the material $\frac{\mathrm{N}}{\mathrm{m}}$ and Δx is the displacement (or strain) in meter. It is valid as long as the material does not reach plastic deformation. The other principle depends on the type of sensing technology. For semiconductor strain gauges it is the piesoresistive effect. As mentioned in Section 1.3.1, the model is the linear function:

$$R = R_o(1 + S_\varepsilon \varepsilon), \tag{3.15}$$

where R is the resistance value in Ω, S_ε is the gauge factor of the conductor, R_o is the resistance with no stress applied in Ω. Combining both physical effects gives the following transfer function:

$$R = R_o(1 + S_\varepsilon \frac{f}{k}) \tag{3.16}$$

Therefore the most used model for predicting the force-torque from the raw strain gauges measurements of the sensor is a linear model. The inverse function is:

$$f = \frac{(R-R_0)k}{S_\varepsilon R_0} \tag{3.17}$$

$$= \frac{Rk}{S_\varepsilon R_0} - \frac{k}{S_\varepsilon} \tag{3.18}$$

$$= cR - O, \tag{3.19}$$

where

$$
\begin{aligned}
c = & \frac{k}{S_\varepsilon R_0} \\
O = & \frac{k}{S_\varepsilon}.
\end{aligned}
$$

Considering possible errors during the calibration procedure linear regression is the most suitable approximation function. Multi-axis force-torque sensors usually contain multiple strain gauges, each of them can be seen as a separate sensor. Because of this, multiple regression is a valid option for this kind of sensors. Therefore each force axis will be calibrated using the information from all strain gauges,

$$f_i = c_1 R_1 - O_1 + c_2 R_2 - O_2 + \ldots c_m R_m - O_m, \tag{3.20}$$

where f_i is the force in the i-th axis in N or N m depending on the axis, R_m is the digital response of the m-th strain gauge in bit counts, c_m is the slope of the linear model of the m-th strain gauge in $\frac{\mathrm{N}}{\mathrm{bit}}$ and O_m is the bias of the m-th strain gauge. The orientation of f_i with regards to the m-th strain gauge will change the value of k required. It depends on the strain being normal, shear or a combination of both. As a result, the array of c_m coefficients C_m and O_m will be different for each i-th axis. Taking this in consideration, the approximation function for these sensors has the following form:

$$\mathrm{f} = Cr + o \tag{3.21}$$

where $\mathrm{f} \in \mathbb{R}^6$ are the 6D forces, $C \in \mathbb{R}^{6\times m}$ is the calibration matrix in $\frac{\mathrm{N}}{\mathrm{bit}}$, $r \in \mathbb{R}^m$ are the raw measurements (sensor's response in bit counts) and $o \in \mathbb{R}^6$ is the offset which is also a 6D force vector. Both the calibration matrix C and the offset o are unknown and need to be estimated.

3.3.2 Calibration procedures

The typical calibration procedure considers first identifying the offset when no load is applied on the sensor. Then, carefully place some weights in specific positions to have well known gravitational forces and torques in order to span the space of the sensor. In order to resolve the coupling effects, is necessary to have calibration points with as many orientations of the force vector as possible based on the sensor's coordinate system. In other words, have as many differnent points as possible in the 3D force space. If the calibration data sets are obtained when the multi-axis forces and torques are applied to the sensor, the coupling effect can be solved [95]. The calibration data should ideally be a representative data set of what the sensor will be subjected to. The methods for obtaining the calibration matrix have been thoroughly studied and although many methods exist, solving with least squares remains the

most popular [19].
In standard operating conditions, a decrease in the effectiveness of the calibration may occur in months. Leading companies for FT sensors [11, 142] recommend to calibrate the sensors at least once a year. The calibration done by the manufacturer usually implies that the sensor must be unmounted, sent back to them and then mounted again. The typical callibration procedure is a quasi-static calibration of the sensor. Dynamic calibration of these kind of sensors has rarely been investigated due to the complexity involved [78]. Few attempts have been done to model and compensate for dynamic effects [78, 14, 39, 148]. Usually this calibration procedures match one of three categories: frequency response, impact response or step response. In general they highlight the difficulty of a repeatable dynamic calibration procedure and do not consider complex load cases.

Ex Situ Calibration Procedures

The task of creating equipment to carry out the calibration with high accuracy is equal in importance to the problem of the design of the FT sensor [151].
For simplifying the time-consuming procedure of careful load placing, some specialized structures have been designed [134, 140, 16, 126]. Even with the help of these specialized structures, human intervention is used in every single calibration point since the change of load is manual.

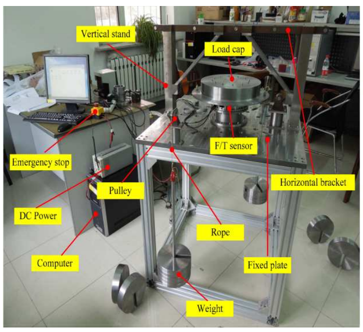

(a) Using specifically designed structures [126].

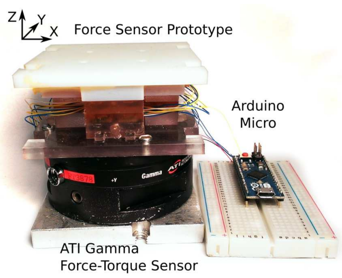

(b) Using another sensor [50].

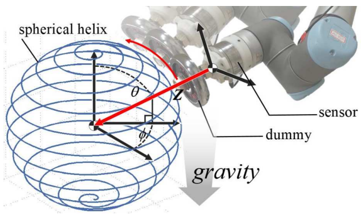

(c) Using robotic arm [96].

Fig. 3.8 Examples of *ex situ* methods.

Some have used complicated structures for the calibration of the sensor, with a combination of four joints with two DoF each and four pulleys [151]. This structure uses a complementary device to change the orientation of the sensor and therefore the application of the load on the sensor. This allows calibrating with less human intervention. The actual mechanism to change the orientation of the sensor is not described.

Others have taken advantage of six DoF robotic arm to span as many orientations of the sensor as possible with a known mass [95, 96]. Even if the sensor is mounted on a robot, it is strictly used as a medium to obtain the calibration data sets, not the working destination of the sensor. In other cases, a previously calibrated sensor is used as reference [36, 94, 3, 50]. This has the disadvantage of trusting on the calibration of another sensor which might not be accurate.

In Situ Calibration Procedures

FT sensors are prone to change performance once mounted in a mechanical structure such as a robot [130, 8]. Different methods have been developed to re-calibrate the sensors once mounted. These *in situ* methods allow to perform the calibration in the sensor's final destination, avoiding the decrease in performance that arises from mounting and removing the sensors from its working structure. The relevance of calibrating *in situ* has become evident, making *in situ* calibration part of the service provided by FT sensor companies [71].
To the best of our knowledge, the first FT sensor *in situ* calibration method exploited the topology of a specific kind of manipulators equipped with joint torque sensors. They assumed the center of mass of the wrist and the objects grasped are known and aligned with the z-axis of the sensor. Using three different sets of masses and some predefined positions they estimate the inverse calibration matrix with least squares. Then an approximate relationship to do the pseudoinverse is applied. The torque measurements in a specific position are exploited to complement the calibration points [120]. Another *in situ* calibration method for FT sensors can be found in [112]. But, the use of supplementary already-calibrated force-torque/pressure sensors, impairs this method since those sensors are prone to be affected by the mounting procedure, propagating the error from sensor to sensor. Some calibrate the sensor mounted in their final position by designing a calibration bench that accommodates the sensor and the mounted structure [146]. This requires the design of a particular structure and the mounting and dismounting of the whole part to calibrate the sensor. Another approach calibrates a FT sensor in a robot leg. The calibration forces and torques are induced manually by a human user through the four handles (black cylinders) of the tilt and pan plate mounted on top of the reference sensor [25]. Even with the novel approach for online calibration, it requires the cooperation of a human and a reference sensor.
Another method has shown that six axis FT sensor can be calibrated based on the shape from motion method with a complex algorithm. This requires the use of three different sets of weights and a minimal setup with a fixed pulley. It requires to calibrate the sensor three times per load so in total nine calibration data sets [125].
Some methods rely on adding other external sensors, such as accelerometers, to obtain a ground truth [130]. This translates the source of error to the accuracy of the accelerometers and

measurement of the transformation matrix between the sensor frames.
In all of these methods, the effect of temperature is either not considered or carefully controlled when calibrating without accounting for changes in the working conditions.

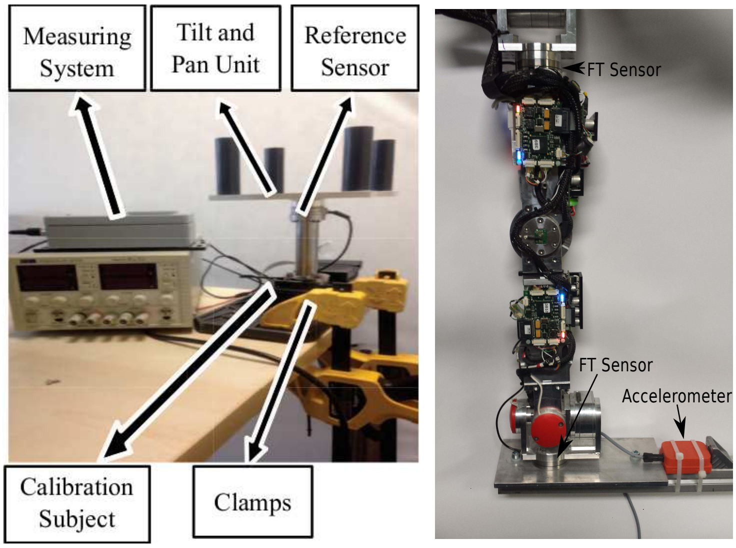

(a) Pan Tilt mechanism on top of foot [25].

(b) Using accelerometers [130].

Fig. 3.9 Examples of *in situ* calibration.

Measurement Accuracy and Resolution

In most of FT sensors, the accuracy is calculated with respect to the full-scale of the sensor. The resolution of the measurements is conditioned by the ADC converter. By changing the value of the gains is possible to affect the limit at which the ADC reaches saturation. As a consequence, the sensor range and resolution are changed. Therefore a higher gain implies lower range and better resolution. With better resolution the calibration of the sensor can be more accurate. By having the option of changing the gains is possible to use the same sensor while optimizing the calibration for a specific range.

3.4 Force Calibration of Tactile Sensor Arrays

Similar to force-torque sensors, in tactile sensor arrays, the Hooke law allows to relate the displacement to a force. The other physical phenomena depend on the technology used. Since a calibration considering piesoresistive effect is described in the previous section, in this section the capacitive effect is used. This happens to aligns with the available technology in the lab.

3.4.1 Mathematical model

For tactile sensor arrays, the shape of the capacitor can be assumed to be flat. As mentioned in Section 1.3.2, for flat capacitors the capacitance Ca in F can be calculated as:

$$Ca = \kappa\varepsilon_0\frac{A}{d}, \tag{3.22}$$

where κ is the dielectric constant of the material in $\frac{\mathrm{F}}{\mathrm{m}}$, ε_0 is a constant if the sensor were found in vacuum also in $\frac{\mathrm{F}}{\mathrm{m}}$, A is the area of the plates in m^2 and d is the distance between the plates in m.

Considering the Hooke law described in eq. (3.15) and the capacitance for a flat capacitor described in eq. (3.22), the transfer function is built on the change of capacitance due to the displacement of the plates when a force is applied as follows:

$$Ca = \kappa\varepsilon_0\frac{A}{d_0+\Delta d}, \tag{3.23}$$

where Ca is the capacitance after a displacement and d_0 is the original distance in m. Using eq. (3.15) and knowing there will only be forces induced by compression the final form of the transfer function is:

$$Ca = \frac{\kappa\varepsilon_0 A}{d_0+\frac{-f}{k}} \tag{3.24}$$

An example of the behavior of this transfer function can be seen in Fig. 3.10. It behaves like an negative logarithmic funciton. This way the inverse transfer function is:

$$f = \frac{\kappa\varepsilon_0 Ak}{Ca} - d_0 k, \tag{3.25}$$

To facilitate the calibration it is possible to use the relationship between the force and the pressure ($p = \frac{f}{A}$) in Pa to generate the stimuli. The inverse transfer function in that case is:

$$p = \frac{\kappa\varepsilon_0 k}{Ca} - \frac{d_0 k}{A}, \tag{3.26}$$

The options for the approximation function are either a negative logarithmic function or a three to fifth order polynomial. Using polynomial approximation allows having robustness towards errors during the calibration process. Each individual tactile array requires calibration

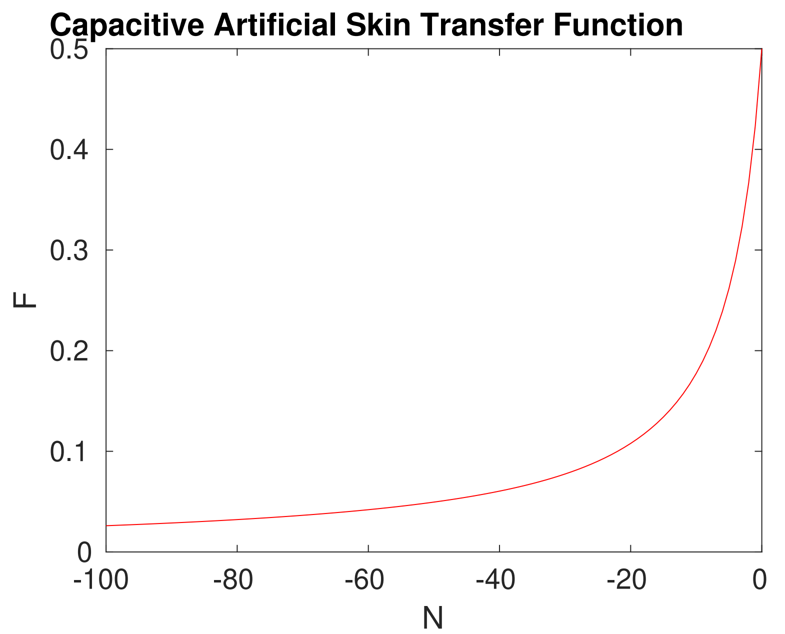

Fig. 3.10 Graphical representation of the transfer function.

and the resulting force can be taken from the sum of calibrated values. This allows to calibrate the artificial skin to retrieve the force measurements perpendicular to its surface, also called the normal force.

$$f_n = \sum_{t=1}^{N} f_t, \tag{3.27}$$

where f_n is the normal force in N, f_t is the force in the t-th tactile sensor in N, N is the number of tactile sensors in the array. This applies only for flat tactile arrays. Special considerations have to be made to calibrate curved surfaces.

To evaluate independent contacts an algorithm to group neighbor tactile sensors that have been activated is required.

3.4.2 Calibration Procedures

Methods covering tactile sensors force calibration can be roughly divided into two categories: individual sensor calibration and tactile surface calibration [66].

Individual sensor calibration

Some attempts have been made to calibrate the tactile sensors to estimate contact forces. One of the methods uses a technique that involves applying various forces mechanically on the individual tactile sensors with a device that enables to measure the applied forces [100, 86, 68]. Therefore, it is possible to create the mathematical models that relate the applied force and the sensor values. However, all the methods that use this technique are very time-consuming, considering there can be hundreds of sensors within a single skin patch and each one of them has to be calibrated separately.

Multiaxis FT sensors measurements can be used to define a linear regression of the unknown local stiffness. Transformation matrices between the FT sensor and each tactile element are able to be calculated in the process [23]. This technique was conducted in a planar array of tactile sensors manually stimulating each tactile element, disregarding the gaps in between, and requires the FT sensors to exist on the robots which is not always the case.

Tactile surface calibration

Another technique applies uniformly distributed pressure on the skin to calibrate the skin [66]. The skin is placed inside a vacuum bag and the pressure is decreased inside the bag with a vacuum pump. The pressure and skin values are extracted during the experiment and the models, that relate pressure to the sensor reading, are generated for all the sensors simultaneously. The calibration takes only a few minutes and can be applied to a variety of skin shapes. The maximum calibration range is equal to the atmospheric pressure.

Based on a similar principle, a device was designed to perform the calibration procedure fast, accurately and with a very simple setup [65]. The pressure calibration range of this device is relatively large (3 bars) and can be used with skins of various shapes and sizes.

In all of the previously mentioned calibration techniques, the space between the tactile elements is neglected.

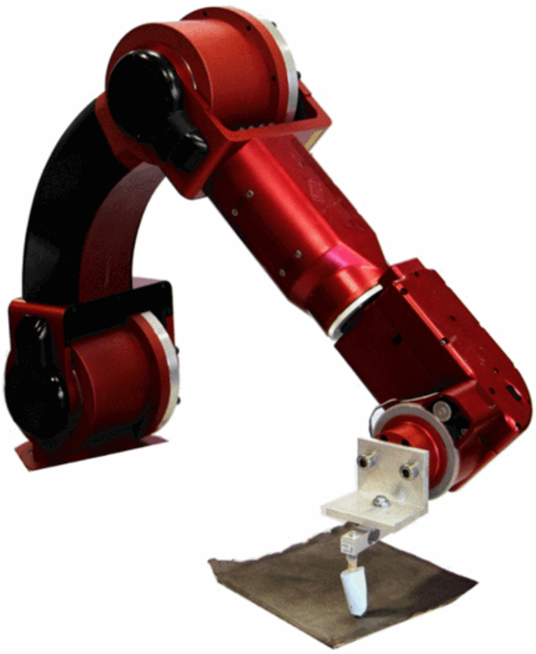

(a) Individual sensor calibration [100].

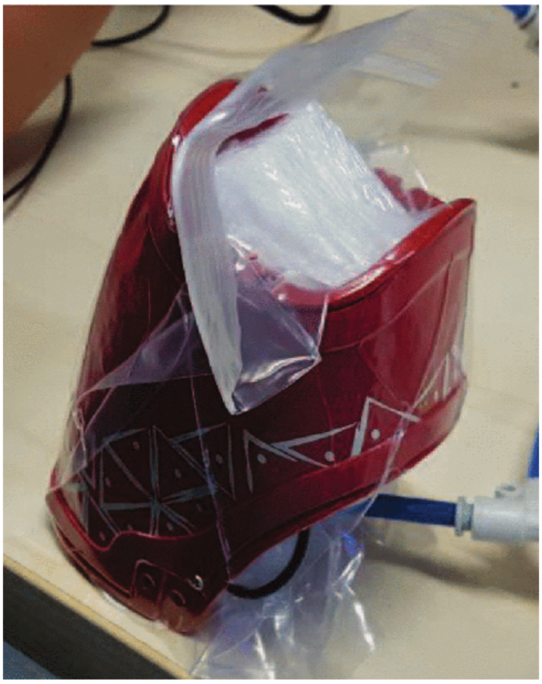

(b) Tactile surface calibration [66].

Fig. 3.11 Examples of artificial skin calibration.

3.5 Conclusions

Given the knowledge of how the senors are built and used, it is possible to realize how important force torque sensing is for robotics and what should a FT sensor accomplish. It is clear that there is room for improvement in the accuracy of contact force estimation. Six axis FT sensors have a long history in fixed base robots and they were sufficiently adapted to the way the were used, but the conditions and scenarios in floating base robots is very different. Even so, calibration and performance of commercially available sensors did not seem to adapt to these new requirements. Although artificial skin is a promising solution for estimation of force torque in multiple contact scenarios, it has not been fully used as a force torque sensor. The gap in between sensing elements is disregarded, but it might be possible to improve force estimation by taking them into account.The knowledge acquired in the field of force torque sensing generated a series of insights that motivated the research in this thesis.

3.5.1 Motivations

The main motivations of the presented research are:

- Given the dynamic equation of motion, eq.(2.1), the knowledge about contact forces and joint torques is fundamental for dynamic motions. Therefore studying how best to estimate these quantities is an interesting and relevant problem to solve. This information can be estimated with the aid of force-torque measurements.

- From the use of force-torque sensing in robotics is possible to see that force-torque sensors have a great potential already depicted theoretically. Therefore further improving this technology is valuable.

- Robots performance in real scenarios proves that in situations outside controlled environments the reliability of these sensors impacts greatly the performance of robots, especially floating base robots. The reliability of these sensors needs to be improved.

- A calibration procedure is fundamental for the reliability of a sensor since is what determines the performance of a sensor once the design is fixed.

- Knowledge of the working principles of the sensor and expected uses of it should guide the calibration procedure design.

- Tools to understand the validity of the calibration data can be very helpful in the calibration process and may also give useful insight in the behavior of the sensors.

- Mounting Force-torque sensors in mechanical structures like robots, affects their performance and besides the need to be calibrated at least once a year. Both issues can be addressed by *in situ* calibration procedures.

- The main technology used based on silicon semiconductor suffers from temperature drift. It should be taken into account in the sensors' calibration.

- Complex loading cases, drift and noise in the sensor ask for a comprehensive excitation of the sensor that could potentially consider dynamic modeling. To achieve this consistently might require a new *ex situ* calibration procedure.

- Six axis FT sensors, are able to sense the sum of forces and torques acting on a body, but struggle to independently identify different contacts. Other sources of force-torque sensing information should be explored.

Given the listed motivations, the objective of this thesis is to provide the knowledge and algorithms needed to have a reliable and accurate estimation of contact forces and joint torques exchanged between the robot, the environment and other objects. It focuses on improving the measurement reliability of the six axis FT sensors. This allowed robots to perform better dynamical motions. This was achieved by developing novel *in-situ* calibration methods and proposing a new *ex situ* calibration device. Other sources of force-torque information, such as tactile arrays, were explored. This should enable the research community to better exploit force-torque sensing in complex structures such as robots.

3.5.2 Objectives

There are three intermediate goals to achieve the general objective previously described:

1. Deep understanding of force-torque (FT) sensors.
2. Improvement of force-torque sensors' performance.
3. Increase performance of dynamical motions in robots through the use of force-torque sensing.

To gain a deep understanding of the force-torque (FT) sensors the following actions were taken:

- Study the functioning principles of the different six axis FT sensing technologies.
- Understand how force-torque sensing is used in robots.
- Revise how force-torque sensing is used in robotics.
- Investigate how six axis FT sensors are usually calibrated.
- Develop tools for evaluating six axis FT sensors data.
- Analyze the performance of six axis FT sensors mounted on robots.

Seeking to improve force-torque sensors' performance the strategies implemented were:

- Development of *in-situ* calibration methods.
- Design of an improved *ex-situ* calibration method.
- Investigate the feasibility of using tactile sensors as force-torque sensors.

Aiming to increase the performance of dynamical motions in robots through the use of force-torque sensing, it was considered necessary to:

- Allow the articulated body to exploit the improved measurements.

- Evaluate the result of improving measurement quality.
- Allow the possibility to exploit other sources of force-torque information, such as tactile sensor arrays.
- Allow the robot to estimate individually forces when more than one force is acting on the same robot.

3.5.3 Assumptions

The thesis focuses mainly on six axis FT sensors and other possible sources of force-torque sensing. In regards to exploring six axis FT sensor behaviors on a robot and their *in situ* calibration, the research assumes the following:

- The model of the robot is known and considered accurate.
- The location of the sensors is known and the robot allows to excite the sensor in all six axis.
- The robot is able to be controlled to some extent without force-torque sensor feedback.
- An algorithm to exploit the measurements to estimate contact forces is implemented on the robot.
- The calibration matrix of the sensor is known. This is not strictly required.
- Ability to actually change the calibration inside the sensor is not required but is useful.

The other sources of force-torque sensing proposed are capacitive tactile sensor arrays. For these sensors the assumptions are:

- The sensor can be calibrated to measure either pressure or forces.
- The location of each individual taxel with respect to the robot is known or able to be calculated.

Chapter 4

Six Axis Force-torque Sensor Performance Evaluation Tools

Understanding the principles behind the sensors is important. But studying the actual behavior of the sensor mounted on a system can help understand how to more effectively improve the performance of the sensors. An easy fast way to evaluate calibration data is important for efficiency when doing sensor calibration. In this Chapter, methods for evaluating the performance of mounted six axis FT sensors are explained. The tools developed to obtain the evaluations are described. This is followed by a series of test to gain insights into the behavior of the sensors and their possible sources of error.

4.1 Performance Evaluation Tools

To analyze a sensor is crucial to be able to distinguish when a sensor is working correctly. To do this, a way to measure the performance of a sensor such that it allows a comparison between sensors is needed. To quantify the performance, a commonly used quantity is the Mean Square Error (MSE). Nonetheless, since the analysis was performed with mounted sensors on a robot is possible to create specially designed evaluation tools. Three tools for understanding and evaluating the sensors were designed. These tools were employed to gain insights into the performance of the available sensors. The tools are :

- Visualization Tool
- Sphere Analysis Tool
- Contact force validation Tool

4.1.1 Visualization tool

Experimental data can have unexpected behaviors. It is crucial to understand what could be the cause of the unexpected behavior. The visualization tool is meant to make this process much more intuitive and fast by providing a connection between the 3D space of either the forces or torques and the position of the robot at a certain point of an experiment. It uses the logged data of the experiment. It could be seen as a way to debug an experiment offline.

The visualization tool has two modes: one in which it runs the experiment as an animation and the other one in which is possible to select a specific sample of the experiment to analyze. It can receive an optional argument to plot the torques instead of the forces. The first mode allows also to record a video of the forces or torques. An example can be seen using the QR code in Fig. 4.1 or following this link. The second mode has some useful features for debugging an experiment:

- A slider to move along in the experiment.
- A text box in which a number can be entered to move the experiment to that specific sample.
- A button for saving a relevant sample and time of the experiment.
- A toggle button to select if the saved sample can be considered the beginning or end of an interesting section of the experiment.

Example of the visualization tool can be sin in Fig. 4.6. For the visualization of the iCub, the iDyntree [129] visualizer is used.

Fig. 4.1 Visualization video mode.

4.1.2 Sphere Analysis tool

Consider a body in which the center of mass does not change and is being moved in a spherical trajectory. When the body is moving slowly, such that acceleration of the body can be neglected, and no other force is acting on the body the only cause of force is the gravity. In this case, the magnitude of the force remains the same and what changes is the orientation with respect to the inertial frame. If we consider all the possible orientations then the gravity direction spans a unit sphere. This motion generates a sphere in the 3D force space where the radius of the sphere is mass times gravity ($m \times g$).

The sphere analysis tool uses this as a ground truth. By generating spherical motions with one of the limbs in which the FT sensor is mounted (an arm or a leg), an ellipsoid is fitted using the measurements of the sensor.

The radii of the ellipsoid correspond to the magnitude of the force when it is fully applied on the respective axis. If the sensor was perfect, the same value would be observed for the three force axis. Thus the difference between the among axes can be considered a value of their performance. The standard deviation (std) between the radii was selected as a performance index to represent the performance of a sensor with a single number. A value closer to zero

represents a better performance.
Furthermore, if the model of the robot can be trusted a reference sphere is generated to calculate what is the error in N of each force axis of the sensor. This can also be used to improve the fitting of the ellipsoid with the knowledge that we are expecting a sphere.

Using the sphere analysis tool a comparison can be made between the measurements of the sensor and the expected value. This is done by looking at how different the ellipsoid is from a sphere. An example can be seen in Fig. 4.2. It has been shown that this difference is related to a change in the effectiveness of the calibration and it can be corrected [130]. This difference can be considered a "deformation" of the calibration since an ellipsoid is considered a stretched (deformed) sphere.

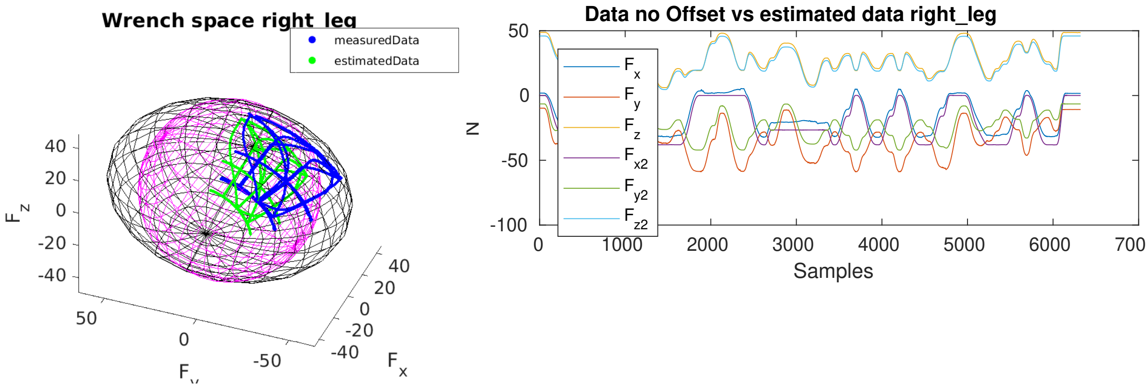

Fig. 4.2 Sphere Analysis Tool graphs.

In summary, we do the following:

- With the robot on the pole span a part of a sphere with the leg.
- Read force-torque measurements and kinematic information.
- Calculate the ellipsoid which fits the forces based in the sensor measurements.
- Obtain the radii of the ellipsoid and divide by gravity to obtain mass values.
- Calculate the std value.

If the model of the robot can be trusted then:

- Calculate expected wrenches at the force-torque sensor positions. To generate the reference sphere.
- Use reference sphere to improve the fitting of the ellipsoid.

- The center of the fitted ellipsoid is considered the offset and can be easily removed.
- Compare mass values or forces as a measure to know how accurate the measurements were.

When the model can not be trusted, it is possible that a sensor has a low std value, but its measurements are not reasonable. For example, if a sensor has a perfect sphere of 70 N radii when the load applied is something around 50 N. Nonetheless, it might mean that the sensor itself is less prone to deformation due to mounting. In this case, the results of the tool give us mainly an insight into the coherence of the sensor with regards to its calibration.

4.1.3 Contact Force Validation

This evaluation tool reproduces offline the behavior of the contact force and joint torque estimation of the robot described in Section 2.4. It simulates the behavior of a sensor as if it was being used by the robot and allows to quantify its performance. In the estimation scheme, the robot is divided into sub-models by cutting the robot in locations where a FT sensor is found. The contact force validation procedure consists of estimating the contact forces in a sub-model where no contact or contact force is experienced. The value of the estimated contact force should be zero. An example of such sub-model in the iCub can be found between the sensor at the hip and the one at the ankle.

The contact 6D force value is estimated at a given contact point. Then, is brought back to the sensor frame being analyzed at the moment. By applying :

$$\mathrm{f}^{\,s} = {}_{s}X^{k}\mathrm{f}^{\,k} \tag{4.1}$$

where ${}_{s}X^{k}$ is the transformation matrix from the contact point to the sensor, $\mathrm{f}^{\,k}$ is the 6D force vector at the contact frame and $\mathrm{f}^{\,s}$ is the 6D force vector at the sensor frame. This way it is possible to know the contact force measured by an axis of the sensor.

The performance evaluation can be done on the magnitude of the force and in each axis separately. When we use the evaluation on the magnitude, it allows to evaluate the performance of a calibration matrix as a whole. Instead when looking at each axis as a separate evaluation, it is possible to measure a calibration matrix performance of that axis.

The estimation scheme combines the information of the sensors found in the sub-model. At any given time of the contact forces estimation, just one calibration matrix is being evaluated, even if the tool itself evaluates more than one sensor and multiple calibration matrices for that sensor in a single run. It has two modalities based in the source of the information of the other FT sensors involved in a sub-model. The first mode uses the estimated wrenches using only the

model for all sensors except the one being evaluated at the moment. The second mode uses the logged measurements of all sensors except the one being evaluated at the moment.
The first modality allows for a cleaner evaluation of the sensor since we are using ideal estimation values for the sensors not being evaluated. This modality is restricted to the fact that the estimation wrenches are only accurate when there is only one contact on the robot. The second modality is able to evaluate a general performance of the robot as long as the sub-model in which is being tested has no contact, but it might suffer from the errors in the measurements of the other sensors. This performance tool was mainly used to select a calibration matrix that had the best results on improving the performance of the robot.

4.2 Application

4.2.1 Comparison of sensors mounted in the Robot

Using the Sphere Analysis Tool provides an objective way of quantifying the performance of a sensor. This allows comparison between sensors even when the experiment data is taken at different times. In here, we enclose just a small representative subset of the sensors that were evaluated.

Description of sensors used in the comparison

There were mainly three kinds of sensors to compare: the FTsense strain 1, FTsense strain 2 and the ATI mini 45. The characteristics of these sensors are described in A.2.1. The naming convention for the FTsense is SNXXX, where 'SN' referrs to 'serial number', and 'XXX' is the actual serial number.

FTsense strain 1 sensors:

- SN138 : mounted on right leg of iCubGenova01
- SN140 : mounted on right leg of iCubDarmstadt01
- SN269 : mounted on right leg of iCubGenova04
- SN233 : mounted on left leg of iCubDarmsdtadt01
- SN106571[1] : mounted on left leg of iCubGenova01.

[1]The SN106571 is a slightly modified version of the strain 1. It has a spine that prevents displacement in the inner mechanics of the sensor once it is closed. This sensor loses its advantage if it has to be reopened for any reason.

FTsense strain 2 sensors:

- $SN282_{insitu}$: mounted on the right leg of iCubGenova04, using the calibration estimated in situ [2].
- SN282 : mounted on the right leg of iCubGenova04
- SN234 : mounted on the right leg of iCubGenova02
- SN233 : mounted on the left leg of iCubGenova02

The ATI mini 45 : temporarily mounted on the right leg of iCubGenova04.

For the sensors FTsense strain 2 and the ATI more than one data set was collected. Only the first and last test are presented.

Test description

In summary, the steps are the following:

- With the robot on the pole run a spherical grid movement on a chosen leg.
- No contact forces should be applied during the grid movement.
- Read and record force-torque measurements and kinematic information.
- Evaluate the degree of deformation of the sensor's calibration using the sphere analysis tool.

Results

The performance of the sensor is evaluated with regards to the std value calculated on the three force axis. From the performance analysis in Table 4.1, it can be concluded that mounting a sensor in the robot does change its performance. An example can be seen in Fig. 4.3. The performance of the ATI is less affected by the mounting procedure as it can be seen from Fig. 4.4. Sensors with a performance index (std) below 0.6 were rare. In comparison to the average sensor, the in situ calibrated sensor had a std value 4 to 10 times smaller. Thus, the best performance is from the FTsense strain 2 using the in situ calibration.
The modified version of the FTsense strain 1, did not seem to have any particular advantage, although the deformation of the calibration in the torque axis was not tested. It can also be

[2] The in situ calibration method is described in Chapter 5 with no temperature compensation

observed for the sensors with multiple tests that the sensors are affected by drift as seen in Table 4.1.

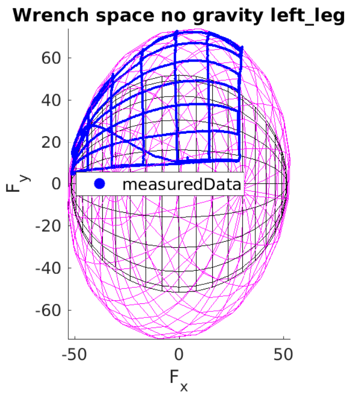

(a) x-y plane no reference

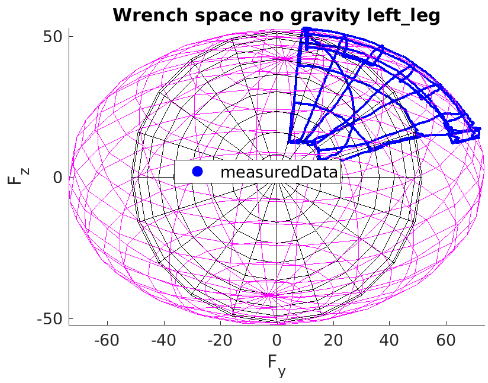

(b) y-z plane no reference

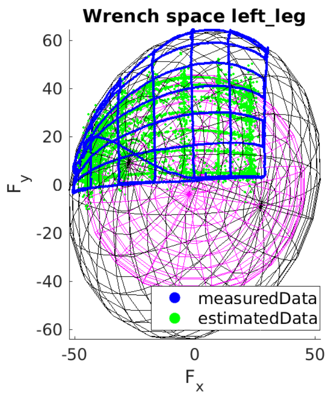

(c) x-y plane with reference

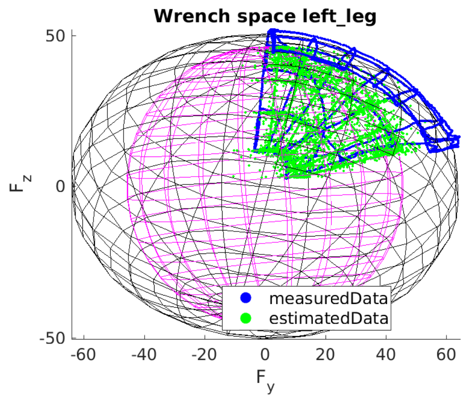

(d) y-z plane with reference

Fig. 4.3 Example of calibration deformation on sensor SN333.

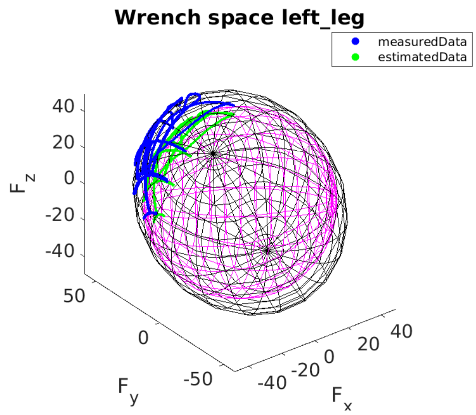

(a) SN233

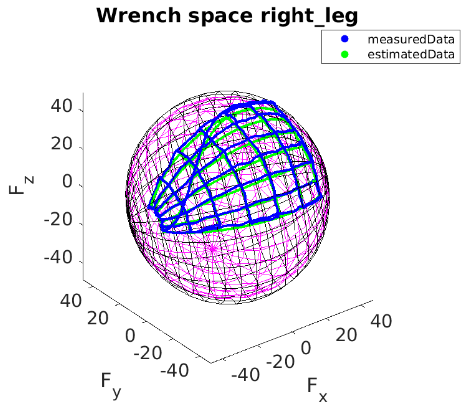

(b) SN282 in situ

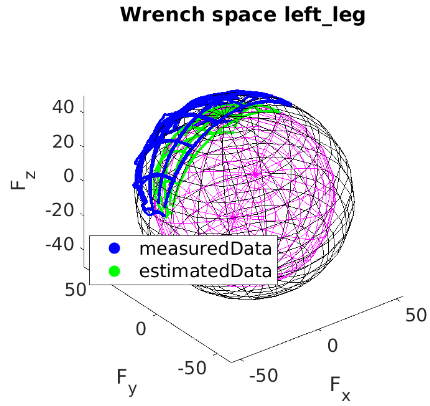

(c) ATI mini 45

Fig. 4.4 Sensors with best performance from each kind

4.2.2 Using Visualizer for Identification of troublesome joint configurations

After an experiment with the sensor SN282, some unexpected behavior of the forces was observed as showed in Fig. 4.5 and Fig. 4.6. This was also confirmed with the Sphere Analysis Tool, by having a std value out of the average when not using the reference as seen in Table 4.1.

By using the visualization tool, it could be observed that reaching the joint configurations in Table 4.2 created the unexpected behavior. After looking at the posture and retrieving the joint configurations (using the sample number at which the behavior was observed), it was possible to replicate the configuration on the robot and verify if the behavior was repeatable.

The reason was found to be that the robot was touching the covers generating an undesired contact force. This allowed to change the sequence to avoid the issue in the future and avoid

	With Reference				No Reference
Sensors	Error x	Error y	Error z	Std	Std
SN169	5.9484	24.5433	2.6872	1.2019	0.9024
SN140	9.5884	15.1658	1.6366	0.6931	0.7998
SN138	−6.5550	17.4981	2.5578	1.2379	0.5249
SN233	2.2601	11.4800	2.4087	0.5383	0.5225
SN106571	19.1296	15.0756	2.7308	0.8707	1.0892
$SN333_1$	5.8339	17.7120	4.1286	0.7543	1.3778
$SN333_2$	5.6101	18.7182	4.2647	0.8139	1.3158
$SN334_1$	7.5575	19.7817	4.5297	0.8231	1.0713
$SN334_2$	8.5443	19.1929	4.3815	0.7787	1.0669
$SN282_1$	9.1065	26.9490	7.0502	1.1155	2.4238
$SN282_2$	9.0371	25.5854	6.4697	1.0576	2.1551
$SN282_{insitu_1}$	0.4174	1.6623	2.7594	0.1194	0.3896
$SN282_{insitu_2}$	0.8401	1.5680	3.3363	0.1309	0.6307
ATI_1	8.0796	15.3603	3.1578	0.6258	0.1828
ATI_2	8.2997	14.6807	5.3031	0.4882	0.2400

Table 4.1 Sphere Analysis Tool results.

'r_hip_pitch'	'r_hip_roll'	'l_hip_pitch'	'l_hip_roll'
−28.3995	6.0040	−28.4382	5.9985
−30.0202	72.8011	−30.0202	72.7956
−12.1784	75.4378	−12.2221	75.5202
5.3119	72.6693	5.3119	72.6198
40.8198	74.0757	40.7319	74.0698
58.3101	75.7894	58.3980	75.7839
76.0640	73.2405	76.0640	73.2350
−28.6140	6.0040	−28.7897	5.9985

Table 4.2 Identified joint configurations with unexpected behavior

using the data of the periods of the experiment were the undesired contact forces were observed. The data of the experiment with those sections removed is showed in Fig. 4.7.

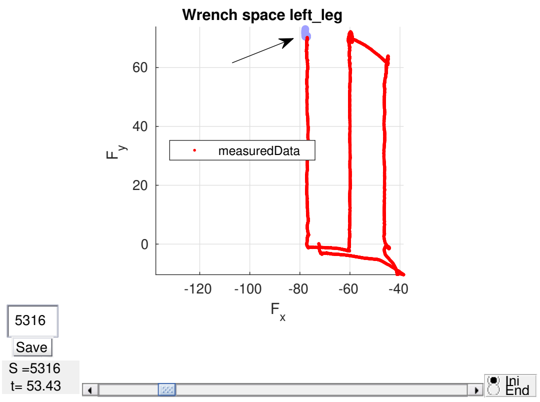

(a) x-y plane of force visualizer

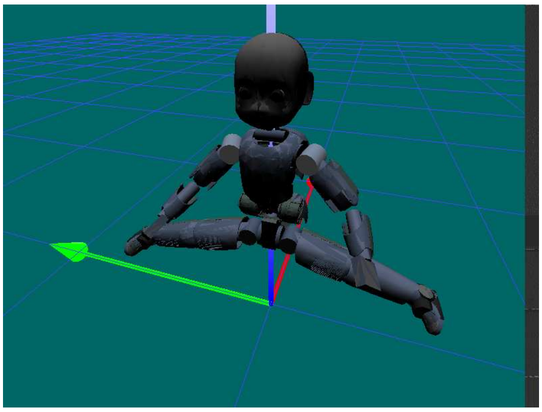

(b) Robot visualizer

Fig. 4.5 Reaching 73^o in the hip roll

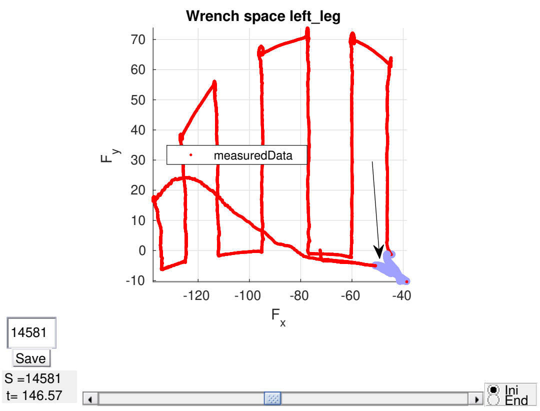

(a) x-y plane of force visualizer

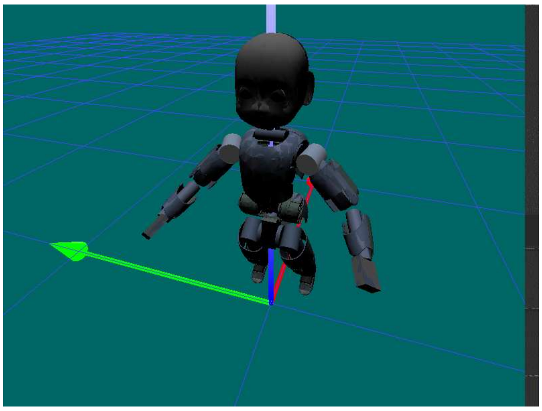

(b) Robot visualizer

Fig. 4.6 Reaching -28.4^o in the hip pitch

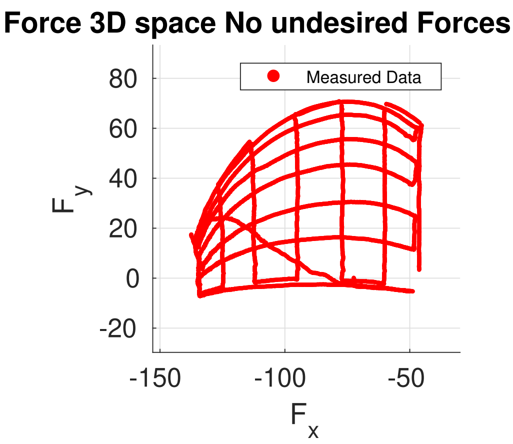

Fig. 4.7 Data experiment with sections removed

4.2.3 Mounting tests

A change in the behavior of a sensor has been observed after mounting [130]. In an attempt to understand the reason for this change, some tests regarding the mounting of the sensor were designed.
The tests performed were related to the value of the torque used when screwing the sensor into the robot. The idea is to see if these torque values affect the sensor and if there is a strategy to minimize the change in behavior. The test steps were defined as:

- In the first iteration, do not change the torque on the screws. In the next iterations progressively reduce the value of the torques starting from 2 Nm.
- Run a spherical grid movement on a chosen leg and record the data.
- No contact forces should be applied during the grid movement.
- Evaluate the degree of deformation of the sensor's calibration using the sphere analysis tool.
- Loose the screws in one leg and repeat the experiments.
- Compare with results obtained from other experiments with different torque values.

Data sets and remarks

Six cases where considered. The cases are: 2 Nm, 1.5 Nm, 1 Nm, 0.5 Nm, 1 Nm on x-axis screws 2 Nm on the others (mixed1-2 Nm), 2 Nm on the x-axis screws 1 Nm on the others (mixed2-1 Nm). The screws aligned with the x-axis can be seen in Fig. A.5. In the figure,

x-axis is pointing to the right of the third image.
For most of them 4 datasets were taken on the right leg of the iCub. Using 2 Nm to screw the sensor seemed to be already at the limit of the screw. Due to some problems with a cable being crushed under some positions of the robot during the execution of the spherical motions, only the 2 Nm datasets where done in the left leg before changing to the right leg. Also, one dataset of the 1 Nm test was incomplete due to issues with the logging application.
At the moment of the tests, the iCub had not been fine-calibrated, so there is no guarantee the calculated wrenches were correct. Therefore the reference sphere generate was created using the smallest radii for easier visual inspection.

Results

Best results according to the Sphere Analysis tool, where achieved on the left leg when the screws were all on 2 Nm shown in Fig. 4.8, followed close by the right leg all screws at 1 Nm. Both of these sets have a sample with 0.5 as std value which is by far outliers w.r.t the general obtained values in all other tests. The resulting std values obtained in the experiments are shown in tables 4.3 and 4.4 . Fig. 4.9 shows the worst performance for comparison.

-	Original	2 Nm
First Trial	1.0090	0.5272
Second Trial	-	0.7245
Third Trial	-	0.8738
Fourth Trial	-	0.7123
Average Std	-	0.7095

Table 4.3 Table comparing std of the experiments on the left leg.

-	Original	1.5 Nm	1 Nm	0.5 Nm	mixed1-2 Nm	mixed2-1 Nm
first Trial	1.0935	0.8974	0.5778	1.0717	0.7938	1.1639
second Trial	-	0.8789	-	1.0893	0.7739	1.0797
third Trial	-	0.9156	0.7143	1.0908	0.8774	1.0860
fourth Trial	-	0.9620	0.8389	1.1203	0.8972	1.1283
average Std	-	0.9135	0.7103	1.0930	0.8356	1.1145

Table 4.4 Table comparing std of the experiments on the right leg.

From the results it could be seen the following observations:

- The std value when different torques where used to screw was higher than using the same torque to screw the sensor. Therefore, a unique torque values to screw the sensor to the robot improves the performance.
- Leaving the screw too loose or having different torque values in the screws generates a higher std value than the one calculated on the ex situ calibration data. This means these scnearios decrease the performance of the sensor.
- Leaving the y-axis more loose has higher std value than leaving the y-axis more loose. So the axis more susceptible to deformation is the y- axis.
- The values that have the best performance are 2 Nm and 1 Nm. This is unexpected since 1 Nm was already below the suggested minimum of the screw which was 1.4 Nm.
- Even having the same value for all screws does not make the performance of the sensors comparable to the one seen with the ATI or the in situ calibrated sensor in subsection 4.2.1.

In Appendix B are reference images to appreciate the deformations found in the different experiments. For a common reference, the third trial was taken from each set.

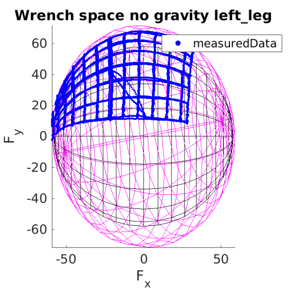

(a) x-y plane

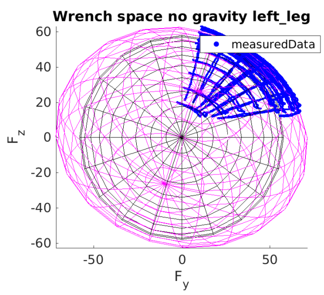

(b) y-z plane

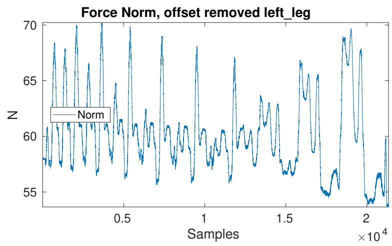

(c) Norm over samples

Fig. 4.8 iCubGenova04 robot sensors ellipsoids, best results

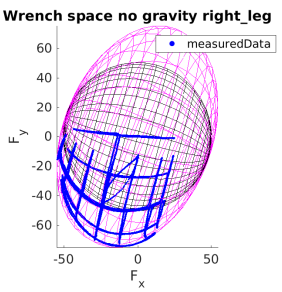

(a) x-y plane

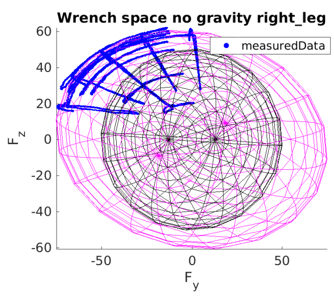

(b) y-z plane

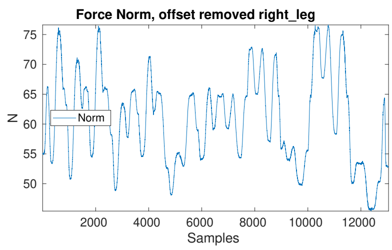

(c) Norm over samples

Fig. 4.9 iCubGenova04 robot sensors ellipsoids, right leg 0.5Nm experiments

4.2.4 Conclusions

Mounting a sensor on the robot makes less effective the calibration of the sensor. Having the same value on all screws seems to help avoid having some deformation on the calibration of the sensor, but it does not solve the problem. There also does not seem to be a correct unique value for screwing but seems something between 2 Nm and 1 Nm is fine. The important thing is to have the same torque in all screws. Having the chosen value close to 2 Nm might be preferable. Depending on the type of screw used it might be possible that 2 Nm is a value to close to the limit of the screw. This has to be taken into consideration.
It seems important to notice the biggest deformations were in the big majority of cases in the y-axis.

Multiple tests on the same sensor have shown a degrade in the performance of the sensor. This is due mainly to drift and affects the measurements. Due to this phenomena it is a common practice to re-estimate the offset or bias of the sensor before starting an experiment.

The use of a calibration estimated in situ shows a big improvement with respect to the other sensors.

4.3 Problems Observed in Silicon Based Six Axis Force-torque Sensors

Given the results and experience working with the sensors, five main issues were identified. This problems prevent to fully trust the measurements of the FT sensors on the robot.

4.3.1 Calibration change after mounting

FT sensors are prone to change performance once mounted in a mechanical structure such as a robot [130, 8]. The Tables 4.1, 4.3 and 4.4 corroborate this behavior. This issue has motivated the creation of in situ methods to re-calibrate the sensor in its final destination. The reason behind this change has not been fully studied. It could be seen in Section 4.2.3, that the torque with which the sensor is mounted does affect the measurements, but is not the only cause. Other sources of this problem could be in the machining of the sensor and the sensor interfaces.

4.3.2 Saturation

Saturation in the sensor arises from the ADC reaching its limit in any of the six channels of the sensor. The behavior of the sensor, when saturated, is to send a saturation message and keep streaming the last valid values before saturation. On the iCub this logic is temporarily

lost in the upper levels where in case of saturation the data is simply not streamed in the ports, but when using the implementation of the estimation scheme in 2.4 on the robot any not-ok force-torque measurements, including saturation, are taken care differently.
The behavior is the following:

- If the measurement is not ok, then the previous measurement value is not replaced.
- Therefore the previous value will be reused in the estimation of joint torques and contact forces.
- The low-level controller receives constant values.

An example of how a saturation looks from the forces and torques perspective can be seen in Fig.4.10a. The actual saturation is much better appreciated when looking at the raw data since the actual saturation happens at the channel level. An example of this can be seen in Fig. 5.8a In the case of the FTsense strain 1, this was a very serious issue creating problems in the controller. The gain selection feature in the FTsense strain 2 allows to overcome this by selecting the right gains.

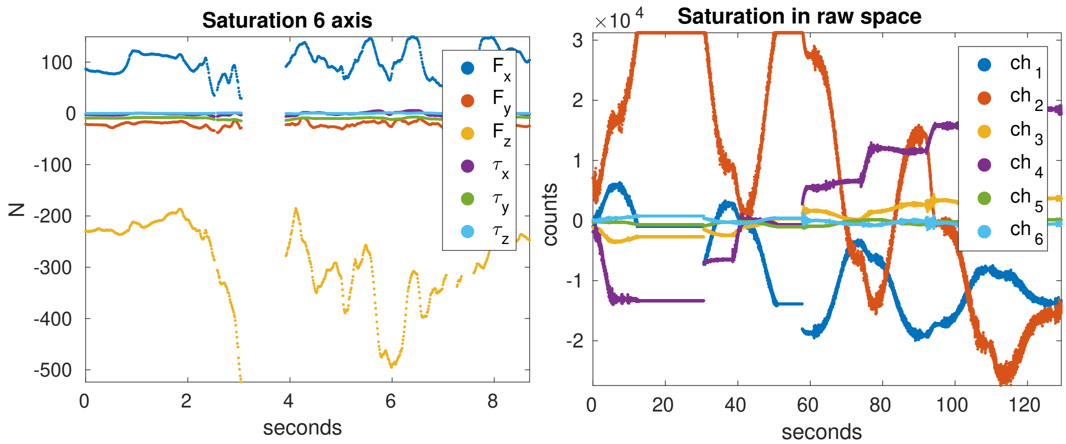

(a) Saturation of sensor in FT values (b) Saturation of sensor in Raw values

Fig. 4.10 FT sensor behavior when suffering saturation.

4.3.3 Temperature Drift

The FTsense Strain 2 includes a temperature sensor. This allows to study the effect of temperature in the measurements. A common solution to compensate temperature effects when using strain gauges is to use the Wheatstone bridge circuit to compensate for temperature [57]. But this method is effective to compensate for temperature only if all strain gauges are subjected to the same temperature change. Given the dimensions and arrangement of the strain gauges inside the FTsense, applying this method to compensate for temperature was not feasible when the sensor was designed. To observe the effect of temperature on the measurements, a heat gun was used to heat a F/T sensor while measuring the load of a 33 kg robot. The initial load is removed to show the change in measurements caused by the change of temperature. The temperature effect is clearly visible on the z-axis, which is the one experiencing most of the load as shown in Fig. 4.11a. The effect of temperature looks close to a linear behavior. The temperature also affects the other axes as shown in Fig. 4.11b and Fig. 4.11c. The temperature seems to affect more the forces than the torques. The observed vibration while heating up was induced by the air coming from the heat gun. The effect of temperature hysteresis can also be appreciated in the figures.

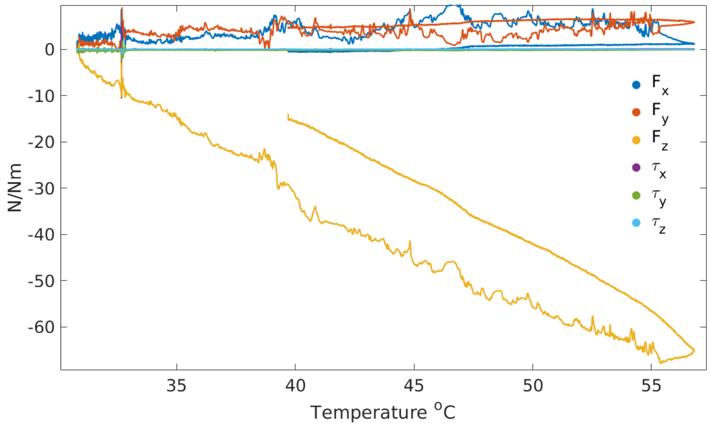

(a) Temperature effect

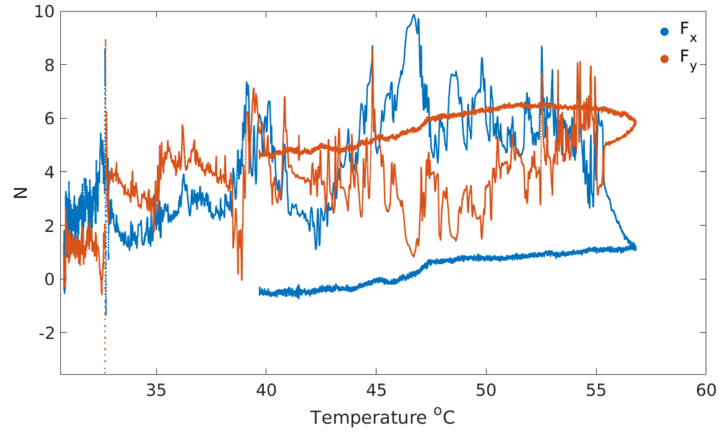

(b) Temperature effect on F_x an F_y

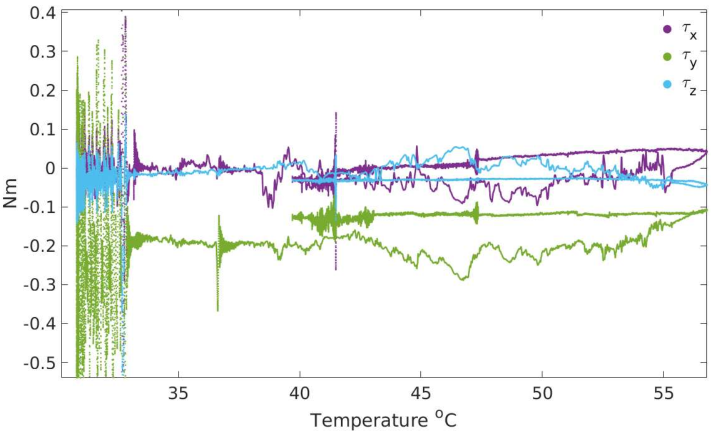

(c) Temperature effect on Torques

Fig. 4.11 Temperature effect on the FT measurements

4.3.4 Full Scale calculation

The current full scale information that appears on the FTsense is based on the maximum value obtained by having saturated values in all channels. This becomes an unrealistic value since the sensors will stop streaming new values as long as one channel is saturated. Given the observed behavior of the raw data of the sensors, it is very unlikely that there will be a case where all channels saturate at the same time as observed in Fig.5.8a. As a result, the limit value specified by the full scale is much higher than the actual values that can be achieved through the usual use of the sensor.

4.3.5 Offset variability

While the higher unit resistance and sensitivity of silicon-based gauges are definite advantages, their greater sensitivity to temperature variations and tendency to drift are disadvantages as mentioned in Section 1.3.1. This plus the effect of hysteresis may result in a different offset value for each experiment, but it is assumed the offset remains constant during the experiment due to the small time frame of each experiment. The effects of drift and hysteresis are currently not considered in the model. This also means that the offset estimation should be done before every experiment. It reduces the reliability of the sensors over a longer period of time.

4.4 Conclusions

Even if the decrease in performance due to mounting can be mitigated by using an specified torque value to screw the sensor, it is considerable. The decrease in performance in repeated experiments shows the consequences of drift. Temperature drift is not negligible. A way to minimize its impact is desirable. The saturation problem can be solved by selecting the gains of the ADC converter based on experimental data. Calibration change, temperature drift and offset variability can be tackled with a proper *in situ* calibration. This is addressed in Chapter 5.

Chapter 5

Model Based In Situ Calibration of Six Axis Force-torque Sensors

In situ calibration methods allow a direct increase in the performance of the sensors. This is due to the fact that the measurements are improved directly in the application system. Many of the identified problems of six axis FT sensors can be tackled by calibrating *in situ*. In this Chapter, the developed *in situ* calibration method used on the iCub is described in detail.

5.1 Proposed approach to *in situ* calibration

Once a sensor is mounted in a complex structure such as a humanoid robot, its calibration matrix may change due to the internal deformation caused by the mounting screws and other mounting deformations as described in Section 4.3.1. For this reason, a reasonable option is to *re-calibrate* the FT sensor using a set of *in situ* samples (r_i, f_i), $i = 1 \ldots N$ obtained directly on the robot.

If it is known that no contact force is acting on the limb on which the FT sensor is mounted, then the expected force-torque applied on the sensor can be computed using the robot model and the instantaneous joints position, velocity and acceleration using the method described in Section 2.4.

In some previous work, a FT sensor was calibrated *in situ* on the iCub by assuming that a single rigid body equipped with an accelerometer was attached to the FT sensor [130]. The inertial parameters (mass, center of mass, 3D inertia tensor) of the attached rigid body were unknown, nevertheless, it was assumed that a set of additional masses of known mass were attached to the FT sensor in the various experiments. Even the (limited) assumptions of [130] complicated the use of the introduced techniques. In particular, the need for knowing *a priori* the accelerometer orientation w.r.t. the FT sensor frame and the assumption that only a rigid body was attached to the FT sensor, complicated the use of such techniques for performing joint torques estimation using the FT embedded in the robot structure [44].

To overcome these limitations, the reference force f is estimated using the model of the robot, which is why the method is named *Model Based In Situ Calibration*. It is assumed that the inertial parameters of robot links are known. While this may seem a rather bold assumption, it is possible if the inertial parameters obtained from the Computer Aided Manufacturing (CAD) model of the robot are validated by weighting experiments on the individual robot links, as was the case. The code implementing this method is available at insitu-ft-analysis repository, a QR code for the code implementation can be found in Fig. 5.1.

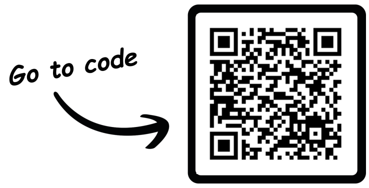

Fig. 5.1 Model Based In Situ Calibration code implementation.

Based on the model of the strain gauge described in Section 3.3 and a sensor with ρ raw measurements, the multiple regression problem for a six axis FT sensor has the following form:

$$\mathrm{f} = Cr + o \tag{5.1}$$

where $\mathrm{f} \in \mathbb{R}^6$ are the 6D forces, $C \in \mathbb{R}^{6\times\rho}$ is the calibration matrix, $r \in \mathbb{R}^\rho$ are the raw measurements and $o \in \mathbb{R}^6$ is the offset. The calibration matrix C and the offset o need to be estimated.

After working with the sensors and gaining a deep understanding of their behavior, a more complete problem statement was developed. There are three main elements to this problem statement. The first element is to formulate the calibration problem in a way such that the offset is no longer explicitly expressed in the model. This is achieved by either decoupling the offset estimation problem from the calibration matrix estimation problem or augmenting the raw space to estimate the offset at the same time the calibration matrix is estimated. The second one is to cast the calibration matrix estimation problem as *regularized least square* problem, in which the regularization takes into account the information known from a previously available calibration matrix. Lastly, having a way to consider other phenomena that might be creating some drift. The assumption considered is that other phenomena are also linear. To the best of our knowledge, no other *in situ* calibration method has been designed to cope with other phenomena that might affect the measurements, such as temperature.

Although the calibration method presented was designed with a floating base robot in mind, it can be easily applied to other systems if the following conditions are met:

- Being able to properly excite the sensor in all axes through the motions of the system.
- Having a sensor of the related linear phenomena close to the sensor.
- Being able to estimate the forces the sensor would be subjected to through the model of the system.
- Having knowledge of previous calibration results of the sensor is optional and might further improve the results.

5.1.1 Least Squares Solution

Assuming that for a series of raw measurements r_i, we have the corresponding 6D forces applied on the sensor f_i, we can cast the problem of finding the calibration matrix and the offset as a multiple linear regression using least squares fitting technique. The calibration matrix estimation can be considered as six different problems in which each row is a separate problem with six independent variables as input and one dependent variable output. For the sake of simplicity, we solve all six axis at once. Thus the problem is stated as follows:

$$\underset{C,o}{\arg\min.} \ \frac{1}{N}\sum_{i=1}^{N} \|\mathrm{f}_i - Cr_i - o\|^2 \tag{5.2}$$

Where N is the number of data samples in the dataset. Because of the problem discussed in Section 4.3.5, it is typically preferred to estimate offset separately from the calibration matrix, as the offset can typically vary across different experiments due to temperature drift, so the offset is removed from the raw measurements separately, and the calibration problem is reduced to:

$$\underset{C}{\arg\min.} \ \frac{1}{N}\sum_{i=1}^{N} \|\mathrm{f}_i - Cr_i\|^2 . \tag{5.3}$$

Regularization

Considering the linear model in (5.1), a least squares technique is used for performing linear regression. In classical calibration matrix estimation algorithms, the input data (r_i, f_i), $i = 1 \dots N$ are obtained by applying a set of known masses in known locations with the sensor mounted on a workbench. For this reason, we refer to this kind of *ex situ* calibration matrix as *Workbench* matrix. Assuming the calibration performed on the sensor was correct, we assume the new calibration matrix must not be very different from the *Workbench* matrix. To enforce this assumption, we introduce a regularization term to penalize the difference with respect to the *Workbench* matrix. The new calibration matrix is obtained through the following optimization problem :

$$C^* = \underset{C \in \mathbb{R}^{6\times 6}}{\arg\min.} \ \frac{1}{N}\sum_{i=1}^{N} \left\| \hat{\mathrm{f}}_i - C\hat{r}_i \right\|^2 + \lambda \left\| C - C_w \right\|^2 \tag{5.4}$$

Where $C_w \in \mathbb{R}^{6\times\rho}$ is the *Workbench* matrix provided by the manufacturer, λ is used to decide how much to penalize the regularization term and N is the number of data points in the data set. The regularization is added in order to try to keep the calibration matrix as close to the *Workbench* matrix, but with an improved performance once the sensor is already mounted on the system.

Even if the six axis can be considered independent problems and solved individually, we solve them all together for convenience purposes. This is performed doing the following steps:

- Consider the Matrix form of the least squares

$$\left\| F^\top - CR^\top \right\|^2 + \lambda \left\| C - C_w \right\|^2, \tag{5.5}$$

  where $F^\top \in \mathbb{R}^{6\times n}$ is the matrix with the reference 6D forces where each columns is $\hat{\mathrm{f}}_i$, $R^\top \in \mathbb{R}^{\rho\times n}$ where each column is $\hat{r}_i$.

- Given $X \in \mathbb{R}^{m\times n}$, $\mathrm{vec}(X) \in \mathbb{R}^{nm}$ denotes the column vector obtained by stacking the columns of the matrix X. In view of the definition of $\mathrm{vec}(\cdot)$, it follows that

$$\mathrm{vec}(AXB) = \left(B^\top \otimes A\right) \mathrm{vec}(X). \tag{5.6}$$

  , where $\otimes$ is the Kronecker product.

- If we consider that $CR^\top = I_6 CR^\top$ then, using the Kronecker property mentioned in eq. 5.6, we can put eq. 5.5 in the column vectorized form:

$$\left\| vec(F^\top) - (R \otimes I_6) vec(C) \right\|^2 + \lambda \left\| vec(C) - vec(C_w) \right\|^2. \tag{5.7}$$

- The minimum of a quadratic form happens when the derivative is equal to 0. By exploiting vector differentiation properties, the solution to eq. (5.7) is given by

$$vec(C^*) = (K_R^\top K_R + \lambda I_{6*6})^{-1} (K_R^\top vec(F^\top) + \lambda vec(C_w)), \tag{5.8}$$

where $K_R = (R \otimes I_6)$. It is important to notice that the size of I multiplying λ should match the length of $vec(C_w)$ which is $a * \rho$, where a is the number of axis (six axis for these type of sensors) and ρ is the number of raw signals.

Adding Linear Variables

When considering other phenomena as linear variables the final form of the problem can be expressed as:

$$C^*, C_t^* = \underset{C \in \mathbb{R}^{6\times 6}}{\arg\min.}\ \frac{1}{N}\sum_{i=1}^{N} \left\|\hat{\mathrm{f}}_i - (C\hat{r}_i + C_t t)\right\|^2 + \lambda \left\|C - C_w + C_t - C_{t_w}\right\|^2. \tag{5.9}$$

where $C_t \in \mathbb{R}^{6\times 1}$ are the added linear variables calibration coefficients and $t \in \mathbb{R}^n$ are the added linear variable values. In this case, the problem is not only to estimate the calibration matrix C and the offset o, but also C_t which accounts for the temperature changes in the sensor.

Given that $C\hat{r}_i + C_t t = \left[\begin{smallmatrix} C, C_t \end{smallmatrix}\right]\left[\begin{smallmatrix} \hat{r}_i t \end{smallmatrix}\right]$ adding a linear variable can be considered adding an extra raw signal to the previous mentioned solution. It comes down to:

- Augment the raw measurements matrix R with the added linear value $R_a = [R, t], t \in \mathbb{R}^n$, in R each column has all the raw measurements of a given raw signal.
- Augment the *Workbench* matrix by including the coefficients regarding the added linear variable $C_{w_a} = [C_w, C_{t_w}]$, where C_{t_w} refers to the added linear variable value at the time of calibration which is currently not available, so is set to 0_6.
- Since $C_{w_a} \in \mathbb{R}^{6\times\rho+1}$ this should be reflected in $L = \lambda * I_{6*(\rho+1)}$, since the *Workbench* coefficients of the added linear variable C_{t_w} are not provided, it is convenient to set the last a values in the diagonal(L) to 0. This reflects the fact that we do not want to influence the coefficients of the added variable with any previous information.
- The final form of the solution is

$$vec(\left[\begin{smallmatrix} C, C_t \end{smallmatrix}\right]^*) = (K_{R_a}^\top K_{R_a} + L)^{-1}(K_{R_a}^\top vec(F^\top) + Lvec(C_{w_a})) \tag{5.10}$$

This formulation allows to easily expand the solution to m number of extra linear variables. The extra linear variable can have its offset removed or not. Assumptions can be made by taking the first value and consider it the offset.

5.1.2 Offset Estimation

Three methods were compared to remove the offset from the estimation problem.

1. *In situ offset estimation* proposed in [130], where the accelerometers measurements are simulated using the kinematic model of the robot.

2. *Centralized offset removal* is obtained by removing the mean value from the raw measurements (μ_r) and the reference values (μ_f).

3. *One shot estimation* estimates the offset as part of the calibration matrix by adding a linear variable in which the reference values are all 1.

In both first 2 cases, we end up with a modified version of the raw data in which the effect of the offset is removed. With a little abuse of notation we have:

$$\hat{r}_i = \begin{cases} r_i - o_r & \text{in situ offset estimation} \\ r_i - \mu_r & \text{centralized offset removal} \end{cases} \tag{5.11}$$

$$\hat{\mathrm{f}}_i = \begin{cases} \mathrm{f}_i & \text{in situ offset estimation} \\ \mathrm{f}_i - \mu_f & \text{centralized offset removal} \end{cases} \tag{5.12}$$

Where $\hat{r}_i$ and $\hat{\mathrm{f}}_i$ are the data used to solve the model based *in situ* calibration problem (5.4). The third case can be treated as an extra linear variable as described in Section 5.1.1; Each offset estimation type is based on a different assumption:

1. physical assumption: gravity generates a sphere in the force space when making spherical movements.

2. mathematical assumption: taking out the mean from the data set implies no offset in the calibration data.

3. no assumption: adding a constant to the linear variables and allow least squares to work it out along with the calibration matrix.

Centralized offset removal from training *in situ* datasets

Once the *in situ* calibration data (r_i, f_i), $i = 1 \dots N$ are available, we need to get rid of the offset, even before estimating the calibration matrix.

A method to obtain a problem in the form (5.3), without the need of computing the offset o, is proposed here.

We centralize the data since for a problem of the form of 5.2, the solution for the optimal calibration matrix C^* and optimal offset o^* is given by

$$o^* = \mu_f - C^* \mu_r. \tag{5.13}$$

So the form of the problem becomes independent of the offset and can be reduced to:

$$\hat{\mathrm{f}}_i = \mathrm{f}_i - \mu_f, \qquad \hat{r}_i = r_i - \mu_r, \tag{5.14}$$

$$\underset{C \in \mathbb{R}^{6\times 6}}{\arg\min.} \ \frac{1}{N} \sum_{i=1}^{N} \left\| \hat{\mathrm{f}}_i - C \hat{r}_i \right\|^2. \tag{5.15}$$

Where $\mu_f \in \mathbb{R}^6$ is the vector of the mean of the wrenches, $\mu_r \in \mathbb{R}^\rho$ the vector of the mean of the inputs, $\hat{\mathrm{f}}_i \in \mathbb{R}^6$ and $\hat{r}_i \in \mathbb{R}^\rho$ are the i-th *centralized* data. Note that even if in eq. (5.15) we did not removed explicitly the offset, the resulting optimization problem has the same form of eq. (5.3), and so for the calibration point of view the proposed algorithm is equivalent to offset removal.

A proof for this statement is provided in 5.1.

Theorem 5.1. *If C^*, o^* are the solutions to the calibration problem* (5.2)*:*

$$C^*, o^* = \underset{C,o}{\arg\min.} \ \frac{1}{N} \sum_{i=1}^{N} \| \mathrm{f}_i - C r_i - o \|^2. \tag{5.16}$$

We have that:

$$C^* = \underset{C}{\arg\min.} \ \frac{1}{N} \sum_{i=1}^{N} \left\| \hat{\mathrm{f}}_i - C \hat{r}_i \right\|^2, \tag{5.17}$$

$$o^* = \mu_f - C^* \mu_r. \tag{5.18}$$

Proof. Using the definitions of $\hat{\mathrm{f}}_i$ and $\hat{r}_i$ we can write the cost function in eq. (5.2) as:

$$\begin{aligned}
&\frac{1}{N} \sum_{i=1}^{N} \left\| \hat{\mathrm{f}}_i - C \hat{r}_i + \mu_f - C \mu_r - o \right\|^2 = \\
&= \frac{1}{N} \sum_{i=1}^{N} \left\| \hat{\mathrm{f}}_i - C \hat{r}_i \right\|^2 + \frac{1}{N} \sum_{i=1}^{N} \left\| \mu_f - C \mu_r - o \right\|^2 + \\
&+ \frac{2}{N} \sum_{i=1}^{N} (\hat{\mathrm{f}}_i - C \hat{r}_i)^\top (\mu_f - C \mu_r - o).
\end{aligned}$$

As $\sum_{i=1}^{N} \hat{\mathrm{f}}_i = 0$ and $\sum_{i=1}^{N} \hat{r}_i = 0$ from their definition in eq. (5.14), we get that the third term of the is always equal to zero, and so we have that the calibration problem reduces to:

$$C^*, o^* = \underset{C,o}{\arg\min.} \quad \left(\frac{1}{N} \sum_{i=1}^{N} \left\| \hat{\mathrm{f}}_i - C\hat{r}_i \right\|^2 + \right. \\ \left. + \left\| \mu_f - C\mu_r - o \right\|^2 \right)$$

Noting that the minimum of the second term is always 0 for $o = \mu_f - C\mu_r, \ \forall C$, we prove the theorem. □

5.1.3 Calibration Data set

In general, there are 4 kinds of data sets that were considered to calibrate a sensor. They were selected based on availability and excitation of the sensor.

- **Grid**: moving the legs in a grid pattern on a fixed pole. The contact is on the waist of the robot. The leg is never bent so the center of mass of the leg during the experiment does not change.
- **Balancing Support leg**: doing an extended one foot balancing demo with widespread leg movements. The contact is on the support leg foot. Either left (BSL) or right (BSR) depending on the support leg.
- **Balancing Non-Support leg**: doing an extended one foot balancing demo with widespread leg movements. The contact is on the other leg foot. Either left (BNSL) or right (BNSR) depending on the support leg.
- **Z-Torque**: doing movements designed to generate torques around the z axis, while the robot is on a fixed pole.

A calibration data set could be formed by one of these kinds of data set or a combination of them.

5.1.4 Estimation Types

Each strategy of offset estimation is considered an estimation type. Including temperature as a linear variable (wT) or not (nT) in the estimation are also considered different estimation types. If the temperature is considered, it is possible to take the first value as an offset (rTO) or not (dTO). Considering the three offset removal possibilities, adding the temperature as a

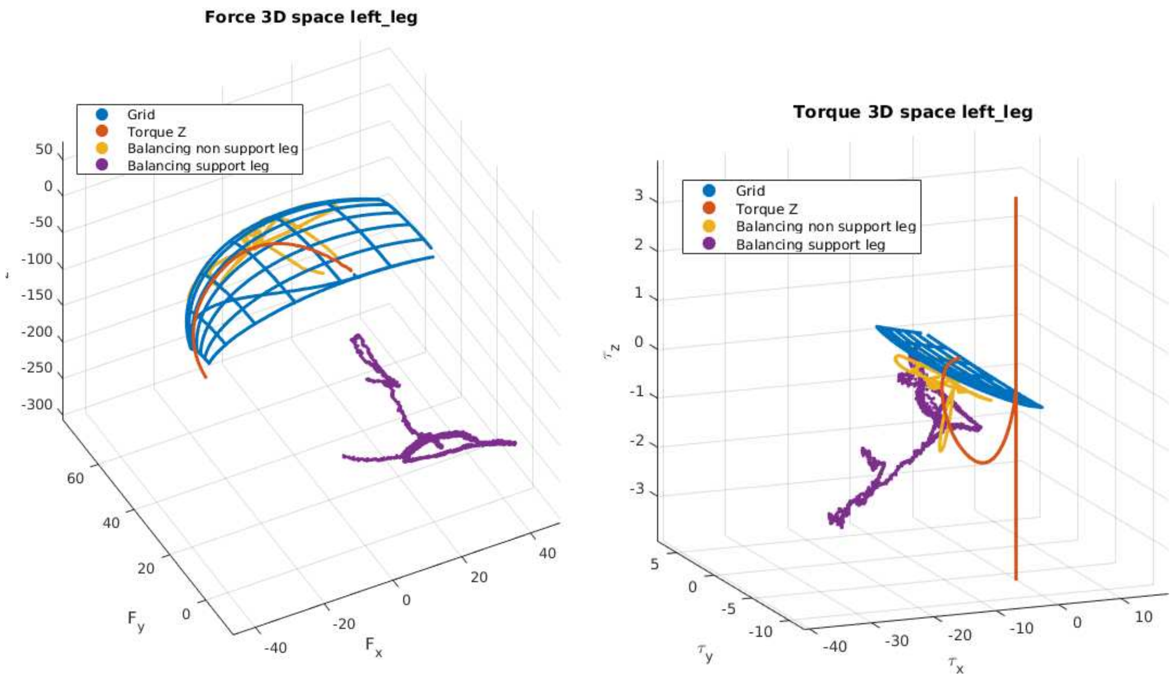

(a) Data set types in force 3D space

(b) Data set types in torque 3D space

Fig. 5.2 Data set types.

linear variable to each of them and the temperature offset option, results in the following nine estimation types:

- Sphere with no temperature (**SnTdTO**): Refers to the fact that the *in situ* offset removal is obtained by expecting a sphere in the force space when generating circular motions. No temperature considered.
- Centralized with no temperature (**CnTdTO**): Refers to the centralized offset removal method without considering temperature.
- One Shot with no temperature (**OnTdTO**): Refers to estimate the offset and the calibration matrix at the same time without considering temperature.
- Sphere with temperature (**SwTdTO**): Refers to including temperature into the sphere type. But no temperature offset is considered.
- Centralized with temperature (**CwTdTO**): Refers to including the temperature into the centralized type. But no temperature offset is considered.

- One Shot with no temperature (**OwTdTO**): Refers to estimate the offset and the calibration matrix at the same time considering temperature. But no temperature offset is considered.
- Sphere with temperature (**SwTrTO**): Refers to including temperature into the sphere type. Removing temperature offset.
- Centralized with temperature (**CwTrTO**): Refers to including the temperature into the centralized type. Removing temperature offset.
- One Shot with no temperature (**OwTrTO**): Refers to estimate the offset and the calibration matrix at the same time considering temperature. Removing temperature offset.

5.2 Experiments

The improvement in the measurements among the six estimation types is compared among the different kinds of possible calibration data sets to select the best way to improve the FT sensor performance. For comparison, results using the *Workbench* matrix are included as an estimation type in its own. At a first stage, the different data set types were compared on their own. Results showed that the sphere estimation type using the Grid data set gave the best results [8]. Adding the temperature required considering more than one data set, to incorporate multiple temperatures. It was proven that adding the temperature lead to a further increase in performance. Mixing types of data sets is better [7]. It was also made evident that the estimation benefits from the knowledge of a *Workbench* matrix. In this case, the sphere estimation type with temperature (SwTdTO) was shown to be better, followed closely by the centralized estimation with (CwTdTO) or without temperature (CnTdTO), using the same λ value. In these tests, no temperature offset was considered, the validation data set was collected in between the calibration data sets and the One shot estimation was not used. To further test the robustness of the *in situ* estimation, a different set of calibration and validation data sets where collected.

5.2.1 Data sets used

The validation data sets were taken on two different days, both different from the day the calibration data sets were collected. This was done to test the robustness to possible different ambient conditions. The data sets and their temperature are showed in Table 5.1. The calibration data sets were grouped into:

- noTz, as indicated by name none of the Z-torque data sets were included.
- onlySupportLegs, from the balancing data sets, only the support leg was included. All other data set types were included.
- AllGeneral, all data set types were included.

The reasoning behind this arrangement of data sets is to see what combination of data sets provides best results. Since it was proven before that Grid and Balancing together improve the calibration, the variables to test are the inclusion of Z-torque and non-support leg data sets. Another aspect to test is the impact of removing a temperature offset in the calibration and contact force estimation.

5.2.2 Evaluation Description

The evaluation could be roughly divided in two parts: one to observe the results of each estimation type and the other to check the expected improvement on the robot of the generated calibration matrices.
To understand better the behavior of the estimation types three comparisons are done. The first uses the mean square error (MSE) calculated between the force-torque data using the new calibration matrix and the model-based estimated data. A lower value would indicate a better fitting of the data. Mean Square Error (MSE) of each axis is calculated as follows:

$$MSE = \frac{1}{N}\sum_{i=1}^{N}(\mathrm{f}_i^r - \hat{\mathrm{f}}_i^c)^2, \tag{5.19}$$

where f_i^r is the 6D force reference vector and $\hat{\mathrm{f}}_i^c$ is the 6D force vector obtained using the estimated calibration matrix of each estimation type.

A second way is to compute the mean of the absolute value of the difference between matrices. This is to get a general idea of how much the calibration matrices differ one from the other. The third way is looking at the offset values. This is to see how the different estimation types affect the estimation of the offset. Although there is no ground truth for the offset to serve as comparison, similarity in the offset values might indicate a general idea of what the true offset might be.

The selection of the best calibration matrix the evaluation is done using the contact force validation described in Section 4.1.3. This emulates the contact force estimation algorithm. This form of evaluation permits to check the performance of the over all magnitude of the force or the value of each axis. This is relevant since there is no guarantee that a λ value or the same type of estimation gives the best results in all axis. The reason is that each axis can be seen as a

		Temperature°C	
Type	Day	Start	End
Validation Data Sets			
Balancing Support Leg	1	38.0	38.2
Balancing No Support Leg	1	38.3	38.4
Grid	2	27.3	27.7
Z-Torque	2	27.7	27.8
Balancing Support Leg	2	34.7	34.8
Calibration Data Sets			
Grid	3	28.8	29.7
Grid_2	3	42.2	41.9
Z-Torque	3	29.7	29.8
Z-Torque_2	3	41.9	41.8
Balancing Support leg Left	3	30.8	31.0
Balancing Support leg Left_2	3	41.8	41.8
Balancing No Support leg Left	3	31.4	31.6
Balancing No Support leg Left_2	3	41.9	41.8

Table 5.1 Used Data sets.

separate problem.

5.3 Results

The sensor to calibrate is located near the hip of the left leg of an iCub robot. The λ values used are: [0, 1, 5, 10, 50, 100, 1000, 5000, 10000, 50000, 100000, 500000, 1000000]. The λ values where selected to span a reasonable range based on the tests to make C converge to C_w, which happened when $\lambda \approx 1e+08$. The validation is performed on each combination of calibration data set (3), estimation type (9), and λ value (13). In total 352 calibration matrices are evaluated counting the *Workbench* matrix.

5.3.1 Estimation types behavior

To verify the behavior of the estimation types only the results from a single calibration data set is showed. The one selected is the onlySupportLegs data set. Nonetheless, the results extend to the other two calibration data sets.

MSE error

The MSE error of each estimation type is showed in Table 5.2. This value is linked to the calibration data set in which the calibration matrix was estimated and is affected by the number of calibration points. So, although the actual value is not something that can translate to other data sets, the tendencies are. One of them is how the MSE reduces by taking into account the temperature. For sphere types (SnTdTO, SwTdTO and SwTrTO), removing the temperature offset further reduces the error while for the centralized (CnTdTO, CwTdTO and CwTrTO) and OneShot (OnTdTO, OwTdTO and OwTrTO) types there seems to be no benefit. It can be observed that the fitting form the centralized and OneShot types are identical.
For the calibration data sets considered, the Centralized/OneShot types give better results in general. The only exceptions appear in the noTz calibration data set. In this data set the sphere types have an slight advantage in three axis: f_x, τ_x and τ_z.

EstimationType	f_x	f_y	f_z	τ_x	τ_y	τ_z
SnTdTO	12.1358	3.4528	62.1595	0.1222	0.0826	0.0299
SwTdTO	8.1290	3.4495	41.7705	0.1193	0.0781	0.0299
SwTrTO	10.8075	3.3826	5.7261	0.1192	0.0823	0.0299
CnTdTO	7.9941	3.4504	56.4681	0.1202	0.0764	0.0298
CwTdTO	8.0358	3.3441	3.5042	0.1188	0.0759	0.0297
CwTrTO	8.0358	3.3441	3.5042	0.1188	0.0759	0.0297
OnTdTO	7.9941	3.4504	56.4681	0.1202	0.0764	0.0298
OwTdTO	8.0358	3.3441	3.5042	0.1188	0.0759	0.0297
OwTrTO	8.0358	3.3441	3.5042	0.1188	0.0759	0.0297

Table 5.2 Mean Square Error on same Calibration data set.

Calibration Matrix differences

Table 5.3,depicted in Fig. 5.3, shows a comparison between the different estimation types including the *Workbench* matrix. In general, the higher values are obtained when comparing with the *Workbench* matrix. From these, the most different matrices are the ones obtained when no temperature is taken into account. Sphere type with no temperature is the most different of all with respect to the *Workbench* matrix.
Is possible to see that the resulting calibration matrix from centralized types is the same as the one obtained through One shot types.

[1] Values are at 10^{-4}

EstimationType	Workbench	SnTdTO	SwTdTO	SwTrTO	CnTdTO	CwTdTO	CwTrTO	OnTdTO	OwTdTO	OwTrTO
Workbench	0	33.0389	28.1952	20.3309	31.0110	18.3735	18.3735	31.0110	18.3735	18.3735
SnTdTO	33.0389	0	6.9890	15.9404	2.8109	16.4152	16.4152	2.8109	16.4152	16.4152
SwTdTO	28.1952	6.9890	0	10.2228	4.5113	10.7766	10.7766	4.5113	10.7766	10.7766
SwTrTO	20.3309	15.9404	10.2228	0	14.3387	2.1403	2.1403	14.3387	2.1403	2.1403
CnTdTO	31.0110	2.8109	4.5113	14.3387	0	14.5363	14.5363	0	14.5363	14.5363
CwTdTO	18.3735	16.4152	10.7766	2.1403	14.5363	0	0	14.5363	0	0
CwTrTO	18.3735	16.4152	10.7766	2.1403	14.5363	0	0	14.5363	0	0
OnTdTO	31.0110	2.8109	4.5113	14.3387	0	14.5363	14.5363	0	14.5363	14.5363
OwTdTO	18.3735	16.4152	10.7766	2.1403	14.5363	0	0	14.5363	0	0
OwTrTO	18.3735	16.4152	10.7766	2.1403	14.5363	0	0	14.5363	0	0

Table 5.3 Mean Absolute difference[1] between estimation types, including *Workbench* matrix.

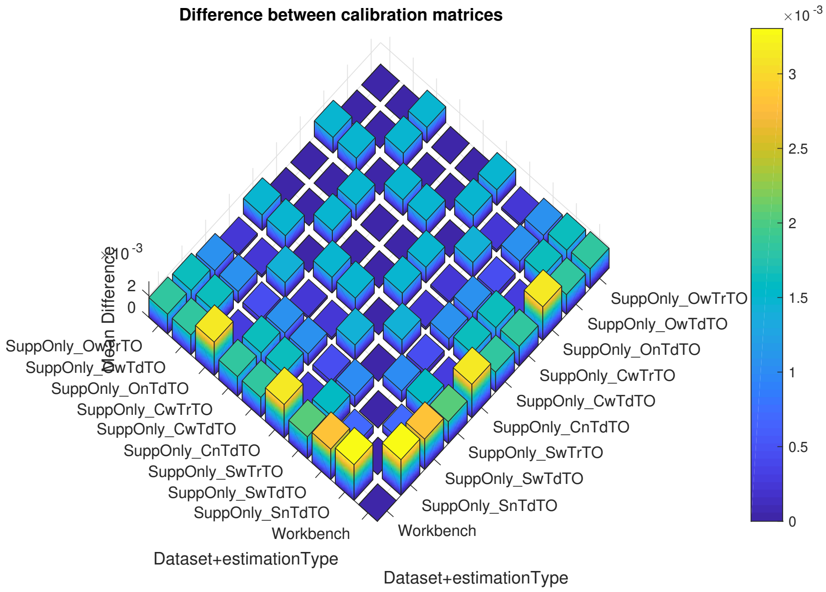

Fig. 5.3 Graphical representation of Table 5.3.

It is interesting to see that also the calibration matrix does not change between using the temperature offset (CwTrTO) or not (CwTdTO) for the centralized types.
The difference between Sphere and Centralized/One Shot is small when both consider the temperature while removing the temperature offset (SwTrTO and CwTrTO/OwTrTO) or not considering the temperature (SnTdTO and CnTdTO/OnTdTO). From this, it is expected that the calibration performance in those cases might be not far from each other.
Taking into account the λ values and looking at the difference with respect to the *Workbench* matrix as shown in Fig. 5.4. The effect of the regularization parameter becomes clear, the higher the value the smaller the difference with respect to the *Workbench* matrix.
Is worth noticing that taking into account the temperature makes the matrix more similar to the *Workbench* matrix even for $\lambda = 0$. Since the new calibration matrix is expected to be

relatively close to the *Workbench* matrix, this similarity even when no penalization is used can be interpreted, to some extent, as a sign of better calibration. Considering this it can be seen that the sphere estimation types benefits form adding the temperature and even more from taking out the temperature offset. The centralized types benefit from adding the temperature, although as mentioned before, there seems to be no added benefit from considering the offset in the temperature.

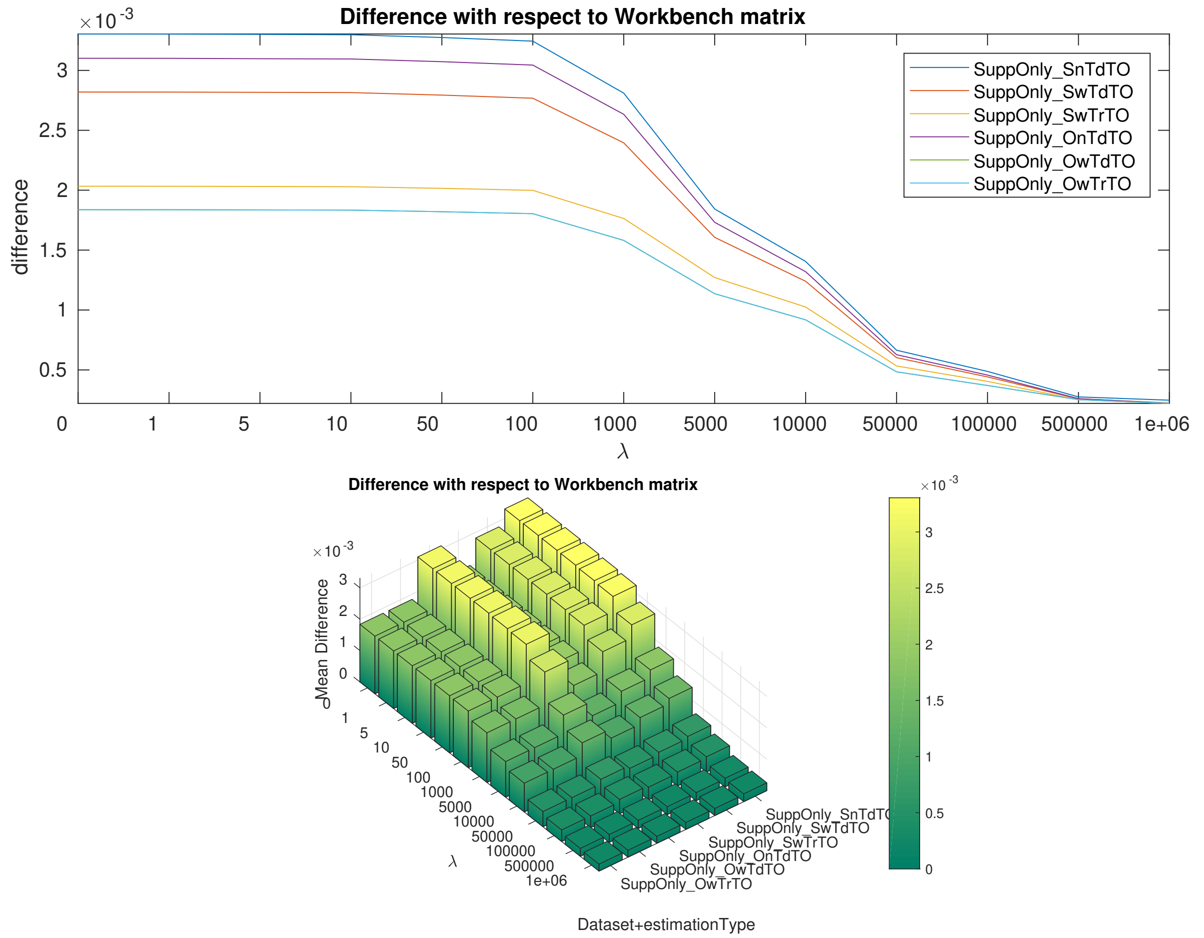

Fig. 5.4 Difference between estimation types and *Workbench* matrix while increasing λ.

Offset comparisons

The estimated offsets can be seen in Table 5.4. It shows that taking into account the temperature offset changes the results of the offset estimation. The estimated offsets without temperatures are not very different between them. Something similar can be seen for the offset obtained considering the temperature offset. In contrast, the offset including temperature, but neglecting the temperature offset, has considerably different behavior between the sphere and the other types.

EstimationType	f_x	f_y	f_z	τ_x	τ_y	τ_z
SnTdTO	55.4488	4.7026	-24.7221	-0.0345	-0.3811	0.5427
SwTdTO	60.0955	4.8701	-35.1782	0.0944	-0.5585	0.5305
SwTrTO	58.8686	5.5569	-42.5960	0.1131	-0.4363	0.5453
CnTdTO	55.1129	4.7137	-24.2897	-0.0422	-0.3659	0.5439
CwTdTO	59.1127	8.4534	-83.3496	0.3281	-0.1478	0.5903
CwTrTO	56.5174	6.0268	-45.0282	0.0878	-0.2893	0.5602
OnTdTO	55.1129	4.7137	-24.2897	-0.0422	-0.3659	0.5439
OwTdTO	59.1127	8.4534	-83.3496	0.3281	-0.1478	0.5903
OwTrTO	56.5174	6.0268	-45.0282	0.0878	-0.2893	0.5602

Table 5.4 Offsets for a calibration data set for each estimation type.

The offset estimation has more impact on the Centralized and Oneshot types , which are once again showed to give the same results between them. Is noteworthy that the fitting of the data is equal even if the offsets are different as seen from the MSE error in Table 5.2. The temperature coefficients and the calibration matrix are the same. What changes is the contribution from temperature. It seems that the offset estimation of the Centralized/OneShot types collects both the force-torque offset and the temperature offset into the force-torque offset if no temperature offset is explicitly removed.

5.3.2 Contact Force Validation

This validation was performed twice. One using only the calibration matrices estimating the offset in a few of the samples and the other using also the estimated offsets. The results of the contact force validation are shown in Table 5.5 and Table 5.6. From the evaluation of the estimation types behavior is clear that the Centralized types and the Oneshot types give the same result. Because of this only the Sphere types and the OneShot were considered.

Using only estimated calibration matrices

In this case, the offset is calculated taking some samples of the test experiments in which is known the robot is on one foot and not moving or moving slowly. The offset calculation includes not only the forces but also the temperature if coefficients are available.
The SwTdTO type in noTz data set has the worst performance. The error is reduced greatly by removing the temperature offset, as seen from the fact that SwTrTO has a consistently lower value than SwTdTO in the each data set. Therefore removing the temperature offset is

relevant for the sphere types. For the OneShot types, the result is the same with or without the temperature offset.
The best result is achieved by OwTdTO and OwTrTO with 5.498 N with $\lambda = 1000$ as the average magnitude of the contact force. In general, better results are achieved by including the temperature and using the OneShot estimation types. The results with the SwTrTO are also close to the best result.
The added benefit of the previous calibration matrix information seems more relevant for estimation types that do not consider the temperature. It is also possible to appreciate that increasing λ is beneficial up to a certain point after which it increases the error. This is expected since the *Workbench* is considered to be correct when the sensor was unmounted, so becoming similar to it has benefits. On the other hand, the mounting changed the effectiveness of it, so being to close instead is not that good. This is quite clear in Fig. 5.5.
It can be appreciated from the contact force magnitude of all the validation data sets, Fig. 5.6, that there is a considerable lower estimated contact force comparing the new matrices against the *Workbench*. It is more critical for the x and y force axes. Even so, the value is not zero, as it would be if the model and the sensor matched perfectly.

Using also estimated offsets

When using the estimated offset, the best results is obtained by OwTrTO with λ 100 on the calibration data set *AllGeneral*, Table 5.6. A graphic representation of the results can be seen in Fig. 5.5. The average magnitude of the external force is 5.8647 N which is slightly higher than the one obtained estimating the offset on the validation data set. This is a very nice result since it means we can avoid estimating the offset every time we start using the robot or doing an experiment and still have a reasonably good performance of the sensor. It also hints that the estimated offset is close to the true offset of the mounted sensor.
It is curious to see that the λ giving the best average behavior is lower than in the case of using an offset estimated on the validation data set. By using the estimated offset the need to be closer to the *Workbench* matrix is reduced.

		λ													Total	
Data set	Estimation Type	0	1	5	10	50	100	1000	5000	10000	50000	100000	500000	1000000	By Type	By dataset
	SnTdTO	14.7353	14.7229	14.6936	14.6531	14.3588	14.0140	10.5665	12.1406	13.3500	13.4198	12.9258	12.1937	12.0329	173.8069	
	SwTdTO	20.8714	20.8546	20.8302	20.7792	20.4633	20.0729	15.2905	11.1392	11.5100	12.2514	12.0020	11.6935	11.8216	209.5798	
	SwTrTO	8.0631	8.0634	8.0598	8.0505	8.0048	7.9535	8.0022	9.6557	10.5474	11.7435	11.8696	11.8197	11.8223	123.6554	
noTz	OnTdTO	21.4168	21.4005	21.3597	21.2985	20.8185	20.2611	13.5881	10.7362	12.2508	12.5915	12.0330	11.4229	11.5627	210.7403	
	OwTdTO	6.8583	6.8588	6.8500	6.8391	6.7752	6.7267	7.5632	10.5579	11.5182	11.8767	11.7000	11.3755	11.5138	117.0134	
	OwTrTO	6.8583	6.8588	6.8500	6.8391	6.7752	6.7267	7.5632	10.5579	11.5182	11.8767	11.7000	11.3755	11.5138	117.0134	951.8093
	SnTdTO	8.9899	8.9870	8.9852	8.9788	8.9340	8.8807	8.1122	7.0044	7.0709	8.7356	9.3448	10.1252	10.3787	114.5273	
	SwTdTO	7.8568	7.8522	7.8563	7.8474	7.8220	7.7810	7.2966	6.7480	6.9413	8.5509	9.1050	9.8410	10.2381	105.7365	
	SwTrTO	5.9704	5.9744	5.9739	5.9719	5.9617	5.9476	5.8722	6.2594	6.8156	8.6707	9.2587	10.0058	10.2779	92.9601	
suppOnly	OnTdTO	8.4813	8.4812	8.4742	8.4694	8.4277	8.3757	7.6485	6.5679	6.5622	7.9906	8.5353	9.3383	9.8301	107.1824	
	OwTdTO	5.5253	5.5224	5.5242	5.5197	5.5159	5.5066	**5.4980**	6.0596	6.6191	8.1749	8.6419	9.3260	9.7944	87.2280	
	OwTrTO	5.5253	5.5224	5.5242	5.5197	5.5159	5.5066	**5.4980**	6.0596	6.6191	8.1749	8.6419	9.3260	9.7944	87.2280	594.8624
	SnTdTO	8.8400	8.8376	8.8288	8.8280	8.7825	8.7298	7.9563	6.7394	6.7075	8.4183	9.1163	10.0199	10.3114	112.1158	
	SwTdTO	7.6831	7.6772	7.6757	7.6696	7.6372	7.6019	7.1228	6.5264	6.6573	8.3207	8.9462	9.8235	10.2860	103.6277	
	SwTrTO	5.9078	5.9070	5.9082	5.9047	5.8935	5.8812	5.7327	5.9845	6.4650	8.3763	9.0411	9.9018	10.2382	91.1419	
All	OnTdTO	8.3123	8.3180	8.3107	8.3098	8.2603	8.2133	7.4991	6.3815	6.3095	7.7947	8.4078	9.3503	9.8907	105.3580	
	OwTdTO	5.6319	5.6321	5.6326	5.6320	5.6240	5.6056	5.5185	5.9089	6.4084	7.9956	8.5170	9.3321	9.8544	87.2930	
	OwTrTO	5.6319	5.6321	5.6326	5.6320	5.6240	5.6056	5.5185	5.9089	6.4084	7.9956	8.5170	9.3321	9.8544	87.2930	586.8295
Total By λ		163.1593	163.1028	162.9699	162.7426	161.1946	159.3902	141.8470	140.9359	150.2790	172.9581	178.3033	185.6028	191.0157		
Workbench		16.6642	16.6642	16.6642	16.6642	16.6642	16.6642	16.6642	16.6642	16.6642	16.6642	16.6642	16.6642	16.6642		

Table 5.5 Average magnitude of the contact force using only estimated calibration matrices.

		λ													Total	
Data set	Estimation Type	0	1	5	10	50	100	1000	5000	10000	50000	100000	500000	1000000	By Type	By dataset
	SnTdTO	14.761	14.751	14.725	14.689	14.426	14.127	11.224	13.534	14.833	14.739	14.207	13.434	13.179	182.63	
	SwTdTO	21.386	21.367	21.349	21.305	21.053	20.725	17.116	14.779	14.856	14.452	14.022	13.594	13.671	229.68	
	SwTrTO	8.7331	8.7367	8.7304	8.7365	8.7305	8.7276	9.1473	10.916	11.609	11.811	11.597	11.059	10.887	129.42	
noTz	OnTdTO	21.959	21.944	21.912	21.859	21.439	20.958	15.469	13.667	14.719	14.673	14.182	13.785	13.973	230.54	
	OwTdTO	7.469	7.4694	7.4693	7.454	7.4014	7.3759	8.1999	10.817	11.619	11.667	11.393	10.94	11.026	120.3	
	OwTrTO	7.469	7.4694	7.4693	7.454	7.4014	7.3759	8.1999	10.817	11.619	11.667	11.393	10.94	11.026	120.3	1012.9
	SnTdTO	9.4503	9.4505	9.4492	9.4439	9.4308	9.3986	9.1777	9.4486	10.032	11.329	11.628	11.967	11.943	132.15	
	SwTdTO	10.132	10.132	10.131	10.124	10.131	10.144	10.313	10.951	11.404	12.072	12.181	12.458	12.6	142.77	
	SwTrTO	7.0649	7.0602	7.0611	7.0615	7.0675	7.0794	7.2527	7.919	8.2931	8.8514	8.9516	9.0766	9.0849	101.82	
suppOnly	OnTdTO	9.9833	9.9845	9.9838	9.9833	9.9844	9.9951	10.069	10.639	11.161	12.163	12.418	12.9	13.14	142.4	
	OwTdTO	6.0123	6.0116	6.0139	6.0117	6.0181	6.026	6.2234	7.0101	7.4735	8.3683	8.6422	9.1567	9.4101	92.378	
	OwTrTO	6.0123	6.0116	6.0139	6.0117	6.0181	6.026	6.2234	7.0101	7.4735	8.3683	8.6422	9.1567	9.41	92.378	703.91
	SnTdTO	9.3042	9.3057	9.298	9.296	9.2784	9.2545	8.9752	9.071	9.5762	10.919	11.254	11.654	11.691	128.88	
	SwTdTO	9.9729	9.9645	9.9677	9.9716	9.9789	9.9759	10.093	10.658	11.074	11.782	11.918	12.228	12.421	140.01	
	SwTrTO	6.9187	6.9182	6.9185	6.9183	6.9151	6.9269	6.9783	7.4763	7.8228	8.4421	8.5773	8.7733	8.8471	98.433	
All	OnTdTO	9.712	9.722	9.7206	9.7194	9.7138	9.722	9.7785	10.278	10.791	11.868	12.14	12.667	12.97	138.8	
	OwTdTO	5.8685	5.868	5.8659	**5.8647**	5.8708	5.8657	5.9457	6.5411	6.99	8.0151	8.3514	8.9122	9.227	89.186	
	OwTrTO	5.8685	5.868	5.8659	**5.8647**	5.8708	5.8657	5.9457	6.5411	6.99	8.0151	8.3514	8.9122	9.227	89.186	684.49
Total		178.08	178.03	177.94	177.77	176.73	175.57	166.33	178.07	188.34	199.2	199.85	201.61	203.73		
Workbench		16.6642	16.6642	16.6642	16.6642	16.6642	16.6642	16.6642	16.6642	16.6642	16.6642	16.6642	16.6642	16.6642		

Table 5.6 Average magnitude of the contact force using also estimated Offset.

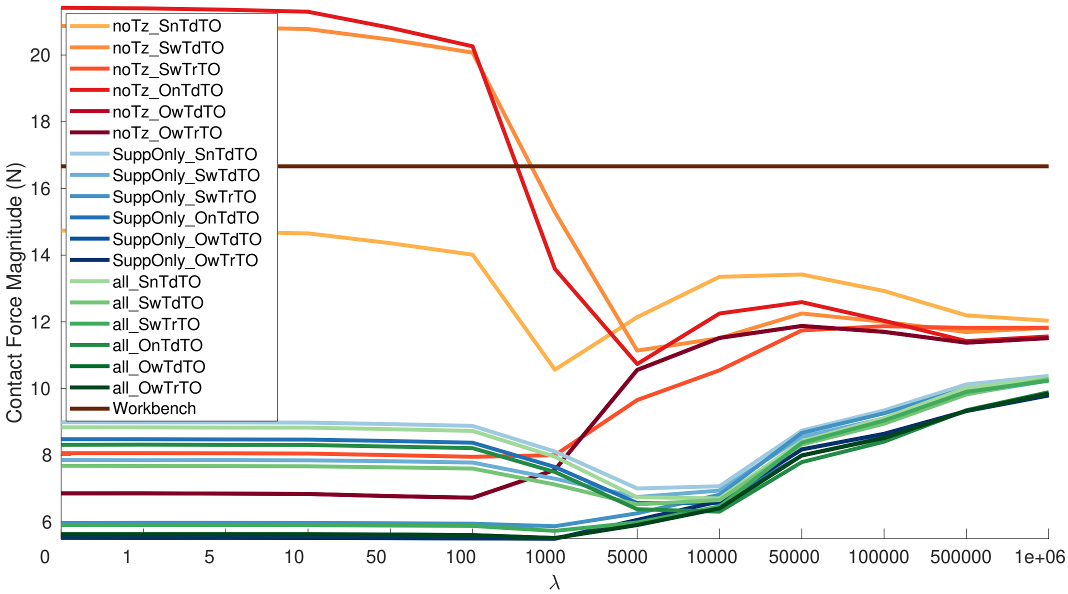

(a) Using estimated only Calibration Matrices, Table 5.5.

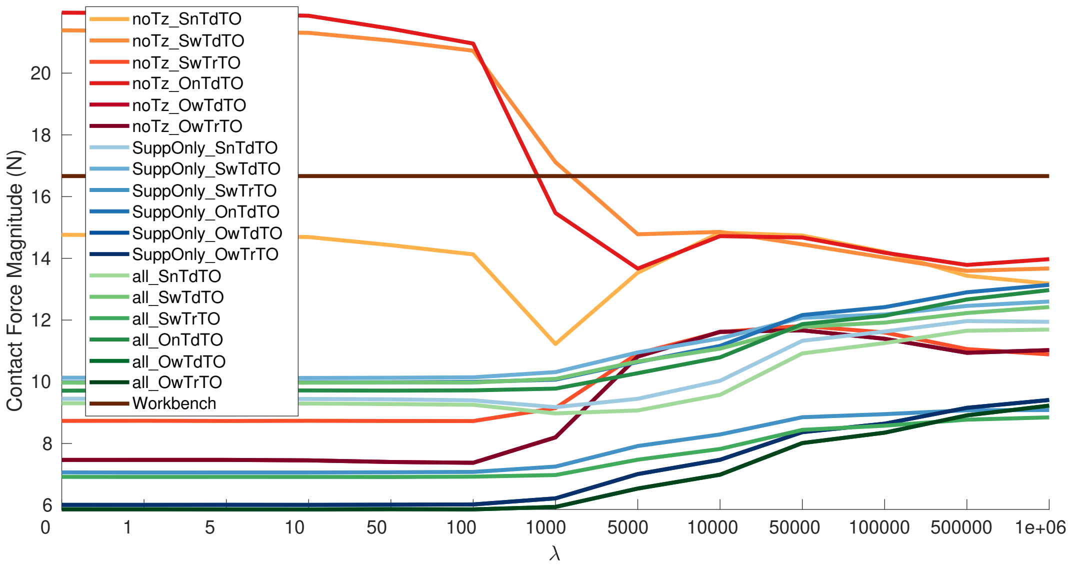

(b) Using also estimated Offset, Table 5.6.

Fig. 5.5 Magnitude contact force versus λ

Grouping by data set types

Grouping the results by data set the calibration data sets can be ordered from best to worst in the following order: AllGeneral, onlySupportLegs and noTz. The behavior of a group of results by data set is clear using the pallets of colors in Fig. 5.5. There is a big improvement when adding the Z-Torque data set and just a small improvement form adding the Balancing Non-Support Leg on top of that. Showing that the Z-Torque gives relevant new information

to the calibration data set, while the Balancing Non-Support Leg adds few more information. Therefore, for the considered data set types the optimal combination is composed of Grid, Z-Torque, Balancing Support Leg. The Balancing Non-Support Leg can be considered optional and not strictly required. The fact that the best results not using the estimated offset is without using the Balancing Non-Support Leg data set reinforces the previous statement. It can be seen that adding the temperature creates a clear difference in the results of a data set. It almost divides each different calibration set results in two. At least two of the optimal calibration data sets are needed for the compensation of temperature.
These results are congruent with the space each data set covers in the forces and torques 3D space, Figure 5.2. In this figure, is possible to see that Balancing Non-Support leg is more or less contained between the Grid and Balancing Support Leg. The other three data set types are clearly different among them. Therefore is possible to use that graphical representation to gauge the expected usefulness of a data set.

By Axis

Table 5.7 shows the best results by axis and the performance of the *Workbench* matrix. From the difference in the results with respect to the *Workbench* is possible to see that the most affected axis by the mounting are f_x and f_y. Is possible to see that f_z, τ_x and τ_y, actually perform better using the estimated offset. The fact that only the f_y and f_z get better results in both cases taking into account the temperature might imply these are the axis mainly affected by the temperature drift.
Although the variation in *lambda* is big looking at Figures 5.6 and 5.7 it can be seen that the difference among the best solutions is actually very small. It is also possible to see that most of the axes obtained best results with *lambda* values of 5000 or lower. This might help refine the search space by adjusting the considered *lambda* values.

	Using only estimated C		Using estimated C +o		
Axis	Best C	value	Best C	value	workbench
f_x	SuppOnly λ5 OnTdTO	3.03893 N	All General λ5000 OnTdTO	3.14859 N	8.9007 N
f_y	SuppOnly λ1000 SwTdTO	2.42722 N	All General λ10 OwTrTO	3.05630 N	11.1776 N
f_z	SuppOnly λ10 OwTrTO	2.61958 N	SuppOnly λ1000 OwTrTO	2.40174 N	3.9954 N
τ_x	SuppOnly λ1 SnTdTO	0.68899 Nm	All General λ100 OnTdTO	0.58208 Nm	0.7901 Nm
τ_y	SuppOnly λ10000 OnTdTO	0.48474 Nm	SuppOnly λ100000 OnTdTO	0.43218 Nm	0.7146 Nm
τ_z	SuppOnly λ100000 SnTdTO	0.15184 Nm	All General λ100 OwTdTO	0.18044 Nm	0.2769 Nm

Table 5.7 Best calibration matrix by axis

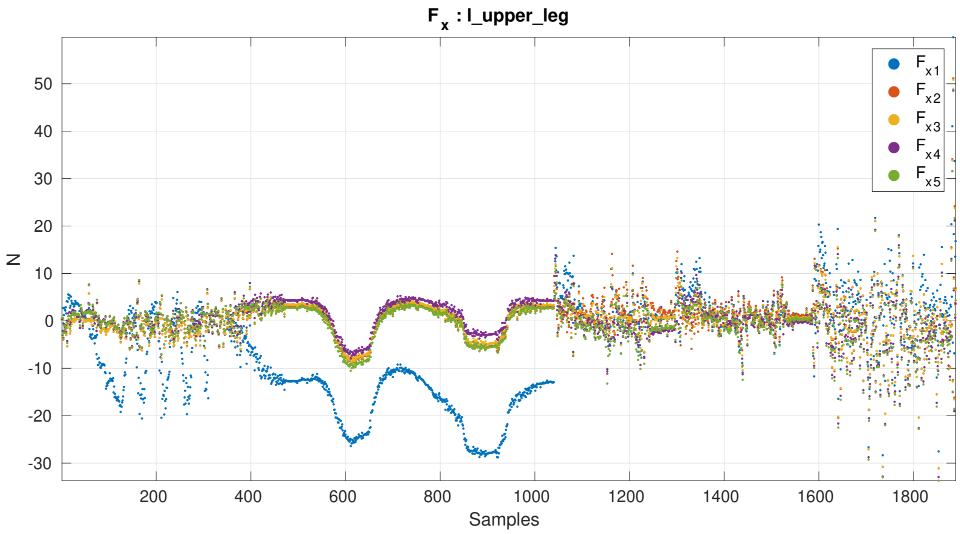

(a) force x-axis.

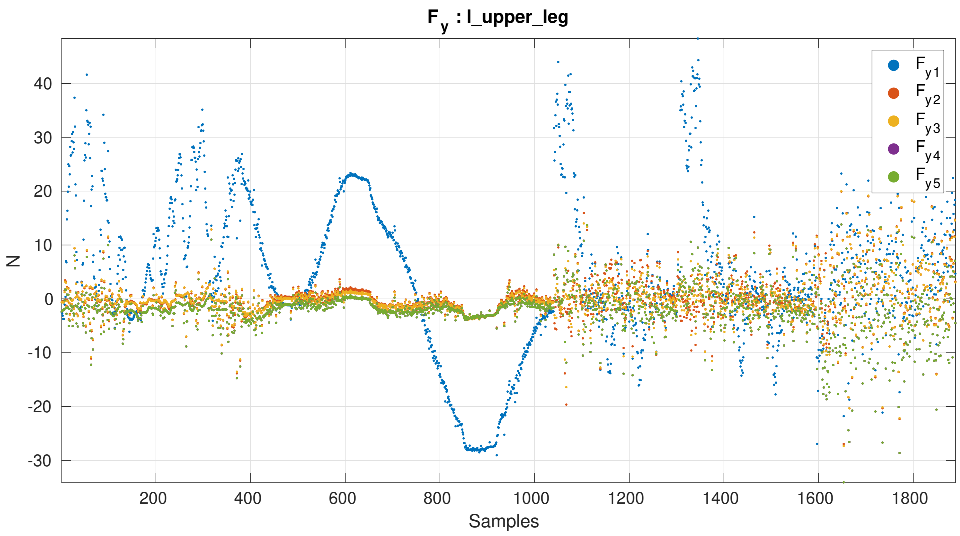

(b) force y-axis

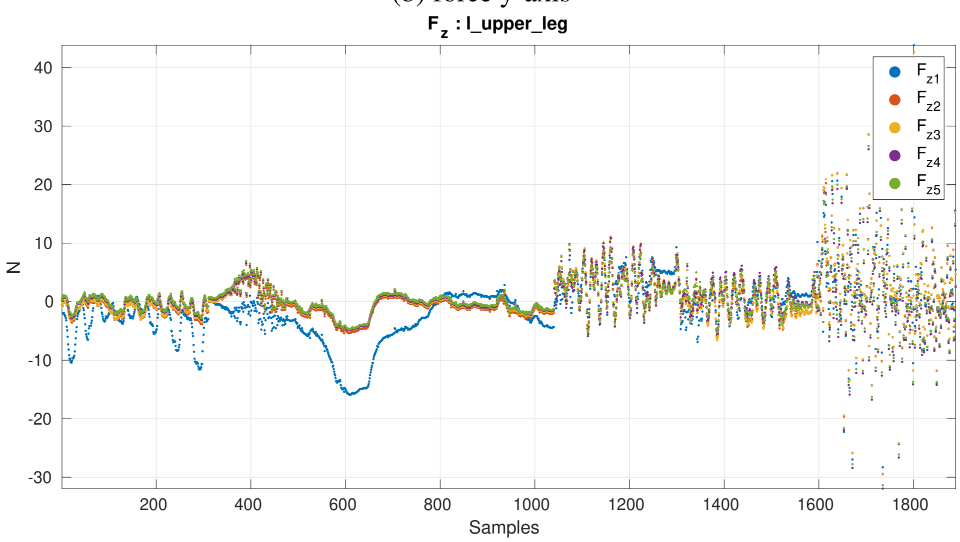

(c) force z-axis.

Fig. 5.6 Contact forces on validation data set; 1) Workbench matrix, 2) Best not using estimated offset, 3) Best by Axis not using estimated offset, 4) Best using estimated offset, 5) Best by Axis using estimated offset.

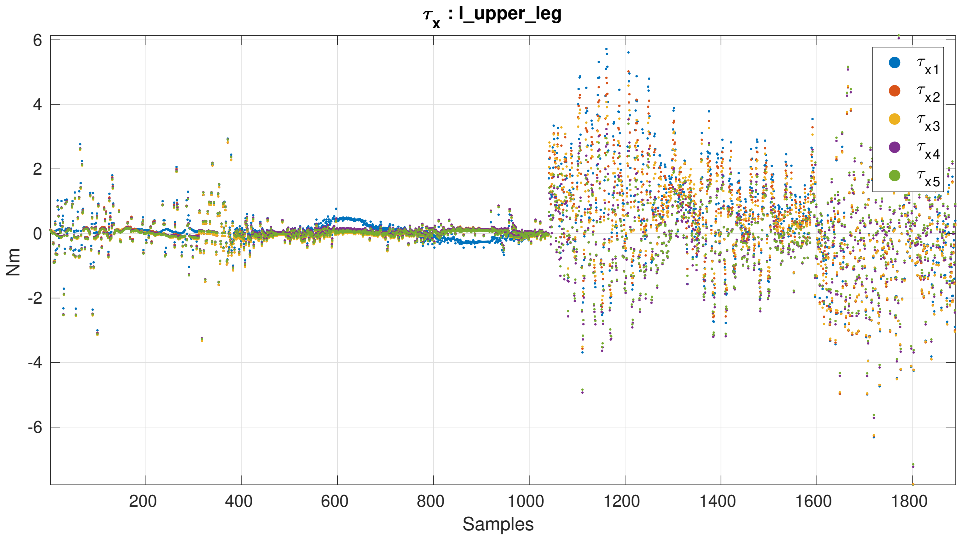

(a) torque x-axis

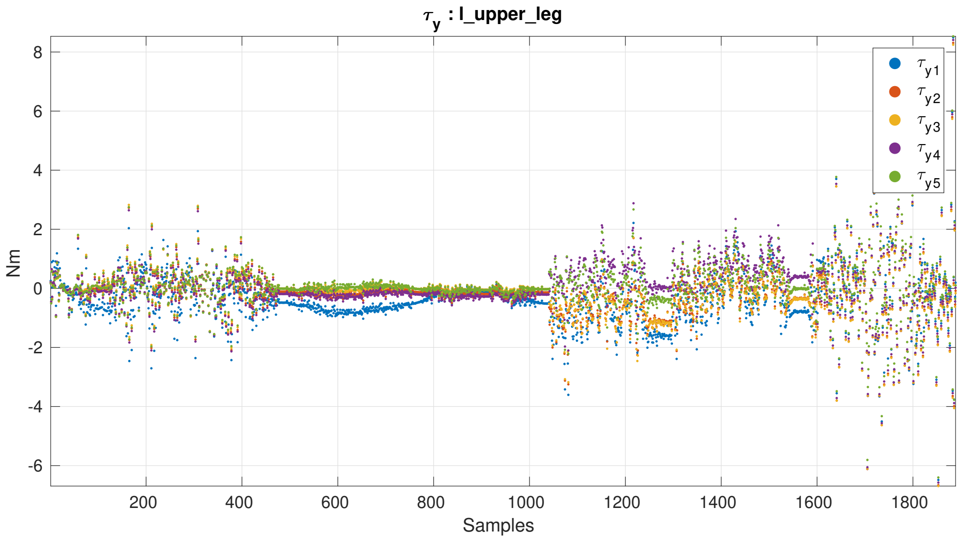

(b) torque y-axis.

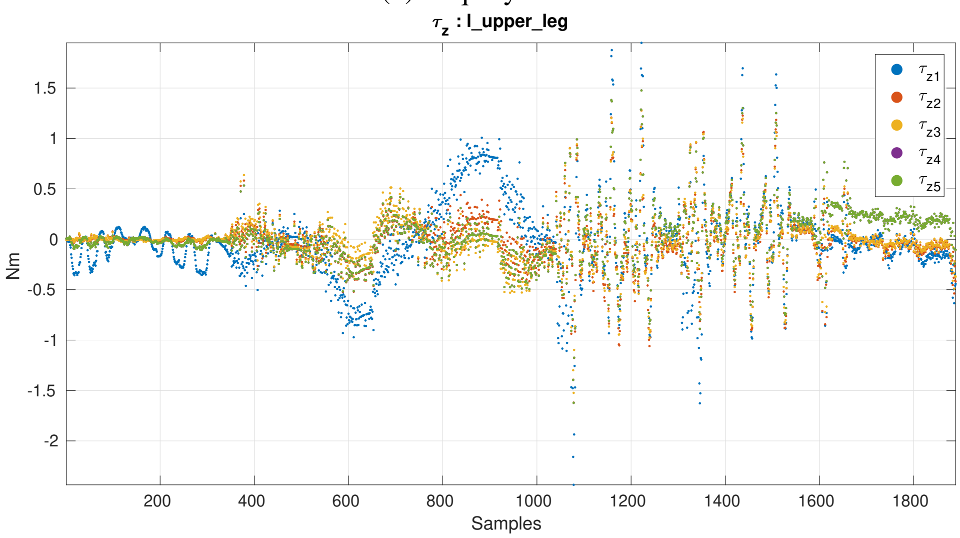

(c) torque z-axis

Fig. 5.7 Contact torques on validation data set; 1) Workbench matrix, 2) Best not using estimated offset, 3) Best by Axis not using estimated offset, 4) Best using estimated offset, 5) Best by Axis using estimated offset.

5.4 Insights

The first thing to notice is the fact that the Centralized types and the One Shot types give the same results to all effects. So only one of the two needs to be considered. Since the problem was formulated to include other variables it is more convenient to use the One Shot type than the Centralized type eliminating the need to do special considerations for the offset estimation. From the results, Section 5.3, it can be seen that the relevance and impact of each offset estimation strategy depend on the amount of data available. For small data, the physical assumption gives the most improvements. Moving to bigger amounts of data seems to allow having no assumptions to estimate more accurately the calibration. The loss of effectiveness when using the physical assumption could be related to the fact that it does not consider temperature at all for the offset estimation, while the other two are able to include the information to some extent. There might be a way to try to consider this by using more than one Grid data set at different temperatures to estimate the offset.

Observing the behavior of the excitation of the sensor in the 3D spaces of forces and torques allows to have valid insights into the worth of a calibration data set. In the Fig. 5.2, is evident to see that Z-Torque type of data set provides new information. It is also visible that the Balancing Non-Support Leg gives redundant information. This was confirmed when looking at the results grouping by calibration data set.

It can be seen that is enough to consider temperature as a linear phenomenon, although exploring nonlinear models is still worth investigating. The fact that by adding the temperature and temperature offset we are able to use the offset estimated as constant proves that the drift is mainly generated by the temperature. Is also very convenient for the general use of the robot since erases the need for estimating the offset every time. Even so, is worth noticing that the sensor performance might be slightly better if the offset is re-estimated before the experiment. The results from the second validation might give a hint to what range of λ values is worth exploring since most of the best results are obtained using a value of 5000 or less.

When observing the results by axis in detail is possible to see that the decrease in performance is centered around the axes f_x and f_y. This might guide an investigation to improve the mounting procedures. These results also suggest that the effect of temperature in the normal use of the robot is mainly on the f_y and f_z axis.

5.5 Exploiting *in situ* methods in a robot

The result from the *in situ* calibration is a new calibration matrix. It is when using this calibration matrix that the improved measurements are obtained. Therefore the new calibration matrix should be used somehow by the robot to obtain the improved measurements and better dynamic performance as a consequence.
The process to obtain the *in situ* calibration data sets can also be exploited to measure the response of the sensor to the excitation produced by the robot.

5.5.1 Gain Selection and calibration of new sensor

A sensor without calibration sends raw measurements. It is possible to calibrate such a sensor directly *in situ*. The Model Based *in situ* calibration can be used without the regularization part by setting λ to zero. Although it has been shown that the calibration procedure can benefit from the regularization, it is still able to achieve very good performance without it.
While gathering the *in situ* calibration data set is possible to observe the true response of the sensor to the excitation produced by the robot. If the sensor allows, it is possible to use this information to select the gains to match the full-scale to the actual use of the sensor. As mentioned in Section 3.3.2, adjusting the range may allow a further increase in the calibration results.
During this process is also possible to verify if a sensor is close or suffering from saturation as mentioned in Section 4.3.2. This was the case for the first FTsense strain 2. This sensor allows to change the gains of each individual channel.
Using the motions to gather *in situ* calibration data sets, it was possible to observe the profile of the raw data with regards to a known excitation. With this information, saturation can be avoided while keeping the maximum allowed range by changing the gains of the sensor.

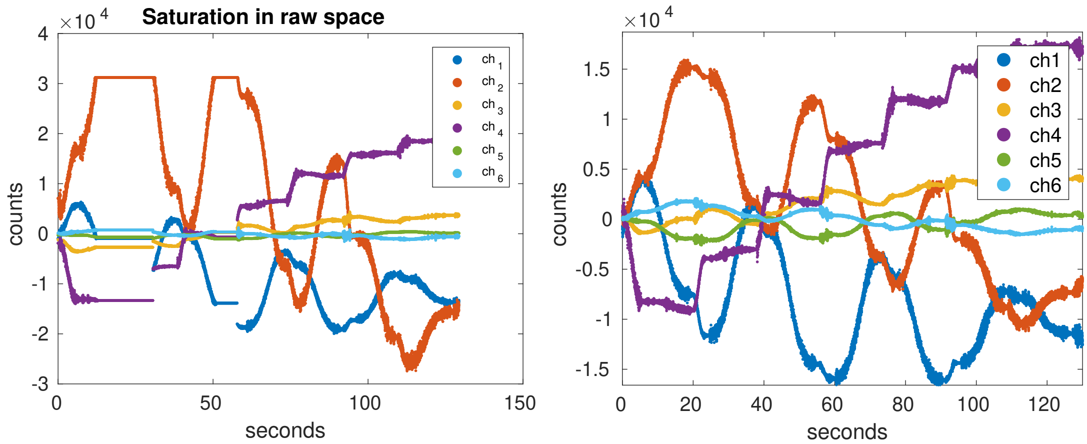

(a) Saturation of sensor in Raw space (b) Same experiment with no saturation.

Fig. 5.8 Results of gain adjustment.

An example of the results from adjusting the gains can be appreciated in Fig 5.8. The proposed procedure is the following:

1. With a non calibrated sensor perform the regular motions for model based *in situ* calibration.
2. Verify looking at the raw data how far or close are the values of the raw data.
3. The robot configuration with the highest excitation can be saved for later using the Visualization tool.
4. Diminish gains if there is saturation, increase gains if for the totality of the experiment a channel is no where near saturation point.
5. Repeat until behavior of the channels is relatively close to saturation, but with enough margin to account for extra forces.

Using this procedure there is no regularization possible since there is no other calibration matrix to use in the penalization term. Therefore, no second validation procedure is required to select an adequate λ value. Fig. 5.9 shows the comparison between a normally calibrated sensor and the *in situ* calibrated sensor during a support leg data set. In both cases the offset was removed. It can be observed that the performance of the *in situ* calibrated sensor is clearly superior.

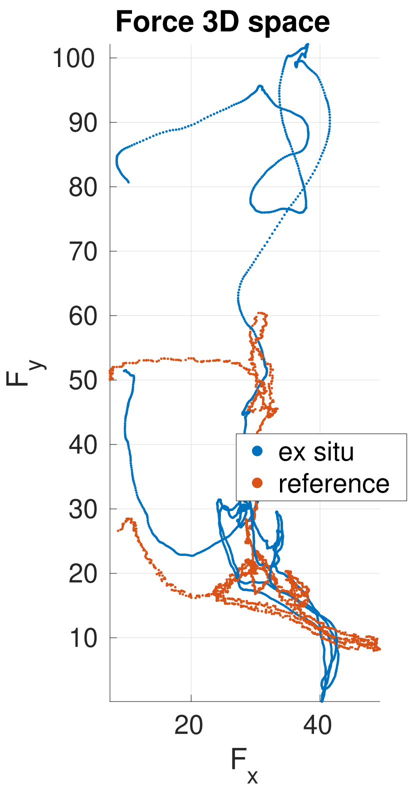

(a) *ex situ* calibrated sensor and reference

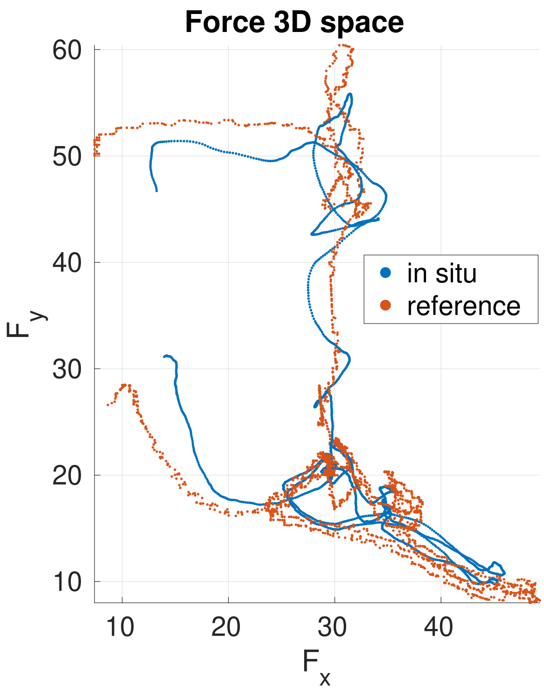

(b) *in situ* calibrated sensor and reference.

Fig. 5.9 Comparison of an ex situ calibrated sensor and an in situ calibrated sensor.

As seen in Section 4.2.1 the sensor calibrated with this method has the best results among all compared sensors. The success of this method arises from both the improvement due to calibrating *in situ* and adjusting the range of the sensor for the specific use.

5.5.2 Secondary Calibration Matrix

It is possible that no access to the raw data of the sensor is available online or that is not possible to change the current calibration matrix. In these cases, the proposed solution takes the form of a secondary calibration matrix. The secondary calibration matrix is the required transformation of the current calibration matrix to the new calibration matrix. It requires the knowledge of the current calibration matrix used by the sensor. It is calculated as follows:

$$C = C_s * C_w \rightarrow C_s = C * C_w^{-1} \tag{5.20}$$

The secondary calibration matrix can be saved as a configuration parameter that is loaded at the launching of the robot. Before using the values obtained through force-torque sensing, they can be corrected by pre-multiplying with the secondary calibration matrix. This way the measurements used by the robot are as good as if the sensor was calibrated using *in situ*.

5.5.3 Adding the temperature

To ensure backwards compatibility with sensors that do not have temperature measurements, the contribution of the temperature is added separately. The coefficients of temperature can be similarly stored as a configuration parameter of the robot. In case no temperature exist or no temperature calibration is available, these coefficients are loaded as zeros by default.

5.6 Observed Improvements in Floating Based robots

By improving the measurements of the six axis FT sensor through *in situ* calibration, it was possible to see improvements in the behavior of the floating base robot iCub.

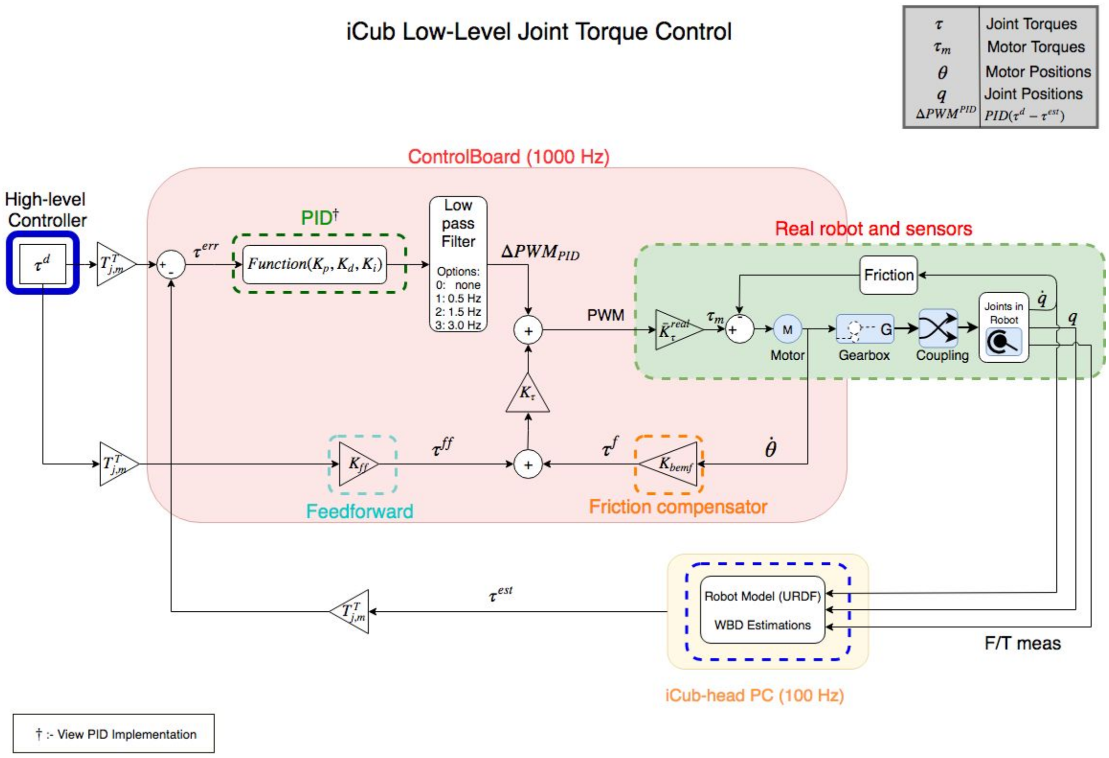

Fig. 5.10 iCub's Joint torque controller.

The force-torque sensing has three main uses in the iCub:

- As a threshold to know if a stable contact has been established between the robot and the ground.

- To give the feedback to the low-level joint torque controller.
- To estimate dynamical quantities used by high-level controllers, such as the center of pressure (CoP) and the zero moment point (ZMP).

As a threshold

The simplest use is as a threshold. When the load on the sensors reaches a chosen value, the controllers change state assuming a stable contact has been achieved. The chosen value can be a percentage of the total body weight of the robot. Example of applications are balancing [106] and standing up [110].

To calculate dynamic quantities

The forces acting on a moving robot can be separated into two categories: forces exerted by contact and forces transmitted without contact (gravity and, by extension, inertia forces). The CoP is linked to the former, and the ZMP to the latter. Nonetheless, it has been shown that both points coincide [115]. Therefore, is possible to use the contact force information to calculate dynamic quantities such as the ZMP and by extension affect the estimation of the center of mass (CoM).

The CoP is defined as the point where the resultant force can be exerted with a zero resultant moment. When the contact is with a flat ground the CoP and ZMP, can be calculated as :

$$P_{CoP} = {}_s\tau / {}_sf, \tag{5.21}$$

where $P_{CoP} = P_{ZMP}$ is the CoP (ZMP), ${}_s\tau$ is the torque measurement of the FT sensor at the ankle and ${}_sf$ is the force measurement of the FT sensor at the ankle.

Using the linear inverted pendulum model constraining the height of the CoM to be constant (P_{CoG_z}), the CoM dynamics can be estimated from the ZMP with the following equation:

$$\ddot{P}_{CoM} = (P_{CoM} - P_{ZMP})\frac{g}{P_{CoM_z}}, \tag{5.22}$$

The FT sensor measurements have a direct impact on the estimation of the ZMP and as a consequence in estimation of the CoM. This information is used in a walking controller [111].

Feedback for joint torque controller

Through the estimation scheme, Section 2.4, the joint torques are obtained and send as feedback to a joint torque controller. The scheme of this controller can be seen in Fig. 5.10. Description of the variables in the scheme can be found in Table 5.8. It is a PID controller with friction

	Description	SI unit
	Gains	
K_p	Coefficient for the proportional term of PID	DC%[2]/N m
K_d	Coefficient for the derivative term of PID	DC%s/N m
K_i	Coefficient for the integral term of PID	DC%/N m s^{-1}
K_{PWM}	Transformation matrix between PWM and joint torque	N m/DC%
K_τ	$K_\tau = 1/K_{PWM}$	DC%/N m
K_{bemf}	Coefficient of Viscous friction	N m $^{\circ -1}$ s^{-1}-1
$\bar{K}_\tau^{real}$	Transformation matrix between PWM and Motor torque	N m/DC%
	Torque variables	
τ^d	Joint Torque set as a reference via high-level controller	N m
τ^{est}	Joint Torque estimated via WBD in the firmware	N m
τ^{PID}	Joint torque error after passing through the PID	N m
τ^{ff}	Feed forward term for the joint torque	N m
τ^f	Joint torque term for compensating friction	N m
τ_m	Motor torque obtained by transformation of PWM	N m
τ_{bias}	Bias Force= CoriolisForce+GravityForce	N m
	Other variables	
q	Joint Position	° or rad
$\dot{q}$	Joint velocity	$^\circ s^{-1}$ or rad s^{-1}
θ	Motor shaft Position	° or rad
$\dot{\theta}$	Motor shaft velocity *	$^\circ s^{-1}$ or rad s^{-1}

Table 5.8 Variables used in the joint torque controller scheme.

compensation. The feedback values are the estimated joint torques using the measurements from the FT sensor.

The dynamic behaviors of iCub are obtained through the high-level controllers. They contain many tuning parameters that affect directly the behavior of the robot. From the uses of the FT sensor on iCub, it can be seen that the measurements of the sensor are used mainly in an indirect way by the high-level controllers. Therefore finding quantitative measures of the improvement in the dynamic motions of the iCub caused by the *in situ* calibrated sensor is a bit challenging. Nonetheless, it was possible to observe clear qualitative changes in the behavior that gives an idea of the improvement.

[2]Duty Cycle Percentage.

Contact force coherence when switching contact

A problem observed during a balancing demo [106], see Fig. 5.11, was that the robot has a hard time switching contacts while using the low-level joint torque controller. As mentioned in Section 5.6, the feedback of the controller is estimated using the six axis FT measurements. After observing the behavior of the sensors when switching contact, it could be observed an incoherent behavior in the value of the contact force.

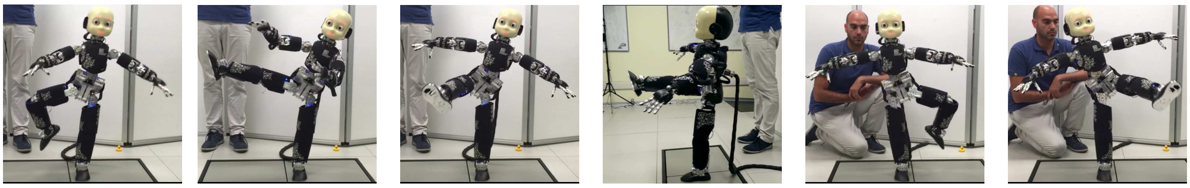

(a) Bending knee on left leg support

(b) Stretched leg on left leg support

(c) Moving back to front and sideways

(d) Stretching to the front, side view

(e) Bending knee on right leg support

(f) Streched leg on right leg support

Watch video

(g) Video QR code

Fig. 5.11 Images from the extended balancing demo with contact switching

A typical sequence before doing the balancing demo, involves removing the offset when is known only one contact exist with the environment. This offset estimation requires the information from the gravity vector. This can be imposed in configuration files or measured using an IMU. This offset is then subtracted to the measurements. There are three possibilities to remove the offset:

- The robot is hanging from the torso and gravity is measured with IMU.
- The robot is standing on one leg and the gravity is measured using IMU.
- The robot is standing on one leg and the gravity is imposed to be acting in the axis normal to the ground.

The test performed consist in switching from single support to double support. If the offset is calculated with the robot standing on one foot the sequence is: single support $\rightarrow$ double

		Contact Forces			Error		
Support	*in situ*	F_x	F_y	F_z	E_x	E_y	E_z
Double	No	-14.0252	-6.8170	342.5232	-14.0252	-6.8170	17.8122
Double	Yes	-5.5024	0.4523	324.2421	-5.5024	0.4523	-0.4689
Left	No	-17.5327	18.1905	342.6850	-17.5327	18.1905	17.9740
Left	Yes	-2.4991	-0.6910	325.3190	-2.4991	-0.6910	0.6080
Right	No	-28.3467	-9.4651	343.5918	-28.3467	-9.4651	18.8808
Right	Yes	-8.3183	-0.0448	323.8349	-8.3183	-0.0448	-0.8761

Table 5.9 Offset estimated while hanging using IMU

		Contact Forces			Error		
Support	*in situ*	F_x	F_y	F_z	E_x	E_y	E_z
Left	No	0.0733	0.0390	323.9000	0.0733	0.0390	-0.8110
Left	Yes	0.0119	0.0543	324.2001	0.0119	0.0543	-0.5109
Double	No	-4.3180	-31.3537	324.2382	-4.3180	-31.3537	-0.4728
Double	Yes	-8.1497	-5.3398	326.7298	-8.1497	-5.3398	2.0188
Right	No	-36.9491	-21.6199	343.4446	-36.9491	-21.6199	18.7336
Right	Yes	7.6190	-7.2226	321.7694	7.6190	-7.2226	-2.9416

Table 5.10 Offset estimated while on left foot imposing gravity.

support $\rightarrow$ other single support. Instead if the offset is calculated with the robot in the air the sequence is: double support $\rightarrow$ single support $\rightarrow$ double support $\rightarrow$ other single support.
Since the robot is standing on flat ground it is expected that the only force acting on the robot feet is gravity on the z axis. With no other force acting on the robot the forces in x and y should cancel each other in double support or be 0 when on single support. With this as ground truth is possible to evaluate the estimated contact forces at the feet when switching. Results are shown in Tables 5.9 and 5.10. It can be observed that using the *in situ* calibrated sensors (by means of the secondary calibration matrix), reduces the error in the contact forces and is therefore more coherent when switching form a contact to another.

Improvement of low-level torque controller on a titled sensor

Seeking to shift the joint limits at the ankle for having a more adequate range for walking motions, a tilted sole was designed for the foot, see Fig. 5.12. Even though the tilt affects also the sensors at the ankle, the model was updated accordingly to account for this tilt. So the change in orientation is accounted for. With the tilted sole mounted, self-sustained oscillations in the centroidal dynamics of the walking controller [111] where observed, Fig. 5.13. These

oscillations prevented the robot to walk using the controller.
When walking on flat ground the load of the sensor is mainly on the z-axis. In the tilted sole, the contact force at the ankle sensor is no longer only in the z-axis. Therefore, the measurements in the x-axis and y-axis played a more important role in the estimation of the CoM and ZMP. The sensors are more affected in the x and y axis by the mounting process, even when a dynamometric screwdriver is used to ensure the torques at the screws are the same. The oscillations disappeared when using *in situ* calibration of the sensors. No other change was required on the robot.

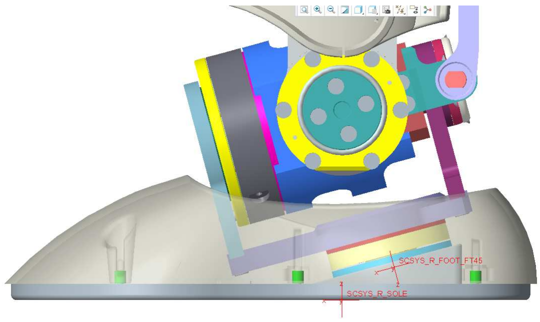

Fig. 5.12 CAD representation of tilted sole.

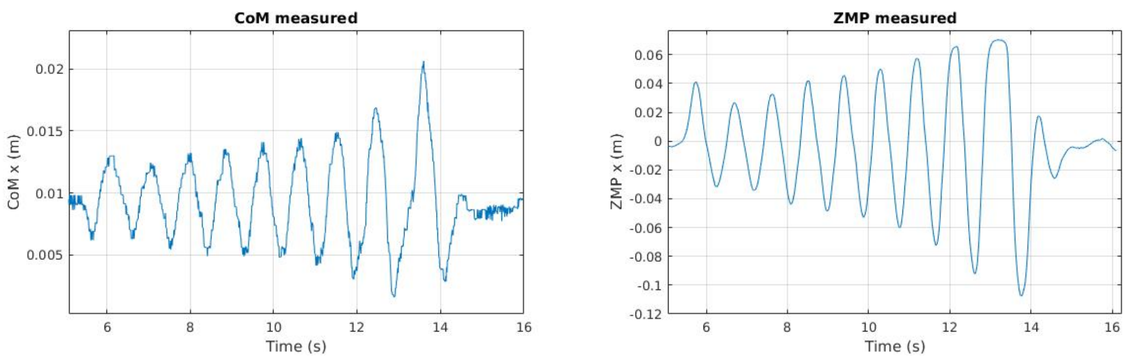

Fig. 5.13 Self-sustained oscillations of the center of mass (CoM) and zero moment point(ZMP).

Less oscillation during balancing demo

The balancing demo [106], was observed to have oscillations of the robot when reaching the different pre-defined position tasks. After the six axis FT measurements were improved, it was considered feasible to increase the gains of the low-level controller.
It was observed that the movements of the robot seemed more defined and there were clearly fewer oscillations and less time required to switch to the next position task. Thanks to the reliability of the measurements, the feedback of the low-level controller is more useful to control the robot creating a faster convergence to the desired value.

5.7 Conclusions

The developed algorithm has been proved to improve the measurements of the sensor and the dynamic behavior of the robot. It successfully accounts for temperature drift and can be extended to account for other lineal phenomena. The possibility to use a constant offset with little sacrifice of sensor performance is a good feature since it can eliminate the need to estimate the offset before every experiment. It minimizes the preparation steps for using the robot. The graphic representation of the sensor excitation in the 3D force and torque space has proven useful to provide intuitive insight on the comprehensive excitation of the sensor. Although the estimation can work without previous knowledge it benefits from an *ex situ* calibration matrix. So *ex situ* calibration methods are not rendered useless. This specially the case for compensation of the dynamic response of the sensor.

Based on the insights gained from the development of the algorithm and the study of *ex situ* calibration methods a calibration device was designed. It is meant to give a fast, easy, reliable, almost human-free, comprehensive way of exciting the sensor in conditions close to the use of the sensor. It also considers the possibility to allow the study of the dynamic response of the sensor. It is detail in Chapter 6.

Chapter 6

A comprehensive Ex Situ Calibration Device for Six Axis Force-torque Sensors

The final stage of FT sensors development is its basic tests to determine the technical and operational characteristics. Particular attention is paid to the calibration of FT sensors, which is the main source of accuracy errors. Although an *in situ* method has been proposed, it still benefits from the knowledge of the *ex situ* calibration matrix. Furthermore it is unable to account for the dynamic behavior of the sensor. Here a review of the current calibration method for FT sensors is described and an alternative solution is presented.

6.1 Current Calibration Method

Current method calibration for the IIT-produced six axis FT sensors (FTsense) requires many manual operations for positioning and weight carrying. This process is slow and quite demanding on the person carrying out the calibration. A recurrent issue is that there is no dedicated room to install and host the calibration setup. This implies positioning the setup each time a new batch of sensors is meant to be calibrated. An appropriate place to put the metal plank is required. Serves as base for positioning the setup perfectly aligned with gravity as in Fig. 6.1. Otherwise, errors are introduced into the calibration. This affects both the time spent and the repeatability of the procedure. Once this is done is possible to move to the acquisition of data. The calibration procedure requires assembling the calibration setup into different positions. Each position shifts the orientation of the sensor with respect to gravity in a different way. In some of them, multiple data points are collected by shifting the load in the different axes. The procedure generates 24 calibration points. The mounting structure weights around 200 gr. The masses used are 5 kg and 25 kg, not considering the weight of the mounting structure. The

Fig. 6.1 Current calibration method position example.

expected FT values are in Table 6.1. The excitation of the sensor in the force and torque space can be seen in Fig. 6.2.

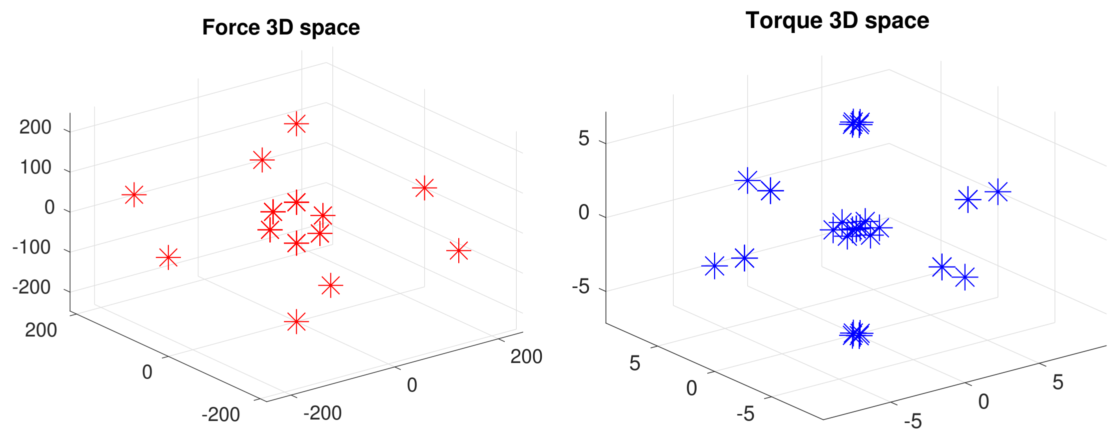

(a) Force 3D space excitation.

(b) Torques 3D space excitation.

Fig. 6.2 Excitation of sensor with current calibration method.

6.1.1 Revision of calibrated sensors

The positions of the calibration method can be grouped, by load, into two groups. Using the resulting grouped positions, Sphere Analysis tool, described in Section , was applied to evaluate the calibration data from over two hundred sensors. The results revealed that there is a relevant error in some positions. Some of the measurements resulted in clear outliers when trying to project them to a sphere in the 3D force space. The sphere was calculated using some of the values in Table 6.1. This behavior can be seen in the figure 6.3 The most affected is the F_x

Table 6.1 Expected forces(N) and torques(Nm) from calibration procedure

Test num	Position description	F_x	F_y	F_z	τ_x	τ_y	τ_z
1	5 kg on y-	0.0000	0.0000	51.0120	-7.5243	0.0000	0.0000
2	5 kg on x+	0.0000	0.0000	51.0120	0.0000	-7.5243	0.0000
3	5 kg on y+	0.0000	0.0000	51.0120	7.5243	0.0000	0.0000
4	5 kg on x-	0.0000	0.0000	51.0120	0.0000	7.5243	0.0000
	heavy loads on strain gauges axes						
5	25 kg on z+	0.0000	0.0000	247.2120	0.0000	0.0000	0.0000
6	25 kg on z-	0.0000	0.0000	-247.2120	0.0000	0.0000	0.0000
7	25 kg on x+ strain axis 1	-247.2120	0.0000	0.0000	0.0000	-1.2361	0.0000
8	25 kg on x- strain axis 1	247.2120	0.0000	0.0000	0.0000	1.2361	0.0000
9	25 kg on strain axis 2	123.6060	214.0919	0.0000	-1.0705	0.6180	0.0000
10	25 kg on strain axis 2	-123.6060	-214.0919	0.0000	1.0705	-0.6180	0.0000
11	25 kg on strain axis 3	123.6060	-214.0919	0.0000	1.0705	0.6180	0.0000
12	25 kg on strain axis 3	-123.6060	214.0919	0.0000	-1.0705	-0.6180	0.0000
	axis x+ pointing up						
13	5 kg on y-	-51.0120	0.0000	0.0000	0.0000	-0.2551	-7.1417
14	5 kg on z+	-51.0120	0.0000	0.0000	0.0000	-9.4372	0.0000
15	5 kg on y+	-51.0120	0.0000	0.0000	0.0000	-0.2551	7.1417
	axis y+ pointing up						
16	5 kg on x+	0.0000	-51.0120	0.0000	0.2551	0.0000	-7.1417
17	5 kg on z+	0.0000	-51.0120	0.0000	9.4372	0.0000	0.0000
18	5 kg on x-	0.0000	-51.0120	0.0000	0.2551	0.0000	7.1417
	axis x- pointing up						
19	5 kg on y+	51.0120	0.0000	0.0000	0.0000	0.2551	-7.1417
20	5 kg on z+	51.0120	0.0000	0.0000	0.0000	9.4372	0.0000
21	5 kg on y-	51.0120	0.0000	0.0000	0.0000	0.2551	7.1417
	axis y- pointing up						
22	5 kg on x-	0.0000	51.0120	0.0000	-0.2551	0.0000	-7.1417
23	5 kg on z+	0.0000	51.0120	0.0000	-9.4372	0.0000	0.0000
24	5 kg on x+	0.0000	51.0120	0.0000	-0.2551	0.0000	7.1417

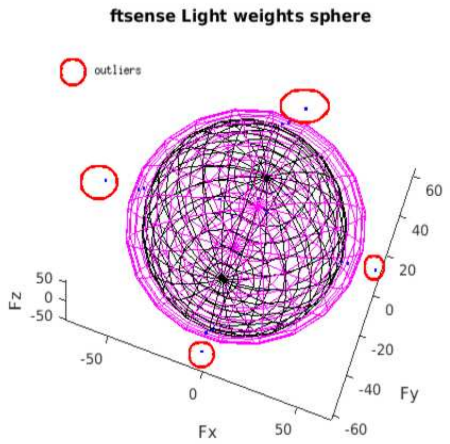

Fig. 6.3 Projection to the expected sphere and outliers.

axis. The error in the F_x axis is shown in the histogram 6.4. This might imply there is an error coming from the way the sensors are calibrated. It is most likely a consequence of the procedure being cumbersome and prone to human error.

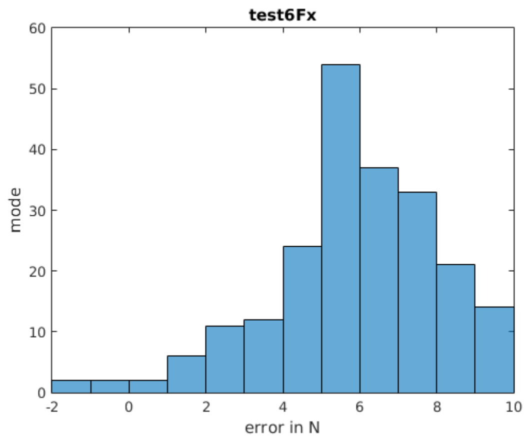

Fig. 6.4 Histogram of errors in F_x .

In summary, even if the sensors calibrated using this procedure have been used in the iCub, it is possible to observe that the calibration is not perfect and the procedure itself suffers from the following disadvantages:

- Cumbersome,
- Susceptible to Human Error,
- Needs to be mounted every time,
- Does not consider temperature.

6.2 Proposed solution

Considering the disadvantages of the current calibration procedure and with the experience of the developed *in situ* calibration algorithms, a solution was envisioned. The objective is to design a new calibration device that would allow fast and easy semi-automatic calibration of six axis FT sensors. It should be self-contained and allow to account for other phenomena, like the temperature, without being very expensive. The possibility to perform dynamic analysis of the sensor response is desirable.

6.2.1 Design requirements

From the desired objective and the expected use of the calibrated sensors, a set of design requirements were compiled. The requirements are:

1. The excitation should be at least equal to the current method
2. The loading of the weight should be done a limited number of times between 3 and 2.
3. The loading of the weights should not be perceived as difficult or dangerous by personnel experienced with the current method.
4. Human intervention should be limited to mounting the sensor once, loading of the weights and give the signal to start the calibration.
5. The device should withstand a load of 35kg.
6. The maximum error of the reference used in calibration should be below 0.5N for the forces and 0.02N·m for the torques.
7. Should allow calibration of up to 3 sensors at a time.
8. The mounting of a sensor should be simple enough to be done in less than 2 min based on feedback from the production department.
9. The total cost should not exceed the budget of €10,000.00.
10. The number of DoF should be less than 6.
11. The motion envelope should be contained in a space smaller than 1.5m^2.
12. The device should allow to excite the sensor with controlled temperature in the range of 15^o to 55^o.

13. It should allow for dynamic behavior analysis of the sensor.

The proposed solution is a device that has been named *iCalibrate*. The device is currently under design.

6.3 Conceptual design

The conceptual design phase provides a description of the proposed system in terms of a set of integrated ideas and concepts about what it should do, how it should behave, and what it should look like, which will be understandable by users in the manner intended.

6.3.1 Degrees of freedom

The aim is to excite the sensor in all six axis. Based on the experience with *in situ* calibration algorithms, the excitation of the sensor was aimed to span a sphere in the force space while exciting all three axis in the torque space.

Knowing that the torques are a linear combination of the forces, with the right combination of three DoF, it should be possible to fully excite the sensor. To achieve this is enough to have a pitch or roll joint followed by a yaw joint. The fact that the yaw comes afterwards is important since it allows the actual shift in the orientation of the sensor frame to span a sphere in the force space. Changing the order of the first two DoF results in an incomplete sphere as shown in Fig. 6.6 and a need for bigger space in Cartesian space to span the sphere. This two DoF alone are unable to fully excite the sensor in the torque space, so a third joint is added. The maximum excitation of the missing torque axis can be achieved having the third joint at 90° with respect to the sensor frame. The third joint is selected to be just binary 0° and 90°.

As a result, the mechanism will have three joints with [pitch,yaw,pitch] configuration. The sphere in force space can be obtained using a range of motion of 180° in the pitch and 360° in the yaw and two positions (0° and 90°) on a second pitch.

6.3.2 Passive Joint

Since its enough for the third DoF to have only two configurations, no actuation is required. Instead of manually changing the position of the third joint, it is possible to use a self-locking mechanism. When pointing the sensor to the ground and releasing the lock on the third joint, gravity itself will make the joint reach the other self-locking position when moving the pitch by 90°. Then the third joint would self lock in the other selected position. This solution helps to reduce the costs and the complexity by not requiring another motor.

6.3.3 Excitation of the FT sensor

Using the model of the device is possible to calculate the force-torque at different positions for a given mass value.

Assuming joint position [0,0,0] is the device in a completely straight position as in Fig. 6.8. A possible sequence to excite the sensor is the following:

1. Start from [-90,0,0];
2. Move to [90,0,0]
3. Shift yaw by 90°
4. Move from [90,0,0] to [-90,0,0]
5. Shift yaw by 90°
6. Repeat this twice
7. Move to [0,0,0]
8. Do a full 360° on the yaw axis.
9. Move to [-90,0,0]
10. Unlock passive joint
11. Move to [0,0,0]
12. Do a full 360° on the yaw axis.

Movements from 1 to 6 excite the sensor by shifting the load from z axis to x or y. Movements 7 and 8 fully excite the sensor in the x-y plane for the current load. Movements 9 and 10 take advantage of gravity to move the passive joint. Finally moves 11 and 12 are specifically designed to excite the sensor mainly with a torque around Z. The resulting motion sequence can be seen in Fig. 6.5.

There are many more possible movements that can be done. These ones where design to create a direct comparison with the current calibration method and show the potential excitation of the sensor using the device. The wrenches of this motion can be compared using a similar mass to the ones used in the current method. A comparison with the positions with 5.2kg can be seen in Fig. 6.7. The resulting excitation is bigger than the current calibration method. These motions include complex loading scenarios as well. Swapping the first two DoF results in the limited excitation in Fig. 6.6.

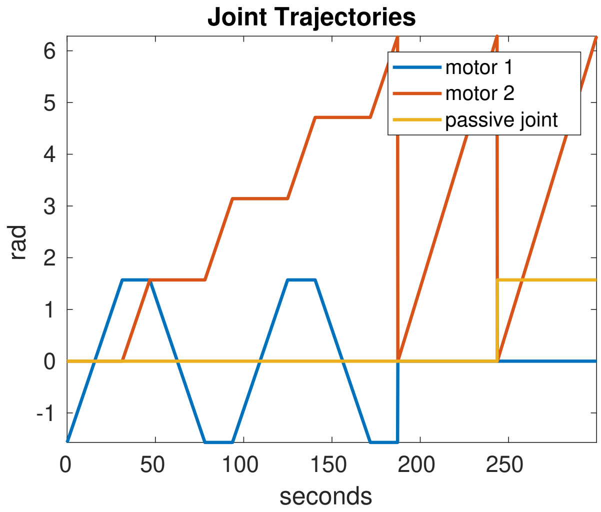

Fig. 6.5 Joint trajectories of the motion sequence.

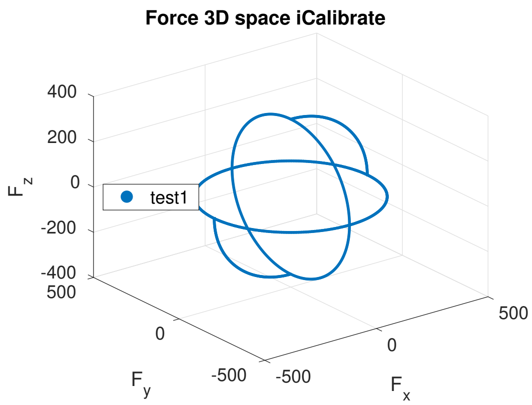

(a) Excitation in force 3D space.

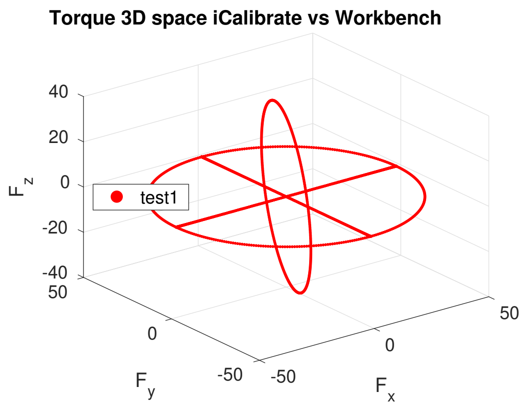

(b) Excitation in torques 3D space.

Fig. 6.6 Excitation with yaw DoF first.

The link lengths should be as small as possible to reduce the torque and the workspace size. The concept design can be seen in Fig. 6.8.

6.3.4 Sensor interfaces

A fast and easy assembly of the sensors should not compromise the sturdiness of the design. This can be achieved by having a low number of screws while reinforcing the coupling of the interfaces with physical features. They should also allow stacking them to calibrate more than one sensor at a time and be sensorized to allow temperature excitation. A Peltier device might be a solution. The design should consider a way to deal with the mounting issues.

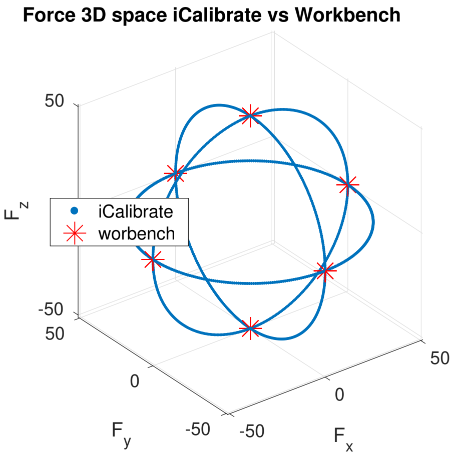

(a) Excitation in force 3D space.

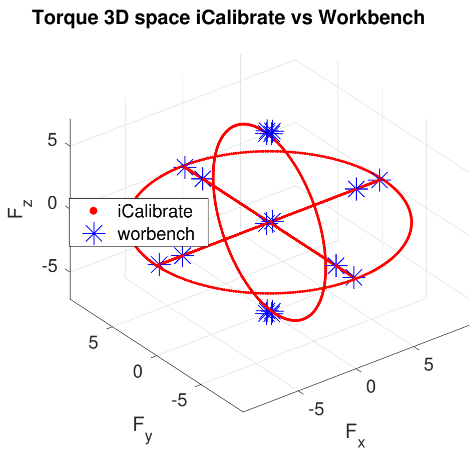

(b) Excitation in torques 3D space.

Fig. 6.7 Excitation of sensor with a 5.2kg mass.

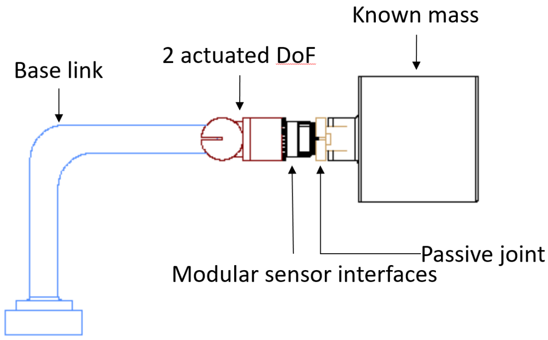

Fig. 6.8 Conceptual Deisgn of iCalibrate

6.3.5 Weights

Attaching the load to the device should be simple and almost effortless for the human, while remain secured in place. For this, the load can be divided into 5kg weights. These weights can be loaded in place one at a time. The structure in which they are loaded can be a tube of non-circular cross-section to avoid the movement of the weights as much as possible. The piece to keep the weights in place should be such that even rotating the orientation in all directions it does not fall down.

6.3.6 Dynamic excitation features

To perform frequency response analysis one solution is to have friction compensation in the second motor. This allows to use the device as a pendulum in certain configurations. Another option is to create a passive joint which allows a rope to be attached and another structure to hold and release the weight hanging from the rope in a repeatable way.

To perform step response is enough to have a passive joint designed to release the weight from the structure upon the reception of an activation signal.

Given the fact that this device can excite the sensor in the full range of the theoretical force sphere, it might allow to perform dynamic calibration even in complex loading scenarios.

6.4 Embodiment Design

Embodiment design is the part of the design process in which, starting from the principle solution or concept of a technical product, the design is developed in accordance with technical and economic criteria and in the light of further information, to the point where subsequent detail design can lead directly to production [102].

6.4.1 Model

To have an accurate estimation of the forces and torques, the CAD model is exported to urdf format following a procedure similar to the export done for the iCub. The CAD is generated with a single sensor. The adaptation when using other sensors is possible thanks to the stacking pattern of the sensor interfaces. Using the iDyntree library [129] is possible to load a urdf model and generate the required estimation. Some scripts were prepared to perform the estimation based on the model. This allows to quickly check and revise different aspects of the performance of the device. Using this the number of sensors in the model can be increased. Verification of the sensors excitation and resulting torque at the motors is possible. It was done in such a way that the software developed for *in situ* calibration can be used to calibrate the sensors later on.

6.4.2 Motor Selection

Since the design only requires two actuated joints, only two motors are required. Using the model is possible to calculate the maximum torque experienced by each motor. The resulting torques can be seen in Fig. 6.9

With the current model, stacking three sensors the peak torques for motor 1 and motor 2 are 131.3495Nm and 39.4500Nm respectively.

The formula proposed by Harmonic Drives for the average torque is:

$$\tau_{av} = \left(\frac{n_1 t_1 |\tau_1|^3 + n_2 t_2 |\tau_2|^3 + \cdots n_n t_n |\tau_n|^3}{n_1 t_1 + n_2 t_2 + \cdots n_n t_n} \right)^{1/3} \tag{6.1}$$

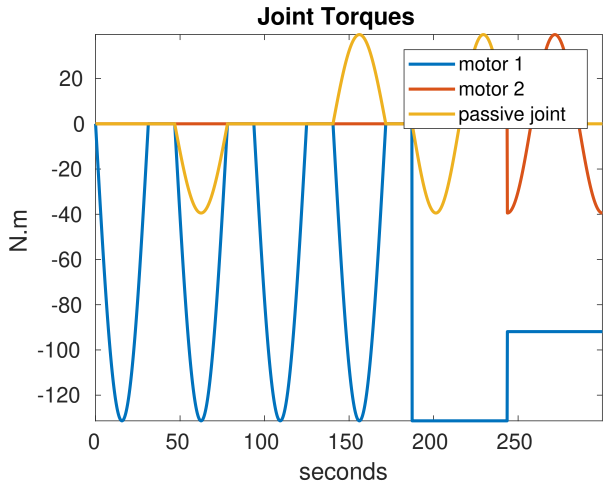

Fig. 6.9 Joint torques of the motion sequence.

motor 1	motor 2
106.1922 Nm	24.4700 Nm

Table 6.2 Average torque

Where τ_{av} is the average torque, t_i is the seconds it stays with the torque, n_i is the speed (in rpm) of the motor during t_i, and τ_i is the torque of the motor during t_i. Using the described motion sequence in 6.5, the speed and time can be calculated by selecting the time it should take to finish the whole sequence. The calculated τ_{av} using this values for a 35 kg mass is shown in Table 6.2.

With the information about the torque peak and average is possible to select a motor.

6.4.3 Inertial and Position Sensor selection

To full fill requirement about the accepted error in the reference wrenches, its important to consider the possible sources of error. The errors can come from:

- Errors in the measured or estimated orientation of gravity
- Errors in the dimensions of the links and components
- Deformation of the link due to load
- Error in the value of the known mass

The mass will be custom made with attention to minimize this error. Similar case for the dimensions of the links and components. The geometry and material of the link will be selected to avoid deformations. The most likely source of error will be in the knowledge about gravity. This knowledge can be obtained from two sources: an estimation using the information from the joint positions or measuring gravity with an inertial sensor. In both cases, commercial solutions were investigated to verify possible noise values.

Selecting noise values in joint positions

The reference was the magnetic rotary encoder AS5045. With a resolution of 12 bits, each bit the least significant bit (LSB) is 0.0879°. In the data sheet is mentioned that in the best case scenario the error is $<\pm 0.5°$ and in worst is $<\pm 1.4°$.

Selecting noise values in measured gravity

The BOSCH BNO055 was taken as reference. At normal mode the accelerometer has a range of ± 4 g it means 8 g in total. Considering the resolution is 14 bits then the LSB is

$$LSB = 8g/2^{14} = 0.00048828g = 0.0048m/s^2 \tag{6.2}$$

If we use the configuration in which range goes from ± 2 g we have that

$$LSB = 4g/2^{14} = 0.0024m/s^2 \tag{6.3}$$

Error is assumed to be ± 4 LSB so:

- $0.0192\,\mathrm{m/s^2}$ for ± 4 g configuration
- $0.0096\,\mathrm{m/s^2}$ for ± 2 g configuration

Error in reference wrenches due to noise

With these values, an amplitude for noise in the measurements can be selected. The exploration for the encoders started at $\pm 0.5°$ noise amplitude and for the inertial sensor the noise amplitude of $0.03\,\mathrm{m/s^2}$ was selected so that we get $\pm 0.15\,\mathrm{m/s^2}$ in the error. Results are presented in Table 6.3

From this is possible to observe that the reference IMU is a good option for the inertial sensor, while the encoder is on the limit with the best case scenario. Looking for other option for the encoders is necessary.

estimation	noise amplitude	Fx (N)	Fy (N)	Fz (N)	Tx (Nm)	Ty (Nm)	Tz (Nm)
IMU	$0.015\,\mathrm{m/s^2}$	0.1519	0.1500	0.1524	0.0170	0.0160	0.0062
IMU	$0.03\,\mathrm{m/s^2}$	0.3404	0.3431	0.3348	0.0387	0.0361	0.0134
encoders	0.5°	0.6003	0.6017	0.6568	0.0960	0.0711	0.0448
encoders	0.25°	0.3105	0.3006	0.3360	0.0484	0.0367	0.0231
encoders	0.1°	0.1208	0.1232	0.1311	0.0197	0.0140	0.0095

Table 6.3 Error in the references due to noise amplitude.

6.4.4 Sensor interfaces

The FTsense strain 2 was used as reference for the mounting holes. The sensor interface was divided into one male and female part to allow stacking. Without counting the screws for mounting the sensor, there are only four other screws required. On the male side, each of these four screws has an extrude that fits a hole in the female side, to make the coupling more robust and easy. The section where the sensor is mounted was designed such that just the border of the sensor is in contact. This is to minimize mounting stress due to a not fully planar surface from the manufacturing process. A through-hole in the middle was added to allow the passing of cables. The hole at one of the borders is pointing to the x axis of the sensor frame. It allows the passing of cables and fast orientation of the sensor with respect to the mounting interface. A CAD of the design can be seen in Fig. 6.10 and Fig. 6.11.

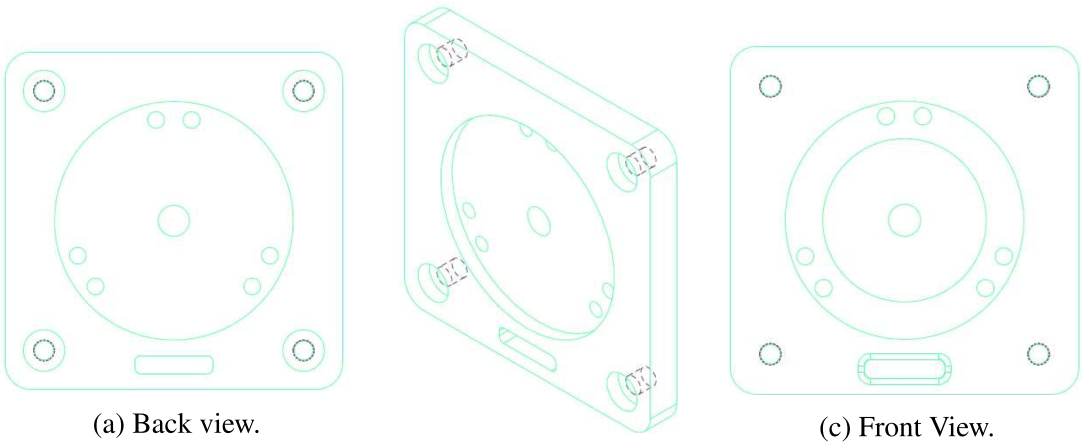

(a) Back view.

(b) Isometric View.

(c) Front View.

Fig. 6.10 Female interface.

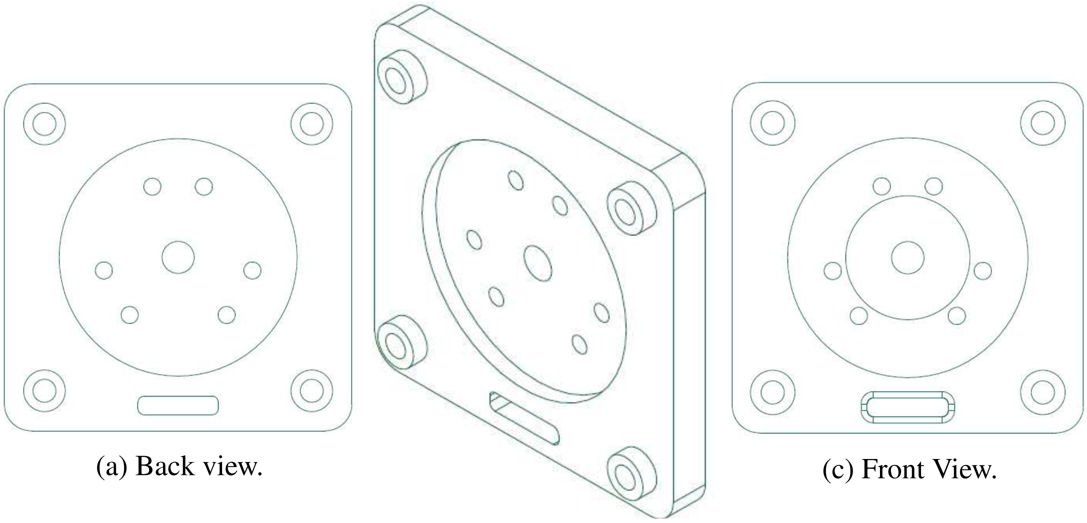

(a) Back view.

(b) Isometric View.

(c) Front View.

Fig. 6.11 Male interface.

6.5 Design status

The status of the current design can be seen in Fig. 6.12. The choice of DoF allows to have a motion envelope that could be easily contained in $1.5\,\mathrm{m}^2$, Fig. 6.13. An assembly of the sensor interfaces can be appreciated in Fig. 6.14 Some of the missing features are not strictly required to build a first prototype. Therefore have a lower priority in the design pipeline.

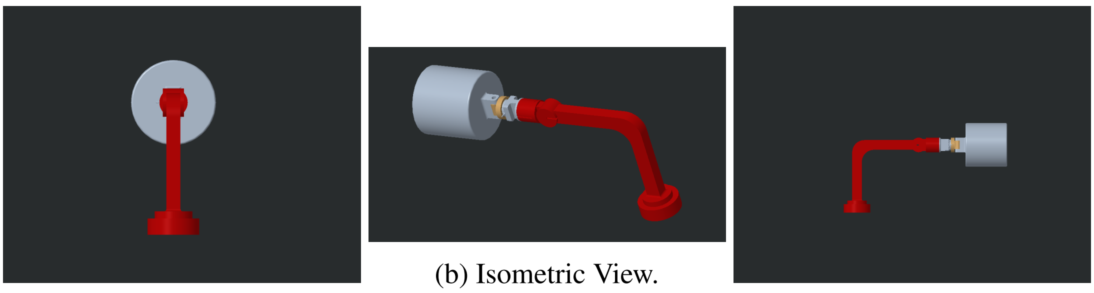

(a) Back view.

(b) Isometric View.

(c) Side View.

Fig. 6.12 Current status of the iCalibrate design.

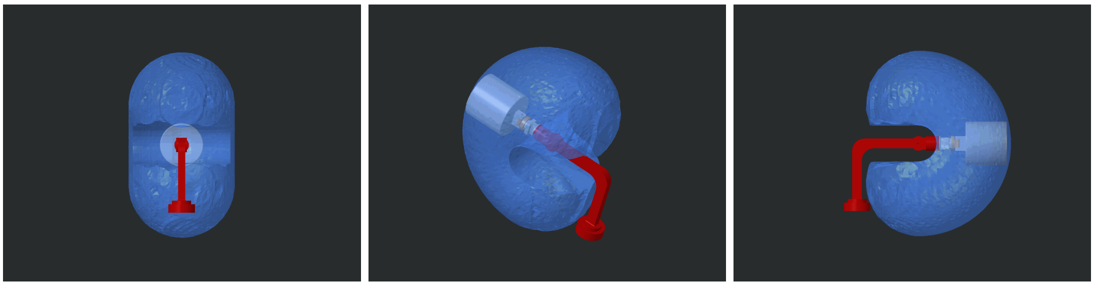

(a) Back view. (b) Isometric View. (c) Side View.

Fig. 6.13 Motion Envelope of iCalibrate.

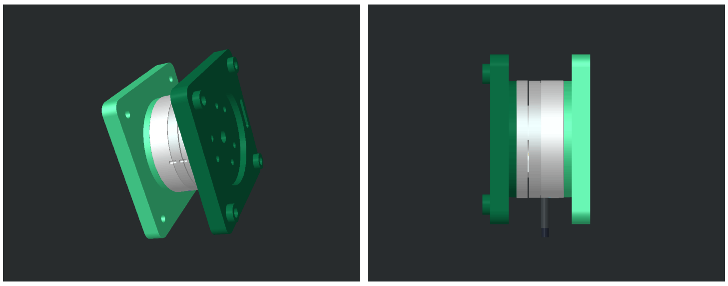

(a) Isometric view. (b) Side View.

Fig. 6.14 Assembly of a sensor with both sensor interfaces.

6.5.1 Components currently under design

As mentioned the full design is still in progress. The features that are still under development are:

1. Shell of the motors
2. Motor and Weight interfaces
3. Weights and load support.
4. Sensorization of sensor interfaces
5. Passive Joint
6. Weight release joint
7. Rope attachment joint

They are ordered in order of relevance, the last four are not strictly required for a prototype.

6.6 iCalibrate As a Benchmark

Benchmark is defined as something that serves as a standard by which others may be measured or judged according to the Merriam-Webster dictionary. Competitive benchmarking is a direct competitor-to-competitor comparison of a product, service, process, or method [5].

All six axis FT sensors have the same relationship with gravity. So any sensor subjected to the motions described in Section 6.3.3, should ideally have the same measurements in force and torque. This allows to have a universal comparison among six axis FT sensors.

The device is designed to be repeatable, easy and fast to use. Considering this, the device could be used to compare the performance of different sensors or even calibration methods. The sensor interfaces would require adaptation to mount other six axis FT sensors.

For benchmarking sensors, there is no need to change the CAD model since they are already calibrated and no reference data is required. Thus the device is able to perform that comparison seamlessly. It would only be necessary to have a way to log the data such that it allows synchronization between experiments. Nonetheless, since the estimation is done using the model from CAD, by updating the model with the new interface and the sensor model, the estimation can be performed. Adding the possibility to add weights in 5 kg intervals allows for an easy way to collect validation data sets with data completely different from the calibration data. This can allow to compare different calibration methods even in different sensors.

The sensorized interfaces may also allow to verify the response of different sensors to temperature. Allowing to include temperature drift response as part of the benchmarking.

Depending on the size of the sensors to compare it might be possible to mount three different sensors at the same time. Having synchronization of the data almost for free. This would guarantee even further the validity of the comparison.

In summary, the device might be a benchmark candidate for both sensors and calibration methods. The reasons are :

- Excitation is based on gravity, which ideally affects all ft sensors alike.
- The motions excite comprehensively the sensors.
- With minimum effort is adaptable to other sensors.
- It is designed to be repeatable and easy to use.
- Chances for human error are kept to a minimum.
- The design for the weights makes fast and easy to collect validation data sets, different from the calibration data.

- The exposure to a controlled temperature allows verification of sensors response to this phenomena.
- Possibility to mount more than one sensor at a time makes data synchronization simple.

6.7 Conclusion

Even if the device is still unfinished, the theoretical bases of its functionality make it look very promising. Not only will it allow to calibrate better and faster, it might also allow study different sensor designs and calibration algorithms at a cost lower than the value of two commercial force torque sensors. It is also interesting the possibility to perform reliable dynamic calibration of the sensor even in complex loading scenarios. This is something that to the best of the authors knowledge is still not present in the literature.
Despite the improvement that can be achieved in the performance of FT sensors, it still holds that they are unable to distinguish multiple contacts in the same sub-model. To grant this functionality to robots exploring the possibility of calibrating and use of other sensors such as tactile sensor arrays is depicted in Chapter 7.

Chapter 7

Artificial Skin as a Force-torque Sensor

Contact detection is possible due to an exchange of forces between bodies. Tactile sensors are made with the main goal of detecting contact. When taking a look at the functioning principles, it is possible to see the potential for measuring forces and torques. In this Chapter, the possibility of using the artificial skin of the iCub as a FT sensor is explored.

7.1 Requirements for using skin as force-torque sensor

To be able to use the skin as a force-torque sensor on the robot there are two elements required beforehand:

- Equate the value of the capacitance of each taxel to a pressure value.
- The location of each taxel with respect to a frame in the piece of cover in which is mounted.

The methods required to achieve these preliminary steps were not directly developed by the thesis author. Nonetheless, as a user the author gained deep understanding of the methods and was involved in improving their usability.

Pressure Calibration

For the pressure calibration of the skin, the most convenient method is to have even pressure distribution over the skin. This allows to calibrate all sensors at the same time, making the process faster and less cumbersome. To achieve this, two methods were available: the first one was vacuum bags [66]. Later on, the calibration device [65] became available. What follows is a brief description of both setups and some of the typical curves of pressure vs capacitance of the taxels.

Vacuum bags

The vacuum bags method [66] is based on the fact that by removing the air from a bag, the difference in pressure with respect to the outside of the bag creates an evenly distributed pressure on the surface of the object inside the bag.

The setup is built with a vacuum pump, a pressure sensor, a customized bag, and the artificial skin connected to a PC, see Fig. 7.1. Typical data collected using this method can be seen in Fig. 7.2. It can be observed that the behavior of each taxel is different from each other although a general tendency can be appreciated. Based on this behavior the mathematical model to relate the capacitance value to the applied pressure for sensors was approximated with a 5th order polynomial calculated as follows:

$$P(C_i) = a_i + b_iC_i + c_iC_i^2 + d_iC_i^3 + e_iC_i^4 + f_iC_i^5 \quad (7.1)$$

where $P(C_i)$ is the pressure applied to a specific sensor and $a_i, b_i, c_i, d_i, e_i, f_i$ are the sensor-specific constants representing the model for sensor i. The model is found by solving a least square optimization problem using the experimental data.

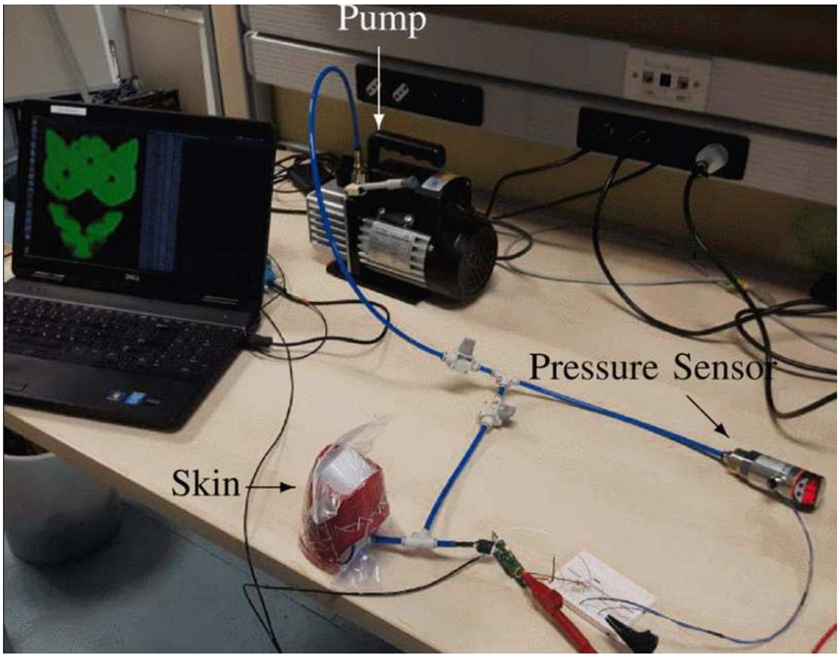

Fig. 7.1 Vacuum bag experiment setup.

This setup was created as a proof of concept. Its advantages are that it using the evenly distributed pressure is possible to excite every taxel at the same time with a known pressure. This saves time and makes it repeatable. Cost is another advantage since, except for the vacuum pump, most of the elements are cheap and easily available. Also, the dimension of the skin that

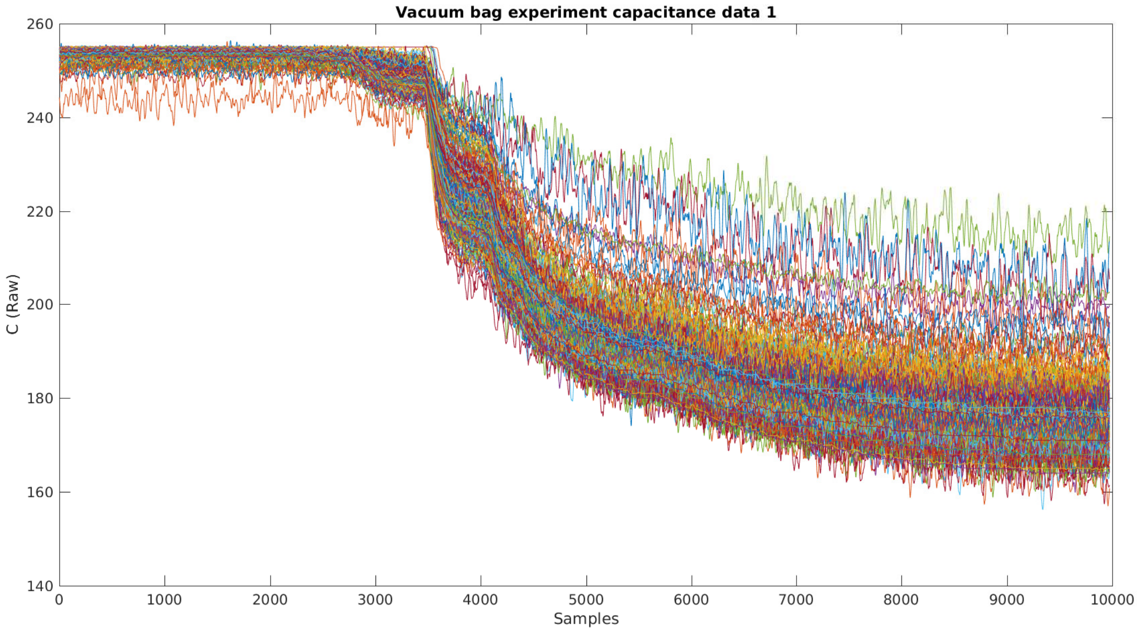

Fig. 7.2 Vacuum bag experiment data.

can be calibrated is determined by the size of the bag.
There are two crucial elements of this method. The first and most important is the customization of the vacuum bag. In the original setup, this bag was sealed with hot glue. This made it so that it was easy to melt the bag and hard to achieve a decent sealing. It was also easy to break the bag, so the bag itself should be considered disposable. Another issue found in the bag was the possibility of the two sides of the bag coming in contact during the suction of air. This prevented the pressure to build up properly in the bag. It is dependent on the choice of skin to calibrate and the place in which the hole of the bag is done.
During the usage of this method, the customization and sealing of the bag were improved by using simple market solutions used for plumbing. This increased the reliability of the bag while decreasing the time required to customize a new bag. The pieces themselves are not glued and therefore reusable avoiding damaging the bag with heat. The used solution can be seen in Fig. 7.3. To avoid having the two sides coming in contact a honeycomb structure was used to allow the passing of air and avoid blocking the hole with the other side of the bag.
The second element is the control of the vacuum pump which was manual. This made the smooth transition of pressure user dependent and susceptible to variation. A more comprehensive solution to deal with issues in both elements was developed by other members of the lab. The result was the Pressure chamber device described below.

Fig. 7.3 Vacuum bag sealing improvement.

Pressure chamber device

As described in [65] a sketch of the device is shown on Fig. 7.4. It consists of a microcontroller, a PC, an air compressor, a regulator, a pressure chamber and a compliant bladder. The compressor pushes the air to the regulator that controls the pressure in its output. The regulator is able to increase the pressure with the rate that is required by the user until the desired maximum pressure is reached. The desired pressure is sent from PC through the microcontroller to the regulator and it separately measures the actual pressure on the output. As the air is pumped into the pressure chamber, the compliant bladder first wraps around the skin piece and then starts applying uniformly distributed pressure on the skin. The information from the skin about the tactile sensor values is also sent to the PC at the same time.

The PC software gathers the data about the skin sensors' values and the pressure inside the chamber and logs it while the pressure is increasing. When the maximum desired calibration pressure is reached, the pressure is released in the chamber with the regulator. Then the gathered data is processed in order to create a mathematical model for each sensor that relates the applied pressure to the sensor capacitance value.

The typical curves for the capacitance and pressure using the device can be seen in Fig. 7.5.

Fig. 7.6 depicts how the fifth order polynomial model, indicated with blue, is fit to the data points, given as red circles. It was observed that all the sensors have slightly different responses, varying in noise level, gain, initial offset, and even the shape of the curve.

This solution improved the control of the pressure, had better sealing and expanded the range of excitation of the artificial skin during calibration. It eliminated the need for having a bag that

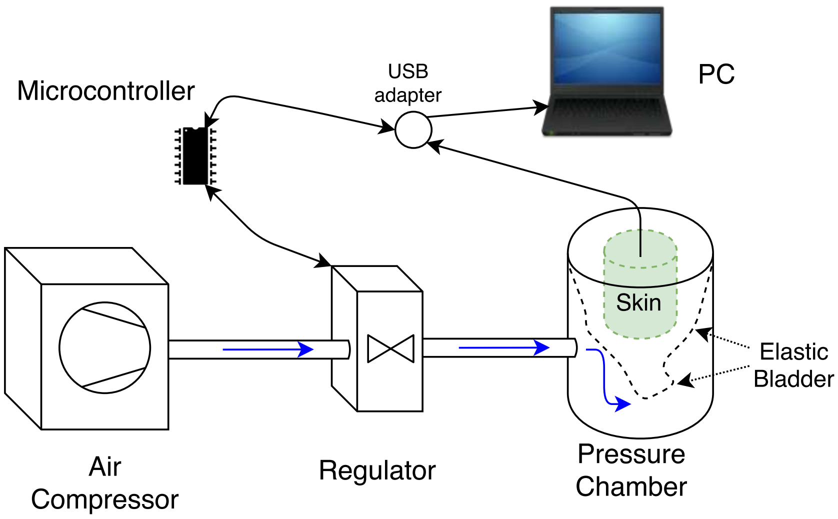

Fig. 7.4 Schematic of the design of the calibration device. The electrical connections are indicated with black solid arrows and the air flow with blue arrows.

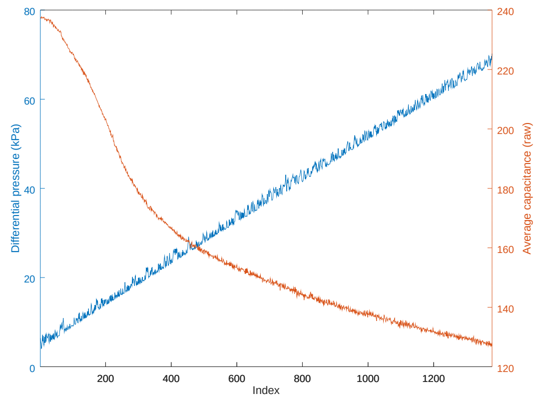

Fig. 7.5 Pressure and average capacitance during the experiment.

had its own hermetic sealing. Nonetheless, it restricted the maximum size of skin components that could be calibrated and could benefit from small design changes to facilitate its use and reliability. One such improvement could be finding a smart way to keep the different types of artificial skin shapes to calibrate in a fixed and centered way. This should allow a better wrapping of the bag around the skin component. Another improvement would be to find the right material for the bag that wraps around the skin.

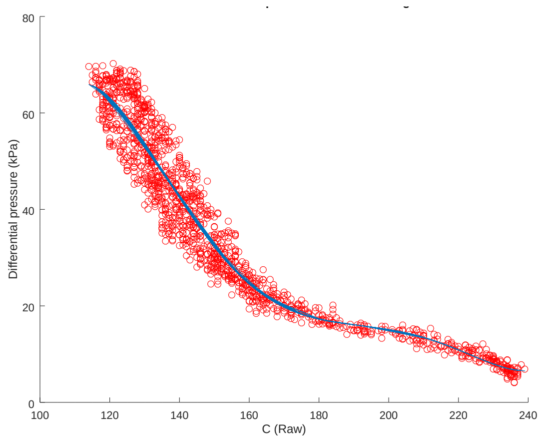

Fig. 7.6 Fifth order polynomial model (blue) fit to data points (red) in order to relate capacitance to pressure for an individual sensor.

3D taxel position

Given the geometry of the cover in which the skin was mounted, directly measuring the exact position of a taxel to a chosen frame seemed a difficult task with low guarantees of success. Instead, the approach for finding the position of the taxel 3D position was an indirect method using the different documentation of its components. A combination of resources of the electrical design, the mounting procedure and the CAD of the cover are employed. The general steps are :

Fig. 7.7 Cover and skin with number id.

- Using this documentation we are able to identify the id of each triangle as shown in Fig.7.7.
- This information is then used to create the appropriate frames in the CAD model.

- The CAD model is exported to simmechanics format.
- Then a tool to export simmechanics format to urdf is used. This tool was originally made for obtaining the model of iCub.
- The icub-model-generator is used to estimate the position of the triangles based on its center and its orientation.

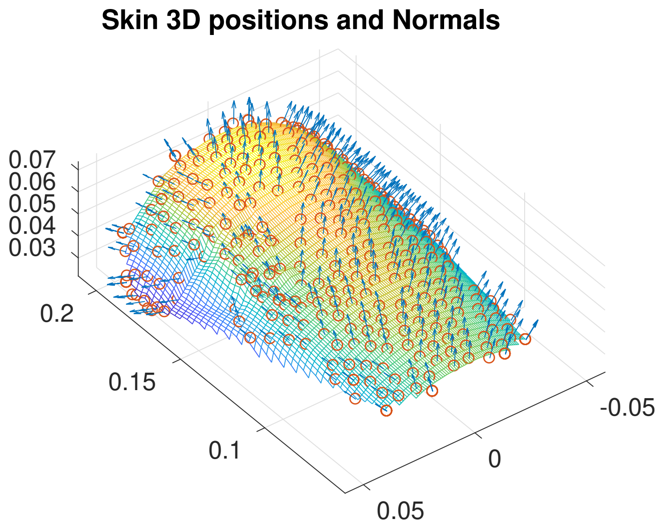

Fig. 7.8 Plot using the generated 3D positions and normals.

From this process, we obtain not only the 3D position of the taxels, but also the normal vector to each taxel. An example of the resulting positions and normals is depicted in Fig. 7.8, where the red circles are the taxels and the blue arrows the normals. A more detailed description of the process can be found in Appendix C.

7.2 Force Estimation Improvement

Once the artificial skin of iCub is calibrated the tactile sensors are able to measure the pressure applied to each one of them individually. However, the sensors are positioned on the surface as an array of discrete taxels with gaps between them. In order to compensate for this shortcoming, the presented algorithm exploit pressure interpolation techniques to deal with the gaps between tactile elements, this improves the accuracy of the tactile sensors by adding information in the spaces where the pressure cannot be explicitly measured.

Every point on the skin covering a given link can be represented by a pair of surface coordinates, that we refer as the couple $(u,v) \in [u_1,u_2] \times [v_1,v_2]$.

The method used for interpolation consists of the following steps:

1. Locations of the sensors in the u-v plane are collected.

2. Pressure values of the sensors are measured. The values are stored in the p axis which is orthogonal to the u-v plane.

3. The sensors are modeled as a circle (with the appropriate area) labeled with a certain number of data points. The pressure is assumed to be constant over the area of the sensor, therefore all the data points of a specific sensor have the same value in the p axis.

4. The trilinear interpolation based on a Delaunay triangulation is used to interpolate the pressure field between the data points [Octave Authors].

The output from the interpolation allows us to define the pressure field $p(u,v)$. An example of the pressure field while a 1 kg mass is put on the skin is shown in Fig. 7.9.

The 3D positions of all the sensors are known but there is no information about the surface between the sensors. Therefore, the surface has to be interpolated between the known values. The positions corresponding to u-v field can be divided into 3 separate interpolation problems, one for each axis. The trilinear interpolation allows us to define the interpolated field of each axis of the position vectors, i.e. $x(u,v)$, $y(u,v)$ and $z(u,v)$.

The position vector expressed in the link frame corresponding to a location on u-v plane can be expressed as follows:

$$r(u,v) = x(u,v)e_1 + y(u,v)e_2 + z(u,v)e_3, \tag{7.2}$$

where e_1, e_2, e_3 are the basis of the 3D space.

The normal vectors of all the sensors are known, but there is no information about the surface normals between the sensors. Therefore, the normals have to be interpolated between the known values. The normals corresponding to u-v field can also be divided into 3 separate interpolation problems, one for each axis. The trilinear interpolation allows us to define the interpolated field of each axis of the unit vectors, i.e. $n_x(u,v)$, $n_y(u,v)$ and $n_z(u,v)$, with the actual normal $\hat{n}(u,v)$ given by

$$\hat{n}(u,v) = \frac{n_x(u,v)e_1 + n_y(u,v)e_2 + n_z(u,v)e_3}{||\, {n_x}^2(u,v) + {n_y}^2(u,v) + {n_z}^2(u,v) \,||}. \tag{7.3}$$

Assuming that $\left| \frac{\partial r}{\partial u} \times \frac{\partial r}{\partial v} \right| \approx 1$ the total force vector can be found as:

$$f = \int_{v1}^{v2} \int_{u1}^{u2} p(u,v)\hat{n}(u,v)dudv, \tag{7.4}$$

while the total torque vector can be found as follows:

$$\mu = \int_{v1}^{v2} \int_{u1}^{u2} ((p(u,v)\hat{n}(u,v)) \times r(u,v))dudv. \tag{7.5}$$

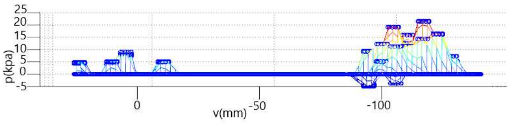

(a) Side view

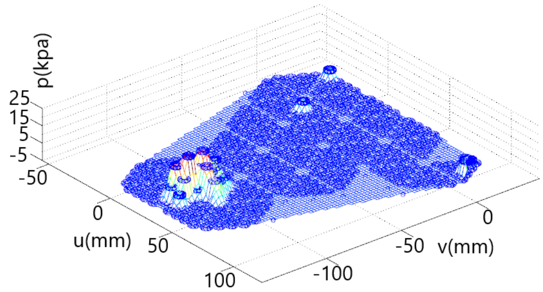

(b) Three-Point Perspective

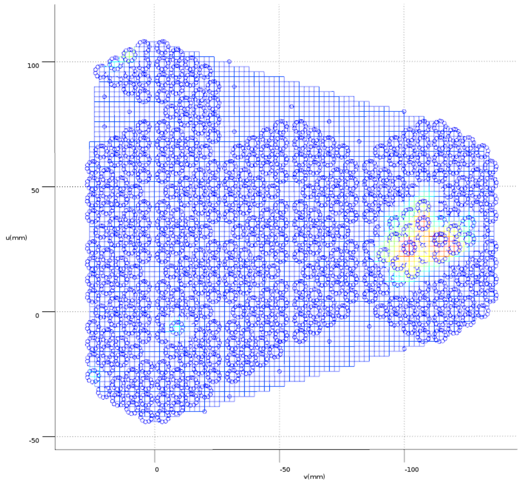

(c) Top view

Fig. 7.9 Pressure field of a skin patch while 1 kg is applied.

So we end up with a force-torque measurement with respect to the frame in which the 3D positions where measured.

7.3 Application

The information gained through the calibration of the artificial skin is a 6D force vector. It can now be used as a force-torque sensor at the contact location. This is particularly useful to measure the forces of multiple contacts individually. A direct application is to endow this capability to the robot.

7.3.1 Contact Force and Joint Torque Estimation using Skin

Once we have the force-torque measurement, we can consider this directly as a contact external force. Finally, we use this information plus the location of the contact obtained from the skin to estimate the joint torques of the robot. The innovation is applying the interpolation techniques to improve the accuracy of the tactile sensor and the inclusion of the tactile sensor into the estimation scheme as a source of force and torque information.

Adding Known External Force-torques To The Joint Torque Estimation Scheme

To consider the effect of having the knowledge of an external force-torque at a known location (${}_K\mathrm{f}_K^k$), it is necessary to extend the current framework detailed in Section 2.4 to include the new type of contact. This is achieved by adding the characteristics of this contact to all parts of the equation $Cx = b$ and equations (2.8b)(2.8c).

In the case of the C matrix, the 4_{th} contact type would be a 6×0 matrix:

$$C_k = 0_{6\times 0} \tag{7.6}$$

and for the b term the equation would be:

$$b = \sum_{L\in\mathfrak{L}_{sm}} {}_B X^L {}_L\phi_L - {}_B\mathrm{f}_B^{tot}, \tag{7.7}$$

where

$${}_B\mathrm{f}^{tot} = \left(\sum_{L\in\mathfrak{L}_{sm}} \sum_{D\in\beth_{sm}(L)} {}_B X^D {}_D\mathrm{f}_{D,L} - \sum_{K\in\mathfrak{K}_{sm}} {}_B X^K {}_K\mathrm{f}_K^k \right) \tag{7.8}$$

$\mathfrak{K}_{sm}$ is the set of force-torque contacts estimated by the skin in a sub-model. This allows the robot to estimate multiple external contact forces correctly as long as most of the contacts happen in the areas covered by skin. This improves the scheme described in Section 2.4.3, where the estimation when multiple contacts happened in the same sub-model relies on assumptions that are often false.

The known force-torques are added to the estimated force-torques to obtain the joint torque as follows:

$$
\begin{aligned}
{}_F\mathrm{f}_{E,F} &= -\,{}_E\mathrm{f}_{F,E} && (7.9)\\
{}_F\mathrm{f}_{E,F} &= \sum_{L \in \gamma_E(F)} {}_F X^L \left({}_L\phi_L + {}_L\mathrm{f}_L^x + \sum_{K \in \mathfrak{K}_L} {}_L X^K \, {}_K\mathrm{f}_K^k \right), && (7.10)\\
{}_E\mathrm{f}_{F,E} &= \sum_{L \in \gamma_F(E)} {}_E X^L \left({}_L\phi_L + {}_L\mathrm{f}_L^x + \sum_{K \in \mathfrak{K}_L} {}_L X^K \, {}_K\mathrm{f}_K^k \right), && (7.11)
\end{aligned}
$$

where $\mathfrak{K}_L$ is the set of force-torque contacts estimated by the skin that belongs to a given link L.

Assumptions

- The inertial parameters of the robot are known.
- The position and orientation of the taxels are known and included in the model of the robot.
- The robot skin has been previously calibrated (up to 50 kPa) using vacuum bags, using the technique described in [66].

Experiments

For the experiments a set of calibration masses (0.2 kg, 0.5 kg, 1 kg and 2 kg) were used. The weights are positioned either directly on the right lower leg of the iCub or hanging from the leg with a cloth stripe as shown in Fig. 7.10.

During experiments, we focus on the right lower leg of the robot and more specifically in the knee joint. Regarding the joint torque estimation using the FT sensors, both sensors at the leg are involved. The skin patch in the right lower leg of the iCub, with 380 discrete sensors, was used for the estimation using the skin.

There were mainly two locations in which the weights were applied. When the calibration weights are placed on the right lower leg in a position close to the ankle, the distance from the knee is between 12 cm and 13 cm. On the other hand, when hanging from the lower leg near the knee, the distance is between 4 cm and 5 cm. The torques are estimated with respect to the frame of the joint in the knee. The external force-torques and joint torques obtained using the FT measurements are estimated using the methods described in Section 2.4. When using the skin, the external force-torques are estimated applying the interpolated technique to the skin measurements as described in Section 7.2. Then these values are included as known external force-torques into the extended estimation scheme described in Section 7.3.1. An example of

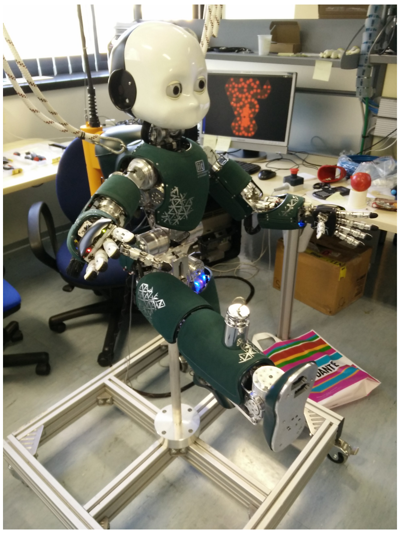

(a) Adding 1 kg mass on top of right lower leg

(b) Hanging 1 kg mass from right lower leg

(c) Set of calibration masses used in the experiments

Fig. 7.10 Positions and weights used in the experiments.

the skin being activated by the contact and its pressure field representation can be seen in Fig. 7.9.

In most of the experiments, the right leg was raised at 90^o. There were two sets of experiments. The first set was used to compare the results of force estimation using the skin with and without interpolation against a known force due to gravity. The second set of experiments was a comparison between the joint torque estimation of the FT sensor and the interpolated skin measurements .

In the set of force skin estimation experiments the weights where added one after the other starting from 0.5 kg up to 3 kg placing most of them on top of the right leg. As it can be appreciated in Fig. 7.11. Since the weights to reach 3 kg are different we had to take off previous weights and then add the 3 kg hanging from the leg, see Fig. 7.10.

In the set of joint torque experiments, the first experiment was to put 1 kg on top of the right leg (Fig. 7.12a). The next experiment consisted in increasing the load on the leg of the sensor to see the performance of sensor when the load varies (Fig. 7.12c) in an attempt to see the response of the scheme to a changing external force. Another experiment was intended to see the performance of the sensor near it's calibration limit, in this case, 3 kg made the skin go near the limit (Fig. 7.12b). And the last experiment was to verify the performance when the angle at which the load is applied changes. This was done by lowering the leg from 90^o to 75^o in intervals of 5^o, we observed that at 70^o the weight would start slipping and fall down (Fig. 7.12d).

Validation

For the validation of the forces, the calibrated masses were placed on top of the skin normal to the ground as shown in Fig. 7.10a. The forces applied by the masses were then compared to the forces estimated with and without using the interpolation method. For comparison, we use the magnitude of the contact forces calculated using equation (7.4).

The magnitude of the forces applied to the robot using the interpolated pressure field can be found with the following equation:

$$f_c = \int_{v1}^{v2} \int_{u1}^{u2} p(u,v) du dv \tag{7.12}$$

where f_c is the total contact force and $p(u,v)$ is the pressure value with respect to the location in the u-v plane.

The estimation without interpolation assumes that the pressure is uniform over the area of the sensor and all sensors are covering an equal area. This estimation method is referred from here forth as simple estimation. The magnitude of the forces using the simple estimation can be found with the following equation:

$$\|f_c\| = \|A \sum_{i=1}^{k} p_i \hat{n}_i\| \tag{7.13}$$

where $f_c \in \mathbb{R}^3$ is the total contact force, $p_i \in \mathbb{R}^+$ is the pressure of a particular sensor, $A \in \mathbb{R}^+$ is the area of the tactile sensor, $\hat{n}_i \in \mathbb{R}^3$ is the normal of the taxel and k is the total amount of taxels.

Table 7.1 Force results

	Forces N			Absolute Error N	
Masses	Ref.	Simple	Interpolated	Simple	Interpolated
0.5 kg*	4.905	4.6376	5.2482	.2674	.3432
1 kg	9.81	7.591	9.935	2.219	0.125
1 kg *	9.81	8.184	10.095	1.626	0.285
1.5 kg	14.715	11.606	14.142	3.109	0.573
1.7 kg	16.667	14.659	17.723	2.008	1.056
1.9 kg	18.639	15.528	19.054	3.111	0.415
3 kg	29.43	22.555	27.697	6.875	1.733

*the mass is on top off the right lower leg

For the torque, finding the exact location of the contact is required for a ground truth. This location is estimated from the taxels that are activated by the contact in both joint torque estimations. In this case, we will consider proximity to the torques estimated with the FT sensor as the validation, since these values currently allow the iCub robot to perform dynamic movements such as balancing [92].

Contact Force Estimation Results

The magnitude of the forces using the interpolated estimation (red), given by the magnitude of Eq.(7.4), is compared to the magnitude of the forces using the simple estimation (blue), given by Eq.(7.13). The green line displays the reference force applied on the skin during the experiment. After every five or six samples, the program was stopped in order to change the weights applied on the skin.

It can be observed in Table 7.1, that the simple estimation underestimates the total force applied. This is due to the fact that some of the force is applied in the areas between the sensors that we cannot measure explicitly. However, interpolation of the pressure field allows us to improve the estimation as can be seen from the graph on Fig. 7.11.

When the pressure on the taxels comes close to the 50 kPa (limit of the calibration) the performance dropped, as seen when using the 3 kg mass. This can be avoided by distributing the forces over a bigger set of taxels. This allows to correctly estimate cases where it otherwise would not be possible using the interpolated skin estimation.

From Table 7.1, it can be seen that the simple method has a mean error of 2.7450 N and 2.0567 N if we avoid the calibration limit. Comparatively, the mean error of the interpolation estimation is 0.6477 N and 0.4662 N respectively. This means that the interpolation method is 4 times better than the simple method.

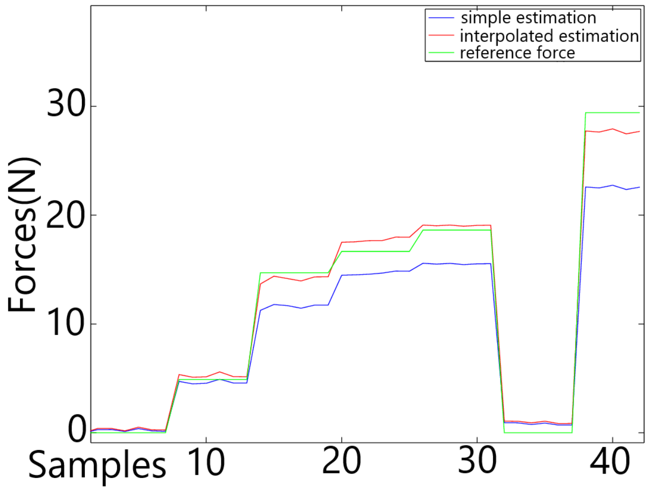

Fig. 7.11 Force comparison between reference force, interpolated estimation and simple estimation.

Table 7.2 Joint torques results

	Joint torques Nm		Std		.
Masses	FT	Interpolated	FT	Interpolated	RMSE
1 kg	4.4184	4.2667	0.0189	0.0207	0.1529
1 kg *	4.7511	4.7666	0.0300	0.0216	0.0356
1.5 kg	4.4908	4.3211	0.0078	0.0117	0.1703
1.7 kg	4.5038	4.3463	0.0077	0.0135	0.1582
1.9 kg	4.5212	4.3578	0.0071	0.0233	0.1653
3 kg	4.3868	4.4806	0.0423	0.0451	0.0964

*the mass is on top off the right lower leg

Joint torque results

The root mean square error (RMSE) between the estimated torques is 0.1298 Nm on average, as it can be verified in Fig. 7.12c . It can be observed from the first experiment (Fig. 7.12a), that when the motors are not so hot the skin estimation is at its best with a RMSE of 0.0356 Nm, but after some time the estimation performance decreases due to temperature drift, as can be seen from the rest of the RMSE values in Table 7.2.

When interacting with the environment, is likely the contacts do not have a constant force due to the movement either of the robot or the object in contact. Fig. 7.12c demonstrates how the estimation would respond to slight variations of the contact forces. It can be observed that it follows the same behavior as the FT sensor.

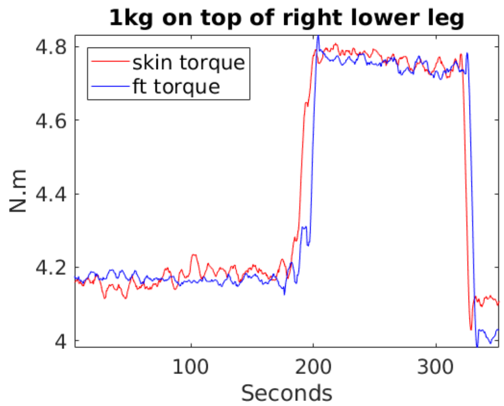

(a) Adding 1 kg mass on top of right lower leg

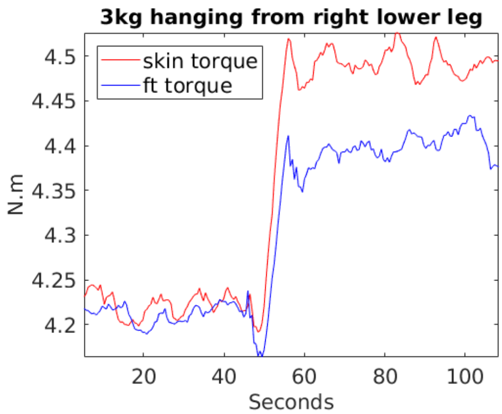

(b) Hanging 3 kg mass from right lower leg

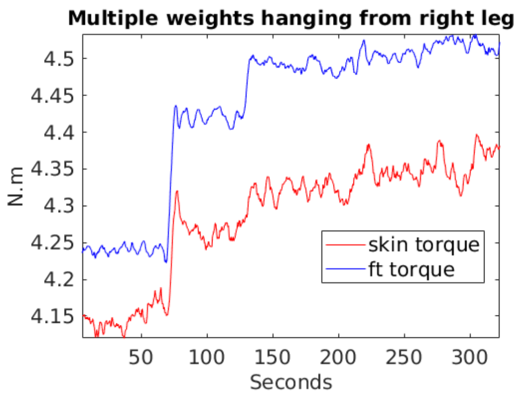

(c) Hanging 1 kg, 1.5 kg, 1.7 kg, 1.9 kg consecutively

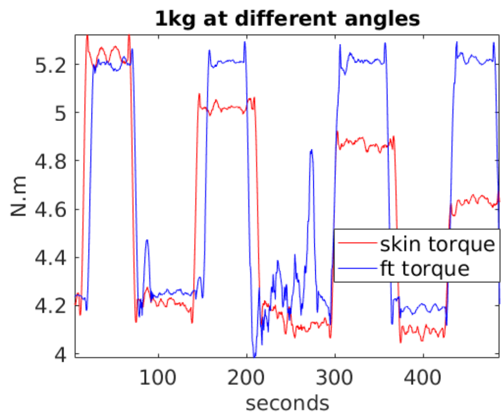

(d) Adding 1 kg with the angles: 90, 85, 80, 75

Fig. 7.12 Joint torque estimation results comparing force-torque sensor and skin at the knee pitch joint.

Considering the FT sensors have been effectively used as joint torque feedback for the current controller [106], these results allow us to consider the joint torques estimated with the skin as a viable candidate to replace the FT measurements. Although verification might be needed, since the joint torque estimation with skin has a higher oscillation in some cases, as can be seen from the standard deviation in Table 7.2 and Fig. 7.12.

Is important to consider that the skin measures only normal forces and this effect can be showcased in Fig. 7.12d and Table 7.3. Where the performance of the joint torques estimated with the skin drop due to the angle with which the external force is applied.

Table 7.3 Joint torque comparison at different contact angles

Degree	FT sensor	Interpolated	avg difference	RMSE
90^o	5.204	5.234	0.07	0.129
85^o	5.205	5.021	0.225	0.265
80^o	5.188	4.886	0.304	0.319
75^o	5.204	4.627	0.539	0.558

7.4 Conclusions

The estimation of contact forces using the interpolation is 4 times better than the estimation without interpolation. This allows us to consider the estimated external forces using the skin as a possible source of force-torque measurements.

Given the performance of the joint torque estimation, it could be considered as feedback for the low-level torque controller described in Section 5.6.

While the experiments show results comparable to the FT sensors, using the iCub skin has the following limitations:

- It is not possible to measure the shear forces, but only normal forces at the contact.
- Unable to detect pure torques or forces aligned with the surface of contact.
- The pressure in any given taxel should not exceed the max pressure used in the calibration.
- The temperature drift is higher than the one of the FT sensor.

This limitations from the skin prevent from using the skin as a reliable force-torque sensor in many scenarios in which we would need a force-torque measurement.

Some of the limitations can be solved by fusing the information with the force-torque sensors. The crucial limitation is the temperature since, after a short time it has been in contact with an object with a considerable different temperature, the measurements become unreliable. Even the temperature of the human body is enough to make the capacitance values to change noticeably. This is especially troublesome since the skin has great potential for the area of physical human-robot interaction. The temperature drift is an issue that must be solved to improve the reliability of the skin as a force-torque sensor over time.

Using the skin as a FT sensor allowed to develop estimation algorithms for contact locations, external forces and joint torques using only skin, joint encoders, and a single IMU. This approach has the advantages to be easy to integrate on the robot (compared to modifying the inner structure of the robot to include other sensors) and to be cheaper compared to other solutions such as FT sensors or joint torque sensors.

To the best of our knowledge, this is the first time the problem of detecting contact locations, estimate contact forces and estimate joint torques has been effectively solved relying only upon a whole body distributed tactile sensor, joint encoders, a single IMU and the robot model.

It allows estimating external forces when more than one external force is acting on each sub-model, which was a limitation of the previous estimation scheme.

Next is the final chapter where a recap of the thesis is presented.

Chapter 8

Summary

In this Chapter, a summary of the thesis can be found. First, the results are confronted with the objectives to see if they were full filled. Then, some conclusions on force-torque sensing are shared. Finally, the ideas for future work are mentioned.

8.1 Recap on Objectives

In this section, a comparison between the work done and the objectives is presented.

8.1.1 Deep understanding of force-torque (FT) sensors

By studying the technologies available for force sensing, it was possible to understand why the silicon strain gauge is the main technology used for force sensing. It was possible to justify the linear model assumption looking at the piezoresistive behavior of this technology.
Looking at how force-torque sensing is used in robotics gave a good perspective of the expectation of this kind of sensors. Allowing to evaluate the impact of improving their measurements and the direction to take to achieve this.
Revising the methods for calibration of sensors in general permitted to broaden the view of how to choose the appropriate function based on the principles of the sensing element.
The need for multiple linear regression for silicon based six axis FT sensors and a polynomial function for capacitive tactile arrays became evident.
Designing evaluation tools targeting the performance of sensors already mounted in the robot was crucial for understanding the sources of error of six axis FT sensors. It also permitted to further understand the sensors by providing easy and intuitive ways to evaluate the performance. By understanding the sources of unreliability of the sensors, it was possible to address effectively the improvement of performance of the sensors.

8.1.2 Improvement of force-torque sensors' performance

The main source of improvement presented is the use of *in situ* calibration methods. More specifically the Model Based *In Situ* Calibration method. Which was created and refined during the whole PhD. Since the improvement is tailored to the use of the robot, the benefits are guaranteed to impact positively the performance of the robot.
The developed method has the advantage of including other variables as long as their behavior can be considered almost linear. To the best of my knowledge, this is the only *in situ* method able to effectively cope with other phenomena that might affect the measurements of the sensor. Tests suggest that through the use of this method the offset can be considered constant and be estimated. This eliminates the need for re-estimating the offset of the robot every time an experiment is scheduled. An analysis of the kind of excitation required for the sensor's calibration is shown. Insights on how to use this method depending on the amount and type of data available are provided.
Another way to improve the performance of the force-torque sensors is by reducing the error in the *ex situ* calibration procedure. To this aim, a calibration device aimed to be fast, repeatable and reduce chances of human error was envisioned. The excitation is proven to be better than the currently used in the IIT-produced six axis FT sensors and quite comprehensive in general. In the final stage of the design, it will be able to account for temperature and the dynamic response of the sensors as well.
The skin shows promising potential as a force-torque sensor. It can be successfully used to estimate multiple contact forces individually. This might enable more complex response algorithms for floating base robots. Unfortunately, it suffers from a fast drift that prevents its extended use. It might also be limited in the sensing range, but knowing the technology is possible to find a solution either by changing the dielectric material, the signal conditioning or improving the calibration procedure.

8.1.3 Increase performance of dynamical motions in floating base robots through the use of force-torque sensing

Improvements in the performance of dynamical motions were observed after providing the improved FT measurements to the robot. Improvements in the contact force estimation were visible through the tests of the offset when switching contacts. The improved measurements allowed the robot to walk after the calibration of the sensors was applied. The benefits of the improved measurements have a direct impact on the performance of the low-level controller and a bit indirect in the balancing controller. Nonetheless, smoother transitions between states were observed after the *in situ* calibration. In general, it allows to trust the force-torque sensing information which results in better feedback information for the controllers. It enables the possibility to use this information directly in high-level controllers.

8.2 Conclusions

The expected excitation of the sensors mounted in a floating base robot are different from fixed based robots where FT sensors have been mostly used. So these sensors might be able to perform better in dynamic scenarios by adapting their behavior to the expected use in floating base robots. An example is that sensors typically have a symmetrical full scale, but their excitation will rarely reach both sides of the scale. A simple case is the sensors at the foot position, they might experience almost all the weight of the robot in one direction, but unless they are hanging from the same foot must likely the excitation in the other direction will be much smaller.
Given the technology employed in the sensors used during the PhD, the multiple linear regression is an appropriate approximation function to calibrate them.
The main causes of unreliability are the change of behavior after mounting, silicon dependency on temperature and saturation. All three can be addressed by employing *in situ* calibration techniques. Saturation can be dealt by adjusting the range of the sensor to the actual use of the robot. Change in behavior and temperature dependency can be addressed by the proposed Model Based *In Situ* Calibration method. This method also deals with the offset variability. The success of using the offsets estimated during calibration proves that the main source of drift in the sensors is the temperature. This should increase the reliability of the sensors in long periods of time.
The developed *In Situ* Method proposed different estimation types. Each can be exploited based on amount and type of available data.
There are clear benefits of calibrating *in situ*, as seen from the change in the performance of the robot after applying the calibration matrices estimated *in situ*.
It is possible to generate a comprehensive excitation of the six axis FT sensors with three degrees of freedom. Is enough to have two actuated degrees of freedom and one degree of freedom with just two configurations. Calibration procedures should aim to reduce the possible sources of error while increasing repeatability and reducing the complexity of use. This is possible with the design of iCalibrate.
A benchmark for calibration of six axis FT sensors could be created using the proposed calibration device. This may allow for easy comparison of different calibration algorithms and models as well as evaluate and compare the performance of different sensors.

The skin shows potential to correctly identify multiple contacts on the same sub-model. Even in the absence of other force-torque sensing sensors. The problem of drift is the major issue preventing reliable use of the skin as force-torque sensor.

8.3 Future Work

It is worth exploring other types of models and algorithms for the six axis FT sensors. There might be complementary models to the linear part to account for the small non-linearities of the silicon strain gauges. Other possible sources of non-linearities to consider are complex loading scenarios coupled with temperature variation.
A useful problem to solve is the calculation of a full scale that is more coherent with how the sensor works and will be excited. This implies a different way to estimate the full scale of the sensor. On the same line the possibility of having an asymmetrical full scale could help further adapt the sensor to comply with the real excitation they are subjected in floating base robots.
Performing temperature compensation on the skin may allow using the skin as a force-torque sensor over extended periods of time. Temperature compensation models for the capacitance should be studied. Explore solutions that allow measuring shear forces to complement the shortcomings of the skin.
We shall look for other ways to improve the estimation of force-torque related quantities. The information of the FT sensors, the skin and possibly the motor current could be fused to improve the estimation of external force-torques and joint torques, beyond the existing current results.
Make use of the acquired knowledge with force-torque sensor technologies in the development of wearable sensors and the study of dynamics in human subjects should be feasible.
Finish the design and building a prototype of the iCalibrate is a must. Since it can later be used as a benchmark for different calibration algorithms. This way a more accurate method for calibration can be found and compared to the current approach. It is also interesting the possibility to perform reliable dynamic calibration of the sensor even in complex loading scenarios. This should allow to adapt the calibration procedure to the expected use and environmental conditions of floating base robots. This is something currently lacking and might be holding back to the reliability of dynamic behaviors in floating base robots. It may also allow for the accelerated testing of FT sensor prototypes and help design improved sensors.
Finding a more objective way to evaluate the performance of dynamic motions in floating base robots can allow for a clearer idea of the improvements of FT measurements. This could also lead to the development of high-level controllers that can fully exploit the feedback from force-torque sensors in complex scenarios. Allow floating base robots to exploit the generation,

use and breaking of contacts through the development of such high-level controllers is alluring as well.

References

[1] Aghili, F., Buehler, M., and Hollerbach, J. (2001). Motion control systems with /sup \infty / positive joint torque feedback. *IEEE Transactions on Control Systems Technology*, 9(5):685–695.

[2] Al-Mai, O., Ahmadi, M., and Albert, J. (2018a). Design, Development and Calibration of a Lightweight, Compliant Six-Axis Optical Force/Torque Sensor. *IEEE Sensors Journal*, 18(17):7005–7014.

[3] Al-Mai, O., Ahmadi, M., and Albert, J. (2018b). Design, Development and Calibration of a Lightweight, Compliant Six-Axis Optical Force/Torque Sensor. *IEEE Sensors Journal*, 18(17):7005–7014.

[4] Alam, H., Soetraprawata, D., and Bahrudin (2015). The Structural Design of Six-Axis Force/Torque Sensor Using Virtual Prototyping Technique. *Journal of Scientific Research and Reports*, 5(2):120–131.

[5] Andersen, B. and Pettersen, P.-G. (1996). *The benchmarking handbook : step-by-step instructions*. Chapman & Hall.

[6] Andrade Chavez, F. J., Kangro, J., Traversaro, S., Nori, F., and Pucci, D. (2018). Contact Force and Joint Torque Estimation Using Skin. *IEEE Robotics and Automation Letters*, 3(4):3900–3907.

[7] Andrade Chavez, F. J., Nava, G., Traversaro, S., Nori, F., and Pucci, D. (2019). Model Based In Situ Calibration with Temperature compensation of 6 axis Force Torque Sensors. *Proceedings 2019 IEEE International Conference on Robotics and Automation*.

[8] Andrade Chavez, F. J., Traversaro, S., Pucci, D., and Nori, F. (2016). Model based in situ calibration of six axis force torque sensors. In *2016 IEEE-RAS 16th International Conference on Humanoid Robots (Humanoids)*, pages 422–427. IEEE.

[9] Asfour, T., Regenstein, K., Azad, P., Schroder, J., Bierbaum, A., Vahrenkamp, N., and Dillmann, R. (2006). ARMAR-III: An Integrated Humanoid Platform for Sensory-Motor Control. In *2006 6th IEEE-RAS International Conference on Humanoid Robots*, pages 169–175. IEEE.

[10] Atkeson, C. G., Babu, B. P. W., Banerjee, N., Berenson, D., Bove, C. P., Cui, X., DeDonato, M., Du, R., Feng, S., Franklin, P., Gennert, M., Graff, J. P., He, P., Jaeger, A., Kim, J., Knoedler, K., Li, L., Liu, C., Long, X., Padir, T., Polido, F., Tighe, G. G., and Xinjilefu, X. (2015). No falls, no resets: Reliable humanoid behavior in the DARPA robotics challenge.

In *2015 IEEE-RAS 15th International Conference on Humanoid Robots (Humanoids)*, pages 623–630. IEEE.

[11] Automation, A. T. I. I. (2014). Six-Axis Force/Torque Transducer Installation and Operation Manual.

[12] Bartolozzi, C., Natale, L., Nori, F., and Metta, G. (2016). Robots with a sense of touch. *Nature Materials*, 15(9):921–925.

[13] Benallegue, M., Gergondet, P., Audrerr, H., Mifsud, A., Morisawa, M., Lamiraux, F., Kheddar, A., and Kanehiro, F. (2018). Model-based external force/moment estimation for humanoid robots with no torque measurement. In *2018 IEEE International Conference on Robotics and Automation (ICRA)*, pages 3122–3129. IEEE.

[14] Bicchi, A., Caiti, A., and Prattichizzo, D. (2002). Dynamic force/torque sensors: theory and experiments. In *1997 8th International Conference on Advanced Robotics. Proceedings. ICAR'97*, number August, pages 727–732. IEEE.

[15] Bicchi, A., Salisbury, J. K., and Brock, D. L. (2007). Contact Sensing from Force Measurements. *The International Journal of Robotics Research*, 12(3):249–262.

[16] Bilz, J., Allevato, G., Butz, J., Schafer, N., Hatzfeld, C., Matich, S., and Schlaak, H. F. (2017). Analysis of the measuring uncertainty of a calibration setup for a 6-DOF force/torque sensor. In *2017 IEEE SENSORS*, pages 1–3.

[17] Bolotnikova, A., Courtois, S., and Kheddar, A. (2018). Contact Observer for Humanoid Robot Pepper based on Tracking Joint Position Discrepancies. In *2018 27th IEEE International Symposium on Robot and Human Interactive Communication (RO-MAN)*, pages 29–34. IEEE.

[18] Bolotnikoval, A., Courtois, S., and Kheddar, A. (2018). Compliant Robot Motion Regulated via Proprioceptive Sensor Based Contact Observer. In *2018 IEEE-RAS 18th International Conference on Humanoid Robots (Humanoids)*, pages 1–9. IEEE.

[19] Braun, D. and Wörn, H. (2011). Techniques for Robotic Force Sensor Calibration. In *13th International Workshop on Computer Science and Information Technologies (CSIT 2011)*.

[20] Callister, W. D. (2007). *Materials science and engineering-an introduction*. John wiley & sons.

[21] Cannata, G., Maggiali, M., Metta, G., and Sandini, G. (2008). An embedded artificial skin for humanoid robots. *2008 IEEE International Conference on Multisensor Fusion and Integration for Intelligent Systems*, pages 434–438.

[22] Chiaverini, S., Siciliano, B., and Villani, L. (1999). A survey of robot interaction control schemes with experimental comparison. *IEEE/ASME Transactions on Mechatronics*, 4(3):273–285.

[23] Ciliberto, C., Fiorio, L., Maggiali, M., Natale, L., Rosasco, L., Metta, G., Sandini, G., and Nori, F. (2014). Exploiting global force torque measurements for local compliance estimation in tactile arrays. In *2014 IEEE/RSJ International Conference on Intelligent Robots and Systems*, pages 3994–3999. IEEE.

[24] Csáji, B. C. (2001). Approximation with artificial neural networks. *Faculty of Sciences, Etvs Lornd University, Hungary*, 24:48.

[25] Cursi, F., Malzahn, J., Tsagarakis, N., and Caldwell, D. (2017). An online interactive method for guided calibration of multi-dimensional force/torque transducers. In *2017 IEEE-RAS 17th International Conference on Humanoid Robotics (Humanoids)*, pages 398–405.

[26] DeDonato, M., Dimitrov, V., Du, R., Giovacchini, R., Knoedler, K., Long, X., Polido, F., Gennert, M. A., Padır, T., Feng, S., Moriguchi, H., Whitman, E., Xinjilefu, X., and Atkeson, C. G. (2015). Human-in-the-loop Control of a Humanoid Robot for Disaster Response: A Report from the DARPA Robotics Challenge Trials. *Journal of Field Robotics*, 32(2):275–292.

[27] DeDonato, M., Polido, F., Knoedler, K., Babu, B. P. W., Banerjee, N., Bove, C. P., Cui, X., Du, R., Franklin, P., Graff, J. P., He, P., Jaeger, A., Li, L., Berenson, D., Gennert, M. A., Feng, S., Liu, C., Xinjilefu, X., Kim, J., Atkeson, C. G., Long, X., and Padır, T. (2017). Team WPI-CMU: Achieving Reliable Humanoid Behavior in the DARPA Robotics Challenge. *Journal of Field Robotics*, 34(2):381–399.

[28] Del Prete, A., Denei, S., Natale, L., Mastrogiovanni, F., Nori, F., Cannata, G., and Metta, G. (2011). Skin spatial calibration using force/torque measurements. In *2011 IEEE/RSJ International Conference on Intelligent Robots and Systems*, pages 3694–3700. IEEE.

[29] Del Prete, A., Mansard, N., Ramos, O. E., Stasse, O., and Nori, F. (2016). Implementing torque control with high-ratio gear boxes and without joint-torque sensors. *International Journal of Humanoid Robotics*, 13(01):1550044.

[30] Del Prete, A., Natale, L., Nori, F., and Metta, G. (2012). Contact force estimations using tactile sensors and force/torque sensors. *Human Robot Interaction*, 2012:0–2.

[31] Doebelin, E. O. (2007). *Measurement Systems Application and Design*, chapter Chapter 5, pages 446–480. Mc Graw Hill.

[32] DRC-Teams (2015). What Happened at the {DARPA Robotics Challenge?}. www.cs.cmu.edu/˜cga/drc/events.

[33] Eljaik, J., Kuppuswamy, N., and Nori, F. (2015). Multimodal sensor fusion for foot state estimation in bipedal robots using the Extended Kalman Filter. In *Intelligent Robots and Systems (IROS), 2015 IEEE/RSJ International Conference on*, pages 2698–2704.

[34] Englsberger, J., Werner, A., Ott, C., Henze, B., Roa, M. A., Garofalo, G., Burger, R., Beyer, A., Eiberger, O., Schmid, K., and Others (2014). Overview of the torque-controlled humanoid robot TORO. In *2014 IEEE-RAS International Conference on Humanoid Robots*, pages 916–923. IEEE.

[35] Everett, L. B. and Perry, D. (2017). Force/torque sensor having instrumentation on fewer than four beam surfaces.

[36] Faber, G. S., Chang, C.-C., Kingma, I., Martin Schepers, H., Herber, S., Veltink, P. H., and Dennerlein, J. T. (2012). A force plate based method for the calibration of force/torque sensors. *Journal of biomechanics*, 45(7):1332–1338.

[37] Featherstone, R. (2008). *Rigid Body Dynamics Algorithms*. Springer.

[38] Felip, J., Morales, A., and Asfour, T. (2014). Multi-sensor and prediction fusion for contact detection and localization. In *2014 IEEE-RAS International Conference on Humanoid Robots*, pages 601–607. IEEE.

[39] Ferraresi, C., Pastorelli, S., and Zhmud', M. S. N. (1995). State and dynamic behavior of a high stiffness stewart platform-based force/torque sensor. *Journal of Robotic Systems*, 12(12):883–893.

[40] Flacco, F. and Kheddar, A. (2017). Contact detection and physical interaction for low cost personal robots. In *2017 26th IEEE International Symposium on Robot and Human Interactive Communication (RO-MAN)*, pages 495–501. IEEE.

[41] Fraden, J. (2016a). Detectors of Humans. In *Handbook of Modern Sensors*, pages 271–333. Springer International Publishing, Cham.

[42] Fraden, J. (2016b). Force and Strain. In *Handbook of Modern Sensors*, pages 413–428. Springer International Publishing, Cham.

[43] Fraden, J. (2016c). *Handbook of modern sensors : physics, designs, and applications.*

[44] Fumagalli, M., Ivaldi, S., Randazzo, M., Natale, L., Metta, G., Sandini, G., and Nori, F. (2012). Force feedback exploiting tactile and proximal force/torque sensing. *Autonomous Robots*, 33(4):381–398.

[45] Fumagalli, M., Randazzo, M., Nori, F., Natale, L., Metta, G., and Sandini, G. (2010). Exploiting proximal F/T measurements for the iCub active compliance. In *Intelligent Robots and Systems (IROS), 2010 IEEE/RSJ International Conference on*, pages 1870–1876.

[46] Girão, P. S., Ramos, P. M. P., Postolache, O., and Pereira, J. M. D. (2013). Tactile sensors for robotic applications. *Measurement*, 46(3):1257–1271.

[47] Göger, D., Alagi, H., and Wörn, H. (2013). Tactile proximity sensors for robotic applications. In *2013 IEEE International Conference on Industrial Technology (ICIT)*, pages 978–983.

[48] Gorinevsky, D. M., Formalsky, A. M. A. M., and Schneider, A. I. (1997). *Force control of robotics systems*. CRC Press.

[49] Guangjun Liu, Iagnemma, K., Dubowsky, S., and Morel, G. (1998). A base force/torque sensor approach to robot manipulator inertial parameter estimation. In *Proceedings. 1998 IEEE International Conference on Robotics and Automation (Cat. No.98CH36146)*, volume 4, pages 3316–3321. IEEE.

[50] Guggenheim, J. W., Jentoft, L. P., Tenzer, Y., and Howe, R. D. (2017). Robust and Inexpensive Six-Axis Force–Torque Sensors Using MEMS Barometers. *IEEE/ASME Transactions on Mechatronics*, 22(2):838–844.

[51] Haddadin, S., De Luca, A., and Albu-Schaffer, A. (2017). Robot Collisions: A Survey on Detection, Isolation, and Identification. *IEEE Transactions on Robotics*, 33(6):1292–1312.

[52] Hashlamon, I. and Erbatur, K. (2013). Ground reaction force sensor fault detection and recovery method based on virtual force sensor for walking biped robots. In *2013 9th Asian Control Conference (ASCC)*, pages 1–6. IEEE.

[53] Haslinger, R., Leyendecker, P., and Seibold, U. (2013). A fiberoptic force-torque-sensor for minimally invasive robotic surgery. In *2013 IEEE International Conference on Robotics and Automation*, pages 4390–4395. IEEE.

[54] Helmick, D., Okon, A., and DiCicco, M. (2006). A comparison of force sensing techniques for planetary manipulation. In *Aerospace Conference, 2006 IEEE*, pages 14—-pp. IEEE.

[55] Hirai, K., Hirose, M., Haikawa, Y., and Takenaka, T. (1998). The development of Honda humanoid robot. In *Proceedings. 1998 IEEE International Conference on Robotics and Automation (Cat. No.98CH36146)*, volume 2, pages 1321–1326. IEEE.

[56] HIROSE, S. and YONEDA, K. (1990). Development of optical 6-axial force sensor and its non-linear calibration. *Journal of the Robotics Society of Japan*, 8(5):523–532.

[57] Hoffmann, K. (1974). *Applying the wheatstone bridge circuit*. HBM Germany.

[58] Iten, R., Metger, T., Wilming, H., del Rio, L., and Renner, R. (2018). Discovering physical concepts with neural networks.

[59] Jaeheung Park and Khatib, O. (2005). Multi-Link Multi-Contact Force Control for Manipulators. In *Proceedings of the 2005 IEEE International Conference on Robotics and Automation*, number April, pages 3613–3618. IEEE.

[60] Johnson, M., Shrewsbury, B., Bertrand, S., Wu, T., Duran, D., Floyd, M., Abeles, P., Stephen, D., Mertins, N., Lesman, A., Carff, J., Rifenburgh, W., Kaveti, P., Straatman, W., Smith, J., Griffioen, M., Layton, B., de Boer, T., Koolen, T., Neuhaus, P., and Pratt, J. (2015). Team IHMC's Lessons Learned from the DARPA Robotics Challenge Trials. *Journal of Field Robotics*, 32(2):192–208.

[61] Kane, B., Cutkosky, M., and Kovacs, G. (2000). A traction stress sensor array for use in high-resolution robotic tactile imaging. *Journal of Microelectromechanical Systems*, 9(4):425–434.

[62] Kaneko, K., Kanehiro, F., Kajita, S., Hirukawa, H., Kawasaki, T., Hirata, M., Akachi, K., and Isozumi, T. (2004). Humanoid robot HRP-2. In *Proceedings - IEEE International Conference on Robotics and Automation*, volume 2, pages 1083 – 1090 Vol.2.

[63] Kaneko, K., Kanehiro, F., Morisawa, M., Akachi, K., Miyamori, G., Hayashi, A., and Kanehira, N. (2011). Humanoid robot hrp-4-humanoid robotics platform with lightweight and slim body. In *Intelligent Robots and Systems (IROS), 2011 IEEE/RSJ International Conference on*, pages 4400–4407. IEEE.

[64] Kang, C. (2005). Performance improvement of a 6-axis force-torque sensor via novel electronics and cross-shaped double-hole structure. *International Journal of Control Automation and Systems*, 3(3):469.

[65] Kangro, J., Sureshbabu, A. V., Traversaro, S., Pucci, D., and Nori, F. (2018). A Plenum-Based Calibration Device for Tactile Sensor Arrays. *IEEE Robotics and Automation Letters*, 3(4):3937–3943.

[66] Kangro, J., Traversaro, S., Pucci, D., and Nori, F. (2017). Skin normal force calibration using vacuum bags. In *2017 IEEE International Conference on Robotics and Automation (ICRA)*, pages 401–406.

[67] Katsura, S., Matsumoto, Y., and Ohnishi, K. (2007). Modeling of Force Sensing and Validation of Disturbance Observer for Force Control. *IEEE Transactions on Industrial Electronics*, 54(1):530–538.

[68] Kheddar, A. and Billard, A. (2011). A tactile matrix for whole-body humanoid haptic sensing and safe interaction. In *2011 IEEE International Conference on Robotics and Biomimetics*, pages 1433–1438. IEEE.

[69] Kim, D., Lee, C. H., Kim, B. C., Lee, D. H., Lee, H. S., Nguyen, C. T., Kim, U. K., Nguyen, T. D., Moon, H., Koo, J. C., Nam, J.-d., and Choi, H. R. (2013). Six-axis capacitive force/torque sensor based on dielectric elastomer. *Proceedings of SPIE - The International Society for Optical Engineering*, page 86872J.

[70] Kim, U., Lee, D.-H., Kim, Y. B., Seok, D.-Y., and Choi, H. R. (2017). A Novel Six-Axis Force/Torque Sensor for Robotic Applications. *IEEE/ASME Transactions on Mechatronics*, 22(3):1381–1391.

[71] Kistler (2018). Calibration Brochure.

[72] Koenemann, J., Del Prete, A., Tassa, Y., Todorov, E., Stasse, O., Bennewitz, M., and Mansard, N. (2015). Whole-body model-predictive control applied to the HRP-2 humanoid. In *2015 IEEE/RSJ International Conference on Intelligent Robots and Systems (IROS)*, pages 3346–3351.

[73] Koiva, R., Zenker, M., Schurmann, C., Haschke, R., and Ritter, H. J. (2013). A highly sensitive 3D-shaped tactile sensor. In *2013 IEEE/ASME International Conference on Advanced Intelligent Mechatronics*, pages 1084–1089. IEEE.

[74] Kosuge, K., Takeuchi, H., and Furuta, K. (1988). Motion control of a robot arm using joint torque sensors. In *Proceedings of the 27th IEEE Conference on Decision and Control*, pages 610–615. IEEE.

[75] Kutner, M. H., Nachtsheim, C., and Neter, J. (2004). *Applied linear regression models*. McGraw-Hill/Irwin.

[76] Lee, D.-H., Kim, U., Jung, H., and Choi, H. R. (2016). A Capacitive-Type Novel Six-Axis Force/Torque Sensor for Robotic Applications. *IEEE Sensors Journal*, 16(8):2290–2299.

[77] Lee, J., Ajoudani, A., Hoffman, E. M., Rocchi, A., Settimi, A., Ferrati, M., Bicchi, A., Tsagarakis, N. G., and Caldwell, D. G. (2014). Upper-body impedance control with variable stiffness for a door opening task. In *2014 IEEE-RAS International Conference on Humanoid Robots*, pages 713–719. IEEE, IEEE.

[78] Li, Y. and Chen, X. (1998). On the dynamic behavior of a force/torque sensor for robots. *IEEE Transactions on Instrumentation and Measurement*, 47(1):304–308.

[79] Liang, Q., Zhang, D., Song, Q., Ge, Y., Cao, H., and Ge, Y. (2010). Design and fabrication of a six-dimensional wrist force/torque sensor based on E-type membranes compared to cross beams. *Measurement*, 43(10):1702–1719.

[80] Liu, G., Abdul, S., and Goldenberg, A. A. (2006). Distributed Modular and Reconfigurable Robot Control with Torque Sensing. In *2006 International Conference on Mechatronics and Automation*, pages 384–389.

[81] Luca, A., Albu-Schaffer, A., Haddadin, S., and Hirzinger, G. (2006). Collision Detection and Safe Reaction with the DLR-III Lightweight Manipulator Arm. In *2006 IEEE/RSJ International Conference on Intelligent Robots and Systems*, pages 1623–1630. IEEE.

[82] Lucarotti, C., Oddo, C. M., Vitiello, N., and Carrozza, M. C. (2013). Synthetic and bio-artificial tactile sensing: A review. *Sensors*, 13(2):1435–1466.

[83] Luh, J., Fisher, W., and Paul, R. (1983). Joint torque control by a direct feedback for industrial robots. *IEEE Transactions on Automatic Control*, 28(2):153–161.

[84] Magrini, E., Flacco, F., and De Luca, A. (2014). Estimation of contact forces using a virtual force sensor. In *2014 IEEE/RSJ International Conference on Intelligent Robots and Systems*, pages 2126–2133. IEEE.

[85] Maiolino, P., Maggiali, M., Cannata, G., Metta, G., and Natale, L. (2013a). A Flexible and Robust Large Scale Capacitive Tactile Sensor for Robots. *IEEE Sensors Journal*, 13(10):3910–3917.

[86] Maiolino, P., Maggiali, M., Cannata, G., Metta, G., and Natale, L. (2013b). A Flexible and Robust Large Scale Capacitive Tactile System for Robots. *IEEE Sensors Journal*, 13(10):3910–3917.

[87] Manuelli, L. and Tedrake, R. (2016). Localizing external contact using proprioceptive sensors: The Contact Particle Filter. In *2016 IEEE/RSJ International Conference on Intelligent Robots and Systems (IROS)*, pages 5062–5069. IEEE.

[88] Marsden, J. E. and Ratiu, T. S. (1999). *Introduction to mechanics and symmetry : a basic exposition of classical mechanical systems*. Springer.

[89] Mattioli, T. and Vendittelli, M. (2017). Interaction force reconstruction for humanoid robots. *IEEE Robotics and Automation Letters*, 2(1):282–289.

[90] Moreira, E., Rocha, L. F., Pinto, A. M., Moreira, A. P., and Veiga, G. (2016). Assessment of Robotic Picking Operations Using a 6 Axis Force/Torque Sensor. *IEEE Robotics and Automation Letters*, 1(2):768–775.

[91] Natale, L., Bartolozzi, C., Pucci, D., Wykowska, A., and Metta, G. (2017). iCub: The not-yet-finished story of building a robot child. *Science Robotics*, 2(13).

[92] Nava, G., Romano, F., Nori, F., and Pucci, D. (2016). Stability analysis and design of momentum-based controllers for humanoid robots. In *2016 IEEE/RSJ International Conference on Intelligent Robots and Systems (IROS)*, pages 680–687.

[Octave Authors] Octave Authors. Griddata.

[94] Oddo, C. M., Valdastri, P., Beccai, L., Roccella, S., Carrozza, M. C., and Dario, P. (2007). Investigation on calibration methods for multi-axis, linear and redundant force sensors. *Measurement Science and Technology*, 18(3):623.

[95] Oh, H. S., Kang, G., Kim, U., Seo, J. K., and Choi, H. R. (2017). Calibration of 6 axis force/torque sensor by using deep-learning method. In *2017 13th IEEE Conference on Automation Science and Engineering (CASE)*, pages 1316–1317.

[96] Oh, H. S., Kim, U., Kang, G., Seo, J. K., and Choi, H. R. (2018). Multi-Axial Force/Torque Sensor Calibration Method Based on Deep-Learning. *IEEE Sensors Journal*, 18(13):5485–5496.

[97] Ohsato, T. and Hirabayashi, Y. (2003). Six-axis force sensor.

[98] Okumura, D., Sakaino, S., and Tsuji, T. (2018). High Dynamic Range Sensing by a Multistage Six-Axis Force Sensor with Stopper Mechanism. In *2018 IEEE International Conference on Robotics and Automation (ICRA)*, pages 1–6. IEEE.

[99] OMEGA (1998). *TRANSACTIONS IN MEASUREMENT AND CONTROL VOLUME 3, FORCE-RELATED MEASUREMENTS*. Putman Publishing Company and OMEGA Press LLC.

[100] O'Neill, J., Lu, J., Dockter, R., and Kowalewski, T. (2015). Practical, stretchable smart skin sensors for contact-aware robots in safe and collaborative interactions. In *2015 IEEE International Conference on Robotics and Automation (ICRA)*, pages 624–629. IEEE.

[101] Owen-Hill, A. (2016). Force_Sensors_in_Robotics_Research. *Robotics Research 101: How Do Force Sensors Work?". Blog.robotiq.com. N.p., 2016. Web. 22 June*.

[102] Pahl, G., Beitz, W., Feldhusen, J., and Grote, K.-H. (2007). *Embodiment Design*, pages 227–438. Springer London, London.

[103] Paine, N., S. Mehling, J., Holley, J., Radford, N., Johnson, G., Fok, C., and Sentis, L. (2015). Actuator Control for the NASA-JSC Valkyrie Humanoid Robot: A Decoupled Dynamics Approach for Torque Control of Series Elastic Robots. *Journal of Field Robotics*, 32.

[104] Parmiggiani, A., Maggiali, M., Natale, L., Nori, F., Schmitz, A., Tsagarakis, N. G., Victor, J. S., Becchi, F., Sandini, G., and Metta, G. (2012). The Design of the iCub Humanoid Robot. *International Journal of Humanoid Robotics*, 09(04).

[105] Pham, T.-H., Caron, S., and Kheddar, A. (2018). Multicontact Interaction Force Sensing From Whole-Body Motion Capture. *IEEE Transactions on Industrial Informatics*, 14(6):2343–2352.

[106] Pucci, D., Romano, F., Traversaro, S., and Nori, F. (2016). Highly dynamic balancing via force control. In *2016 IEEE-RAS 16th International Conference on Humanoid Robots (Humanoids)*.

[107] Qiang Huang and Nakamura, Y. (2005). Sensory reflex control for humanoid walking. *IEEE Transactions on Robotics*, 21(5):977–984.

[108] Raucent, B., Campion, G., Bastin, G., Samin, J., and Willems, P. (1991). On the identification of the barycentric parameters of robot manipulators from external measurements. In *Proceedings. 1991 IEEE International Conference on Robotics and Automation*, pages 1169–1174. IEEE Comput. Soc. Press.

[109] Ren, C., Gong, Y., Jia, F., and Wang, X. (2016). Theoretical analysis of a six-axis force/torque sensor with overload protection for polishing robot. In *2016 23rd International Conference on Mechatronics and Machine Vision in Practice (M2VIP)*, pages 1–6. IEEE.

[110] Romano, F., Nava, G., Azad, M., Camernik, J., Dafarra, S., Dermy, O., Latella, C., Lazzaroni, M., Lober, R., Lorenzini, M., Pucci, D., Sigaud, O., Traversaro, S., Babic, J., Ivaldi, S., Mistry, M., Padois, V., and Nori, F. (2018). The CoDyCo Project Achievements and Beyond: Toward Human Aware Whole-Body Controllers for Physical Human Robot Interaction. *IEEE Robotics and Automation Letters*, 3(1):516–523.

[111] Romualdi, G., Dafarra, S., Hu, Y., and Pucci, D. (2018). A Benchmarking of DCM Based Architectures for Position and Velocity Controlled Walking of Humanoid Robots.

[112] Roozbahani, H., Fakhrizadeh, A., Haario, H., and Handroos, H. (2013). Novel Online Re-Calibration Method for Multi-Axis Force/Torque Sensor of ITER Welding/Machining Robot. *IEEE Sensors Journal*, 13(11):4432–4443.

[113] Rotella, N., Herzog, A., Schaal, S., and Righetti, L. (2015). Humanoid momentum estimation using sensed contact wrenches. In *2015 IEEE-RAS 15th International Conference on Humanoid Robots (Humanoids)*, pages 556–563. IEEE.

[114] Sandini, G., Metta, G., and Vernon, D. (2004). RobotCub: an open framework for research in embodied cognition. In *4th IEEE/RAS International Conference on Humanoid Robots, 2004.*, volume 1, pages 13–32. IEEE.

[115] Sardain, P. and Bessonnet, G. (2004). Forces Acting on a Biped Robot. Center of Pressure—Zero Moment Point. *IEEE Transactions on Systems, Man, and Cybernetics - Part A: Systems and Humans*, 34(5):630–637.

[116] Schneider, A. and Schmucker, U. (2006). Force sensing for multi-legged walking robots: Theory and experiments part 1: Overview and force sensing. In *Mobile robotics, moving intelligence*. InTech.

[117] Scibilia, A., Laghi, M., De Momi, E., Peternel, L., and Ajoudani, A. (2018). A Self-Adaptive Robot Control Framework for Improved Tracking and Interaction Performances in Low-Stiffness Teleoperation. In *2018 IEEE-RAS 18th International Conference on Humanoid Robots (Humanoids)*, pages 280–283. IEEE.

[118] Seminara, L., Pinna, L., Valle, M., Basirico, L., Loi, A., Cosseddu, P., Bonfiglio, A., Ascia, A., Biso, M., Ansaldo, A., Ricci, D., and Metta, G. (2013). Piezoelectric Polymer Transducer Arrays for Flexible Tactile Sensors. *IEEE Sensors Journal*, 13(10):4022–4029.

[119] Sentis, L., Jaeheung Park, and Khatib, O. (2010). Compliant Control of Multicontact and Center-of-Mass Behaviors in Humanoid Robots. *IEEE Transactions on Robotics*, 26(3):483–501.

[120] Shimano, B. and Roth, B. (1977). On force sensing information and its use in controlling manipulators. In *Proceedings of the IFAC International Symposium on information-Control Problems in Manufacturing Technology*, pages 119–126.

[121] Shujun Lu and Chung, J. (2005). Collision detection enabled weighted path planning: a wrist and base force/torque sensors approach. In *ICAR '05. Proceedings., 12th International Conference on Advanced Robotics, 2005.*, pages 165–170. IEEE.

[122] Siciliano, B. and Khatib, O. (2008). *Springer handbook of robotics*. Springer.

[123] Smith, S. (2014). Setra fuild guide to understanding pressure transducers. Technical report, Setra.

[124] Stassi, S., Cauda, V., Canavese, G., and Pirri, C. F. (2014). Flexible tactile sensing based on piezoresistive composites: A review. *Sensors*, 14(3):5296–5332.

[125] Sun, Y., Li, Y., Liu, Y., and Liu, H. (2014a). An online calibration method for six-dimensional force/torque sensor based on shape from motion combined with complex algorithm. In *2014 IEEE International Conference on Robotics and Biomimetics (ROBIO 2014)*, pages 2631–2636.

[126] Sun, Y., Liu, Y., and Liu, H. (2014b). Analysis calibration system error of six-dimension force/torque sensor for space robot. In *2014 IEEE International Conference on Mechatronics and Automation*, pages 347–352.

[127] Sun, Y., Liu, Y., and Liu, H. (2016). Temperature compensation for a six-axis force/torque sensor based on the particle swarm optimization least square support vector machine for space manipulator. *IEEE Sensors Journal*, 16(3):798–805.

[128] Tar, A. and Cserey, G. (2011). Development of a low cost 3D optical compliant tactile force sensor. In *2011 IEEE/ASME International Conference on Advanced Intelligent Mechatronics (AIM)*, pages 236–240. IEEE.

[129] Traversaro, S. (2017). *Modelling, Estimation and Identification of Humanoid Robots Dynamics*. PhD thesis, Italian Institute of Technology.

[130] Traversaro, S., Pucci, D., and Nori, F. (2015). In situ calibration of six-axis force-torque sensors using accelerometer measurements. In *2015 IEEE International Conference on Robotics and Automation (ICRA)*, pages 2111–2116.

[131] Traversaro, S., Pucci, D., and Nori, F. (2017). A Unified View of the Equations of Motion used for Control Design of Humanoid Robots. *Submitted to Multibody System Dynamics*.

[132] Tsetserukou, D., Tadakuma, R., Kajimoto, H., and Tachi, S. (2006). Optical torque sensors for implementation of local impedance control of the arm of humanoid robot. In *Proceedings 2006 IEEE International Conference on Robotics and Automation, 2006. ICRA 2006.*, pages 1674–1679.

[133] Tsuji, T. and Hanyu, R. (2010). Fault tolerance measurement using a six-axis force/torque sensing system with redundancy. In *2010 IEEE/RSJ International Conference on Intelligent Robots and Systems*, pages 1890–1895. IEEE.

[134] Uchiyama, M., Bayo, E., and Palma-Villalon, E. (1991). A systematic design procedure to minimize a performance index for robot force sensors. *Journal of Dynamic Systems, Measurement, and Control*, 113(3):388–394.

[135] Valizadeh, A., Akbarzadeh, A., and Heravi, M. H. T. (2015). Effect of structural design parameters of a six-axis force/torque sensor using full factorial design. In *2015 3rd RSI International Conference on Robotics and Mechatronics (ICROM)*, pages 789–793. IEEE.

[136] Van Brussel, P., Belien, I., and Thielemans, I. (1986). Force sensing for advanced robot control. *Robotics*, 2(2):139–148.

[137] Vorndamme, J., Schappler, M., and Haddadin, S. (2017). Collision detection, isolation and identification for humanoids. In *2017 IEEE International Conference on Robotics and Automation (ICRA)*, pages 4754–4761. IEEE.

[138] Wang, Y., Liang, G., Mei, D., Zhu, L., and Chen, Z. (2016). A flexible capacitive tactile sensor array with high scanning speed for distributed contact force measurements. In *2016 IEEE 29th International Conference on Micro Electro Mechanical Systems (MEMS)*, pages 854–857. IEEE.

[139] Wang, Y., Zuo, G., Chen, X., and Liu, L. (2017). Strain Analysis of Six-Axis Force/Torque Sensors Based on Analytical Method. *IEEE Sensors Journal*, 17(14):4394–4404.

[140] Watson, P. C. and Drake, S. H. (1975). Pedestal and wrist force sensors for automatic assembly. In *Proceedings of the 5th International Symposium on Industrial Robots*, pages 501–511.

[141] Webster, J. G. (1999). *The measurement, instrumentation, and sensors handbook*. CRC Press published in cooperation with IEEE Press.

[142] Weiss Robotics (2013). KMS 40 Assembly and Operating Manual.

[143] Weng, S., Xia, Z., Deng, H., Gan, Y., and Xiong, J. (2016). Design of an overload protection device for six-axis force/torque sensors. In *2016 IEEE International Conference on Real-time Computing and Robotics (RCAR)*, pages 239–242. IEEE.

[144] West, H., Papadopoulos, E., Dubowsky, S., and Cheah, H. (1989). A method for estimating the mass properties of a manipulator by measuring the reaction moments at its base. In *Proceedings, 1989 International Conference on Robotics and Automation*, pages 1510–1516. IEEE Comput. Soc. Press.

[145] Wu, B. and Cai, P. (2013). Decoupling analysis of a sliding structure six-axis force/torque sensor. *Measurement Science Review*, 13(4):187–193.

[146] Wu, B., Wu, Z., and Shen, F. (2010). Research on calibration system error of 6-axis force/torque sensor integrated in humanoid robot foot. In *2010 8th World Congress on Intelligent Control and Automation*, pages 6878–6882.

[147] Wu, C.-h. W. C.-h. and Paul, R. P. P. R. P. (1980). Manipulator compliance based on joint torque control. *1980 19th IEEE Conference on Decision and Control including the Symposium on Adaptive Processes*, 19.

[148] Xu, K.-J., Li, C., and Zhu, Z.-N. (2007). Dynamic Modeling and Compensation of Robot Six-Axis Wrist Force/Torque Sensor. *IEEE Transactions on Instrumentation and Measurement*, 56(5):2094–2100.

[149] Xu Chunshan, Wang Jianping, Cao Guangi, and Zhao Xifang (2004). Design of a new current sensing device for joint torque force control of the precision assembly robot. In *Fifth World Congress on Intelligent Control and Automation (IEEE Cat. No.04EX788)*, pages 4609–4613. IEEE.

[150] Yousef, H., Boukallel, M., and Althoefer, K. (2011). Tactile sensing for dexterous in-hand manipulation in robotics-A review. *Sensors and Actuators A: physical*, 167(2):171–187.

[151] Zarutckii, N. and Bulkin, R. (2016). Accuracy specifications of calibration device for force-torque sensors. In *2016 IEEE International Conference on Multisensor Fusion and Integration for Intelligent Systems (MFI)*, pages 78–83.

[152] Zhang, H., Ahmad, S., and Liu, G. (2015). Torque Estimation for Robotic Joint With Harmonic Drive Transmission Based on Position Measurements. *IEEE Transactions on Robotics*, 31(2):322–330.

[153] Ştefănescu, D. M. (2011). Classification of Elastic Elements. In *Handbook of Force Transducers*, pages 375–388. Springer Berlin Heidelberg, Berlin, Heidelberg.

Appendix A

Experimental Resources

This Chapter contains the detail of the resources used in the research presented in this thesis. Mainly specifications of the sensors and a description of the experimental platform.

A.1 Experimental Platform

The experimental platform is the iCub. It is a humanoid robot developed by the *iCub Facility* at the *Italian Institute of Technology*. It is a child-sized humanoid robot originally developed by the RobotCub European Project for research in embodied cognition [114].

It is 104 cm tall, weighs around 33 kg and has 53 degrees of freedom (DoF). The DoFs are distributed as follows: 6 for each leg, 3 for the torso, 6 for the head and eyes, 7 for each arm and 9 for each hand. One additional servo motor is used to open and close the eyelids. In this thesis, we consider only a subset of 32 DOFs (legs, torso, arms, and neck) that are actuated with Brushless DC electric motor (BLDC) with an Harmonic Drive transmission, making them suitable for joint torque control. The version of iCub used is known as 2.5. More details on the actuation and mechanics of the iCub 2.5 can be found in [104]. An image of the robot is presented in Fig. A.1.

The iCub has various sensors including inertial measurement units (IMU), force-torque (FT) sensors, cameras, microphones, joint encoders and tactile sensor arrays, that cover the surface of the robot. Six custom-made six axis FT sensors (described in A.2.1) are placed as shown in Fig. A.2. The force-torque sensors mounted on the arms of iCub are Strain 1. The ones in legs and feet are now Strain 2.

The distribution of the skin on the robot can be observed in Fig. A.2. The skin of iCub is described in A.2.3. The skin of iCub is calibrated using the vacuum bags, to create a uniform pressure distribution on the skin's surface that enables us to relate the capacitance value to

Fig. A.1 iCub 2.5, code name iCubGenova04

the applied pressure [66]. Therefore, we are able to know the pressure that is applied to each separate sensor in the array.

The interface to interact with the iCub is through Yet Another Robot Platform (YARP). More specifically, YARP supports building a robot control system as a collection of programs communicating in a peer-to-peer way, with an extensible family of connection types (tcp, udp, multicast, local, MPI, mjpg-over-http, XML/RPC, tcpros, ...) that can be swapped in and out.

A.2 Available Sensors

The thesis is focused on sensors that can be directly used as force-torque sensors. Therefore, the main sensors are six axis FT sensors and tactile sensor arrays. During the research, there were three varieties of six axis FT sensors. Two of them produced in IIT and an ATI mini 45 acquired for comparison. The RoboSkin is an artificial skin based on capacitive tactile sensor arrays. By mounting it in the covers of the robot, the sense of touch is distributed through the whole body of the robot.

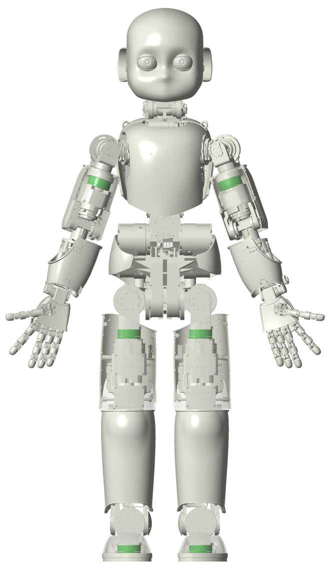

(a) The six axis FT sensors location on the iCub.

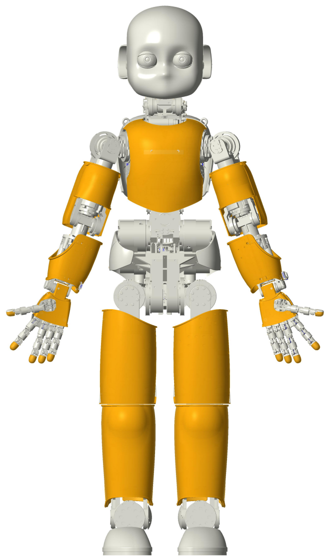

(b) Skin distribution on the iCub.

Fig. A.2 iCub sensors used to estimate external sensors

A.2.1 FTsense

The FT sense is a custom force-torque sensor produced in Istituto Italiano di Tecnologia (IIT) [45]. It has silicon strain gauges in Wheatstone bridge configuration. The signal conditioning and the analog to digital converters are embedded in the sensor. During the research, a new version of the sensor became available. To distinguish between them, the first will be called Strain 1 and the new Strain 2.

For both versions the maximum bandwidth is 500 Hz. Its dimensions are the same and can be seen in Fig. A.4. The orientation of the coordinate frame can be seen in Fig. A.5. They have a "Y" shape elastic element and provide six raw measurements also called channel signals, Fig. A.3.

Many FTsense Strain 1 and 2 where available for analysis due to the replacement of sensors on the robot and availability of different robots.

The ADC has a resolution of 16 bits. The sensors have a negative and positive measurements therefore the limit of the ADC is ± 32768. The sensor saturates if any individual channel reaches that value.

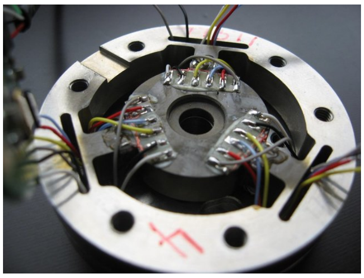

Fig. A.3 Ftsense elastic element.

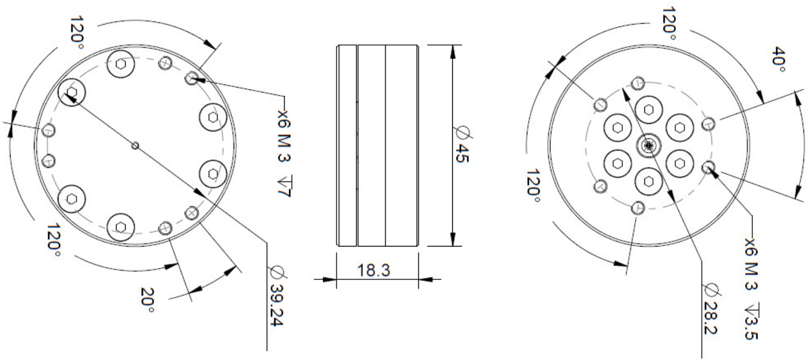

Fig. A.4 Ftsense CAD drawing.

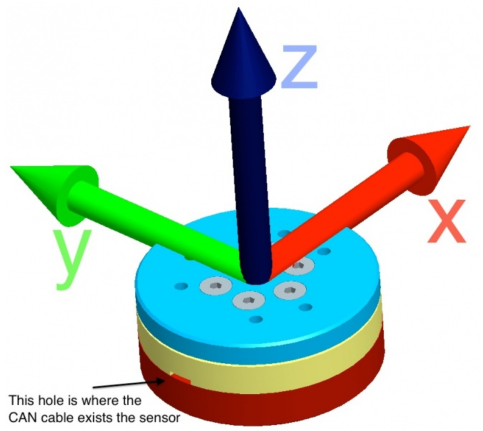

Fig. A.5 Coordinate Frame of FTsense.

Strain 1

The embedded electronics specifications are:

	Fx ,Fy	Fz	Tx,Ty	Tz
Range	1500 N	2000 N	35 Nm	25 Nm
Resolution	0.25 N	0.25 N	0.005 Nm	0.004 Nm

Table A.1 Ftsense strain 1 range specifications

- Power supply:5 V ±10%, current consumption max 100 mA, provided from CAN Bus connector.
- Communication :CAN Bus 2.0B, 1 Mbps Channels.
- Output data :16 bit, 6 channels, up to 1K messages/sec.
- Microcontroller :dsPIC30F4013 16 bit,30 MIPS, 48 K Flash, 2 K RAM, CAN, SPI.
- A/D Converter :16 bit, 250 ksps.
- Gain settings :Fixed analog gain.
- Offset correction :digital offset correction.

Unfortunately, the Wheatstone bridge configuration inside the sensor was designed for amplification of the signal, not for temperature compensation. Having a configuration for temperature compensation would have higher constraints in the arrangement of the strain gauges. Details on the range of the sensor can be seen in Table A.1. It weights 0.122 kg. Its dimensions are 45 mm of diameter and 18.4 mm of height.

Strain 2

Similar to Strain 1 no temperature compensation was done at hardware level. Nonetheless, the presence of extra sensors such as temperature sensors and IMU allow the possibility to explore software compensation. This extra information coupled with the option of variable gains allow for a much greater potential of the sensor. The temperature sensor was placed within 2 mm of the strain gauges.

The embedded electronics specifications are:

- Power supply:5 V ±10%, current consumption max 100 mA, provided from CAN Bus connector.
- Communication :CAN Bus 2.0B, 1 Mbps Channels.
- Output data :16 bit, 6 channels, up to 1K messages/sec.
- Microcontroller :STM32L4 Cortex M4 32 bit, 100 DMIPS, 512 KB Flash, 64 KB RAM, CAN, SPI, A/D.

	Fx ,Fy	Fz	Tx,Ty	Tz
Range	580 N	1160 N	20 Nm	20 Nm
Resolution	0.25 N	0.25 N	0.005 Nm	0.0026 Nm

Table A.2 ATI mini 45 range specifications

- A/D Converter :16 bit, 250 ksps.
- Gain settings :6 Independent Programmable Gain Amplifiers.
- Offset correction :digital offset correction.
- Additional Sensors :2 digital temperature sensor , 1 BOSCH IMU.

The sensor range and resolution vary due to the selected gains and the calibration procedure. The gains range are from 2.67 up to 9600. Higher the gain means higher sensitivity, so less force/torque range and higher accuracy.

So far using the gains [08,24,24,10,10,24], the sensor has been successfully used in a range of 800 N Fz, 20 Nm Tx and Ty, the excitation of the other axis were much lower.

A.2.2 ATI mini 45

The ATI Mini45 has a compact, low-profile design with high capacity and a through-hole to allow passage of linkages or cables, Fig. A.6. Made from high yield-strength stainless steel. With maximum allowable overload values are 5.7 to 25.3 times rated capacities. It uses silicon based strain gauges. This signal is amplified, resulting in near-zero noise distortion. It requires a netbox which outputs an Ethernet connection. The maximum bandwidth is 7000 Hz. The maximum amount of error for axis varies between 1.75% and 1% of the full scale. Details can be found in Table A.2. The ATI mini 45 was selected because the range was similar to the FTsense Strain 1. The mechanical structure was also very similar. This allowed to mount the sensor in the robot without the need of many adaptations. Special consideration had to be made since the orientation of the coordinate frame is different than the FTsense.

Fig. A.6 ATI mini 45.

A.2.3 RoboSKIN

The skin of iCub [21] is an array of capacitive pressure sensors composed of the flexible printed circuit boards (fPCB) covered by a layer of elastic fabric further enveloped by a thin conductive layer. As the skin is touched (i.e. pressure is increased), the distance between the capacitive sensors and the conductive layer decreases and therefore the capacitance increases. However, the sensors output the inverted values of the capacitance, and therefore the raw capacitance values of the sensors tend to decrease as the pressure is increased. Each sensor has 8 bits of resolution.

The skin is composed of triangular modules of 10 sensors each (shown on Fig. A.7), which act as capacitive pressure sensors, plus two temperature sensors for drift compensation. The temperature compensation is achieved by having two taxels that do not change capacitance based on the distance to the dielectric layers. This would imply that their change would only be induced by temperature change. The difference is then subtracted from the other taxels in the same triangle. This kind of temperature compensation works mainly for temperature change coming from the inside to the outside. The tactile sensors have a measurable pressure range up to 180 kPa [12]

The skin of iCub is divided into skin patches (also known as skin pieces) that consists of the mentioned triangular modules. The iCub has skin patches for forearms, arms, hands, torso, upper and lower legs. This patches can be appreciated on Fig. A.1, the distribution shown is mirrored under the covers on the other side. A single skin patch of iCub can have more than 500 individual tactile sensors. The skin is mainly used to detect contact locations.

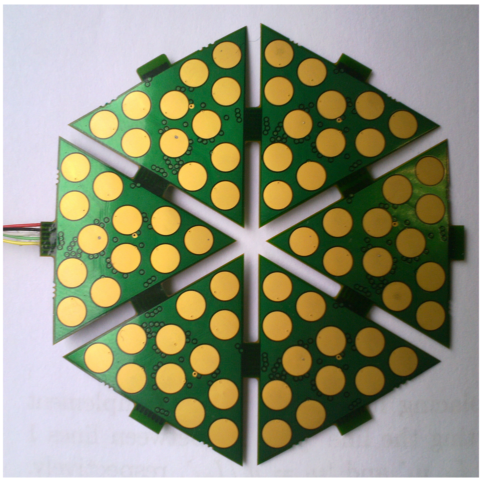

Fig. A.7 Patch of RoboSKIN.

Appendix B

Images from Sphere Analysis Tool

B.1 Mounting Tests

Here all the graphs from the 3rd trial of each test is shown.

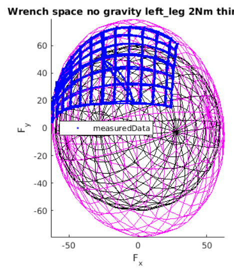

(a) x-y plane

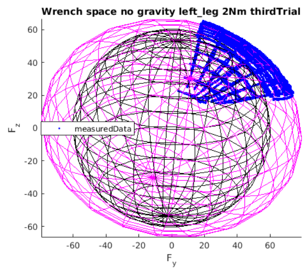

(b) y-z plane

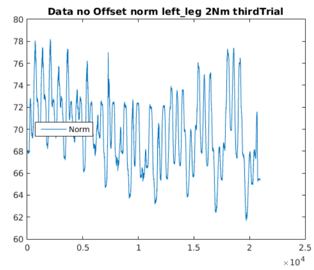

(c) Norm over samples

Fig. B.1 iCubGenova04 robot sensors ellipsoids, left leg 2Nm experiments

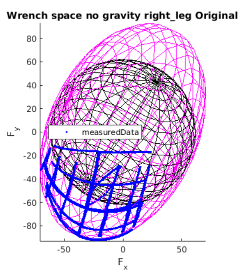

(a) x-y plane

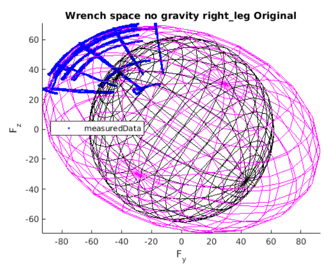

(b) y-z plane

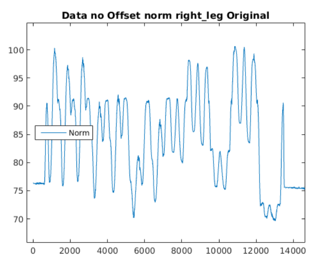

(c) Norm over samples

Fig. B.2 iCubGenova04 robot sensors ellipsoids, right leg unknown torque values experiments

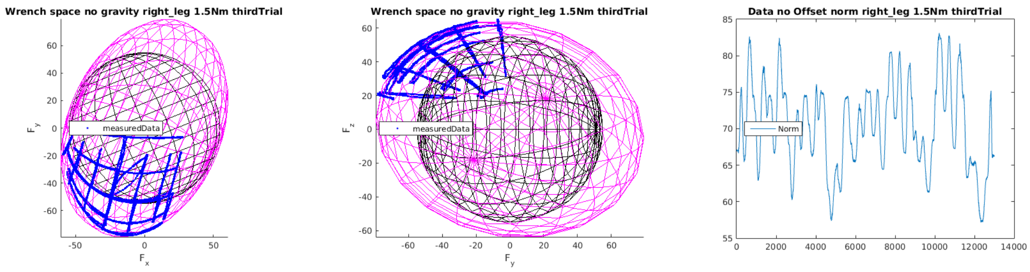

(a) x-y plane (b) y-z plane (c) Norm over samples

Fig. B.3 iCubGenova04 robot sensors ellipsoids, right leg 1.5Nm experiments

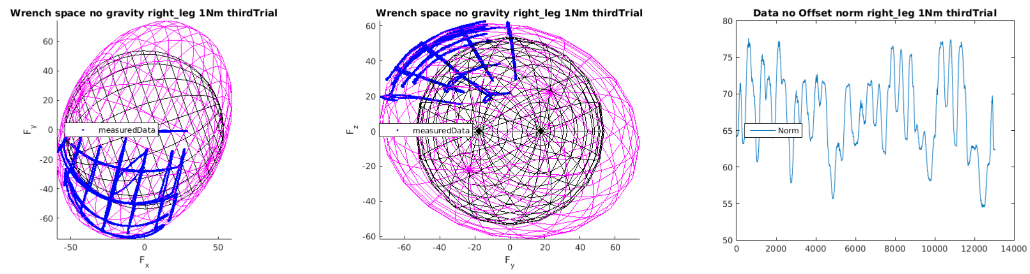

(a) x-y plane (b) y-z plane (c) Norm over samples

Fig. B.4 iCubGenova04 robot sensors ellipsoids, right leg 1Nm experiments

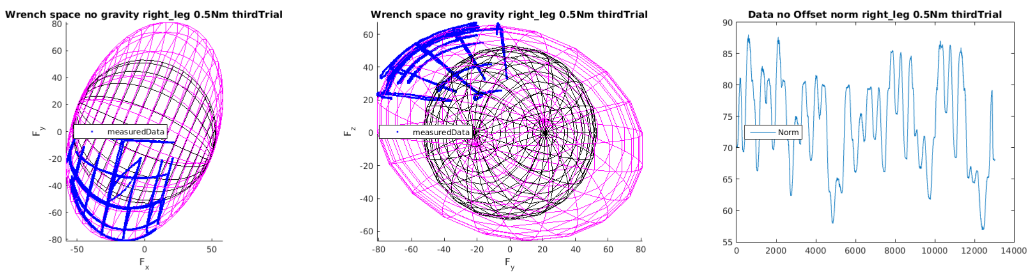

(a) x-y plane (b) y-z plane (c) Norm over samples

Fig. B.5 iCubGenova04 robot sensors ellipsoids, right leg 0.5Nm experiments

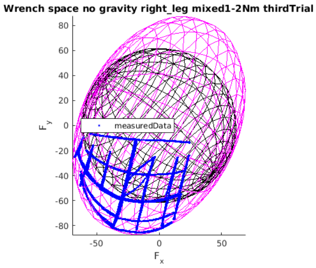

(a) x-y plane

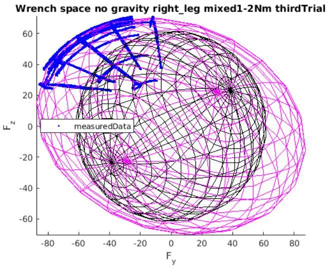

(b) y-z plane

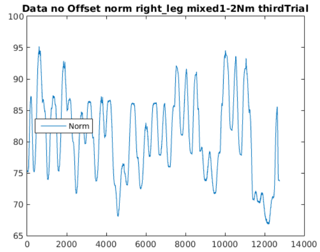

(c) Norm over samples

Fig. B.6 iCubGenova04 robot sensors ellipsoids, right leg mixed1-2Nm experiments

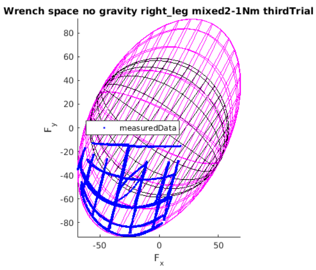

(a) x-y plane

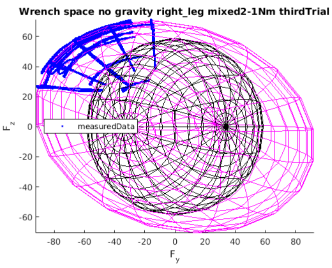

(b) y-z plane

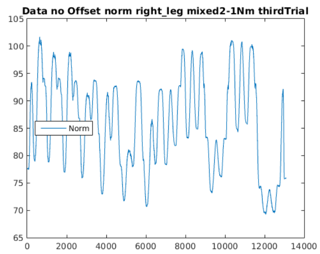

(c) Norm over samples

Fig. B.7 iCubGenova04 robot sensors ellipsoids, right leg mixed2-1Nm experiments

Appendix C

Getting 3D taxel positions and normals

The following steps are required to obtain the 3D taxel positions and the Normals.

Identify using the electronic logic documentation of the piece of skin and match the id of the spread sheet in which the id information is contained as in Fig. C.1. Since, the diagrams

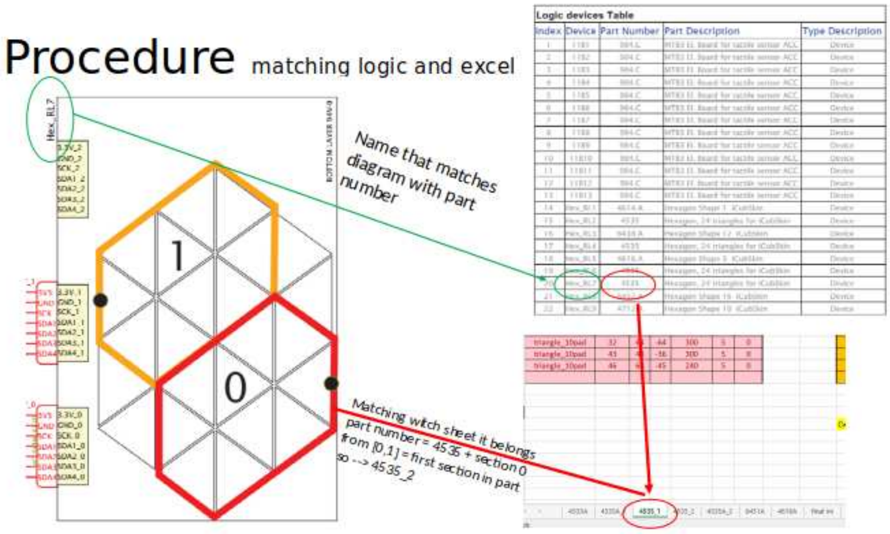

Fig. C.1 Match circuit logic with spread shit ID.

in the spreadsheet and the electronic circuit are from different views. The correct location is found by mirroring the image and then using a rotation by 90^o. This way the position of the piece of skin matches the position in the spread sheet diagram. Example shown in Fig. C.2. In the spread shit looking at the position and the number in the diagram the actual ID of the triangle can be identified following the logic depicted in Fig. C.3. Using this information the ID of the triangles can be stored. It is useful to add the information using the images of the mounting process documentation. That way we first match the ids into the 2D skin like in Fig.

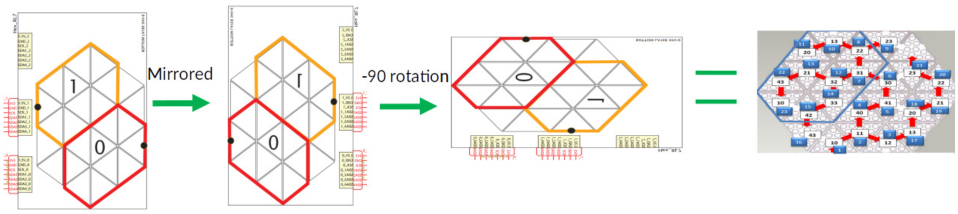

Fig. C.2 Transformations required to match ID of files.

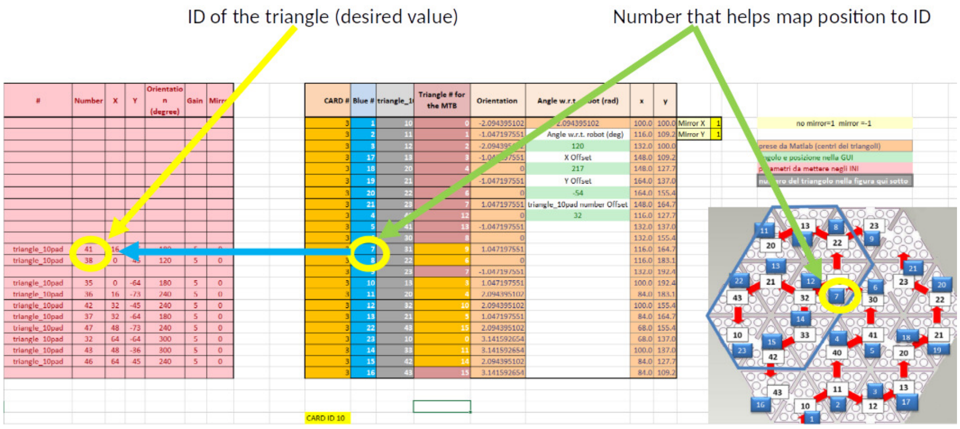

Fig. C.3 Finding the triangle ID

C.4. Later, we can identify which holes in the cover are actually covered by the skin and which holes are not by looking at the mounted skin as in Fig. C.5.

Fig. C.4 Cover and skin with number id.

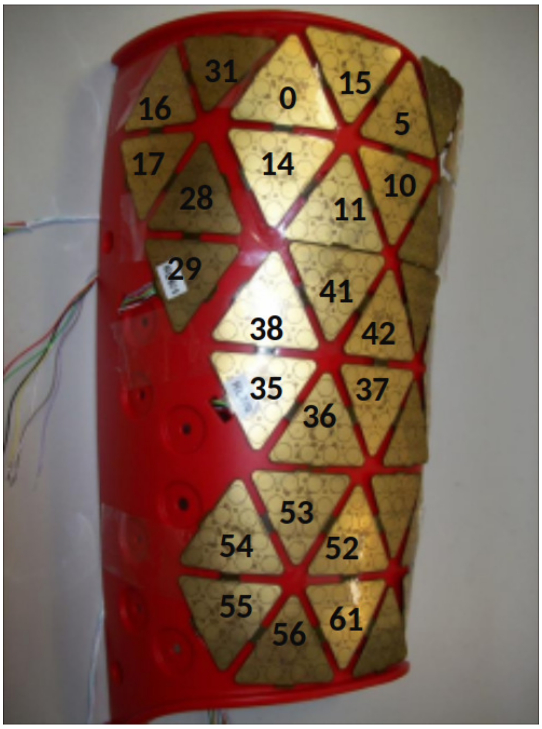

Fig. C.5 Numbers on Skin mounted on cover.

This information is useful when adding the frames in the CAD model. An image with the holes identified to be used and the ones that are not in the CAD format is used as base to add the frames. Example in Fig. C.6. The resulting frames are exported to a shrinkwrap which is the format actually used during the simmechanics export. They contain only the 3D position of the center of the triangle. The frames in the shrinkwrap are showed in Fig. C.7.

The cad is then exported to URDF including the new triangle center frames by following the simmechanics-to-URDF procedure as described in icub-mmodel-generator. The QR code for the link to the wiki/tutorial for the process can be found in Fig.C.8.

The export process includes a hard coded knowledge of the the reconstruction in 2D of the triangles and a interpolation procedure to get the 3D position and the normals of the taxels. The result is shown in Fig. C.9.

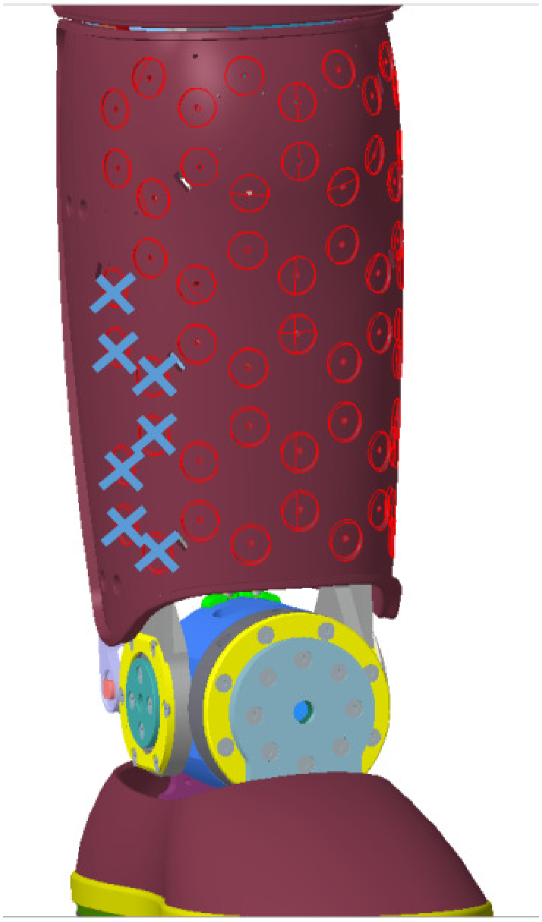

Fig. C.6 CAD with identified centers to use.

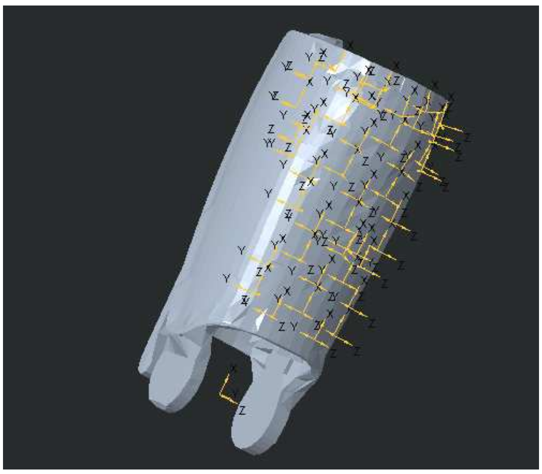

Fig. C.7 Frames added on CAD model.

Fig. C.8 QR for link to simmechanics to urdf tutorial.

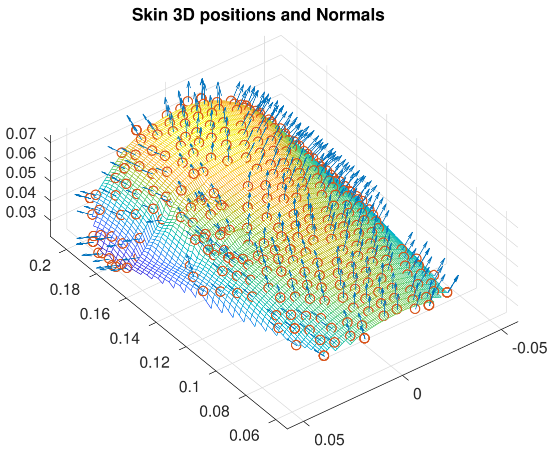

Fig. C.9 Plot using the generated 3D positions and normals.